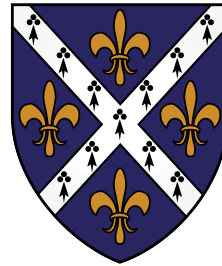# Biophysical Studies of Membrane Protein Structure and Function

Patricia M. Dijkman

St Hugh's College

University of Oxford

Thesis submitted to the Board of the Medical Sciences Division
in partial fulfilment of the requirements for the degree of

Doctor of Philosophy

Trinity term 2014

Abstract

Membrane proteins play a key role in numerous physiological processes such as transport, energy transduction in respiratory and photosynthetic systems, and signal transduction, and are of great pharmaceutical interest, comprising more than 60% of known drug targets. However, crystallisation of membrane proteins, and G protein-coupled receptors (GPCRs) in particular, still relies heavily on the use of protein engineering strategies, which have been shown to hamper protein activity. Here, a range of biophysical methods were used to study the structure and function of two membrane proteins, a prokaryotic peptide transporter, $PepT_{So}$ and a GPCR, neurotensin receptor 1 (NTS1), using different membrane reconstitution methods to study the proteins in a native-like environment. Firstly, using the pulsed EPR method of DEER (double electron-electron resonance) the conformation of $PepT_{So}$ reconstituted into lipid bilayers was assessed and compared to previous structural data obtained from crystallography and modelling. The influence of the membrane potential and the presence of substrate on the conformational heterogeneity of this proton-coupled transporter were investigated. Secondly, NTS1 purification was optimized for biophysical study. Cysteine mutants were created and a labelling procedure was developed and optimized for fluorophore and nitroxide labelling studies. NTS1 was then studied by continuous-wave EPR, to assess the influence of ligand on local protein dynamics, and to assess the structure of a receptor segment known as helix 8, that was proposed to be an α-helix, but was only observed to be helical in one of the NTS1 crystal structures. The signalling mechanism of NTS1 was also investigated using the novel biophysical method of microscale thermophoresis (MST) to assess the affinity of the receptor for G protein *in vitro* in the absence of ligand, or in the presence of agonist or antagonist. MST measurements were performed in detergent and in nanodiscs of different lipid compositions, to assess the influence of the lipid environment on receptor function. Finally, ensemble and single-molecule FRET, and DEER were combined to study the dimerisation interface of NTS1, showing novel dynamics of the interfacial associations. In summary, this thesis demonstrates the potential of biophysical techniques to study various aspects of membrane protein structure and function in native-like lipid systems, complementing *e.g.* structural data obtained from crystallographic studies with functional data for receptors in more native environments, as well as giving insights into protein dynamics. The work presented here provides novel insights into $PepT_{So}$ transport, and in particular into NTS1 structure, signalling, and oligomerisation, opening up several avenues for future research.

Acknowledgements

work towards optimising the labelling procedure of NTS1, and Patricia ("Paty") Suemy Kumagai, for her hard work in the NTS1 H8 EPR project, helping to express, purify, label and measure the many mutants!

To my friends and family.

To Stijn.

List of publications and presented work

Published

1. S.A.I. Seidel, **P.M. Dijkman**, W.A. Lea, M. Jerabek-Willemsen, A. Lazic, J.S. Joseph, P. Srinivasan, P. Baaske, A. Simeonov, I. Katritch, G. van den Bogaart, F.A. Melo, J.E. Ladbury, G. Schreiber, A. Watts, D. Braun, and S. Duhr, **Microscale thermophoresis quantifies biomolecular interactions under previously challenging conditions.** Methods, vol. 59, pp. 301-315, 2013.

2. A.D. Goddard, **P.M. Dijkman**, R.J. Adamson, and A. Watts, **Lipid-Dependent GPCR Dimerization.** Methods Cell Biol., vol. 117, pp. 341-357, 2013.

In preparation

3. P.W. Fowler, M.C. Orwick-Rydmark, S. Radestock, N. Solcan, **P.M. Dijkman**, J.A. Lyons, J. Kwok, M. Caffrey, A. Watts, L.R. Forrest, and S. Newstead, **Gating topology of the proton coupled oligopeptide symporters.** *(Submitted)*

4. A.D. Goddard, **P.M. Dijkman**, R.J. Adamson, R. Inácio dos Reis, and A. Watts, Working title: **Reconstitution of membrane proteins with a GPCR as an example.** Methods Enzymol. *(To be submitted)*

5. **P.M. Dijkman**, P. Suemy Kumagai, J.C. Muñoz García, P.J. Judge, and A. Watts, Working title: **Structure and local dynamics of membrane-reconstituted neurotensin receptor 1.** *(In preparation)*

6. **P.M. Dijkman**, A.D. Goddard, O.K. Castell, M.I. Wallace, and A. Watts, Working title: **Dynamic GPCR oligomerisation revealed for neurotensin receptor 1.** *(In preparation)*

7. **P.M. Dijkman**, and A. Watts, Working title: **Elucidating lipid dependence of early GPCR signalling using nanodiscs and microscale thermophoresis.** *(In preparation)*

Oral and poster presentations

1. **P.M. Dijkman**, M.C. Orwick, and A. Watts, **Probing conformational changes upon GPCR activation by DEER.** (Poster at 45th Annual International Meeting of the ESR Group of the RSC, Manchester, UK, 2012, *Awarded poster prize.*)

2. **P.M. Dijkman**, M.C. Orwick, and A. Watts, **Probing conformational changes upon GPCR activation by DEER.** (Poster at British Biophysical Society Biennial Meeting, Durham, UK, 2012, *Awarded poster prize.*)

3. P.W. Fowler, M.C. Orwick-Rydmark, S. Radestock, N. Solcan, **P.M. Dijkman**, J. Kwok, A. Watts, L.R. Forrest, and S. Newstead, **Probing membrane protein structure by double electron-electron resonance.** (Oral presentation at 1st Workshop CNRS-Oxford Membrane Proteins Network, Paris, France, 2012)

4. **P.M. Dijkman**, L.R. Forrest, P.W. Fowler, J. Kwok, S. Newstead, M.C. Orwick-Rydmark, S. Radestock, F. Samsudin, N. Solcan, and A. Watts, **Probing membrane protein structure and dynamics by DEER modelling and MD.** (Oral presentation at Bionanotechnology - Recent Advances Satellite Meeting to the 9th European Biophysics Congress, Sesimbra, Portugal, 2013, *Awarded presentation prize.*)

5. **P.M. Dijkman**, A.D. Goddard, and A. Watts, **Probing G protein-coupled receptor dimerisation by FRET and DEER.** (Poster at 9th European Biophysics Congress, Lisbon, Portugal, 2013)

6. **P.M. Dijkman**, A.D. Goddard, O.K. Castell, M.I. Wallace, and A. Watts, **Probing G protein-coupled receptor dimerisation by FRET and DEER.** (Poster at 58th Annual Meeting of the Biophysical Society, San Francisco, US, 2014)

7. **P.M. Dijkman**, A.D. Goddard, O.K. Castell, M.I. Wallace, and A. Watts, **Dynamic GPCR dimerisation shown by pulsed EPR, and ensemble and single molecule FRET.** (Oral presentation at Bio-NMR Workshop, Oxford, UK, 2014)

8. **P.M. Dijkman**, A.D. Goddard, O.K. Castell, M.I. Wallace, and A. Watts, **Dynamic GPCR dimerisation shown by ensemble and single molecule FRET, and DEER.** (Oral presentation at GLISTEN, Budapest, Hungary, 2014)

Contents

List of figures

List of tables

Abbreviations

A	hyperfine coupling tensor
A488/555/647	Alexa Fluor 488/555/647
AFM	atomic force microscopy
B	magnetic field
BLM	black lipid membrane
BPL	porcine brain polar lipid extract
CHAPS	3-[(3-cholamidopropyl)-dimethylammonio]-1-propanesulfonate
cAMP	3'-5'-cyclic adenosine monophosphate
CFP	cyan fluorescent protein
CHS	cholesteryl hemisuccinate
CHO	Chinese hamster ovary cells
CMC	critical micellar concentration
CV	column volume
CW(-EPR)	continuous wave (EPR)
ΔC	cysteine-depleted (NTS1B)
$D_{(T)}$	(thermo)diffusion coefficient
DDM	n-dodecyl-β-D-maltoside
DEER	double electron-electron resonance
DIB	droplet-interface bilayer
DLS	dynamic light scattering
DMPC	1,2-dimyristoyl-sn-glycero-3-phosphocholine
DMSO	dimethylsulfoxide
DOPC	di-oleoyl-sn-glycero-3-phosphocholine
DOPE	di-oleoyl-sn-glycero-3-phosphoethanolamine
DPC	n-dodecyl-phosphocholine
DPhPC	1,2-diphytanoyl-sn-glycero-3-phosphocholine
DTT	dithiolthreitol
ε	extinction coefficient
E	energy or resonance energy transfer efficiency (in FRET)
EC	extracellular (loop)
EDTA	ethylenediaminetetraacetate
EM	electron microscopy
EPR	electron paramagnetic resonance
ESR	electron spin resonance
FP	fluorescent polarisation or fluorescent protein
FRAP	fluorescence recovery after photobleaching
FRET	Förster resonance energy transfer
g	g (value) tensor
Gα	α subunit of the heterotrimeric G protein
Gβγ	βγ subunit dimer of the heterotrimeric G protein
GABA	γ-amino butyric acid
GDP	guanosine diphosphate
GEF	guanine-nucleotide exchange factors
GFP	green fluorescent protein
GPCR	G protein-coupled receptor
GPI	glycosylphosphatididylinositol
G protein	Guanine nucleotide binding protein
GSL	glycosphingolipid
GTP	glycosylphosphatididylinositol
GTPγS	guanosine 5'-O-(3-thiotriphosphate)

GUV	giant unilamellar vesicle
$\hat{H}$	Hamiltonian operator
H	helix
IC	intracellular (loop)
IMAC	immobilized metal affinity chromatography
IP_3	phosphatidylinositol-4,5-bisphosphate
IPTG	isopropyl β-D-1-thiogalactopyranoside
IR	infrared
ITC	isothermal titration calorimetry
J	overlap integral (in FRET), exchange coupling (in EPR), flux (in MST)
κ	orientation factor (in FRET)
KPi	potassium phosphate
L:P	lipid-to-protein ratio
LUV	large unilamellar vesicle
μ_B	Bohr magneton
MBP	*E. coli* maltose binding protein
MSP	membrane scaffold protein
MST	microscale thermophoresis
MTS	(1-acetoxy-2,2,5,5-tetramethyl-δ-3-pyrroline-3-methyl)-methanethiosulfonate
MTSL	(2,2,5,5-tetramethyl-δ-3-pyrroline-1-oxyl-3-methyl)-methanethiosulfonate
MWCO	molecular weight cut-off
ν	frequency
NMR	nuclear magnetic resonance
NT	neurotensin (ELYENKPRRPYIL)
$NT_{8\text{-}13}$	C-terminal hexapeptide of NT (RRPYIL)
NTS1	neurotensin receptor 1
NTS1B	MBP-TEV-rT43NTS1-TEV-TrxA-His$_{10}$
NTS1BH$_6$	MBP-TEV-rT43NTS1-His$_6$-TEV-TrxA-His$_{10}$
OD	optical density
3p	3-pulse DEER
4p	4-pulse DEER
Φ	(fluorescence) quantum yield
PA	phosphatidic acid
PCR	polymerase chain reaction
PDB	protein data bank
PEGm	methoxypolyethylene glycol 5000 maleimide
PELDOR	pulsed electron-electron double resonance
PIPES	piperazine-N,N'-bis(2-ethanesulfonic acid)
PLC	phospholipase C
POPC	1-palmitoyl-2-oleoyl-*sn*-glycero-3-phosphocholine
POPE	1-palmitoyl-2-oleoyl-*sn*-glycero-3-phosphoethanolamine
POPG	1-palmitoyl-2-oleoyl-*sn*-glycero-3-phospho-(1'-*rac*-glycerol)
PS	phosphatidylserine
PI	phosphatidylinositol
Pr	probability
PROXYL	2,2,5,5-tetramethyl-1-pyrrolidinyloxy
r	interlabel distance
R_0	Förster radius
r.m.s.d.	root-mean-square deviation
ROI	region of interest
rpm	rotations per minute
RT	room temperature
rT43NTS1	N-terminally truncated NTS1
SDS	sodium dodecyl sulphate

SDS-PAGE	sodium dodecyl sulphate poly acrylamide gel electrophoresis
SDSL	site-directed spin labelling
SM	sphingomyelin
SMA	styrene maleic acid (polymer)
SPR	surface plasmon resonance
SR14	SR142948A (NTS1 antagonist)
SR48	SR48692 (NTS1 antagonist)
S_T	Soret coefficient
SUV	small unilamellar vesicle
τ_c	rotational correlation time
T_1	longitudinal relaxation time
T_2	transverse relaxation time
T4L	T4 lysozyme
TCEP	tris(2-carboxyethyl)phosphine
TEV	tobacco etch virus protease (recognition site)
T_m	phase memory
TM	transmembrane (helix)
Tris	2-amino-2-hydroxymethyl-1,3-propanediol
TrxA	*E. coli* thioredoxin
UV	ultraviolet
v/v	volume per volume
WT	wild-type
w/v	weight per volume
w/w	weight per weight
YFP	yellow fluorescent protein

1 | Introduction

1.1 Biological membranes

1.1.1 Lipids

Biological membranes form the boundaries of life, separating organisms from the outer world, cells from one another, and compartmentalising cellular processes. Membranes are made up of amphipathic lipids, whose hydrophobic tails have the propensity to self-associate, entropically driven by the aqueous environment of the cell with which their hydrophilic headgroups interact (Figure 1.1). Indeed, the importance of lipids is manifested by the fact that
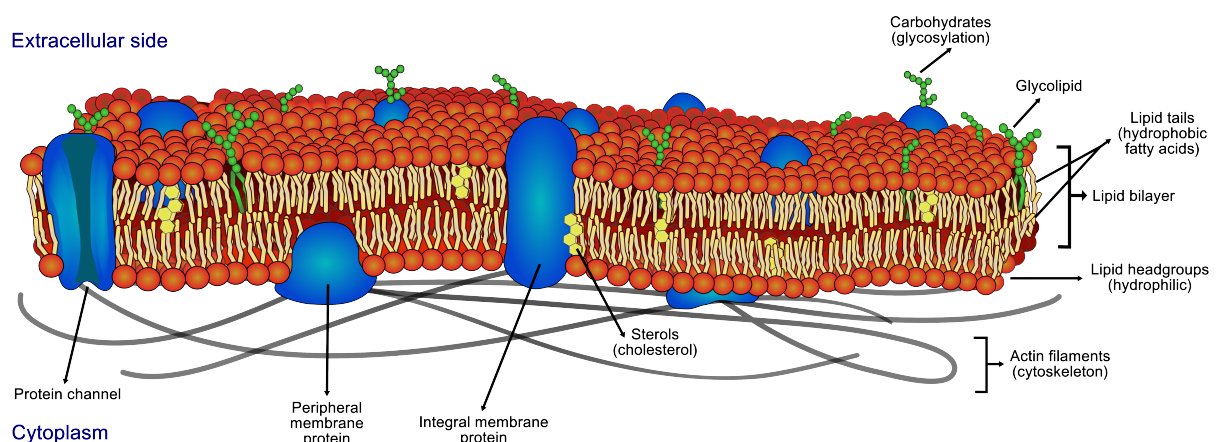
Figure 1.1: Biological membrane. Schematic of the plasma membrane, showing a lipid bilayer with integral and peripheral membrane proteins, sterols, glycolipids, protein glycosylation, and actin filaments from the cytoskeleton (adapted from wikipedia).

eukaryotic cells use about 5% of their genes to synthesise thousands of different lipids [1]. Most of this lipid synthesis takes place in the endoplasmic reticulum, followed by the Golgi apparatus and the mitochondria (although this can vary substantially in certain cell types), from which lipids are transported to other organelles and the plasma membrane via vesicular or protein-mediated transport [2]. Glycerophospholipids are the major structural lipids in eukaryotic membranes (Figure 1.2A). They are made up by fatty acids and phosphoric
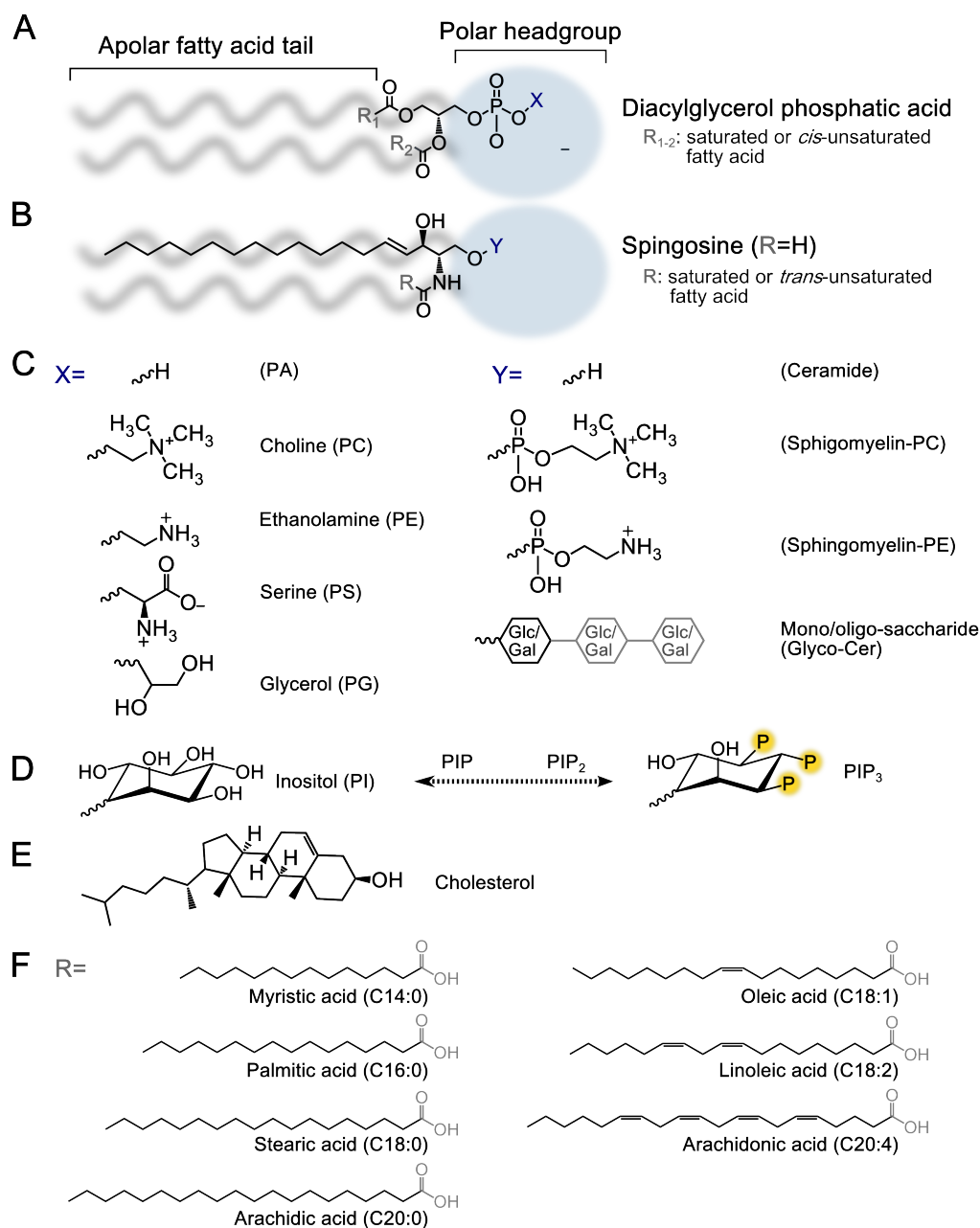
Figure 1.2: Biological lipids. The common structure for main classes of biological lipids found in eukaryotic membranes (**A**) glycerophospholipids and (**B**) sphingolipids are shown. They roughly consist of a hydrophilic headgroup (blue) and a hydrophobic tail (grey). Lipids can have a variety of headgroups (**C**). The inositol headgroup (**D**) can be phosphorylated resulting in the important signalling molecule PIP$_3$. Membranes also contain sterols, with (**E**) cholesterol being the sterol commonly found in mammals. (**F**) The lipid tails are composed of fatty acids. Common saturated (left) and *cis*-unsaturated (right) are shown, with the Cx:y code giving the number of carbons (x) and double bonds (y) present.

acid esterified to a glycerol moiety. The phosphoric acid is typically linked via a phosphoester bond to a variety of polar groups (Figure 1.2C), together forming the headgroup of the lipid. The main structural eukaryotic glycerophospholipids are phosphatidylcholine

(PC), phosphatidylethanolamine (PE), phosphatidylinositol (PI), phosphatidic acid (PA), and phosphatidylserine (PS). Positively charged headgroup moieties neutralize the negative charge of the phosphate, creating an overall neutral, zwitterionic lipid (PC, PE), while lipids with neutral headgroup moieties carry a net negative charge (PS, PG, PI). The diacylglycerol moiety contains saturated or *cis*-unsaturated acyl chains (Figure 1.2F). PC lipids are the most abundant, accounting for >50% of the phospholipids in most eukaryotic membranes [2]. They typically have one unsaturated chain, making them "fluid" at physiological temperatures, and nearly cylindrical in overall geometry, giving them a propensity to readily form planar bilayers. Other lipids, like PE (Figure 1.2C), have small or compact headgroups giving them an overall conical geometry, which imposes curvature stress onto membranes [3]. PE lipids are also able to form direct hydrogen bonds with other membrane(-associated) components [4]. The curvature imposed by conically shaped lipids can be used for budding, fission and fusion processes, but could also play a role in accommodating membrane proteins and potentially modulating their activity [5].

Apart from glycerophospholipids, sphingolipids are also found as structural lipids in eukaryotes (Figure 1.2B). Their basic structural unit is a ceramide moiety (sphingosine amide-linked to an acyl fatty acid), which in linked to a polar headgroup. In mammalian cells, the main sphingolipids are sphingomyelin (SM), which has a choline headgroup, and the glycosphingolipids (GSLs), which have an (oligo)saccharide headgroup. In contrast to the glycerophospholipids, sphingolipids have saturated or *trans*-unsaturated acyl chains, allowing them to adopt a taller and narrower cylindrical geometry for lipids of the same chain length. Furthermore, the amide group in the interfacial region of SM lipids can act as both a hydrogen bond donor and acceptor, whereas the carbonyl group in glycerophospholipids can only act an hydrogen bond acceptor [6]. Taken together, the cylindrical geometry of SM lipids and their ability to form both intra- and intermolecular hydrogen bonds allows them to pack more tightly [7]. This causes them to be in a solid gel phase (at physiological temperatures), which is turned into a liquid-ordered phase when sterols are present, where the lipid order is maintained, but lateral diffusion is faster than in the gel phase (see Figure 1.3) [8]. Indeed, sterols, and specifically cholesterol in mammals, are the main non-polar lipid in component of membranes (Figure 1.2E). Plasma membranes are relatively rich in sphingolipids and sterols compared to internal membranes, which has been suggested to make them more resistant to mechanical stress because of the denser packing [2]. Experiments have shown that sphingolipid-sterol patches can form laterally segregated microdomains within membranes, often called lipid 'rafts', which could play a role in signalling and trafficking, although their precise nature *in vivo* remains somewhat controversial [7–13].

The specific lipid content of membranes varies with species, cell type and organelle, as shown in Table 1.1, which gives an overview of the predominance of phospholipid headgroup composition for a few types of membrane. Membranes not only differ in their lipid headgroup composition but also in the types of fatty acyl chains, the length and saturation level of which can vary widely, from 12 up to 26 carbons with up to six double bonds (Figure 1.2F shows a few examples commonly found in biological membranes and used in model membranes) [14]. This diversity in lipid composition is likely to have consequences for the functionality of the different membranes and the proteins embedded therein [15].

Table 1.1: Phospholipid composition of different membranes. Typical composition of lipid headgroups of a few biological membranes is given, as well as the molar fraction of sterols (typically cholesterol) found. All are given in in mol% of total lipid content except for *Sf9* (whole cell) which is in weight%. Abbreviations: PC, phosphatidylcholine; PE, phosphatidylethanolamine; PS, phosphatidylserine; PG, phosphatidylglycerol; PI, phosphatidylinositol; PA, phosphatidic acid; SM, sphingomyelin; CL, cardiolipin; Synaps PM, Synaptosomal plasma membranes; Sf9, *Spodoptera frugiperda*; Ref., reference.

Cell type	Phospholipid composition (%)									Sterol (mol/mol)	Ref.
	PC	PE	PS	PG	PI	PA	SM	CL	Other		
E. coli inner membrane	-	70-80	-	15-20	-	-	-	5	-	-	[16]
Erythrocyte (human)	29	27	14	0	0.7	2	26	0	1.3	0.85	[17]
Erythrocyte (rat)	42	25	11.2	0	5	<0.3	12.8	0	4	0.37	[18, 19]
Synaps PM (rat brain)	41.6	34.2	13.2	0	3.5	0.3	5.1	0	2.1	0.45	[20]
Sf9 insect cells	35	36	-	-	23	-	-	4.6	1.4	0.04	[21]

1.1.2 Lipid signalling

Apart from their structural role, lipids also play a role in signalling, being able to act as first and second messengers. Hydrolysis of amphipathic lipid molecules results in hydrophobic components that can signal within the membrane, *e.g.* by recruiting proteins to the membrane, and in more hydrophilic components that can leave the membrane and interact with cytosolic signalling partners or membrane receptors. Phosphorylated PI moieties (PIP, PIP_2 and PIP_3, with phosphate groups added to the inositol headgroup, see Figure 1.2D) are especially well-known for their role in cell signalling [22, 23]. Large-scale lipid hydrolysis can also affect the physical properties of the membrane itself, as seen for example in the production of large quantities of ceramide during apoptosis [24]. However, typically, the levels of signalling lipids are very small compared to bulk lipid and they rely on site-specific transient high concentrations and combinatorial recognition for their effector function [25].

1.1.3 Membrane asymmetry

Another interesting feature of biological membranes is that they are asymmetric in their lipid distribution over the two leaflets. This asymmetry arises through (1) differences in physical properties of different lipids that enable them to readily cross the bilayer spontaneously or not, (2) retentive mechanisms that trap lipids in either leaflet, and (3) the presence or absence of transporters that mediate lipid translocation across the membrane [26]. The rate of spontaneous flipping of lipids between leaflets depends on their size, charge and the polarity of the headgroup. In model membranes it was shown to be slow for PC lipids and GSLs (hours-days) but fast for ceramide, diacylglycerol and sterols (seconds) [27–29]. Much slower rates ($t_{1/2} \approx 200$ min) were found for cholesterol in a more recent neutron scattering study [30], where the authors attributed the discrepancy to the chemical tags used in other studies, suggesting that active transport must play an important role in creating cholesterol asymmetry across the membrane as well. Indeed, many lipids depend on the activity of ATP-dependent transporters [31, 32]. Through these mechanisms the plasma membrane attains an asymmetric distribution with SM and GSL enriched on the outer leaflet and PS and PE lipids on the inner leaflet [33]. Some studies suggest that cholesterol is also enriched in the outer leaflet due to its affinity for sphingolipids, but the data is controversial [34].
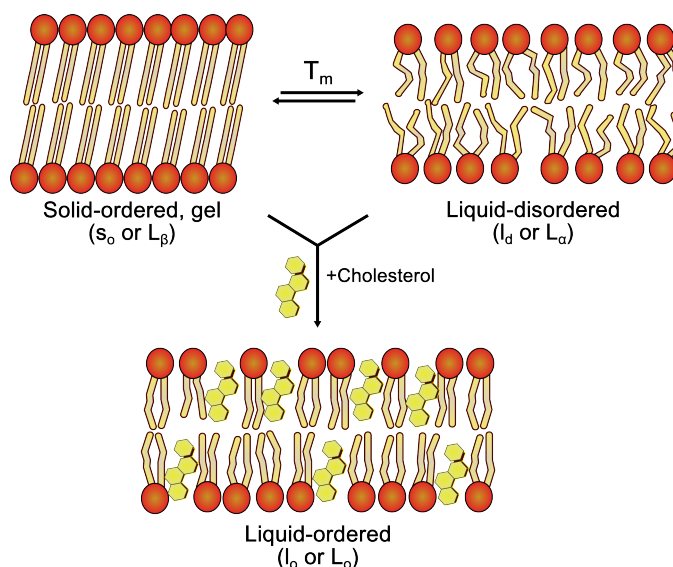
Figure 1.3: Membrane lipid phases. Schematic of phases lipids can adopt in a membrane: liquid-disordered phase (or liquid-crystalline), solid-ordered gel phase, and liquid-ordered phase. In the liquid-disordered phase diffusion is fast (~1 $\mu m^2 s^{-1}$), while it is slow in the gel phase (~10^{-3} $\mu m^2 s^{-1}$). In the liquid-ordered phase that is often described as a gel-phase "fluidized" by cholesterol, order is high as in the gel phase, but diffusion rates are similar to those in the liquid-disordered phase.

1.1.4 Lipid phase and membrane compartmentalization

Lipid bilayers can adopt different polymorphic phases (see Figure 1.3) depending on their physical properties and their environment, affecting the order in the bilayer and diffusion rates. Much of the work on the phase behaviour of lipids has been conducted in pure lipid vesicles of varying lipid content; under such conditions it was shown that lipids can segregate into large domains of liquid-ordered and liquid-disordered phase [35]. Studies on (living) cells, especially recently with the advent of single-molecule imaging techniques, suggest that the *in vivo* picture is more subtle; the consensus is that microdomains do exist, but that they are small and transient, and likely rely on lipid-protein and protein-protein interaction rather than solely on lipid-lipid interactions [36, 37]. This is not surprising, given that membrane proteins on average they make up approximately fifty percent of the dry weight of biological membranes. In addition, the cytoskeleton also influences lateral diffusion in the plasma membrane, acting as a 'fence' compartmentalizing the membrane into domains (~30-200 nm), between which membrane components can jump via so called 'hop diffusion' [12, 37]. This complex organisation of the plasma membrane is likely to influence protein function and signalling.

1.1.5 Lipid-protein interactions

Lipids can also modulate protein function and activity. Indeed, many examples can be found in the literature of proteins requiring specific lipids or classes of lipids, *e.g.* to bind ligand [38–40], to couple to intracellular signalling partners [41, 42], or to oligomerise [43, 44] (reviewed in [16]). Electron paramagnetic resonance (EPR) studies with spin-labelled lipids have shown that many proteins preferentially interact with negatively charged lipids, compared to neutral PC lipids [45]. Functional studies have shown that other membrane proteins require curvature-inducing lipids, such as PE, and often cholesterol [16, 40]. Acyl chain length also influences the protein-lipid interaction; discrepancy between the thickness of the apolar
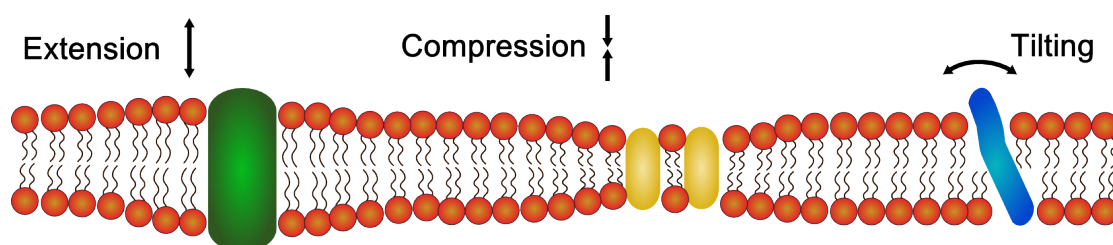
Figure 1.4: Hydrophobic mismatch. Schematic showing how proteins and lipids might be distorted to accommodate hydrophobic mismatch (discrepancy between the thickness of the apolar region lipid bilayer and that required by the transmembrane protein): extension or compression of acyl chains and/or tilting of the protein.

region of the lipid bilayer and the length of the hydrophobic portion of the transmembrane protein, called hydrophobic mismatch, can lead to distortions of the lipid and/or protein (Figure 1.4) [46]. For example, it was seen by x-ray scattering that the presence of gramicidin leads to stretching and thinning of a DLPC (C12) and DMPC (C14) bilayer, respectively [47]. Nuclear magnetic resonance (NMR) studies on the transmembrane helix of viral protein Vpu showed a linear dependency of helix tilt angle on acyl chain length [48]. Spin-label EPR studies on rhodopsin [49], and a fluorescence study with peptides [50] showed that in PC membranes integral membrane proteins interact more favourably/strongly with lipid that requires no change in the bilayer thickness. Taken together, these findings illustrate the importance of using the right, physiologically relevant, membrane mimetic in membrane protein *in vitro* studies.

1.2 Membrane proteins

1.2.1 Introduction

Membrane proteins represent a significant part of cellular membranes; but more importantly, they play a key role in numerous physiological processes, such as transport, energy transduction in respiratory and photosynthetic systems, and signal transduction. They make up about 30% of the total proteome of most organisms [51], and are of great pharmaceutical interest, comprising more than 60% of known drug targets [52, 53].

Membrane proteins can either be integral (or intrinsic), peripheral (or extrinsic), or lipid anchored (Figure 1.1). Peripheral membrane proteins are associated with the membrane without the polypeptide chain inserting in it. They can be bound to the membrane reversibly (amphitropic proteins), and regulated by their binding to the membrane, *e.g.* due to proximity of effector molecules or substrate, or structural changes induced by the binding [54]. They bind through interactions with integral membrane protein, and/or with the lipids themselves; apart from hydrophobic interactions [55] these are typically electrostatic interactions with charged residues and anionic lipids [56]. Some have specific lipid binding motifs, such as PH (pleckstrin homology) [57] or C2 domains [58], which bind phoshpolyrated PI lipid and negatively charged phospholipids, respectively, and are found in various kinases, phosphatases and phospholipases [59]. Apart from signalling and enzymatic functions, peripheral membrane proteins can have a structural role, *e.g.* linkage of the cytoskeleton to the membrane [60].

Lipid-anchored proteins are linked to the membrane via a glycosylphosphatididylinositol

(GPI) lipid. They are common in animals, making up approximately 0.5% of all eukaryotic proteins [61], and are typically found on the outer leaflet of the plasma membrane [62]. They have been shown to associate with sphingolipid/cholesterol-rich membrane domains ('rafts') in a cholesterol-dependent manner [63, 64]. The GPI anchor is typically linked to the protein close to its C-terminus via an ethanolamine moiety which is linked to the PI lipid via several sugar residues, and its sugar and fatty acid composition varies [65, 66]. GPI-anchored proteins have been shown to be important for viability in yeast and embryogenesis in higher eukaryotes, where GPI has been found to be anchored to a variety of proteins such as receptors, adhesion molecules, and enzymes [67].

Integral membrane proteins are embedded in the membrane. They can be either (1) mono-topic, inserted in the membrane without without traversing it; (2) bitopic, having only one transmembrane (TM) segment; or (3) polytopic, having multiple elements traversing the membrane connected by loops, with most membrane proteins falling into the latter two cat-egories. So far only α-helical and β-barrel intrinsic protein structures have been found [51]. Helical integral membrane proteins are made up of one or more α-helices of ~15-30 amino acids spanning the membrane bilayer [68]. The TM region contains mostly hydrophobic residues with the chains pointing outwards, shielding the imino and carbonyl groups, sta-bilised by van der Waals interactions with the hydrophobic membrane core. Several studies have looked at the overall distribution of amino acids in transmembrane proteins, and found that hydrophobic residues (Ala, Ile, Val, Leu) are most prevalent in the middle of the TM section, while the number of aromatic residues (Tyr and Trp, but not Phe) peaks at the interface region of the membrane, in both α-helical and β-barrel proteins [69]. These aro-matic residues are thought to be help position the TM protein in the membrane correctly, through complex electrostatic interactions of the flat rigid ring with the hydrophobic core [70]. Basic and acidic residues are encountered less frequently in TM sections, but are not entirely excluded and can be found *e.g.* in salt bridges that neutralise the overall charge, or in co-factor binding sites [71]. Polar residues are sometimes accommodated by 'snorkelling', where the polar group is oriented towards the interface, which is most often seen for Tyr, Lys and Arg [72, 73], although other polar residues (Asp, Glu, Asn, and Gln) can also snorkel [74]. Positively charged residues are found more frequently on the cytoplasmic side than on the exoplasmic side of the protein ("positive-inside rule") [75, 76]. Interestingly, the helix-breaking amino acids glycine and proline are commonly found in TM helices, and the kinks they introduce are thought to aid close protein packing [77]. Hydrogen bonds are also important in TM protein packing, and in "capping" of TM segments through interaction of an H-bond donor residue with the backbone carbonyl [78]. They have also been found to be

important in oligomerisation interfaces [79, 80].

Both integral and peripheral membrane proteins can also have post-translational modifications, *e.g.* acylation or prenylation, that penetrate the bilayer, (further) anchoring the protein to the membrane [81]. Acylated proteins typically have a myristoyl (C14) or palmitoyl (C16) group added to N-terminal Gly or to Ser/Cys groups, respectively, and can have multiple acyl anchors ensuring stable attachment to the membrane. Prenylated proteins are modified with terpenes, typically farnesyl or genarylgenaryl, via a thioether link to Cys. Prenylated proteins are generally found on the intracellular side of the membrane; for example, the Ras superfamily of GTPases interact with the plasma membrane via farnesyl [82]. Guanine nucleotide binding (G) proteins are also post-translationally modified, with the Gα subunit being acylated and the Gγ subunit prenylated, aiding their interaction with the transmembrane G protein-coupled receptors (GPCRs) [83].

1.2.2 Transporters

Biological membranes form a permeability barrier, regulating passage of substances across the membrane. They are permeable to gasses such as O_2 and CO_2, and somewhat permeable to small uncharged polar molecules like urea and ethanol, and to a lesser extent water, which can cross the membrane down their concentration gradient by passive (normal) diffusion, at a rate dependent on molecule size, charge and hydrophobicity [84]. Membrane protein transporters are responsible for the uptake of most other molecules for which the membrane is normally impermeable, or for increasing the rate of transport of poorly permeable molecules such as water. These proteins are highly important for cell function, not only regulating the uptake of metabolites and nutrients, but also maintaining the ionic balance in cells, and thus the electric potential, regulating cell pH, and playing a major role in osmoregulation [85]. They also play crucial roles in neuronal signalling, where they are responsible for signal detecting in the synapses either directly (ligand-gated ion channels) or indirectly (GPCR signalling-dependent ion channels), and for signal propagation along axons [86, 87]. Some transporters also have the ability to take up drugs and are thus major targets for improving the bioavailability of drugs [88].

Membrane protein transporters can be roughly divided into three classes (see Figure 1.5): channel proteins, ATP-powered pumps, and transporters (uniporters and cotransporters) [89]. Transport is generally specific with each protein only transporting one species or a group of closely related species. These proteins rely on cycles of conformational changes for
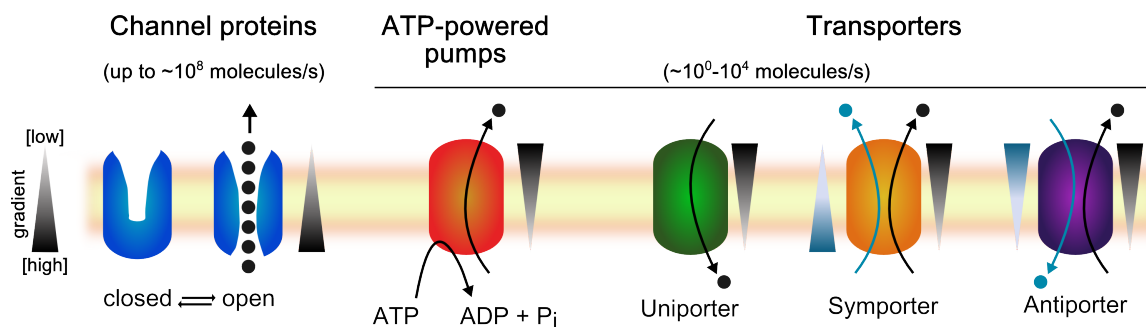
Figure 1.5: Membrane transport proteins. Schematic the three main classes of transporter proteins: ion channels, ATP-powered pumps and transporters.

transport in which they are alternately open to either site of the membrane [90–92]. Transport rates in channel proteins, which shuttle through a closed and open state in which many molecules can pass per cycle, are much higher (up to ~10^8 molecules/s) than those found for in ATP-powered pumps and the transporters (~$10^0 - 10^4$ molecules/s) in which only one or a few molecules can pass per cycle [85, 93–95]. The ATP-powered pumps are ATPases that use the energy of ATP hydrolyses to catalyse transport of a wide variety of molecules such as ions, toxins, drugs, lipids, peptides and proteins, against their concentration gradient (*i.e.* active transport) [95]. Channel proteins, such as ion channels and aquaporin, transport ions, water and small hydrophobic molecules down their concentration gradient (*i.e.* facilitated diffusion). Transporters (or carriers) facilitate the movement of ions and molecules such as sugars and amino acids. They can be either uniporters transporting one type of molecule down its concentration gradient, or cotransporters, which transport two substrates in the same (symporters) or opposite direction (antiporters) [89]. Cotransporters work through secondary active transport and use the energy stored in the electrochemical gradient across the membrane, coupling the thermodynamically favourable movement of one molecule down its concentration gradient to the unfavourable transport of another against its concentration gradient [96].

1.2.3 G protein-coupled receptors

GPCRs represent one of the largest families of proteins in mammals, accounting for ~1% of genome-encoded proteins. With over 800 GPCRs encoded for in the human genome, they form the largest class of cell surface receptors [97]. GPCRs are characterized by seven membrane-spanning α-helices connected by flexible loop regions (Figure 1.6). They can be grouped into five families, based on sequence similarities: family or class A (rhodopsin), B (secretin), C (glutamate), the adhesion receptors, and the frizzled-taste receptors [98]. The rhodopsin family is the largest by far with almost 700 members [99]. Although all have the
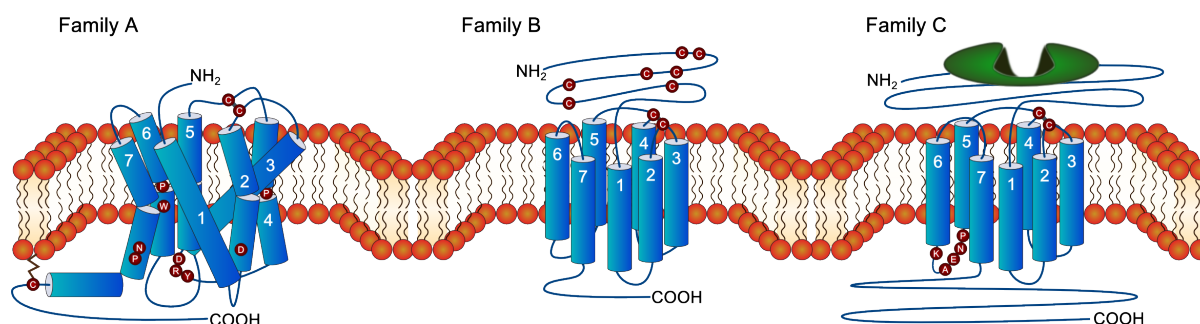
Figure 1.6: G protein-coupled receptor (GPCR). Schematic depiction of the three main families of GPCRs. All three are characterized by seven membrane-spanning α-helices connected by flexible loop regions. Conserved residues for each family are shown as red spheres. Family A, has several highly conserved residues and a disulfide bridge that connects extracellular loops 1 and 2, and most of the family A GPCRs have a palmitoylated cysteine in the carboxyl-terminus, which anchors it to the membrane. Family B GPCRs have a relatively long N-terminus, containing several cysteines. Family C GPCRs have a long C-terminus, and an overall large N-terminal domain which harbours the ligand-binding site (green). Figure redrawn from [100].

same 7-TM topology, the five families share little sequence identity (SI < 20% in the TM-domain) and differ substantially in their extracellular N-terminal domains [101]. GPCRs act as receptors for a plethora of different ligands, ranging from hormones, peptides, nucleotides and neurotransmitters, to lipids, ions, odours and photons, and they are involved in important physiological processes, including cell-to-cell communication, mediation of hormonal activity and sensory transduction [102]. In the classical G protein-coupled signalling mechanism, ligand binding on the extracellular side results in conformational changes in the receptor leading to activation of a heterotrimeric G protein (with an α, a β and a γ subunit) on the intracellular side, by catalysing GTP for GDP exchange on the heterotrimeric G protein α subunit [103]. This leads to a conformational change in the α subunit, causing the G protein to dissociate into the Gα and Gβγ subunit, which activate downstream effectors, leading to the generation of second messengers, and activation of signalling cascades and ultimately eliciting a range of cellular responses (see Figure 1.7). The activated α subunit hydrolyses its bound GTP to GDP which inactivates the subunit. The inactivated α subunit reforms an inactive complex with a βγ complex, turning off downstream signalling. Besides these G protein-coupled signalling pathways, GPCRs have also been shown to signal in a G protein-independent manner [105]. Activated receptors can signal, and activate G proteins until they are desensitised, typically through intracellular phosphorylation and subsequent recruitment of β-arrestins [106], or through phosphorylation-independent mechanisms [107]. Arrestin-bound GPCRs can be internalised via recruitment to clatherin-coated pits, and are then either dephosphorylated and recycled to the plasma membrane, degraded in lysosomes, or involved in the activation of new signalling pathways [108–110].
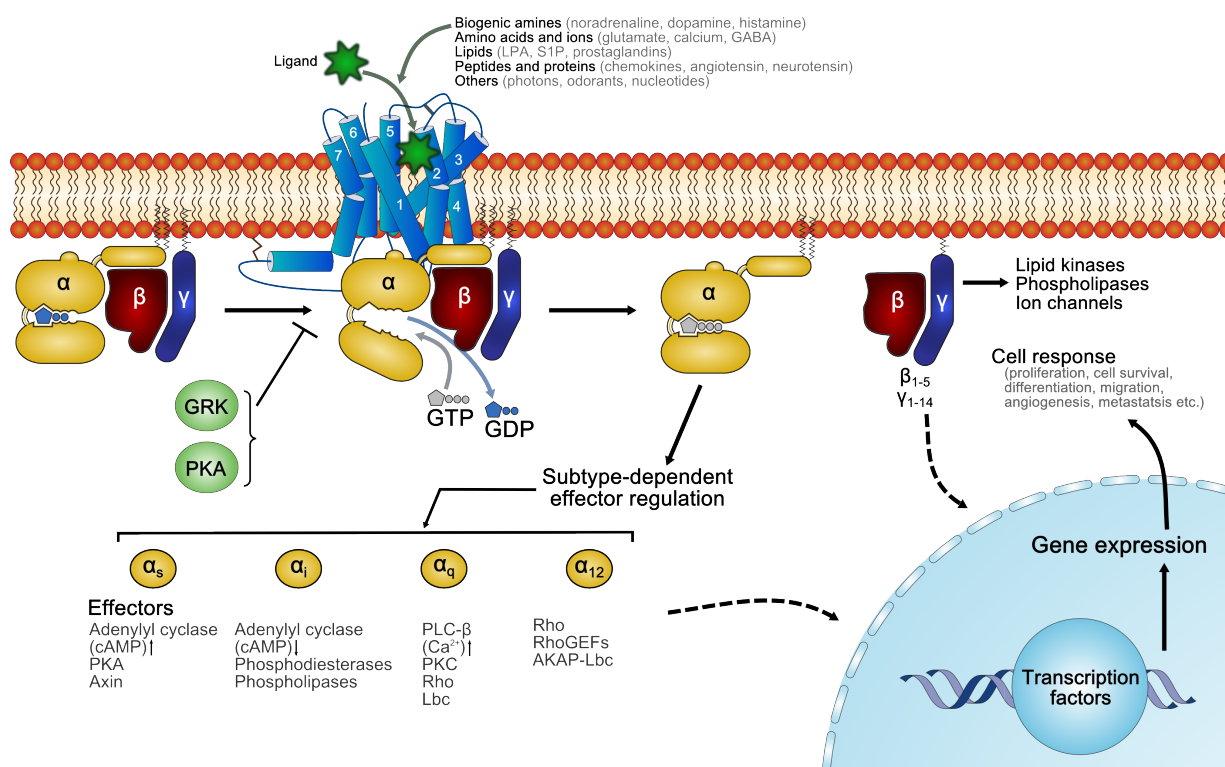
Figure 1.7: GPCR signalling. GPCRs bind a wide array of ligands (examples of different classes are shown). Agonist binding leads to conformational changes in the receptor and promotes interaction with heterotrimeric G proteins, composed of an α, β and γ subunit. Upon activation, GDP is exchanged for GTP in the Gα subunit. The activated G protein dissociates into Gα and G$\beta\gamma$, each of which can activate downstream effectors. The specific cell response depends on the G protein subtype; specific GPCRs can couple through one or more G protein subtypes. The four Gα subfamilies, Gα_s, Gα_i, Gα_q and Gα_{12} are indicated here, together with some of their associated downstream signalling targets. Typically signalling through Gα_s or Gα_i increases or decreases cAMP levels through stimulation and inhibition of adenylyl cyclase, respectively; Gα_q activates phospholipase C (PLC) leading to increased levels of diacylglycerol and IP$_3$ and raised calcium levels. G$\beta\gamma$ also activate a wide variety of effectors, such as ion channels, lipid kinases and phospholipases. The G protein subunits can also modulate cytosolic targets such as GTP-binding proteins (Ras and Rho families), mitogen-activated protein kinases (MAPK family), serine-threonine kinases (*e.g.* ERK, JNK, p38 and ERK5). These pathways lead to a variety of cellular responses (examples shown in grey), including cancer progression and metastasis. Activated receptors are de-activated through phosphorylation and subsequent processes. Other abbreviations: GABA, γ-aminobutyric acid; LPA, lysophosphatidic acid; S1P, sphingosine-1-phosphate; RhoGEFs, RhoGTPase nucleotide exchange factors (activate Rho); GRK, GPCR kinase; PKA and PKC, protein kinase A and C; AKAP-Lbc, A-kinase anchor protein (regulates PKA); lbc, lymphoid blast crisis (a RhoGEF). Figure based on [104], [100] and [102].

GPCRs are of enormous interest to the pharmaceutical industry, with ~40% of drugs acting as modulators of GPCR function, targeting a wide range of human diseases, such as allergic rhinitis, pain, hypertension and schizophrenia [52, 53, 111]. However, these drugs act on only approximately 5% of GPCRs, leaving ample opportunities for further drug discovery in the field of GPCRs [112]. A better structural and functional understanding of GPCRs would of course be beneficial as it can help target drug design.

1.3   Reconstitution of membrane proteins

1.3.1   Detergents

Purification of membrane proteins from heterologous expression systems usually requires solubilisation in detergents [113, 114]. Detergents are water-soluble amphiphilic surfactants, with a polar or ionic headgroup and a non-polar tail, that self-associate into spherical assemblies (micelles, Figure 1.8) in aqueous environments above a threshold concentration, the critical micellar concentration (CMC). They can be (1) ionic, having a charged headgroup, (2) non-ionic, or (3) zwitterionic [115, 116]. Non-ionic detergents, such as Triton X-100 and n-dodecyl-β-D-maltoside (DDM), are typically milder (less-denaturing) than ionic detergents, such as sodium dodecyl sulfate (SDS). However, the ionic derivatives of the naturally occurring bile salts, such as sodium cholate, which have a tetracyclic apolar region similar to that of cholesterol, are much less denaturing than hydrocarbon tail ionic detergents with the same headgroup. Zwitterionic detergents, such as CHAPS (3-[3-(cholamidopropyl) dimethyl-ammonio]-1-propanesulfonate, also a bile salt derivative), and LDAO (lauryldimethylamine oxide), combine the properties of ionic and non-ionic detergents, and can thus be useful in initial membrane solubilisation steps. Additionally, short-chain detergents (*e.g.* OG, *n*-octyl-β-D-maltoside) are typically more denaturing than their longer-chain counterparts (*e.g.* DDM). DDM and Triton X-100 are most widely used in membrane protein research because of their relative mildness, allowing retention of biological function, and are often used in combination with lipid or cholesterol-like additives (*e.g.* cholesteryl hemisuccinate, CHS) in mixed detergent-lipid micelles [115, 117]. Nevertheless, the extraction of membrane proteins from their lipid environment is often accompanied by a loss of activity and stability [115, 116, 118]. Thus membrane proteins are often reconstituted into lipid environments following purifications in detergents. Detergent can be removed by a variety of methods such as gel filtration, dialysis, and adsorption to polystyrene beads (*e.g.* Bio-Beads) [114, 119]. The first two methods work best for high CMC detergents, while the last is generally applicable.

1.3.2   Bicelles

Bicelles are a type of mixed detergent-lipid micelles, but with a more elongated rather than spherical structure, more closely mimicking a lipid membrane environment than regular micelles (Figure 1.8C) [120]. They are usually composed of short-chain phospholipids (*e.g.* DMPC), forming the main bilayer component, which is edge-stabilized by detergent (*e.g.* CHAPSO, 3-[(3-cholamidopropyl)dimethyl-ammonio]-2-hydroxyl-1-propanesulfonate) or a shorter-chain lipid (*e.g.* DHPC, 1,2-dihexanoyl-sn-glycero-3-PC). They are widely used in

NMR studies as their elongated structure allows them to be aligned in magnetic fields [121, 122].
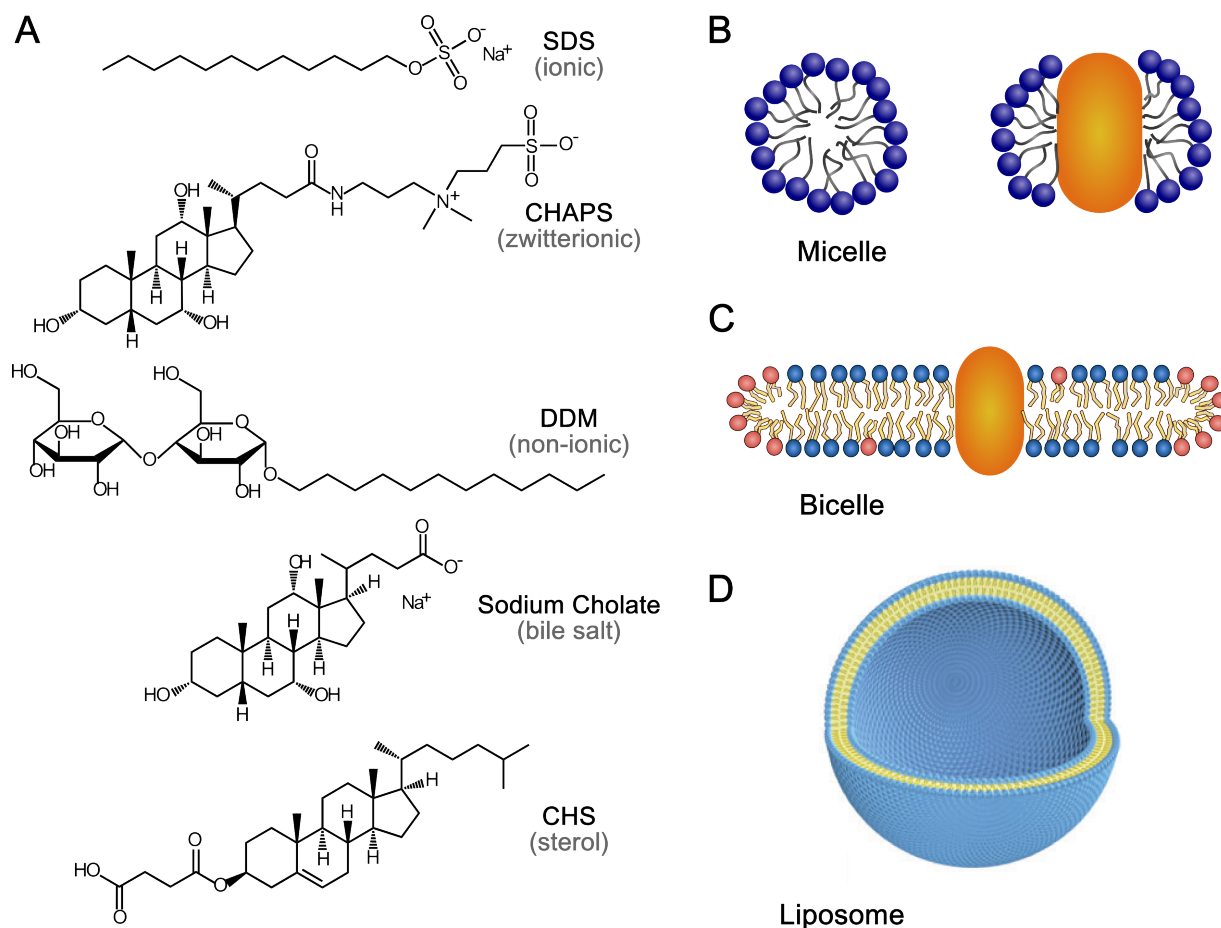
Figure 1.8: Detergents and membrane mimetics. **(A)** Structure of ionic, zwitterionic, non-ionic, and bile salt detergents used in this thesis are shown, as well as a cholesterol-like additive; SDS, sodium dodecyl sulfate; CHAPS, 3-[3-(cholamidopropyl) dimethyl-ammonio]-1-propanesulfonate; DDM, *n*-dodecyl-β-D-maltoside; CHS, cholesteryl hemisuccinate. **(B)** Schematic of cross-sectional view of a detergent micelle and a membrane protein surrounded by a micelle. **(C)** Schematic of a membrane protein incorporated into a bicelle. **(D)** Schematic of a unilamellar liposome (figure reproduced from [123]).

1.3.3 Planar lipid bilayers

Planar lipid bilayers are commonly used, for example in the form of black lipid membranes (BLMs) [124] or as supported bilayer systems on top of a solid support, such as glass, mica or gold [125]. BLMs stretch across small apertures separating two aqueous compartments, which can have varying ionic compositions to mimic the membrane electrochemical potential [126]. They can be used in conductance measurements to study channel activity [127, 128]. Supported bilayers are made by the fusion of lipid vesicles on surfaces in an aqueous environment or by the sequential deposition of monolayers [125, 129]. Artefacts can arise from the

solid support if extramembranous portions of inserted proteins adhere to the surface, and this can be counteracted by increasing the distance between the membrane and the support, *e.g.* by using lipid-tethered polymer cushions linked to the support [130]. Supported bilayers are used in many biophysical applications, such as atomic force microscopy, surface plasmon resonance, and fluorescence [131]. As both BLMs and supported bilayers can be made from separate monolayers, this provides a manner to control the lipid composition of each leaflet for making asymmetric bilayers.

1.3.4   Liposomes

Liposomes are closed vesicles of bilayer-forming lipids, encapsulating an aqueous lumen (Figure 1.8D) [123]. Unlike planar bilayers, they do not allow access to the inner compartment, but they can be preloaded with specific buffers and compounds from their formation medium. They can be either uni- or multilamellar, and can be further divided based on their size into four major classes: small unilamellar vesicles (SUVs); large unilamellar vesicles (LUVs); giant unilamellar vesicles (GUVs); and multilamellar vesicles (MLVs) [123, 132]. MLVs are made up concentric rings of bilayers, and vary in size from ~0.2-10 μm. They are made by shaking dried lipid films into aqueous solution. SUVs are made by extensive sonication of MLVs or extrusion through polycarbonate filters, and typically have diameters of ~20-50 nm. Their small size means they have very high curvature, making it difficult to incorporate protein. LUVs are larger, ranging from ~50-1000 nm, and have a larger encapsulated volume. They can be made *e.g.* by fusion of SUVs (through freeze-thaw cycles), and extrusion of MLVs. LUVs are generally preferred over SUVs, because their larger size and smaller curvature more closely resembles the membrane of biological cells [132, 133]. GUVs can have diameters in the range of ~5-300 μm. They can be made *e.g.* by slow hydration of lipid films followed by sucrose density gradients to purify them from MLVs, or by electroformation. GUVs are large enough to insert microelectrodes, to mechanically manipulate or to image surface sections by optical methods, but are much more fragile than LUVs [134]. Liposomes are routinely used for reconstituting membrane proteins into lipid bilayers, as they are relatively easy to form, and can be made with complex lipid mixes [123]. Another benefit is that, unlike discoidal reconstitution methods discussed below, they do not confine the protein into a small space, and thus do not hamper protein diffusion which is preferable when studying dynamic protein-protein interactions in the membrane which rely on lateral diffusion.

1.3.5   Nanodiscs

 Nanodiscs are a discoidal reconstitution method, developed by Sligar and co-workers [135, 136]. Discoidal reconstitution methods have the benefit over liposomes that they allow simultaneous access to both sides of the incorporated membrane protein. Nanodiscs consist
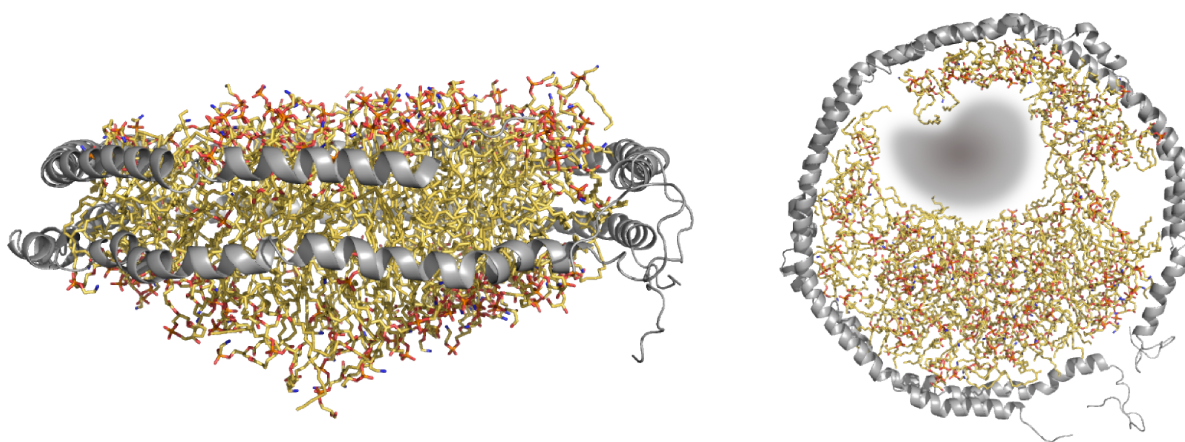
Figure 1.9: Nanodisc. Side (left) and top view (right) of a nanodiscs. Nanodiscs are discoidal lipid membranes stabilised by two copies of MSP (membrane scaffold protein, grey helices), which can be used to reconstitute membrane proteins (protein outline in shaded grey). Figure based on the structure SecYE-ribosome-nanodisc solved by cryo-EM (PDB ID:3J00 [137]), with the inserted protein removed and replaced by shaded outline in the top view.

of a lipid bilayer disc around which an amphiphilic so-called membrane scaffold protein (MSP) is wrapped (Figure 1.9). MSP is an engineered construct of the human apolipoprotein A-1, which is a plasma protein responsible for lipid transport in the blood [135]. A dimer of MSP wraps around a lipid bilayer forming a disc with a diameter of 10 nm or larger depending on the length of the MSP construct used; several constructs are available containing multiples of the same repeat domain, allowing formation of larger discs, to suit the incorporation of membrane proteins of varying sizes [138]. Nanodiscs can in principle be made with any bilayer forming lipids to suit individual protein requirements, although in practice some lipids yield better results than others, and reconstitution conditions need to be determined empirically for each membrane protein and lipid mix [139]. They have been successfully used in structural studies, *e.g.* of a tranlocase protein [137], and in functional studies of GPCRs investigating G protein and ligand binding, and dimerisation [42, 140–142].

1.3.6   Lipodisqs

Lipodisqs are similar to nanodiscs, forming discoidal particles in which both sides of the inserted membrane protein remain accessible [143]. Instead of using MSP, lipodisqs are formed using a styrene-maleic acid polymer (SMA). The use of a polymer rather than a

protein to form the discs makes them attractive for techniques such as protein NMR as it eliminates undesirable signals arising from the MSP belt. They are formed by mixing lipid suspensions with SMA; if these are mixed at a certain pH, the critical collapsing pH, the extended polymer looses its charge and collapses, and lipodisqs can spontaneously form. Unlike for the MSP construct used in nanodisc formation, the length of the polymer is not exactly fixed. This means that the range of particle sizes obtained in lipodisq formation can be more variable and experimental conditions may need to be adjusted to obtain a more homogeneous sample size, in combination with careful selection of sample fractions after size-exclusion chromatography (unpublished observations from our laboratory). Particle diameters of ~10-30 nm have been reported in the literature [144–146]. Lipodisqs have been used to reconstitute membrane proteins directly from (native) membranes, for example bacteriorhodopsin [144], mitochondrial complexes [147] and bacterial cell division machinery [145], or to reconstituted purified membrane proteins, for example after labelling for spectroscopy studies [148].

1.4   Biophysical methods to study membrane proteins

1.4.1   Introduction

Despite their obvious importance in biology, underlined by their prevalence, the variety of functions they perform, and their pharmaceutical relevance, membrane proteins are under-represented in the protein data bank (PDB) [149]. X-ray crystallography of membrane proteins is a field lagging behind, with relatively few crystal structures having been solved for membrane proteins compared to their soluble counterparts (Figure 1.10A). This is largely due to difficulties with heterologous expression, purification and crystallisation of membrane proteins [150]. However, recent experimental progress, especially in the field of GPCR crystallography, have lead to an exponential growth in the number of available structures (Figure 1.10B). This includes the use of lipidic-cubic-phase for crystallisation [152]; small antibodies, such as FABs and nanobodies, to stabilise protein conformations and complexes [153]; improved yields and/or sample quality by using alternative expression systems like baculovirus-induced insect cell expression [150, 154]; and the use of protein engineering to stabilize membrane proteins in detergents, such as thermostabilisation techniques [155]. Technological advances such as microfocus beamlines, and more recently x-ray free electron lasers, enable the use of small, even sub-micrometre-sized crystals, opening up the field to proteins which do not easily form large crystals [156, 157]. Although the use of lipidic-cubic-phase for the crystallisation of membrane proteins is becoming more widely spread [158], many are still being crystallised in detergents which are not always conducive to native
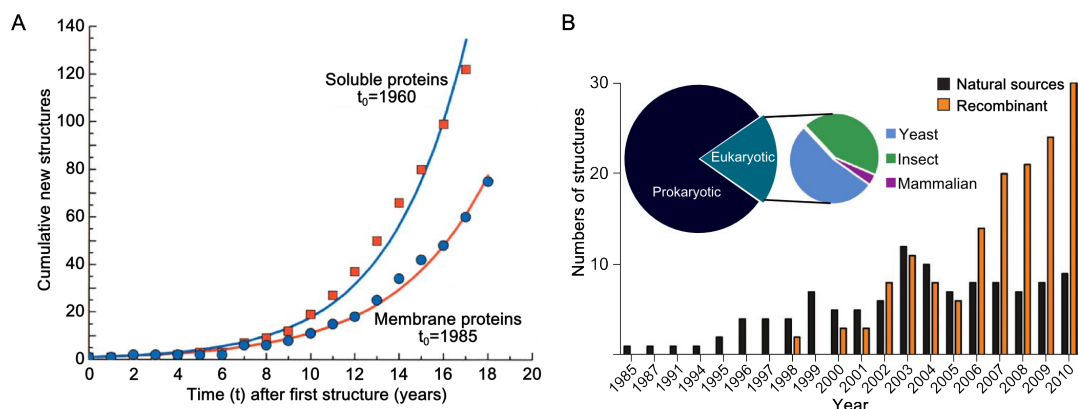
Figure 1.10: Progress in membrane protein structure determination. **(A)** Shows the cumulative totals of new high-resolution structures published since the publication of the first at t_0 for soluble proteins (red squares) and membrane proteins (blue circles); adapted from [151]. **(B)** Shows the progress in structures solved for membrane proteins; adapted from [150]. The circle diagram illustrates the proportional use of different types of host cells (prokaryotic or eukaryotic) for the production of recombinant membrane proteins. The bar diagram shows the number of new membrane protein structures deposited in the PDB per year, differentiating between structures solved using proteins from natural (black) or heterologous (orange) sources; this diagram illustrates that while early membrane protein structural biology relied largely on being able to obtain sufficient amounts of protein from natural sources, advances in heterologous expression of membrane proteins has seen an increase in structures determined of recombinant proteins.

structure; a recent review critically assessed a variety of structures of membrane proteins available in the PDB, concluding that many appeared to be distorted by the membrane mimetic (often detergent) used [159]. Despite these issues, crystallography has brought a wealth of knowledge on membrane protein structure and function. Nevertheless, there has been great effort in applying a wide range of other biophysical techniques, that allow working in more physiologically relevant environments, to obtain structural and functional data on membrane proteins and their dynamics, such as Förster resonance energy transfer (FRET), electron microscopy (EM), atomic force microscopy (AFM), nuclear magnetic resonance (NMR), and electron paramagnetic resonance (EPR) spectroscopy [160–165]. The relatively new technique microscale thermophoresis (MST) is also being applied to membrane proteins, mostly to study membrane protein-ligand interactions [166].

EPR, FRET and MST were used extensively in this work to study peptide transport (Chapter 2) and GPCR structure and function (Chapters 4, 5, and 6,), and will be discussed in more detail below.

1.4.2   Electron paramagnetic resonance

1.4.2.1   Introduction

Electron paramagnetic resonance, also called electron spin resonance (ESR), is a spectro-scopic technique which detects unpaired electrons, and can be used to study protein structure and dynamics. It is a magnetic resonance technique very similar to NMR; however, electronic instead of nuclear transitions are detected in an applied magnetic field (Figure 1.11). In continuous-wave (CW)-EPR continuous microwave frequency radiation is applied to the
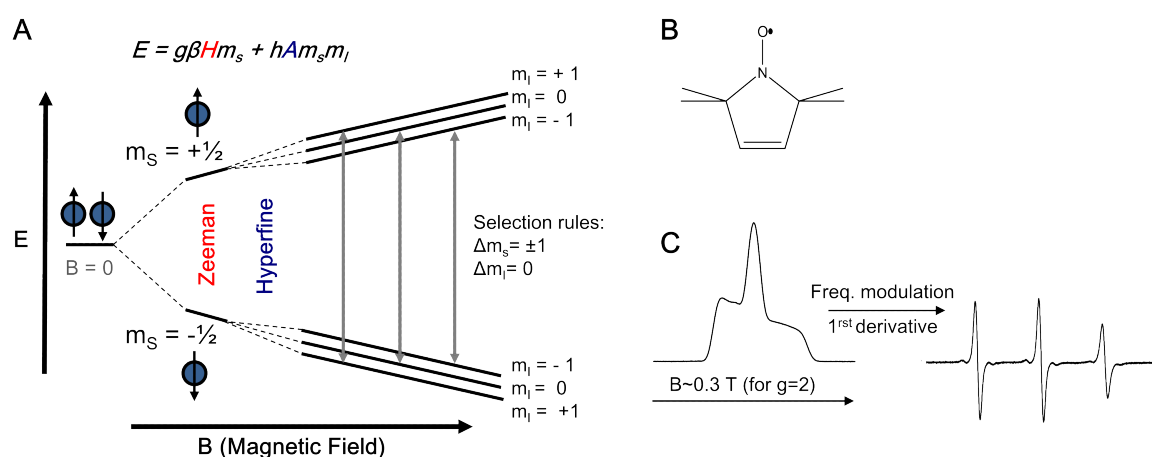
Figure 1.11: Energy diagram of nitroxide spin label in magnetic field. (A) Pictorial representation of the energy levels of an unpaired electron of a nitroxide spin label (depicted in **(B)**) in the presence of a magnetic field; the energy levels of the two spin states are split by the Zeeman effect (field dependent) and by hyperfine interaction with the nitrogen nucleus (field independent); the quantum-mechanical selection rules result in three allowed transitions, and the spectrum shown in **(C)**. In CW-EPR frequency modulation of the signal is applied, and the first derivative (right) of the absorption spectrum (left) is recorded.

sample, while in pulsed-EPR short (ns) and intense microwave frequency pulses are applied to induce transitions. CW-EPR has been widely used to study membrane proteins, for example to gain insights into protein mobility, secondary structure, local solvent accessibility (*i.e.* membrane penetration), and structure by distance measurements up to ~20 Å. Pulsed EPR can be used to probe distances and structural heterogeneity, being suited to measure longer electron-electron distances (*e.g.* up to ~80 Å using DEER/PELDOR, see 1.4.3), while it can also provide information on electron-nuclear interactions (*e.g.* via ESEEM, HYSCORE, and pulse ENDOR experiments) [167].

1.4.2.2   Site-directed spin labelling

Most proteins do not contain a paramagnetic centre (exceptions are *e.g.* those binding transition metal co-factors), so in order to study them by EPR one can introduce a paramagnetic

centre by site-directed spin labelling (SDSL) [168]. In SDSL, stable nitroxide centres that react specifically with (typically) cysteine residues are introduced into a biomolecule of interest (Figure 1.12). Thus, by introducing cysteines on the desired location by site-directed mutagenesis, one can obtain a biomolecule sample with nitroxide spin labels attached at specific sites of interest.
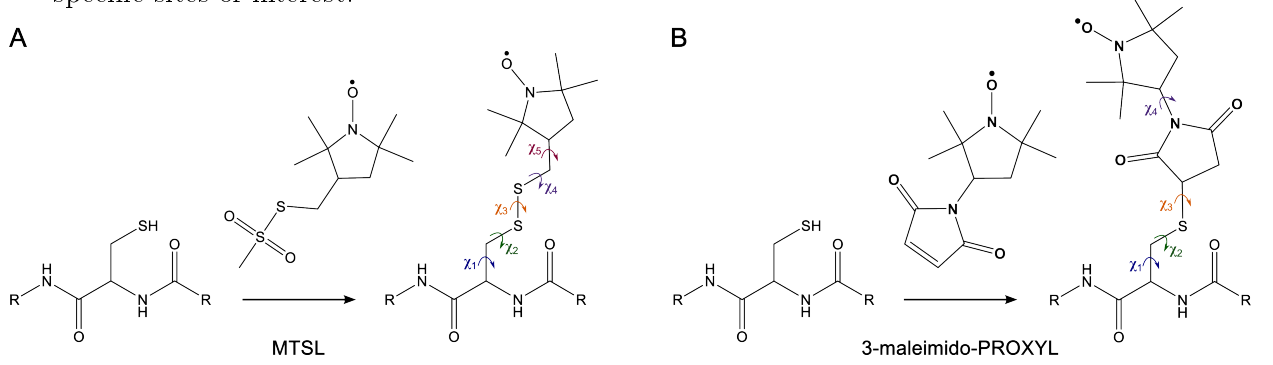
Figure 1.12: Site-directed spin labelling. Nitroxide spin labels with thiol-reactive groups can be introduced in proteins through site-directed reactions with cysteines. **(A)** (2,2,5,5-tetramethylpyrroline-1-oxyl-3-methyl)methanethiosulfonate, or MTSL, and **(B)** 3-maleimido-2,2,5,5-tetramethyl-1-pyrrolidinyloxy, or 3-maleimido-PROXYL, are typically used. The spin label tethers are flexible and can rotate over a number of bonds (dihedral angles 1-5 and 1-4 are shown for MTSL and 3-maleimido-PROXYL, respectively).

1.4.2.3 Basics of EPR: Zeeman effect and hyperfine splitting

Electrons possess a magnetic moment and have a spin quantum number (S) of $1/2$ and can therefore be in two spin states, $m_s = 1/2$ or $m_s = -1/2$. The energy levels of these two spin states are split in the presence of a magnetic field (the Zeeman effect, see Figure 1.11) and are described by the spin Hamiltonian, $\hat{H}_{Zeeman}$

$$\hat{H}_{Zeeman} = \mu_B \bullet \vec{B} \bullet \boldsymbol{g} \bullet \hat{\boldsymbol{S}} \tag{1.1}$$

where μ_B is the Bohr magneton $\vec{B}$ the magnetic field tensor, $\boldsymbol{g}$ the g tensor of the electron and $\hat{\boldsymbol{S}}$ the spin operator for the electron. If the field $\vec{B}$ defines the z-direction, and B is the magnitude of $\vec{B}$, and $\boldsymbol{g}$ is taken to be isotropic, the expression for the spin Hamiltonian becomes

$$\hat{H}_{Zeeman} = g\mu_B S_z B \tag{1.2}$$

with eigenvalues

$$E = g\mu_B m_s B = \pm \frac{1}{2} g\mu_B B \tag{1.3}$$

Application of microwave frequency radiation to a sample in a magnetic field leads to resonance transitions between the two states at the right magnetic field strength, when the resonance condition

$$\Delta E = h\nu = g\mu_B B_0 \tag{1.4}$$

is fulfilled, where h is Planck's constant, ν the microwave frequency, and B_0 the applied magnetic field. Both absorption and stimulated emission of photons occurs, but due to the Boltzmann equilibrium, more electrons will be in the lower spin state leading to more transitions from that state to the higher spin state, resulting in a net absorption of energy that can be detected. In CW-EPR the electromagnetic radiation frequency is kept constant and the magnetic field is scanned. Absorption occurs when the magnetic field is such that the energy difference between the two spin states matches the (constant) energy of the radiation, *i.e.* when the resonance condition (Equation 1.4) is fulfilled. The radiation applied is in the microwave range of the electromagnetic spectrum with common bands listed in Table 1.2. Apart from the Zeeman interaction, the total stationary spin Hamiltonian for a paramagnetic

Table 1.2: Typical microwave bands used in EPR. Some of the microwave bands used in EPR are listed, designated by their letter. The typical frequencies and the range of frequencies corresponding to each band are given, as well as the field of resonance, B_{res}, for a $g = 2$ signal.

Microwave band	Typical frequency (and range, GHz)		B_{res} (G)
L	1	(1-2)	~360
S	3	(2-4)	~1100
X	9.5	(8-12)	~3400
Q	34	(30-50)	~12000
W	94	(75-110)	~33500

centre S in the ground state interacting with nuclear spins I is given by [167, 169]

$$\hat{H}_0 = \hat{H}_{Zeeman} + \hat{H}_{ZFS} + \hat{H}_{HF} + \hat{H}_{NucZeeman} + \hat{H}_{NQ} + \hat{H}_{NN} \qquad (1.5)$$

where $\hat{H}_{Zeeman}$ is the electron Zeeman interaction described above; $\hat{H}_{ZFS}$ the zero-field splitting; $\hat{H}_{HF}$ the hyperfine interaction between the electron spin and nuclear spins; $\hat{H}_{NucZeeman}$ the nuclear Zeeman interaction; $\hat{H}_{NQ}$ the angular quadrupole interactions for spins with nuclear spin quantum numbers $I > 1/2$; and $\hat{H}_{NN}$ the spin-spin interactions between pairs of nuclear spins. For dilute systems of nitroxide radicals $\hat{H}_{ZFS}$, $\hat{H}_{NucZeeman}$, $\hat{H}_{NQ}$, and $\hat{H}_{NN}$ can be neglected and only the electron Zeeman and hyperfine interactions are considered, giving

$$\hat{H} = \mu_B \bullet \vec{B} \bullet \boldsymbol{g} \bullet \hat{\boldsymbol{S}} + \hat{\boldsymbol{I}} \bullet \boldsymbol{A} \bullet \hat{\boldsymbol{S}} \qquad (1.6)$$

where $\hat{\boldsymbol{I}}$ is the nuclear spin operator, and $\boldsymbol{A}$ the hyperfine tensor. For $S = 1/2$ spin systems, $\hat{H}_{Zeeman}$ is typically the dominant term at X-band frequencies. In nitroxide spin labels, hyperfine interaction of the unpaired electron with the nitrogen nucleus results in splitting of the energy levels of the electron spin states (Figure 1.11); the unpaired electron resides in the p_z orbital of the ^{14}N atom, which has a spin quantum number of 1, and thus three possible

spin states (+1, 0, and -1), giving three absorption lines (under the quantum selection rules $\Delta m_s = \pm 1$, $\Delta m_I = 0$). This hyperfine splitting can be used to study the polarity of the spin label environment [170]. The unpaired electron of the nitroxide resides in the p_z orbital of the nitrogen and oxygen of the N-O bond. The spin density at nitrogen determines the hyperfine splitting (as ^{16}O has no spin); in a more polar milieu the electron density on oxygen will be higher, increasing the radical density on nitrogen, resulting in a larger hyperfine splitting.

1.4.2.4   Anisotropy of the nitroxide spin Hamiltonian

The effective spin Hamiltonian for nitroxides (equation 1.6) contains the $\boldsymbol{g}$ and $\boldsymbol{A}$ tensors describing the interactions of the electrons with the magnetic field and the nuclear hyperfine interactions, respectively. Due to the directionality of the orbitals in which electrons reside, the spin-orbit coupling effect on $\boldsymbol{g}$ and the electron-nuclear dipole-dipole contribution to the hyperfine interaction make these tensors anisotropic [171]

$$\boldsymbol{g} = \begin{pmatrix} g_{xx} & g_{xy} & g_{xz} \\ g_{yx} & g_{yy} & g_{yz} \\ g_{zx} & g_{zy} & g_{zz} \end{pmatrix} \quad \boldsymbol{A} = \begin{pmatrix} A_{xx} & A_{xy} & A_{xz} \\ A_{yx} & A_{yy} & A_{yz} \\ A_{zx} & A_{zy} & A_{zz} \end{pmatrix} \tag{1.7}$$

In the principal axis system with x aligned along the N-O bond (Figure 1.13), these matrices can be diagonalised, with typical values of the tensor components for a nitroxide spin labels given in Table 1.3, although these values may differ depending on the specific compound and polarity of the environment [172, 173]. In this principal axis system, equation 1.6 becomes
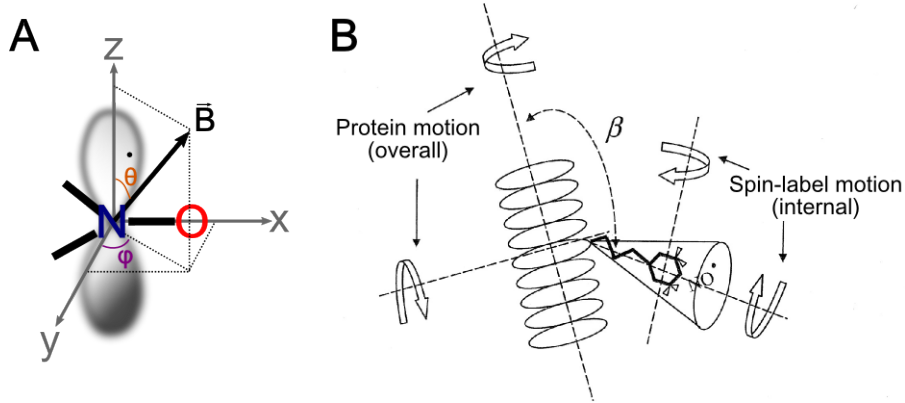
Figure 1.13: Nitroxide principal axis system {x, y, z}. (A) Using the principal axis system leads to simpler, diagonalised $\boldsymbol{g}$ and $\boldsymbol{A}$ tensors. The orientation of the magnetic field $\vec{B}$ is given by polar angles θ and ϕ. **(B)** Motional averaging through protein and spin label motion leads to averaging of the spectral anisotropies (adapted from [174]).

$$\begin{aligned} \hat{H} &= \mu_B \bullet \vec{B} \bullet \boldsymbol{g} \bullet \hat{\boldsymbol{S}} + \hat{\boldsymbol{I}} \bullet \boldsymbol{A} \bullet \hat{\boldsymbol{S}} \\ &= \mu_B(g_{xx}B_x\hat{\boldsymbol{S}}_x + g_{yy}B_y\hat{\boldsymbol{S}}_y + g_{zz}B_z\hat{\boldsymbol{S}}_z) + (A_{xx}\hat{\boldsymbol{I}}_x\hat{\boldsymbol{S}}_x + A_{yy}\hat{\boldsymbol{I}}_y\hat{\boldsymbol{S}}_y + A_{zz}\hat{\boldsymbol{I}}_z\hat{\boldsymbol{S}}_z) \end{aligned} \tag{1.8}$$

Table 1.3: Principal values of the g and A tensor of nitroxide spin labels. Values for the diagonal elements of the tensors in the principal axis system with x aligned along the N-O bond.

Component	Value
g_{xx}	2.009
g_{yy}	2.006
g_{zz}	2.002
A_{xx}	0.6 mT
A_{yy}	0.6 mT
A_{zz}	3.2 mT

Using polar coordinates to express the magnetic field $\vec{B}$

$$B_x = B \sin \theta \cos \phi \tag{1.9a}$$

$$B_y = B \sin \theta \sin \phi \tag{1.9b}$$

$$B_z = B \cos \theta \tag{1.9c}$$

with B being the magnitude of the magnetic field ($|\vec{B}|$), a first-order solution of equation 1.8 yields

$$\Delta H = h\nu = \mu_B g(\theta, \phi) B + A g(\theta, \phi) m_I \tag{1.10a}$$

where

$$g(\theta, \phi) = \sqrt{g_{xx} \sin^2 \theta \cos^2 \phi + g_{yy} \sin^2 \theta \sin^2 \phi + g_{zz} \cos^2 \theta} \tag{1.10b}$$

and

$$A(\theta, \phi) = \sqrt{A_{xx} \sin^2 \theta \cos^2 \phi + A_{yy} \sin^2 \theta \sin^2 \phi + A_{zz} \cos^2 \theta} \tag{1.10c}$$

Motional averaging through protein and spin label motion leads to averaging of the spectral anisotropies (see Figure 1.14). For spins rapidly re-orienting in an isotropic manner ($\tau_c \approx 10^{-10} - 10^{-9}$ s) g and A can be approximated by their isotropic counterparts (Figure 1.14A)

$$g_{iso} = \frac{1}{3}(g_{xx} + g_{yy} + g_{zz}) \tag{1.11a}$$

and

$$A_{iso} = \frac{1}{3}(A_{xx} + A_{yy} + A_{zz}) \tag{1.11b}$$

1.4.2.5   Electron-electron interactions

Equations 1.6 and 1.5 consider a lone paramagnetic species, and do not take into account electron-electron interactions. For a system of m interacting nitroxides, the electron-electron interactions introduce two additional terms to the effective Hamiltonian

$$\hat{H}_0 = \sum \hat{H}_{Zeeman} + \sum \hat{H}_{HF} + \hat{H}_{Exch} + \hat{H}_{DD} \tag{1.12}$$

where $\sum \hat{H}_{Zeeman}$ and $\sum \hat{H}_{HF}$ represent the sum of the Hamiltonians for the Zeeman and hyperfine interactions, respectively, for each of the m electron spins of the system; $\hat{H}_{Exch}$ is the exchange (or J) coupling between electron spins; and $\hat{H}_{DD}$ the electron dipole-dipole interaction. Spin exchange interaction (also called Heisenberg exchange coupling) occurs between electrons in overlapping orbitals, and for a two spin system (S_1 and S_2) can be described by

$$\hat{H}_{Exch} = \hat{S}_1 \bullet J \bullet \hat{S}_2 \tag{1.13}$$

where J is the exchange coupling tensor. It is observed for unpaired electrons in close proximity ($< \sim 15\text{Å}$), but can also be observed for strongly delocalized electrons separated by a longer distance connected through a conjugated path.

Dipole-dipole coupling between two electron spins S_1 and S_2 is given by

$$\hat{H}_{DD} = \hat{S}_1 \bullet D \bullet \hat{S}_2 \tag{1.14a}$$

$$= \frac{\mu_o \mu_B^2}{4\pi} \frac{g_1 g_2}{r^3} \left(\hat{S}_1 \hat{S}_2 - 3 \frac{(\hat{S}_1 \bullet \vec{r})(\hat{S}_2 \bullet \vec{r})}{r^2} \right) \tag{1.14b}$$

where g_1 and g_2 are the g-factors for electrons 1 and 2 (taken here to be isotropic point charges), D is the dipole-dipole coupling tensor, $\vec{r}$ the interspin vector, and r the magnitude thereof. By choosing a principal axis system with the magnetic moments aligned parallel to the z-axis, and the z-projection of the distance vector $\vec{r} = r cos\theta$, the dipolar interaction is given by

$$\hat{H}_{DD} = \frac{\mu_o \mu_B^2}{4\pi} \frac{g_1 g_2}{r^3} \left(1 - 3cos^2\theta \right) S_1 S_2 \tag{1.15}$$

with θ the angle between $\vec{r}$ and the principal axis z. Thus the energy of the dipolar interactions depends on inverse cubed distance between the electrons, and the angle θ.

1.4.2.6   CW-EPR data analysis

Appendix H.1 briefly describes the CW-EPR experimental set-up. EPR uses phase sensitive detection to enhance the sensitivity (see Figure H.3); the derivative of the absorption spectrum is recorded by modulating the magnetic field B_0, increasing the signal-to-noise ratio, as noise that does not oscillate with the modulation frequency is rejected (Figure 1.11).

1.4.2.6.1   Spin label dynamics   As the spin Hamiltonian is anisotropic, the EPR spectrum is sensitive to motion of the nitroxide spin label, which can lead to anisotropy averaging, and local constraints. The EPR spectrum can thus be used to study the dynamics of the side chain, giving insights into protein structure and topography, at the level of the backbone fold. If the spin label rotates fast enough ($\tau_c < 10^{-9}$ s) in an isotropic manner, the
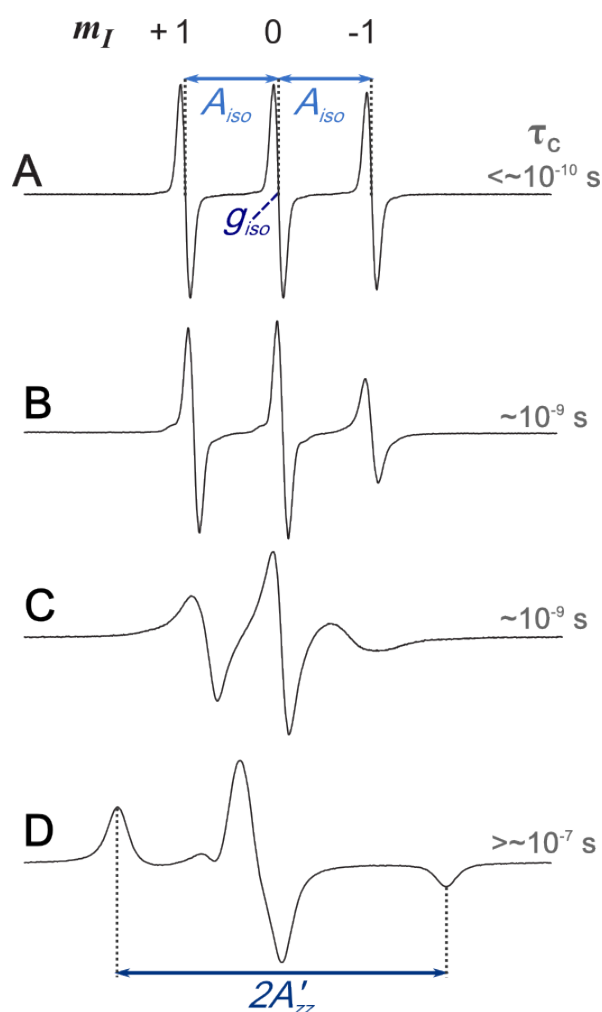
Figure 1.14: Influence of side chain motion on EPR spectrum. (A) A dilute solution of MTSL, **(B)** MTSL bound to a small 15-residue peptide in aqueous solution, **(C)** the same spin-labelled peptide folded into an α-helix, and **(D)** the spin-labelled peptide in frozen solution. The approximate rotational correlation time τ_c for each motional regime is given. Adapted from [175] Spectral parameters used in analyses are indicated and further explained in the text.

anisotropy of the $\boldsymbol{g}$ and $\boldsymbol{A}$ tensors is averaged out, and the nitroxide EPR spectrum consists of three sharp lines. Slower motion will result in changes in the EPR spectrum. Figure 1.14 shows a series of EPR spectra corresponding to different rates of rotational motion of MTSL [175]. Only isotropic motion is considered here, although non-isotropic motion also leads to changes in the EPR spectrum, which is often used to study the motion of axially-symmetric

spin-labelled lipids in membranes [176, 177]. Figure 1.14A shows the fast motional regime ($\tau_c \lesssim 10^{-10}$s). Slower motion results in line broadening (Figure 1.14B and C, $\tau_c \sim 10^{-9}$s). The intensity of each line is proportional to the product of its amplitude and the square of its width, thus as lines broaden their amplitude decreases. Even slower motion ($\tau_c \gtrsim 10^{-7}$s) yields an EPR spectrum as shown in Figure 1.14D, corresponding to spin label approaching the so-called rigid motion limit (also often called a frozen or powder spectrum). The overall mobility of a spin label attached to a protein is determined by (1) the motion of the spin label itself relative to the protein backbone, due to rotations over the spin label tether bonds, influenced by restrictions imposed by the primary, secondary, tertiary, and potentially quaternary structure of the protein (Figure 1.12); (2) local backbone motion in the protein; and (3) the overall rotational correlation time of the whole protein (Figure 1.13B). For proteins
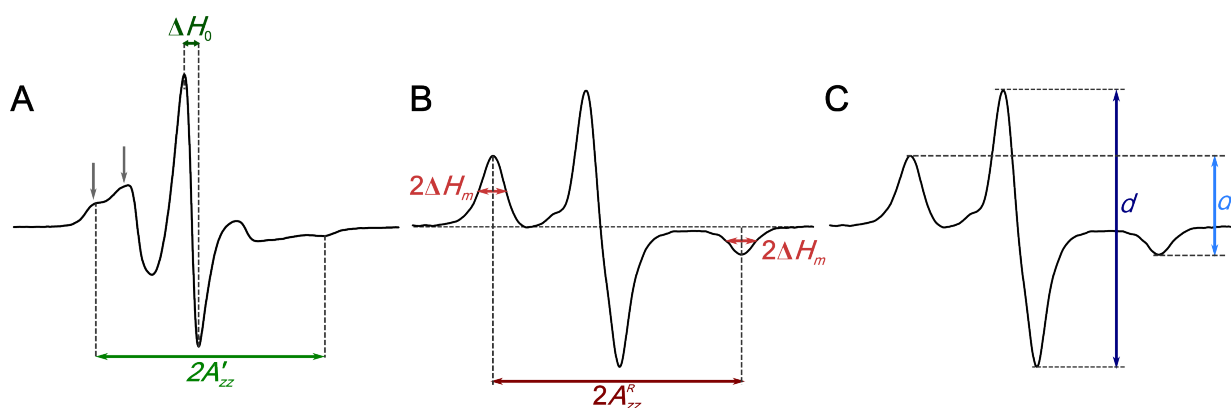
Figure 1.15: CW-EPR spectral parameters. A variety of spectral parameters can be used to assess spin label mobility, such as **(A,B)** peak width ΔH, **(B)** the maximum apparent splitting ($2A'_{zz}$). EPR spectra can be complex, and contain multiple components as indicated by the grey arrows in **(A)**, arising from different protein conformations, or specific slowly exchanging spin label rotamer populations. **(C)** Relative peak heights of 'frozen' spectra can be used to gauge spin-spin proximity.

larger than ~15 kDa in liposomes or detergents, the third contribution is negligible, as the rate of tumbling ($\tau_c \approx 50$ ns, estimated from Stoke's law) is too slow to affect the EPR spectrum [175], which is then dominated by local effects. For example, spin labels in loop regions often have a high degree of mobility, resulting in a spectrum with small apparent hyperfine splitting and narrow linewidths, while spin labels embedded in structured elements, or buried in the protein interior or between subunits, typically exhibit a broadened line shape and increased apparent hyperfine splitting due to motionally restricting interactions with neighbouring residues and/or the backbone [178]. This sensitivity to motion can be used to probe protein secondary structure or conformational changes which might affect the local spin label environment. A variety of spectral parameters (indicated in Figure 1.15)

can be used to assess spin label mobility, such as the maximum splitting $(2A'_{zz})$, peak width ΔH, and the spectral second moment $((\langle H^2 \rangle))$.

1.4.2.6.2   Secondary structure   Measuring the EPR spectra for a sequence of residues and determining reciprocal width of the central peak $(\Delta H_0^{-1}$, Figure 1.15A) can be used to probe secondary structure of proteins, as the relative mobility of the sequential sites should follow a pattern corresponding to the structural element. Thus ΔH_0^{-1} *vs.* residue number would show *e.g.* a periodicity of 3.6 for α-helices or of 2 for β-strands (Figure 1.16A and B). In addition, the second moment of the absorption spectrum can be used to probe structure; being the variance in the spectral shape, it is a measure of the 'broadness' of the spectrum and thus spin label mobility. The relation between ΔH_0^{-1} and the reciprocal spectral second moment $(\langle H^2 \rangle^{-1})$ reports on the protein topology, as first determined empirically for T4 lysozyme and later for other proteins (Figure 1.16C) [178, 179].
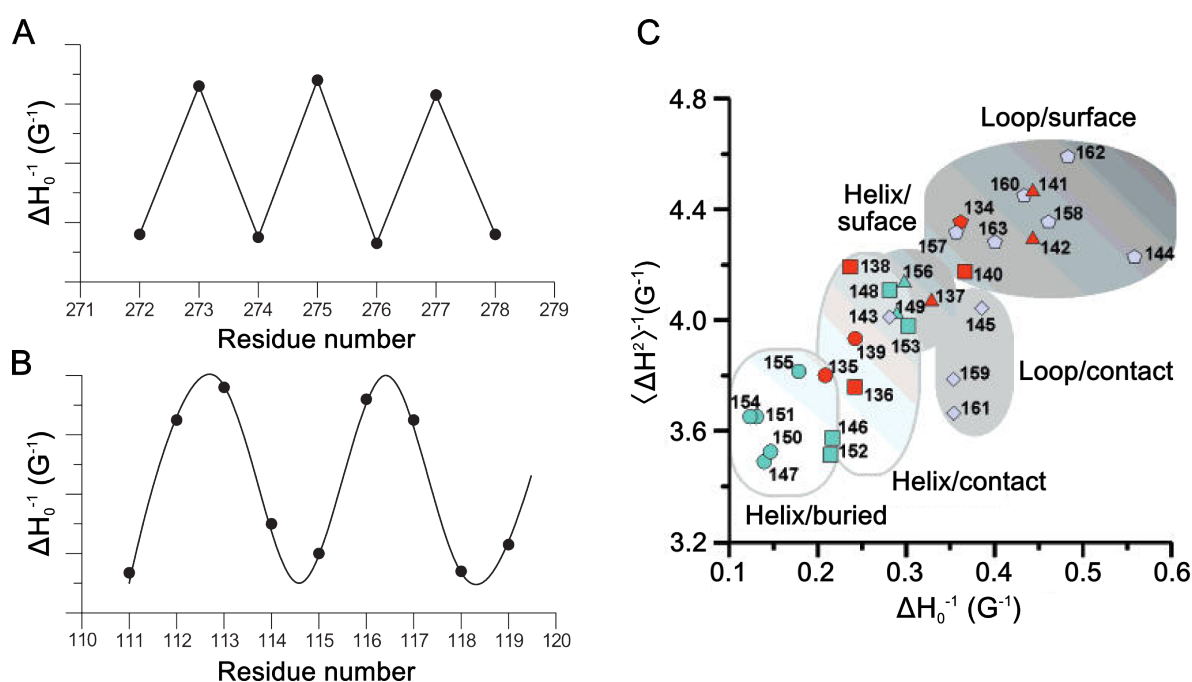
Figure 1.16: Probing protein secondary structure by CW-EPR. Idealized ΔH_0^{-1} (reciprocal width of the central peak) *vs.* residue number plots for an **(A)** β-strand and **(B)** α-helical secondary structure. Adapted from [175]. **(C)** Empirical relation between ΔH_0^{-1} and the reciprocal spectral second moment $(\langle H^2 \rangle^{-1})$ reports on the protein topology as first determined empirically for T4 lysozyme, and here for annexin 12; figure adapted from [179].

1.4.2.6.3   Spin label mobility and rotational correlation times   Another parameter that can be used to gauge relative spin label mobility is the apparent maximum splitting, $2A'_{zz}$ (Figure 1.14C and D), with slower motion giving rise to larger splitting. EPR spectra

can be complex, and contain multiple components (indicated by the grey arrows in Figure 1.15A), arising from different protein conformations, or specific slowly exchanging (on the ~50-100 ns time scale) spin label rotamer populations, with different motional properties (and thus different $2A'_{zz}$). Approximate rotational correlation times can be calculated from experimental spectral parameters using semi-empirical formulas deduced from simulations. In the intermediate to fast motional regime ($\tau_c \sim 10^{-11} - 10^{-9}$, Figure 1.14A, B and C), when three distinct lines can be observed in the EPR spectrum, the peak-to-peak line height h of the middle ($h(0)$) and high field peak ($h(-1)$) varies with the inverse square of the width ΔH, and can be used to calculate an approximate τ_c using [180]:

$$\tau_c = 6.5 \times 10^{-10} \Delta H_0 \left(\sqrt{\frac{h(0)}{h(-1)}} - 1 \right) \tag{1.16}$$

In the slow motion regime ($\tau_c > 10^{-9}$) either the apparent maximum splitting or linewidths can be used [181–183]:

$$\tau_c = a'_m \left(\Delta H_m / \Delta H_m^R - 1 \right)^{b'_m} \tag{1.17a}$$

or

$$\tau_c = a \left(1 - A'_{zz} / A_{zz}^R \right)^{b'_m} \tag{1.17b}$$

where ΔH_m and $\Delta H_m^R - 1$ are the half-width at half-height for the outer extreme peaks (Figure 1.15B) for the slow motion spin and that in the rigid limit, respectively; A_{zz}^R is the maximum splitting in the rigid limit; and a'_m, b'_m, a, and b are calibration constants dependent on the chosen diffusion model and the intrinsic peak-to-peak derivative Lorentzian linewidth, $\delta = (2/\sqrt{3})\Delta H_m^R$, for which values can be found in the literature [184]. Although these equations can only give approximate correlation times, they are still useful for determining relative mobilities, and changes thereof.

1.4.2.6.4   Interspin distance determination   EPR can be used for distance measurements between and within molecules. Together with EPR dynamics studies, EPR distance measurements provide a powerful method to determine structural details of proteins with unknown structure, or to study conformational changes related to function. CW-EPR is suited to short distances of ~8-20 Å. These measurements are based on through-space dipolar interactions between two spin labels (equation 1.15), which give rise to distance-dependent line-broadening in the EPR spectrum by a so-called Pake pattern (Figure 1.17). The maxima of the Pake pattern are related to the inter-spin distance. At shorter distances ($r < 8$ Å) J-coupling starts contributing substantially to line broadening, while at longer distances

$(r > 20$ Å$)$ dipolar line broadening becomes too small compared to other line broadening effects (*e.g.* inhomogeneous broadening) to be measured by CW-EPR [185, 186]. Inter-spin distances can be determined from CW-EPR spectra by computational methods based on Fourier deconvolution [185], on convolution of the spectra from non-interacting spins with a broadening function [187], or by simulating spectra taking into account both the distance between the spin labels and their relative orientation [188]. The resolution is limited by the inherent flexibility of the spin probes, which results in a distribution of distances, and is typically in the order or 1-2 Å. Line broadening leads to a decreased amplitude (as the total
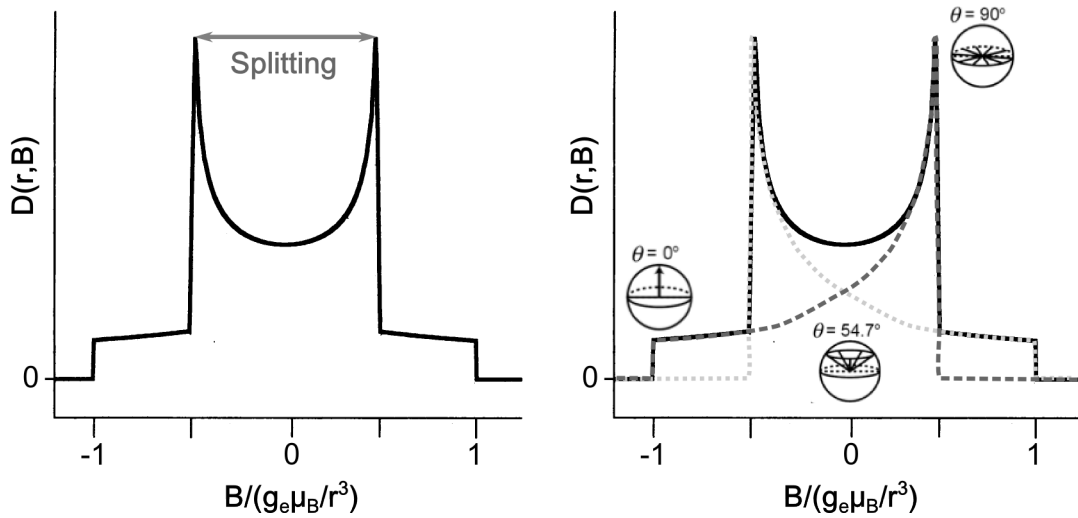
Figure 1.17: Pake pattern. A 'Pake pattern' dipolar broadening function $D(r, B)$, against $B/(g_e \beta r^3)$ is shown, where $2B$ is magnitude of splitting of the absorption lines, g_e the isotropic g-value of the electron, μ_B the Bohr magneton, and r the distance between the dipoles. The shape of the Pake pattern arises due to the fact that there are only two possible orientations along the external magnetic field (parallel and anti-parallel), giving a minimum at $\theta = 0°$ (θ being the angle between the interspin vector and the magnetic field), but many orientations perpendicular to the magnetic ($\theta = 90°$) as illustrated in the right panel. Figure adapted from [185].

area stays constant); as dipolar broadening affects the height of the centre peak to a larger extent than the broader peaks at low and high field, the ratio between these peaks can be used in a more qualitative manner to assess relative interspin distances using [189]

$$k = \frac{d_1}{d} \tag{1.18}$$

where d and d_1 are the peak-to-peak amplitudes of the middle and outer peaks of the frozen EPR spectrum, respectively, as defined in Figure 1.15C. This ratio can be used as a proxy for relative distance and/or to calculate an approximate interspin distance using the empirical relation

$$r = [2.2 - 6.3(k - 0.34)] \, \text{nm} \tag{1.19}$$

for distances of ~12-22 Å [189, 190], which was found to be in good agreement with simulation methods in a study of the membrane channel protein KscA [191]. For non-interacting nitroxide spins $k \approx 0.32 - 0.35$, as determined from both simulated and experimental spectra [190, 191], and k increases with decreasing interspin distance. The accuracy of the method is affected by the presence of unlabelled protein, which leads to underestimation of the spin-spin interaction and concomitant overestimation the interspin distance; this problem is more significant for shorter distances with simulations estimating the error to be 20% at 12 Å and 4% at 20 Å [191].

Alternatively the spectral second moment ($\langle H^2 \rangle$) of the frozen EPR spectrum can be used to quantify short-range internitroxide distances (<20 Å). As $\langle H^2 \rangle$ reports on the broadness of the spectrum, the second moment of a spectrum with interacting nitroxides ($\langle H^2 \rangle_D$) will be larger compared to that of a spectrum of the same sample in the absence of dipolar interactions ($\langle H^2 \rangle_S$). The internitroxide distance (r in Å) is calculated using the relation [186, 192]

$$\langle \Delta H^2 \rangle = \frac{3}{5} \frac{\mu_B^4 g^4 \mu_0}{(4\pi)^2 h^2} S(S+1) \sum \frac{1}{r^6} \tag{1.20a}$$

with $\langle \Delta H^2 \rangle$ in Hz^2 can be converted into field units (T^2) and solved for r to give

$$r = \frac{23.2}{(\langle \Delta H^2 \rangle \cdot 10^8)^{1/6}} \tag{1.20b}$$

with $\langle \Delta H^2 \rangle$ in in T^2 being the second moment of the dipolar interaction, *i.e.* the difference between the second moment of the coupled and non-coupled sample

$$\langle \Delta H^2 \rangle = \langle H^2 \rangle_D - \langle H^2 \rangle_S \tag{1.20c}$$

where S is spin quantum number of the electron, and μ_0 the permeativity of a vacuum. As the second moment analysis method relies on broadening, it is limited by other inhomogeneous broadening effects, and the accuracy is influenced by underlabelling, and the quality of the baseline of the spectra.

1.4.3 Double electron-electron resonance

1.4.3.1 Principles

For longer distances, the spectral broadening due to dipolar interactions becomes too small to distinguish from other contributions, *e.g.* inhomogeneous broadening. By using pulse sequences at a constant magnetic field, like in NMR, the magnetisation can be manipulated so that inhomogeneous broadening is negated. Using a rotating frame depiction, Figure 1.18

shows the generation of a spin (or Hahn) echo; the magnetisation is transferred to the x-y-plane by applying a 90° (or $\pi/2$) pulse; spins will precess with varying speeds due to local magnetic field inhomogeneities, and phase out; application of a 180° (or π) pulse flips the spins, which then continue to precess at the same varying speeds as before, and eventually refocus giving rise to a spin echo. The pulsed EPR technique double electron-electron
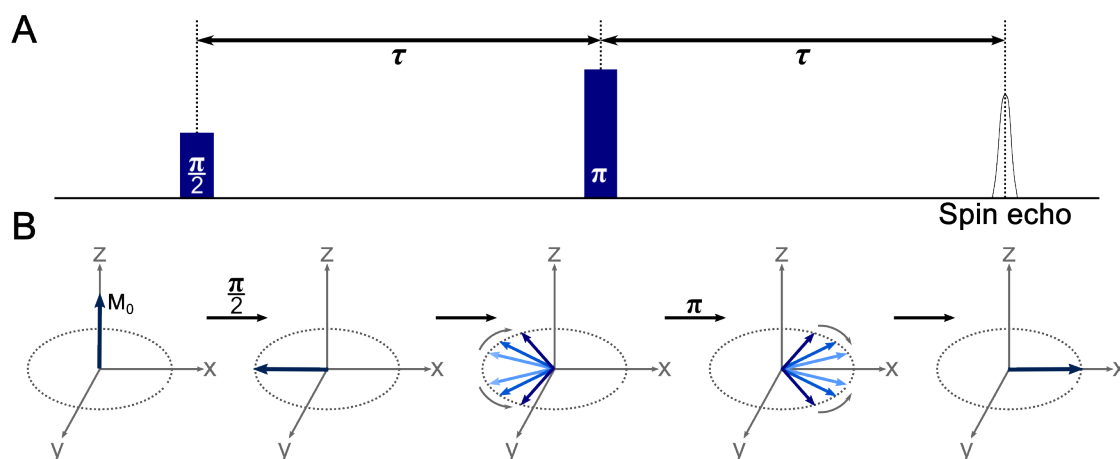
Figure 1.18: Hahn echo pulse sequence. **(A)** Hahn echo pulse sequence and **(B)** pictorial representation its effect on the magnetization in the rotating frame, with pulses along x, and dephasing of the magnetisation only due to inhomogeneous effects (*i.e.* no relaxation), giving a fully refocussed echo.

resonance (DEER), also known as pulsed electron-electron double resonance (PELDOR), uses a Hahn echo to refocus the inhomogeneous broadening, at one frequency, the probe frequency (ν_1 in Figure 1.19B). Then, to observe the dipolar coupling between spins, a second π pulse, at a different frequency, the pump frequency (ν_2) is applied in between the $\pi/2$ and the π pulse of the Hahn echo sequence; in the absence of overlap of the excitation windows of the probe and pump pulses, probe pulses excite one group of spins (spins A) and pump pulses another (spins B, Figure 1.19A). The pump pulse at time t flips the B spins, influencing the local field of the A spins when the spins are dipolarly coupled, affecting the precession frequency of spins A, and the extent to which they are refocused by the observer π pulse (*i.e.* the echo intensity). Thus, by applying the pump pulse at varying time t the dipolar coupling can be determined from the modulation of the spin echo intensity. This is known as a 3-pulse (3p) DEER sequence [193, 194]. This experiment has an inherent deadtime (typically ~30-100 ns) due to distortion of the data at times when the π pump and the $\pi/2$ probe pulse overlap. To overcome this deadtime, the 4p DEER experiment uses a refocused Hahn echo, with the pump pulse applied between the two refocussing probe π pulses (Figure 1.19C) [195]; zero-time can now be measured and corresponds to $t = \tau_1$, as here the A spins are refocused and the pump pulse has no effect.
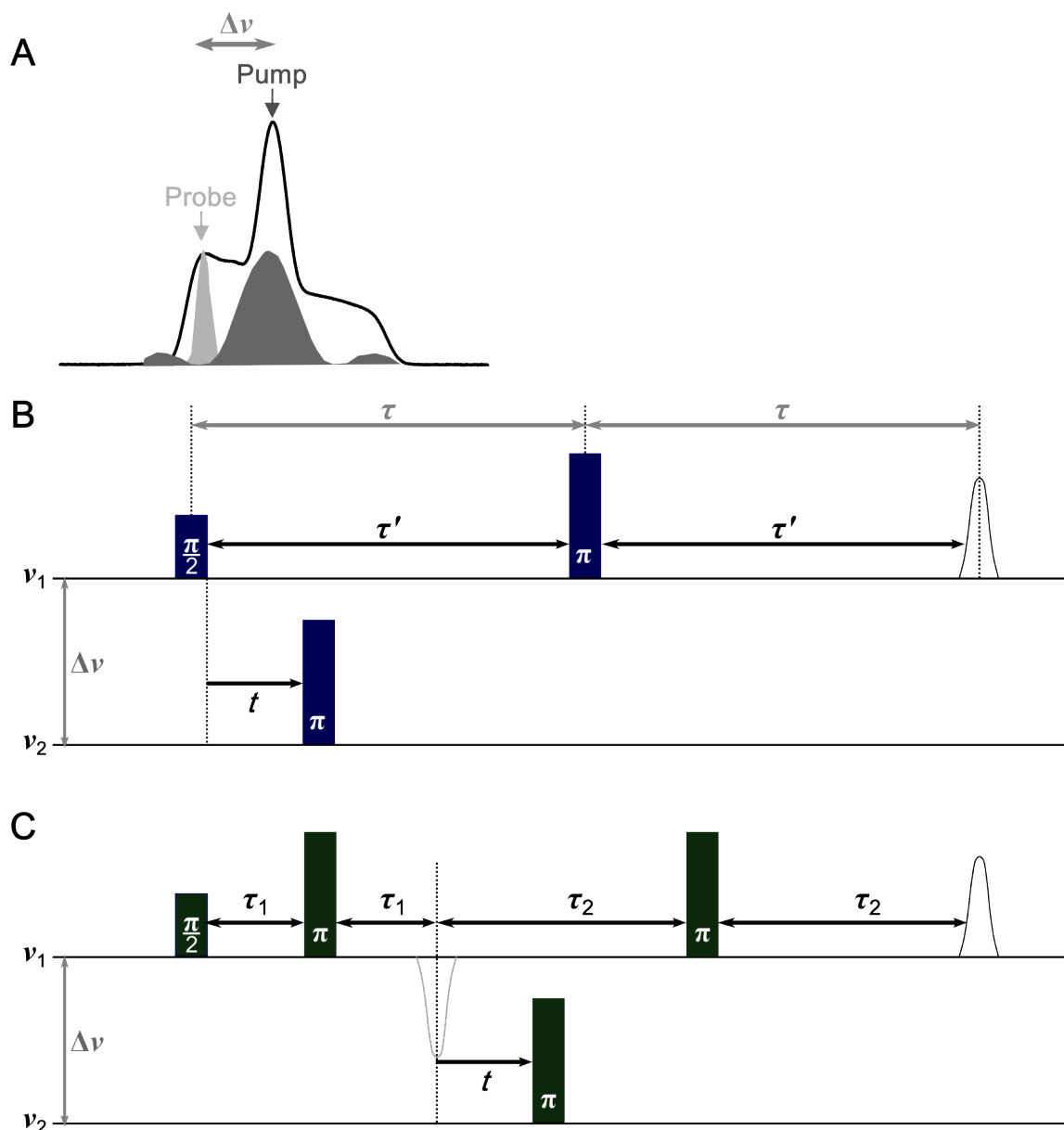
Figure 1.19: Pulse sequences for 3p and 4p DEER. (A) Shows the relative positioning of the probe and pump pulses on an X-band absorption spectrum for a nitroxide (pulse excitation profiles are simplified approximations). **(B)** 3p DEER, the π pulse at ν_2 (pump frequency) is applied at variable time t between the Hahn echo sequence at ν_1 (probe frequency). This flips the pump electron spins (B spins) that are coupled to the probed spins (A spins) such that the local field of the A spins is perturbed and the spin echo is modulated as a function of interpulse distance t. This sequence has an inherent deadtime due to distortions from overlapping π pump and the $\pi/2$ probe pulse. **(C)** 4p DEER, a refocused Hahn echo sequence is applied at the probe frequency with the pump pulse stepped over the interval τ_1-τ_2 so that the pumping takes place over the Hahn Echo, eliminating the 3p deadtime. However, sensitivity of the 4p experiment is lower as not all magnetisation can be refocused, and due to the increased time in between the first pulse and the echo (for the same experimental t_{max}).

Correct determination of zero-time is important especially for the correct detection of short distances and broad distributions [196, 197]. The observed echo intensity as a function of time t is called the dipolar evolution function ($D(t)$), and can be separated into (1) a background factor ($B(t)$) arising from interactions of spins within the biomolecule (or complex) of interest with other bulk spins, and (2) the form factor ($F(t)$) arising from the desired intramolecular contributions

$$D(t) = B(t)F(t) \tag{1.21}$$

where the form factor is given by

$$F(t) = 1 - \lambda + \lambda \int_0^{\pi/2} \left(\left(3\cos^2\theta - 1\right) \omega_{dd}t \right) sin\theta \, d\theta \tag{1.22a}$$

where ω_{dd} is the angular dipolar frequency between two point dipoles

$$\omega_{dd} = \frac{g_1 g_2 \mu_B^2 \mu_0}{4\pi r^3} \tag{1.22b}$$

and λ is the modulation depth parameter that depends on the fraction of spins excited by the pump pulse; this gives a relation between the dipolar frequency which can be obtained from the experimental data and the interspin distance r. The background factor depends on the spatial distribution of the bulk spins in the sample. For a homogeneous distribution where the distance between biomolecules is much larger than the interspin distance, the background function can be approximated by a stretched exponential

$$B(t) = \exp{-kt^{d/3}} \tag{1.23}$$

where k is inversely related to the spin concentration, and d is the background dimension; for a non-confined membrane protein in detergent the dimension should approximate 3, while for a bilayer-embedded protein a theoretical dimension of 2 is expected, although experimentally determined background dimensionality may well deviate from ideality [198].

1.4.3.2   Practical considerations

As long relaxation times are required to allow long echo evolution times, these measurements need to be performed at cryogenic temperatures (typically ≤ 80 K). The positioning of the pump and probe can be varied to optimise for modulation depth and/or sensitivity; maximum modulation depth (*i.e.* number of spins excited by the pump pulse) is maximised by pumping at the maximum of the nitroxide spectrum (as shown in Figure 1.19A). Alternatively, positioning of the observer frequency to coincide with the spectral maximum optimises the spin echo intensity (and thus signal-to-noise of the DEER trace). The maximum distance that can be reliably determined from a DEER experiment (r_{exp}) depends on

the maximum evolution time t_{max} (corresponding to τ' and τ_2 in Figure 1.19B and C for 3p and 4p, DEER respectively) as

$$r_{exp} = r_{max,i} \sqrt[3]{\frac{t_{max}}{2\,\mu s}} \qquad\qquad (1.24)$$

with t_{max} in μs, and where $r_{max,i}$ is chosen depending on the desired information, $r_{max,mean} = 5\,\mu s$, $r_{max,width} = 4\,\mu s$, $r_{max,shape} = 3\,\mu s$ to elucidate the mean distance, the width of the distance distribution, and the shape thereof, respectively [198]. The maximum attainable t_{max} depends on the phase memory time T_m. The T_m is an empirical relaxation parameter that describes the spin echo decay, and is affected by a variety of processes such as spin-spin (or transverse) relaxation (T_2), spectral, spin and instantaneous diffusion; *e.g.* nuclear spin flip-flops, molecular motion, and molecular rotation can affect the precession frequency of spins packets, and thus the extent to which they are refocused [167, 171]. The whole length of the pulse sequence should not considerably exceed the T_m [195]. Deuteration of the matrix, and measuring at lower temperature can increase the T_m [198]. The spin-lattice (or longitudinal) relaxation time T_1 however also increases at low temperatures, leading to longer experimental delay times (which need to be ~5×T_1), and thus overall acquisition time, to avoid saturation.

Small residual pulse overlap between the pump and observer excitation bands, can lead to excitation of forbidden electron-nuclear transitions, giving rise to additional nuclear modulations (ESEEM, electron spin echo envelope modulation) of the DEER signal [167, 198]. In a non-deuterated sample at X-band frequencies (~9.4 GHz), proton transitions (of ~14.5 MHz), dominate the ESEEM, introducing a spurious distance of ~1.5 nm in to the measured distance distribution [199, 200]. These nuclear modulations can be suppressed by variation of interpulse delays and summation of the resulting echoes; in 4p DEER τ_1 is incremented by 8 ns to average proton modulation, and typically summed over eight traces [195, 199]. Alternatively, experiments can be performed at higher frequencies, such as Q-band (~34 GHz), where the modulation depth of the proton ESEEM is much reduced and the frequency of the residual modulations (~45 MHz) corresponds to distances which are beyond the DEER distance range [200]. For deuterated samples, deuterium ESEEM must be suppressed (also at Q-band), in a similar strategy, but using 56 ns pulse-delay increments [200].

1.4.3.3   DEER-Stitch

As mentioned in section 1.4.3.1, while 4p DEER allows deadtime-free measurements, the longer pulse sequence means a loss of sensitivity compared to 3p DEER (Figure 1.20A). This negatively affects the maximum dipolar evolution time t_{max} over which can be measured, and thus the maximum distance that can be reliably detected. By combining 3p and 4p
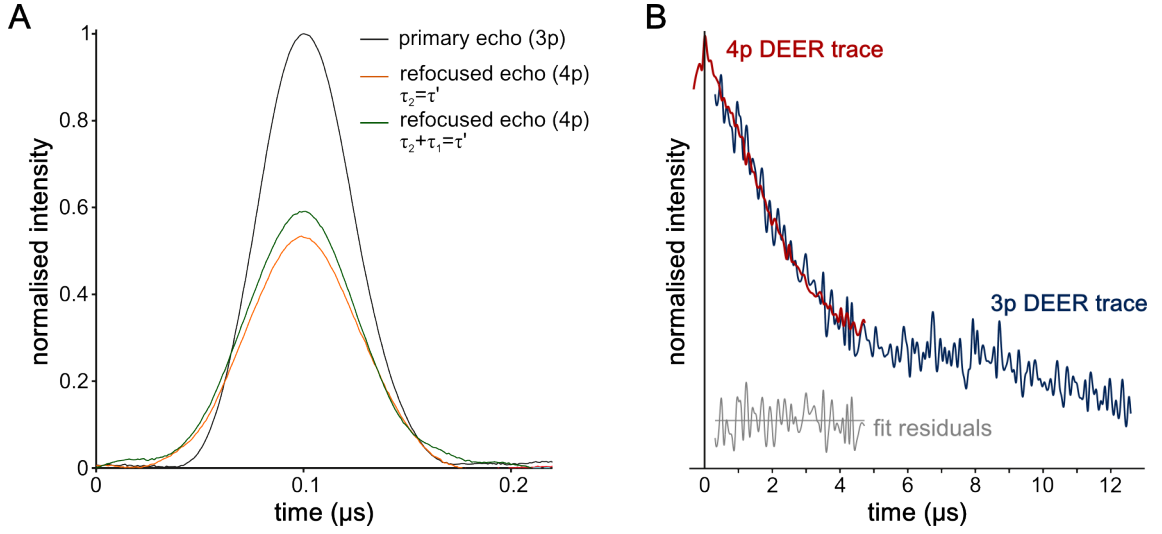
Figure 1.20: Combining 3p and 4p DEER (DEER-Stitch). (A) Echo intensity for a 3p DEER experiment (primary echo) and 4p DEER experiment with corresponding pulse delay (see Figure 1.19); refocussed 4p echoes are significantly less intense. **(B)** DEER-Stitch for spin-labelled protein CD55; 4p DEER data (red) is fitted to 3p DEER data (blue) to obtain a longer overall trace, with data around time zero (fit residuals are shown in grey). Figures adapted from [197].

DEER time domain data by the DEER-Stitch method [197]; the zero-time can be accurately determined from a shorter 4p trace, while a longer, more sensitive 3p experiment is used to maximize the dipolar evolution time. The data are overlaid (after distorted regions of the spectra arising from pulse overlap are discarded) and combined using a least-squares difference analysis, while scaling the spectra to account for differences in decay rate and echo intensities (Figure 1.20B). DEER-Stitch is particularly beneficial for samples with rapidly decaying signals (due to short T_m), such as membrane proteins reconstituted into bilayers [201].

1.4.3.4   DEER data analysis

As mentioned in section 1.4.3.1, the dipolar evolution function $D(t)$ (which is the DEER time domain signal) is composed of a background factor $B(t)$ and a a form factor $F(t)$ which contains the angular dipolar frequency that is related to the interspin distance. Thus, analysis of DEER data typically entails deconvolution of the primary data into $B(t)$ and $D(t)$ (Figure 1.21). Reliable background fitting requires traces to be recorded beyond the decay of the dipolar modulation, or in other words, the longest detectable distance, determined by t_{max} (equation 1.24), must exceed the longest intramolecular distance in the sample [199]. To aid background correction, experimental background data can be used, obtained by measuring control samples lacking intramolecular spin-spin interactions.

Background corrected DEER data can then be subjected to distance distribution analysis.
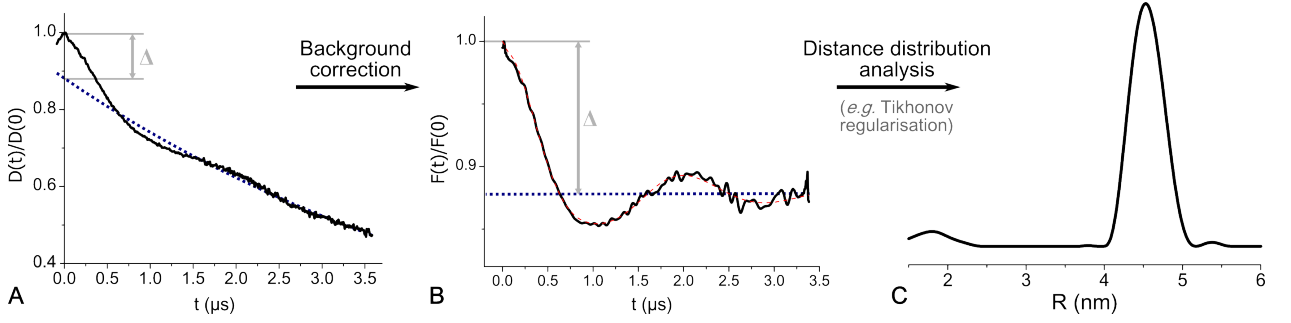
Figure 1.21: DEER data analysis. DEER data for peptide transporter PepT$_{\text{So}}$ in detergent where **(A)** shows the dipolar evolution function ($D(t)$) with the three-dimensional background fitted to it; **(B)** the form factor ($F(t)$) arising from $D(t)$ after background correction; and **(C)** the distance distribution obtained from model-free Tikhonov regularisation. The experimental modulation depth of the data Δ is also indicated, which is related to the earlier mentioned modulation depth λ as $\Delta = 1 - (1 - \Delta)^{n-1}$ where n is the number of coupled spins in the system, thus for 2 coupled spins $\Delta = \lambda$.

DeerAnalysis is an often-used programme for fitting DEER data [202]. It supports model-free and model-based (*e.g.* distance distributions of one or more Gaussian peaks) analysis. Model-free fitting of DEER data is an ill-posed mathematical problem due to the instability of the solution; the data can be fit by many distributions, with small changes in background correction or in the noise level of the data affecting the final result. DeerAnalysis uses Tikhonov regularisation to stabilize the solution [202]. Least squares analysis compares simulated DEER data $S(t)$ to $F(t)$, under the constraint that the probability distribution of the distance $P(r) > 0$ (equation 1.25a); as a straightforward minimization of the r.m.s.d. would lead to a large number of very narrow peaks, an additional term introduces smoothness to the distance distribution

$$G_\alpha(P) = \|S(t) - F(t)\|^2 + \alpha \left\| \frac{d^2}{dr^2} P(r) \right\|^2 \tag{1.25a}$$

where the simulated data $S(t)$ is computed by multiplying a given distance distribution $P(r)$, with a kernel function K(t,r)

$$S(t) = K(t, r)P(r) \tag{1.25b}$$

and the kernel function is given by

$$K(t, r, \triangle\omega) = \int_0^1 \exp\left(-\frac{\omega_{dd}^2}{\Delta\omega^2}\right) \cos\left((3x^2 - 1)\,\omega_{dd}t\right)\,\mathrm{d}x \tag{1.25c}$$

with

$$\omega_{dd} = \frac{2\pi \cdot 52.04\,\text{MHz nm}^{-3}}{r^3} \tag{1.25d}$$

The second term of the fitting function $G_\alpha(P)$ is the regularisation-parameter (α) weighted square norm of the second derivative of the distance probability distribution $P(r)$, and is thus a measure for the smoothness thereof. The optimal value of α (*i.e.* the best compromise between low m.s.d. and smoothness of the distance distribution) can be determined by the corner of an L-curve, that plots the log of the m.s.d. *vs.* the log of the square norm of the second derivative of $P(r)$ for different values of α [202].

1.4.4 Förster resonance energy transfer

1.4.4.1 Principles

Förster resonance energy transfer (FRET) is a powerful technique to measure distances between fluorophores. It has been extensively used to study protein-protein interactions, *e.g.* GPCR oligomerisation [203–206], and conformational changes [207–210]. When there is overlap of the emission spectrum of one fluorophore, the donor, with the excitation spectrum of another fluorophore, the acceptor, resonant non-radiative energy transfer can take place, leading to quenching of the excited state of the donor, and excitation the acceptor, which can then in turn relax back to the ground state by fluorescence, or other relaxation pathways (Figure 1.22) [211]. This energy transfer arises through long-range dipole-dipole interactions,
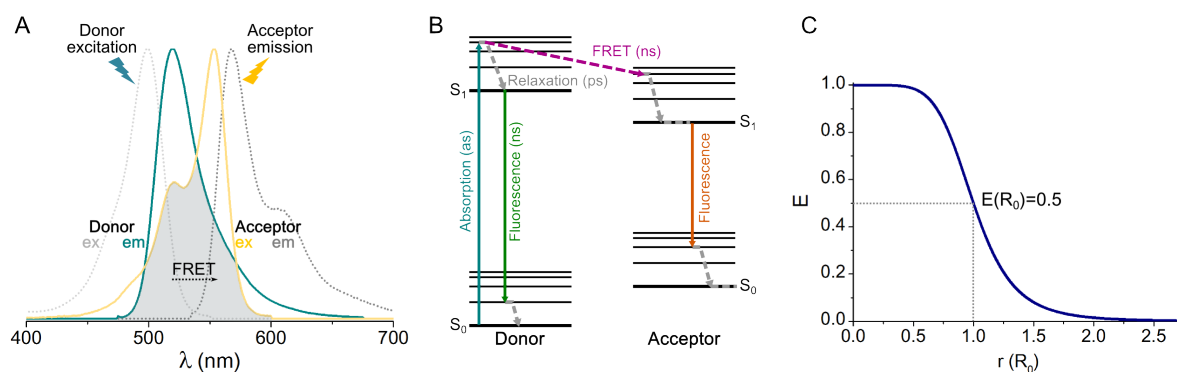
Figure 1.22: Förster resonance energy transfer. Schematic showing the basic theory of FRET through **(A)** the overlap between the donor emission and acceptor excitation spectrum; **(B)** a Jablonski diagram showing the processes of absorption, fluorescence, (vibrational) relaxation, and FRET with their associated time scales; and **(C)** the relation between the FRET efficiency (E) donor-to-acceptor distance (r) expressed in the characteristic FRET pair Förster radius (R_0), which is defined as the intermolecular distance at which energy transfer efficiency is 50%.

but instead of magnetic dipole interactions like in DEER, in FRET the interaction occurs through the electronic dipoles of the fluorophores.

The efficiency of energy transfer depends on the distance between the donor and acceptor (r) and their the Förster radius R_0 which is a property of the fluorophores used and is defined

by the distance at which energy transfer efficiency (E) is 50 % (Figure 1.22C) [212]:

$$E = \frac{R_0^6}{R_0^6 + r^6} \tag{1.26}$$

The Förster radius in turn depends on the overlap integral between the donor emission spectrum and acceptor excitation spectrum J; the relative orientation between the emission and excitation dipole moments of the donor and the acceptor as described by the orientation factor κ; the refractive index of the medium n; and the fluorescence quantum yield of the donor in the absence of the acceptor Φ_0:

$$R_0{}^6 = \frac{9000 \, \Phi_0 \, (\ln 10) \kappa^2 \, J}{128 \, \pi^5 \, n^4 \, N_A} \tag{1.27}$$

where N_A is Avogadro's number. The spectral overlap integral calculated calculated as such

$$J = \int f_D(\lambda) \, \epsilon_A(\lambda) \, \lambda^4 \, d\lambda \tag{1.28}$$

where f_D is the normalized donor emission spectrum, and ϵ_A is the acceptor molar extinction coefficient. In practice, for non-fixed small dyes, it is usually assumed that they are isotropically oriented resulting in $\kappa^2 = 2/3$. Errors in the orientation factor will only linearly affect the Förster radius, and do not hamper relative distance determination for one particular system, assuming other experimental factors are kept constant.

Experimentally, donor fluorescence quenching in the presence of acceptor, or increase in acceptor fluorescence when exciting the donor, can be monitored as a measure for FRET [213]. In the latter case the contributions of "bleedthrough" and "crosstalk" need to be taken into account [214]. Often, there is some overlap between the emission spectrum of the used donor and acceptor, thus some direct emission of donor will take place at the acceptor maximum wavelength, called bleedthrough, which needs to be subtracted. Additionally, the excitation spectrum of the acceptor can overlap with that of the donor. Then, the direct excitation of the acceptor at the wavelength used to excite the donor, giving rise to acceptor emission that does not originate from resonance energy transfer, needs to be taken into account. Other factors that influence the amount of FRET observed are the donor-to-acceptor molar ratio, and the extent of protein-protein interaction (*e.g.* oligomerisation rate) when looking at intermolecular FRET [214, 215]. Data analysis will be described in more detail in chapter 5.

1.4.4.2 Labelling strategies for FRET of membrane proteins

Intermolecular FRET studies require the labelling of each of the interacting partners with a donor or acceptor from a suitable FRET pair. A common and straightforward strategy

is fusion of an autofluorescent protein (FP), such as green fluorescent protein (GFP) or a variant thereof [216, 217], to the membrane protein of interest. They are typically fused to the N- or C-terminus of the target protein, to minimize problems with folding and retain functionality; generally a linker region with high glycine and/or serine content is included as these flexible and hydrophilic residues are thought to form a random coil structure, and are thus unlikely to interact with the protein domains or to interfere with their folding [218]. The use of FPs has the benefit that the protein is directly labelled during expression, and no cofactors or additional labelling steps are required. However, fusion proteins are relatively large (~27 kDa), and can impair protein function, when inserted into functionally important domains [219].

Table 1.4: Examples of fluorescent tags targeting genetically-encoded recognitions sites.

Tag	Description	Reference
SNAP-tag	182 aa sequence encoding mutated human O^6-alkylguanine alkyltransferase, that recognizes fluorescent benzylguanine derivatives, of which many are commercially available, including FRET-compatible Alexa Fluor dyes	[220]
CLIP-tag	Variant of SNAP-tag which reacts specifically with O^2-benzylcytosine derivatives, and can also be used to aid intramolecular orthogonal labelling	[221]
ACP-tag	80 aa sequence encoding acyl carrier protein which can be labelled with fluorescent CoA derivatives in a reaction catalysed by the phosphopantetheinyl transferase AcpS, with CoA-Cy3 and Cy5 commercially available	[222]
MCP-tag	Variant of ACP tag requiring a different enzyme, Sfp, again allowing orthogonal labelling	[223]
Tetracysteine- or Lumio-tag	CCXXCC motive that binds biarsenical dyes, for example FlAsH which has better fluorescence properties than YFP and can be used in combination with CFP	[224]

Cell-free expression of membrane proteins [225] also allows labelling prior to purification, *e.g.* by the incorporation of 'non-natural amino acids' linked to fluorescent dyes (*e.g.* BODIPY) [226, 227], or by linkage of fluorophore-puromycin conjugates (*e.g.* Cy3/Cy5 conjugates) to the C-terminus [228]. These dyes are substantially smaller than fusion proteins, and thus less likely to impair function. However, this technique is less straightforward as its applicability depends on the possibility to express the protein of interest via *in vitro* methods; furthermore, these dyes are often not commercially available and need to be synthesized in-house.

Alternatively, labelling can be performed after purification, for example, using techniques relying on the association of fluorophores to specific genetically-encoded recognition sequences. These tags are typically smaller than FPs (~10-20 kDa) and can be labelled with a variety of fluorescent probes (see Table 1.4). Post-translational labelling can also be done using organic dyes, such as Alexa Fluor dyes (*e.g.* Alexa488/Alexa647) [229], or Cy dyes (*e.g.* Cy3/Cy5) [230], which are commercially available in a wide range of wavelengths, optimized for brightness and photostability. They are functionalized with reactive moieties, such as maleimide or succinimidyl esters, for site-directed labelling of sulfhydryl or amino groups in the protein, resulting in a modest (typically <1-2 kDa) modification compared to the large FPs.

1.4.4.3 FRET *vs.* DEER

Both FRET and EPR (particularly DEER) are now routinely used to measure inter- and intramolecular distances. Table 1.5 gives an overview of how the two techniques compare. Firstly, the distance range accessible by both techniques is similar, and suited to the typ-

Table 1.5: FRET *vs.* DEER Summarised comparison between spectral FRET and EPR (specifically DEER) for inter- and intramolecular distance measurements in biomolecules, including the accessible distance range, the size of the labels (after attachment) and labelling scheme required, data analysis considerations and results, the sensitivity of the techniques, and the temperature at which each can be performed.

	EPR(DEER)	FRET
Distance Range	CW-EPR: 8-20 Å DEER: 20-80 Å	10 - >150 Å (depending on R_0) Range $(0.5 - 2) \times R_0$
Label Size	190 Da (MTSL)	700 - >1000 Da (*e.g.* Alexa488&555)
Label Strategy	Same label both sites; accessible distance range not dependent on label	Differential labelling (donor/acceptor); fluorophore choice needs to be tailored to expected distance
Data Analysis	(Model-free) Tikhonov regularisation or model-based analysis $\rightarrow$ Distance distribution	Uncertainty from labelling efficiency, orientation parameter (κ^2) $\rightarrow$ Average distance (or relative E)
Sensitivity	Micromolar	Nanomolar
Temperature	<80 K	Can be chosen freely

ical dimensions of (membrane) proteins, although for longer distances (>8 nm) FRET is better suited. A clear advantage of DEER is the smaller size of nitroxide spin labels compared to fluorophores (see Figure 1.23). The smaller label and shorter tether make distance determination using DEER more precise than FRET distance measurements, as the uncertainty in the distribution of the label is much smaller, as was also demonstrated in an
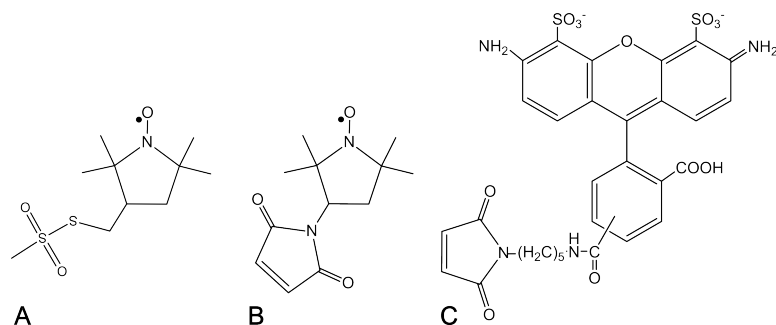
Figure 1.23: Nitroxide spin labels compared to Alexa Fluor dye. Chemical structure of typically used spin labels **(A)** MTSL and **(B)** 3-maleimido-PROXYL showed alongside that of the fluorescent dye **(C)** Alexa Fluor 488.

experimental and computational comparison [231]. Furthermore, the need for differential donor/acceptor labelling in FRET is absent in DEER, simplifying labelling procedures, especially for intramolecular distance measurements. Additionally, DEER gives insight into the distance distribution, allowing to distinguish multiple conformations, giving insight into structural heterogeneity, while typical spectral FRET measurements can only provide an average FRET efficiency and distance. However, EPR is less sensitive than fluorescence measurements, and thus far more protein is required; typically nanomole amounts at concentrations of ~100-200 μM are used in DEER experiments, while FRET can be carried out at low micromolar-nanomolar concentration (and even at the single-molecule level) using approximately ten times less protein per sample. Furthermore, FRET can be performed at physiologically relevant temperatures, while DEER measurements are performed in the frozen state (<80 K) due to the relaxation properties of the spin labels.

Both techniques provide only sparse distance constraints per measurement for structure determination, meaning that typically many different samples have to be measured. Furthermore, unlike for distance determination by NMR and crystallography, protein backbone distances cannot be directly obtained, due to the use of tethered labels, although approaches for extrapolation have been documented, especially for DEER [198, 232]. Nevertheless, as already apparent from the examples cited above, both techniques have been extensively, and successfully applied to the study of membrane proteins, and are especially suited to assess structure/function questions.

1.4.5 Microscale thermophoresis

1.4.5.1 Principles

Microscale thermophoresis (MST) is a relatively new technique that can be used to study biomolecular interactions. The technique relies on the physical phenomenon of thermophoresis (also known as the Soret effect or thermodiffusion), by which molecules move along

temperature gradients, which was already observed in the 19$^{\text{th}}$ century, but only recently applied to the study of biomolecules [233, 234] and their interactions [235, 236]. For dilute solutions where the molar fraction of the molecule of interest (i) is much smaller than that of the solvent (s, $n_i \ll 1$ and $n_s \simeq 1$) [237], thermophoretic movement, with speed $\vec{v}$, in a temperature gradient ∇T can be described by

$$\vec{v} = -D_T \nabla T \tag{1.29}$$

where D_T is the thermodiffusion coefficient D_T. In a steady state, thermal diffusion is balanced by ordinary diffusion (with diffusion coefficient D), and the overall flux of particles (J) can be described by an extension of Fick's first law of diffusion

$$J = -D \nabla c - D_T c \nabla T \tag{1.30}$$

where c is the concentration of particles. This leads to an exponential depletion law, which describes the concentration distribution, assuming constant diffusion coefficients, for particles relative to a concentration c_0 for a temperature difference $T - T_0$

$$\frac{c}{c_0} = e^{-S_T(T-T_0)} \tag{1.31}$$

where the Soret coefficient S_T is defined as the ratio of the thermodiffusion and the Brownian diffusion coefficient

$$S_T = \frac{D_T}{D} \tag{1.32}$$

and is a measure for the magnitude of the thermophoretic diffusion in the steady state [238]. For small temperature gradients where $\Delta T D_T / D \ll 1$, equation 1.31 linearises to

$$\frac{c}{c_0} = e^{-S_T(T-T_0)} \approx 1 - S_T(T - T_0) \tag{1.33}$$

Although thermophoresis is typically regarded as a local non-equilibrium phenomenon, for moderate temperature gradients (~1 K/10 μm) particles can be described by a local thermodynamic equilibrium, and thus by a succession of local Boltzmann laws [239]. It was also shown that minimizing the sample chamber size, for example in a microfluidic device or a microcapillary, removes artefacts from thermal convection [234]. Thus, from Boltzmann it then follows that the Soret coefficient is related to the entropy of the system, S, as

$$\frac{c}{c_0} = e^{(-G(T)-G(T_0))/kT} \tag{1.34a}$$

for small concentration changes δc with small Gibbs-free energy differences δG gives

$$\frac{\delta c}{c} = -\delta G / kT \tag{1.34b}$$

and equation 1.33 gives us

$$\frac{\delta c}{c} = -S_T \delta T \tag{1.34c}$$

which combines to

$$S_T = (kT)^{-1} \times \delta G / \delta T \tag{1.34d}$$

$$= -S/kT \tag{1.34e}$$

based on the thermodynamic relation $dG = -SdT + Vdp + \mu dN$ [238]. The following relation for the Soret coefficient was then derived and validated experimentally [238], which takes into account the two main contributions to the entropy of a molecule in aqueous solution, the entropy of ionic shielding and that of hydration,

$$S_T = \frac{A}{kT} \left(-\Delta s_{hyd}(T) + \frac{\beta \sigma_{eff}^2}{4\epsilon \epsilon_0 T} \lambda_{DH} \right) \tag{1.35}$$

where A is the molecule area, s_{hyd} the particle-area-specific hydration entropy ($s_{hyd} = S_{hyd}/A$), and the third (green) term describes the contribution from ionic shielding where ϵ is the dielectric constant, σ_{eff} the effective surface charge density, λ_{DH} the Debye length, and β a factor arising from the temperature derivative of the ionic Gibbs-free enthalpy ($\beta = 1 - (T/\epsilon)\delta\epsilon/\delta T$).

1.4.5.2   MST experiment

In simple terms, it can be seen from equation 1.35 that the Soret coefficient, and thus thermophoretic behaviour of a molecule depends on its size (first term, red), its charge (third term, green) and its hydration shell (second term, blue). Microscale thermophoresis exploits this dependency for the study of biomolecular interactions. The diffusion of a molecule of interest in a thermal gradient is optically probed, either through its native fluorescence (*e.g.* Trp fluorescence for proteins) or that of a conjugated fluorophore. Binding of another (not directly observed) molecule will affect the size, charge and/or hydration shell of the molecule under study, and thus influence its thermophoretic behaviour. By performing a titration experiment with varying concentrations of the non-observed partner while keeping the concentration of the fluorescent partner constant, a binding affinity can be extracted from the concentration-dependent change of the thermophoretic behaviour of the fluorescent partner. The general experimental set-up is depicted in Figure 1.24. Samples are loaded into capillaries which are put on a (temperature-controlled) tray (up to 16 per titration). By working in a capillary format, as mentioned above, artefacts from thermal convection are minimized, and the spatial restriction of the temperature gradient allows for
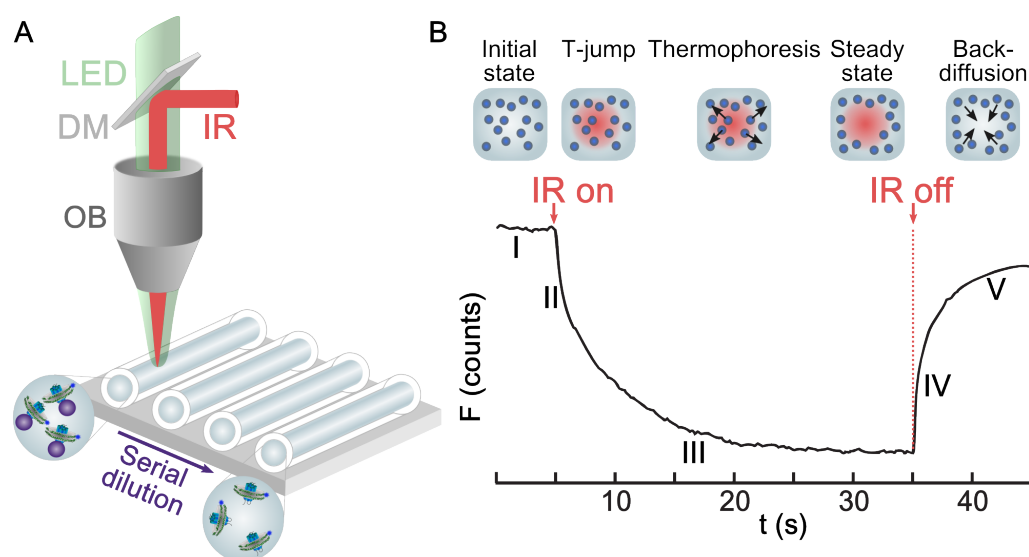
Figure 1.24: MST experimental scheme. (A) Schematic of MST set-up: samples are loaded into capillaries, placed on a (temperature-controlled) sample tray, and fluorophores are excited by an LED which is focussed onto the sample through an objective (OB) and fluorescence is detected with a CCD camera. The sample is locally heated with an IR-laser (IR) using a dichroic mirror (DM) which transmits the fluorescence excitation and emission and reflects the IR beam. **(B)** Schematic of a single MST recording: the initial fluorescence is recorded for typically ~5 s (I). The IR-laser is turned on, giving rise to a sudden (~100 ms time scale) change in fluorescence, termed temperature jump or T-jump (II), which can be both positive or negative depending on the fluorophore used. Molecules then diffuse due to diffusion-limited thermophoresis (III). Both the T-jump and thermophoresis can be influenced by (bio)molecular interactions. After 30 s, in which a steady state might be reached as in the example shown, the IR laser is turned off, giving rise to an inverse T-jump (IV), and back-diffusion (V). The fluorescence after thermodiffusion (III) is normalized to the fluorescence before heating (I) or after T-jump (II). Figure based on [166].

short measurement times (<1 min per sample in total). An objective focuses the LED for fluorophore excitation and an infra-red (IR) laser ($\lambda = 1480nm$) on the same spot. The IR radiation creates a steep localised temperature gradient, while the overall heating of the sample is only a few (~1-6) degrees depending on the IR (MST) power used and capillary type. The fluorescence intensity of the molecules is recorded by a CCD camera before (I, Figure 1.24B), during (III) and after IR radiation (V). When the IR-laser is turned on (II) or off (IV), a sudden change in fluorescence occurs, termed temperature jump or T-jump, which is due to the temperature sensitivity of the fluorophore and can be either positive or negative. Thermophoresis (III) leads to the formation of a concentration gradient of the fluorescent molecules, and thus a change in the fluorescence of the observed spot. When a steady state is reached, where thermodiffusion is counterbalanced by mass diffusion, one observes a plateau in the fluorescence, although reaching a steady state is not necessary for reliable data analysis as distinguishable concentration gradients typically form within a few seconds [235]. After the IR-laser is turned off particles diffuse back into the depleted region (V).

1.4.5.3   MST data analysis

Both the T-jump and thermophoresis can be influenced by (bio)molecular interactions, and both can be used in the analysis. For analysis of the thermophoresis, the fluorescence during/after thermodiffusion (III, Figure 1.24B), F_1, is normalized to the fluorescence before heating (I) or after T-jump (II), F_0:

$$F_{norm} = \frac{F_1}{F_0} \tag{1.36}$$

Inclusion of the T-jump typically leads to a better signal-to-noise ratio in the resulting binding curve, as it is often influenced by the interaction studied. However, when the effect of binding on the T-jump and thermophoresis have opposite signs, the T-jump should not be included, or should be studied separately. For small temperature gradients as used in the MST experiment, the linearised depletion law (equation 1.33) can be applied

$$\frac{c_{1,hot}}{c_{0,cold}} \approx 1 - S_T \Delta T \tag{1.37}$$

where $c_{1,hot}$ is the concentration of fluorescent molecules in the observed spot after thermophoresis, and $c_{0,cold}$ that before heating or after T-jump. As the concentration of the fluorophore in the focal spot is directly proportional to the fluorescence intensity observed, it follows that

$$F_{norm} \approx 1 + \left(\frac{\delta F}{\delta T} S_T \Delta T \right) \tag{1.38}$$

taking into account a possible contribution from the temperature dependency of the fluorophore $\delta F / \delta T$. Thus F_{norm} reports on S_T, which as stated above bears information on a the size of a molecule, its charge, and its hydration shell. As these can all be influenced by interactions with other molecules, or in other words a binding event, the change in S_T due to binding is directly proportional to a change in F_{norm}. Thus the equilibrium constant of a molecular interaction, between the observed fluorescent molecule and the non-fluorescent titrated binding partner, can be quantified from the change in F_{norm} as a function of the concentration of the titrated partner, by performing MST on a dilution series of the unlabelled partner (spanning concentrations well below and above the expected K_d) in the presence of a constant amount of fluorescent partner. The observed fluorescence is made up of contributions from molecules both bound ($F_{norm,bound}$) and unbound ($F_{norm,unbound}$) to the binding partner

$$F_{norm} = (1 - x)F_{norm,unbound} + xF_{norm,bound} \tag{1.39}$$

where x gives the fraction of bound molecules. This equation, in combination with a model for the binding event, such as the law of mass action or more complex models such as the

Hill equation for cooperative systems, can be used to calculate binding affinities for the interaction studied. For the simple, but often applicable, law of mass action, binding can be described by

$$A + B \leftrightarrows AB$$
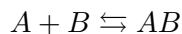
for binding partners A and B forming complex AB with equilibrium dissociation constant K_d

$$K_d = \frac{[A]_{free}[B]_{free}}{[AB]} \tag{1.40}$$

where $[A]_{free}$ and $[B]_{free}$ are the concentrations of free, unbound partners A and B and $[AB]$ that of the complex AB. As only total ($[A]$ and $[B]$) and not the free concentrations of A and B are known,

$$[A] = [A]_{free} + [AB]$$
$$[B] = [B]_{free} + [AB] \tag{1.41a}$$

equation 1.40 is adjusted accordingly:

$$K_d = \frac{([A] - [AB])([B] - [AB])}{[AB]} \tag{1.41b}$$

As F_{norm} obtained from the MST experiment is linearly related to the fraction of bound molecules (equation 1.39) solving equation 1.41b for the fraction of bound molecules and combining it with equation 1.39 gives a direct relation between F_{norm} and the K_d which can by used to fit MST data (see further in section 6.2.5).

1.4.5.4   Biomolecular interactions: MST *vs.* other approaches

Other biochemical and biophysical approaches can also give access to quantitative information on binding affinities. Radio-ligand binding assays for example, are often used, but are limited to those systems for which a radioactive analogue of the ligand exists.

Fluorescence polarisation (FP), like MST, uses optical detection of the ligand. FP measures the (de)polarisation of the fluorescence emitted by a small labelled ligand upon excitation with polarised light; binding of the ligand to a (larger) molecule (*e.g.* a protein) dampens its rotation, and thus the depolarisation of the fluorescence compared to the strong depolarisation observed for the free fast-rotating ligand [240]. This means that the technique is limited to relatively small fluorescent ligands (less than a few thousand Dalton) and systems with a sufficiently large size change upon binding to observe a change in depolarisation [241].

Another traditionally used technique for the study of molecular interactions is isothermal titration calorimetry (ITC). In ITC the change in heat compared to a reference cell upon binding of a ligand is monitored during a titration experiment, from which binding affinity,

stoichiometry and thermodynamic parameters can be determined [242]. The sensitivity of the technique is however relatively low, requiring large amounts of sample (μg) compared to MST (pg-ng).

Dynamic light-scattering (DLS) can also be used to measure molecular interactions, and like FP it relies on a change in size. In DLS the time-dependent fluctuations in light scattered by biomolecules in solution is measured, from which the hydrodynamic radius (R_H) can be determined [243]. To use DLS to measure binding, the size of the complex must be sufficiently different from that of the separate partners, limiting it to systems where the binding partners differ no more that a factor two in R_H [244].

Another powerful method is surface plasmon resonance (SPR), which unlike the aforementioned techniques, works with immobilised samples; one of the binding partners is coupled to a noble metal film, and light at the resonance wavelength is used to induce surface plasmons [245]. Binding of another molecule to the immobilised molecule leads to a change in refractive index and thus in the resonance frequency which can be measured. SPR not only gives access to binding affinities (ranging from sub-nM to low mM)) but also the kinetics of the interactions (on- and off-rates) for a interactions. The immobilised nature of the technique does mean that assay set up for new systems can be challenging, and measurements can be complicated by mass transport and rebinding [245, 246]. Moreover, the concern exists that immobilization may affect the bound molecule and its dynamics, and thus the intermolecular interaction [247–249].

The main limitation of MST is the need to be able to optically probe one of the two binding partners under investigation. MST equipment with LED wavelength and filter sets optimised to use Trp fluorescence is available, which enables label-free measurements for Trp-containing proteins, but this requires the other binding partner to not be fluorescent in the same range [250]. In all other cases, in the absence of natural fluorescence at wavelengths suited to MST equipment (blue, excitation 460-480 nm, emission 515-530 nm; green, excitation 515-525 nm, emission 560-585 nm; and red, excitation 605-645 nm, emission 680-685 nm) fluorescent labelling of one of the partners is required [166]. Nevertheless, MST is a powerful method to study biomolecular interactions, as it does not only rely on a change in particle size like FP or DLS, but also reports on changes in charge and hydration shell. It is especially this last aspect of MST that renders the technique powerful enough to study the binding of small molecules, which do not have a big effect on the complex size or charge. Indeed MST has been used to study the binding of single ions, $e.g.$ Ca^{2+} [251] and NO_3^- [252]. Sample consumption is very low (pg-ng per titration), especially of the fluorescent binding partner which is used at low ($\lesssim$ 25 nM) concentrations, which is ideal for the study of membrane proteins which are often difficult to express in large amounts. Furthermore,

it is a free-solution technique and as such free from surface artefacts and immobilization procedures as needed in SPR. Although, it does not readily give insights into binding kinetics like SPR, binding affinities as well as thermodynamic parameters can be obtained by performing K_d experiments at different temperatures through the capillary tray temperature control [253]. In a recent review it was also demonstrated that MST can be used to determine binding stoichiometry, to get insights on biding modes and conformations, and to analyse protein unfolding and enzyme kinetics (on a s time scale) [253]. The technique is not limited by buffer conditions and can be used in complex bioliquids (such as blood serum or cell lysates), as long as the conditions are kept constant along the titration series [235]. Practical considerations for assay set-up are discussed in detail in [166].

1.5   Aims of the thesis

The main aim of this thesis is to further our understanding of membrane protein structure and function in lipid bilayers through *in vitro* studies of minimal systems for two membrane proteins: a prokaryotic homologue for human peptide transporters, PepT$_{So}$, and a mammalian GPCR, neurotensin receptor 1 (NTS1).

Chapter 2 looks at the effect of ligand and electrochemical gradient on the structure of the proton-coupled peptide transporter PepT$_{So}$, using DEER for intramolecular distance measurements on the transporter reconstituted in liposomes.

To be able to apply FRET and DEER on NTS1, the current purification protocol and labelling protocol are optimised (Chapter 3).

Two recent x-ray crystallography structures of engineered NTS1 constructs bound to its peptide agonist revealed only small conformational changes compared to structures of other activated GPCRs, and only one of the structures included an eighth helix (H8), a structural element common to many class A GPCRs. Thus, the structure and dynamics of NTS1 in a more native lipid bilayer environment are investigated using CW-EPR (Chapter 4); specifically the effect of ligand on (local) protein dynamics at the G protein-interacting interface, the presence of H8, and the effect of ligand has thereon.

While previous *in vitro* studies have shown that NTS1, like many GPCRs, can dimerise in lipid bilayers, there is no experimental data available on the structure of the dimer. Chapter 5 attempts to fill that gap by probing the dimerisation interface using FRET and DEER experiments on site-directedly labelled NTS1 reconstituted into liposomes, combined

with collaborative single-molecule FRET studies on the dynamics of NTS1 dimerisation using a droplet-interface bilayer system.

Finally, a method to study native membrane proteins in lipid bilayers by MST without the need for direct fluorescent tagging is established, and applied to NTS1 (Chapter 6), to study the effect of membrane lipid composition on G protein coupling, and the effect of various ligands (agonist and antagonist) on G protein affinity.

General conclusions and outlook are presented in Chapter 7.

2 | Peptide transport studied by DEER

2.1 Introduction

2.1.1 PepT$_{So}$

PepT$_{So}$ is a prokaryotic peptide transporter from the organism *Shewanella oneidensis*. It is an analogue of the human peptide transporters PepT1 and PepT2 [254]. They belong to the POT family of proton-dependent oligopeptide transporters, which are found both in prokaryots and eukaryots [255], and symport mainly di- and tripeptides together with protons using the energy stored in the electrochemical gradient across the membrane [256, 257]. The POT family is part of the larger major facilitator superfamily (MFS) of transporters, comprising nearly 80 different families with many well-studied members, including LacY, the lactose permease in *E. coli* [258].

PepT1 and PepT2 are interesting targets of study as they are responsible for the absorption of dietary nitrogen, but especially because they are also involved in the uptake of a variety of orally administered drugs, such as β-lactam antibiotics, antivirals and anticancer agents, which is most likely due to the similarity in stereochemical properties to the natural peptide substrates [259–262]. This activity provides therapeutic potential, in that these transporters could be actively targeted to increase the bioavailability of drugs, for example by the addition of so-called "peptide pro-drugs" to facilitate their uptake by these receptors, a strategy that is being increasingly exploited [260, 263–265].

As there is currently no suitable over-expression system for PepT1 and PepT2 for *in vitro* studies on purified transporters, attention has turned to their more malleable prokaryotic analogues. So far, structures for four bacterial POT transporters have been reported: PepT$_{So}$ [266], PepT$_{St}$ from *Streptococcus thermophilus* [267], and more recently GkPOT from *Geobacillus kaustophilus* [268], and PepT$_{So2}$ also from *Shewanella oneidensis* [269]. These transporters all have a conserved topology comprising of 12-14 TM helices arranged in two symmetry-related six-helix bundles around a central substrate-binding cavity (Figure 2.1A). The consensus is that they function by an alternating access mechanism in which the two six-helix bundles undergo conformational changes where the transporter goes from an outward-
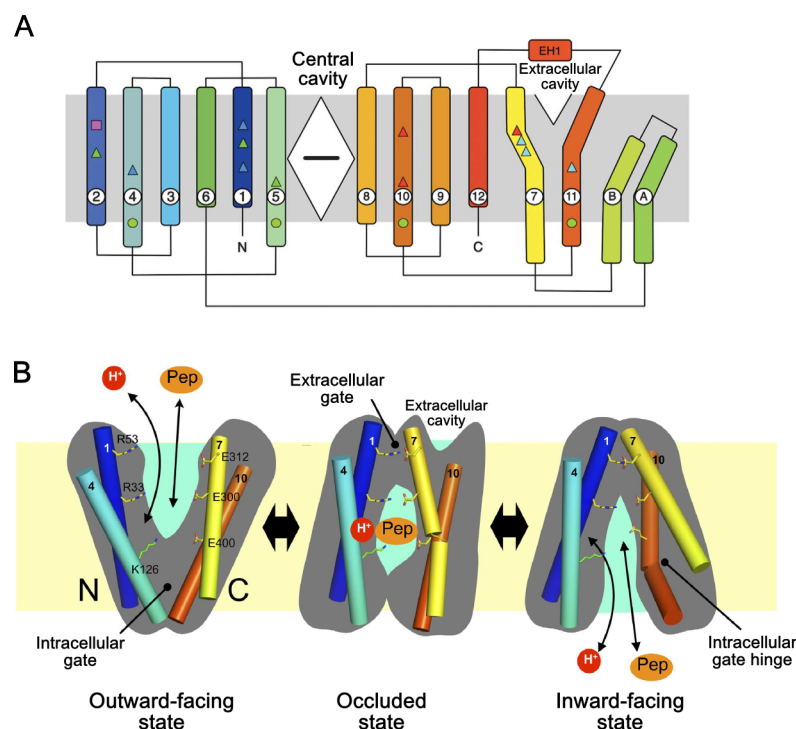
Figure 2.1: PepT$_{So}$ topology and the alternating access mechanism for transport. (A) Shows the overall topology of PepT$_{So}$, comprising two six-helix bundles around a central cavity. A small extracellular cavity observed in the crystal structure is also indicated. **(B)** Schematic of the alternating access mechanism for proton-driven symport by POT transporters is shown; substrate/peptide (Pep) and proton (H$^+$) bind from the extracellular side, inducing a conformational change via an occluded state in which bound substrate is inaccessible from both sides of the membrane; this leads to an inward-facing state and release of the substrate and proton into the cytoplasm. Salt bridges that were found to be important for transport gating in PepT$_{St}$ are shown. Figures adapted from [266] and [267].

open conformation to take up substrate, via an occluded conformation, to an inward-open conformation, leading to substrate release, thus making the substrate binding site alternatively accessible to either side of the membrane (Figure 2.1B). The opening and closing of the substrate binding site is thought to be due to the breaking and formation of critical salt bridges, acting as gates, in response to substrate binding and release. [267, 270]

PepT$_{So}$ shares 45% sequence similarity and 35% sequence identity to PepT1 [266]. There are some structural discrepancies however, as PepT1 and PepT2 each have only 12 helices, while PepT$_{So}$ has two extra helices, the function of which is currently unknown. Nevertheless, all previously identified functionally important residues are conserved, and PepT$_{So}$ and the human transporters exhibit similar pharmacology, with respect to the substrates they carry, and similar transport kinetics, supporting a common mechanism of peptide transport. Thus PepT$_{So}$ is often employed as a model for the human transporters [266].

Currently, structural data on PepT$_{So}$ is limited to a crystal structure of the transporter

in an inward-occluded state (PDB ID: 2XUT) [266], and in an inward-facing state (PDB ID: 4UVM) that is as yet unpublished (Fowler *et al.*, submitted). Modelling efforts using the symmetry between the two six-helix bundles have produced a so-called repeat-swapped model (RSM) of the transporter in an outward-facing state (Fowler *et al.*, submitted). This model was generated based on the observation that each of the six-helix bundles in MFS transporters appears to be composed of two inverted topology repeat units (Figure 2.2) [271]; in the N-terminal bundle helices 1-3 form unit A, which is related to unit B formed by helices 4-6, via a two-fold symmetry axis parallel to the plane of the membrane, and the same is found for unit C (helices 7-9) and D (helices 10-12) in the C-terminal bundle. By swapping the structures of symmetry-related repeat units, *i.e.* threading the sequence of unit A onto the structure of unit B, and *vice versa*, and doing the same for units C and D, a model could be built of an outward-facing conformation from the structure of an inward-facing conformation, as previously shown for LacY [271], and several other transporters [90, 272]. However, information on intermediate states, and what triggers conformational changes between states is still scarce.

2.1.2 EPR studies of proton-coupled MFS transporters

As explained in section 1.4.2, EPR is a powerful technique for studying protein conformation in solution. Both CW-EPR and DEER studies have been used to shed light on the mechanism of ion-coupled transport for a number of MFS transporters. A DEER study on LacY, combined with computational modelling, showed that the transporter probed inward- and outward-facing, as well as occluded states in detergent; furthermore it was shown that in the apo state LacY was biased towards the inward-facing state, and that addition of substrate shifted the conformational equilibrium towards the outward-facing state [273]. For the sodium-coupled aspartate transporter Glt$_{Ph}$, DEER measurements in both detergent and liposomes showed that protomers sample the outward-facing and inward-facing states with nearly equal probabilities [274, 275]. The observed distances in liposomes were overall shorter than in detergent, suggesting a more compact structure, potentially due to the trimeric structure of the transporter in membranes. In addition, the transporter in liposomes seemed to be somewhat biased towards the outward-facing conformation; the addition of sodium together with substrate or inhibitor modestly shifted the distributions (further) toward the outward-facing state [274]. Interestingly, adding only coupling ions (Na$^+$) resulted in similar changes to those observed upon addition of both substrate and ions, although conformation-shuttling of the Na$^+$-bound transporter is not expected, as this would lead to uncoupled Na$^+$ leaks [275]. Hänelt *et al.* did not observe a shift towards outward-facing conformations upon substrate addition for all label site pairs, but rather different effects
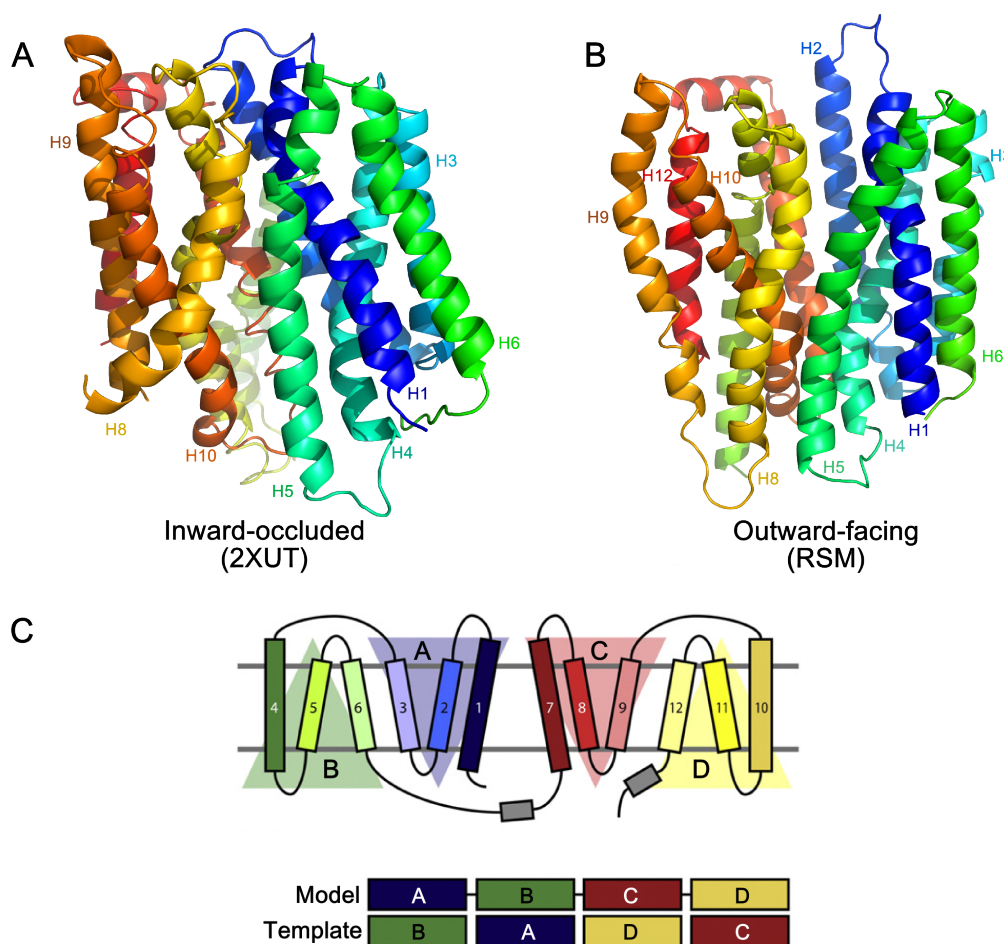
Figure 2.2: PepT$_{So}$ structure and repeat-swapped model. (A) Currently available high-resolution structure of PepT$_{So}$ (PDB ID: 2XUT) is shown [254]. **(B)** A repeat-swapped model (RSM) of PepT$_{So}$ in an outward-facing state, built using inverted topology repeat units **(C)** by swapping the structures of symmetry-related repeat units, *i.e.* threading the sequence of unit A onto the structure of unit B, and *vice versa*, and doing the same for units C and D using the 2XUT structure. The RSM was built by Sebastian Radestock and Lucy R. Forrest (Fowler, *et al.*, submitted).

for different pairs which they ascribed to the apparent low energy barrier associated with the conformational equilibrium, which might be perturbed by the cysteine mutations, spin labelling or freezing of the sample [275]. A CW-EPR/DEER study on the sodium-coupled leucine symporter LeuT showed Na$^+$-dependent formation of a different outward-facing intermediate state, for one particular label site pair, not observed in the substrate-bound state, and this intermediate state was proposed to facilitate substrate binding [276].

The effect of protonation on two proton-coupled transporters was also recently studied. Solvent-accessibility CW-EPR studies on the liposome-reconstituted drug/H$^+$ antiporter EmrD revealed a local opening of the cytoplasmic side of the N-terminal at low pH [277]. DEER studies on the proton-coupled multidrug antiporter LmrP in detergent, showed that

substrate binding stabilised an outward-open conformation at high pH, while a shift in the conformational equilibrium from outward-open to outward-closed was observed in the apo state with decreasing pH [278]. The effect of both substrate and low pH was not investigated. These two studies provide some insight into the role the proton gradient might play in transport, although, as the authors already point out, an overall change in pH as used in these studies, is not the same as the proton-gradient under which these transporters normally function. Thus, it could be that effects are more subtle than portrayed by these studies.

Nevertheless, so far all DEER studies suggest that MFS transporters are dynamic and probe multiple conformations, and that the equilibrium between these conformations can be affected by the presence of substrate.

2.1.3 Aim

To investigate how peptide transport by $PepT_{So}$ is influenced by the electrochemical gradient, in collaboration with Nicolae Solcan and Simon Newstead (Department of Biochemistry, University of Oxford), I performed DEER measurements on the transporter reconstituted into liposomes. Inter-residues distances on the periplasmic and cytoplasmic side of $PepT_{So}$ were measured in the presence and absence of substrate, with or without an electrochemical gradient applied. Thus we aimed to elucidate how peptide and the proton gradient influence the conformational state of the transporter, to get further insight into the overall mechanism of peptide transport.

2.2 Materials and method

2.2.1 $PepT_{So}$

$PepT_{So}$ was expressed, purified and then reconstituted by Nicolae Solcan after spin labelling by me. Double cysteine mutations were introduced in $PepT_{So}$ at the cytoplasmic (S141C/S432C and R201C/E364C) and periplasmic side (N174C/S466C) at positions equivalent to those in a previous SDSL study of the related LacY transporter [273]. The mutants were produced by site-directed mutagenesis, and expressed and purified as described previously [254]. Purified mutants were labelled with MTSL, after which they were reconstituted into liposomes of acetone-ether washed *E. coli* total lipid extract and POPC (Avanti Polar Lipids) at a 3:1 ratio (w/w) by rapid dilution as described in Appendix A.2. Substrate (di-alanine: diAla) transport was either initiated in a electrochemically ($\Delta\Psi$) driven manner, or substrate gradient-driven manner (counterflow), by using different internal and external liposome buffers (explained in Figure 2.4 and Table A.1). Thus, DEER samples
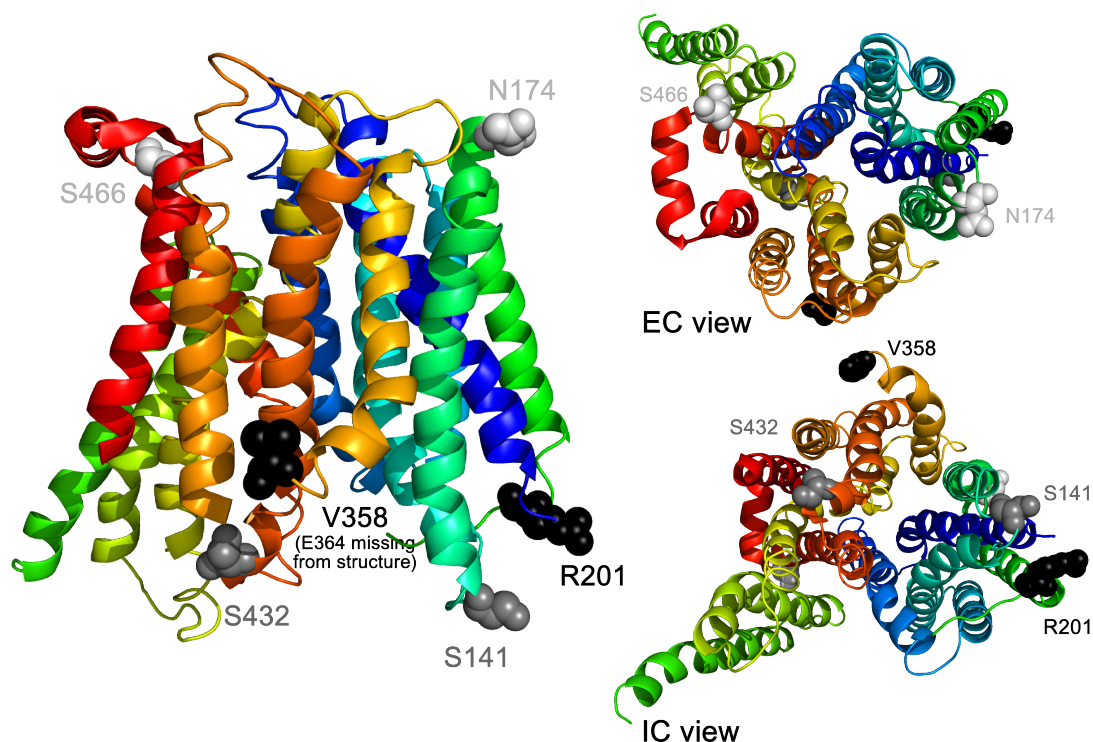
Figure 2.3: Labelling sites on PepT$_{So}$ for DEER. Residues pairs that have been mutated to Cys for SDSL of PepT$_{So}$ for DEER experiments are highlighted on the inward-occluded crystal structure of PepT$_{So}$ (PDB ID: 2XUT): N174 and S466 on the periplasmic (EC) side (light grey); and S141 and S432 (grey), and R201 E364 on the cytoplasmic (IC) side (black). As the loop in which E364 resides is not resolved in the crystal structure the nearest resolved residue, V358, is highlighted instead. Helices are coloured as in Figure 2.1.

were prepared in four conditions: with electrochemical gradient and substrate ($\Delta\Psi$+diAla), with electrochemical gradient, without substrate ($\Delta\Psi$ apo), without gradient with substrate (counterflow, CF+diAla), and without gradient without substrate (CF apo). A fifth condition was tested for one mutant, where the same buffers as for the $\Delta\Psi$ sample were used, but without valinomycin, to control for any buffer effects ($\Delta\Psi$ control). As transport assays have shown that transport of added substrate completes within ~5-15 min, 10 μL of the external buffer ($\Delta\Psi$ buffer with valinomycin, with or without diAla, or CF buffer with or without diAla) was added shortly before transfer to high precision 3 mm quartz tubes to initiate transport. Samples were then quickly flash-frozen in liquid nitrogen to trap the protein in a transporting state, and to avoid water crystallisation.

2.2.2 DEER

DEER distance measurements were performed at X-band on a Bruker Elexys 680 spectrometer, using a 3 mm split-ring resonator (ER-4118X-MS3, see also Appendix A.8.2). Samples were cooled to 50 K using a helium cryostat. DEER traces were recorded using both 4p

A. ΔΨ-driven
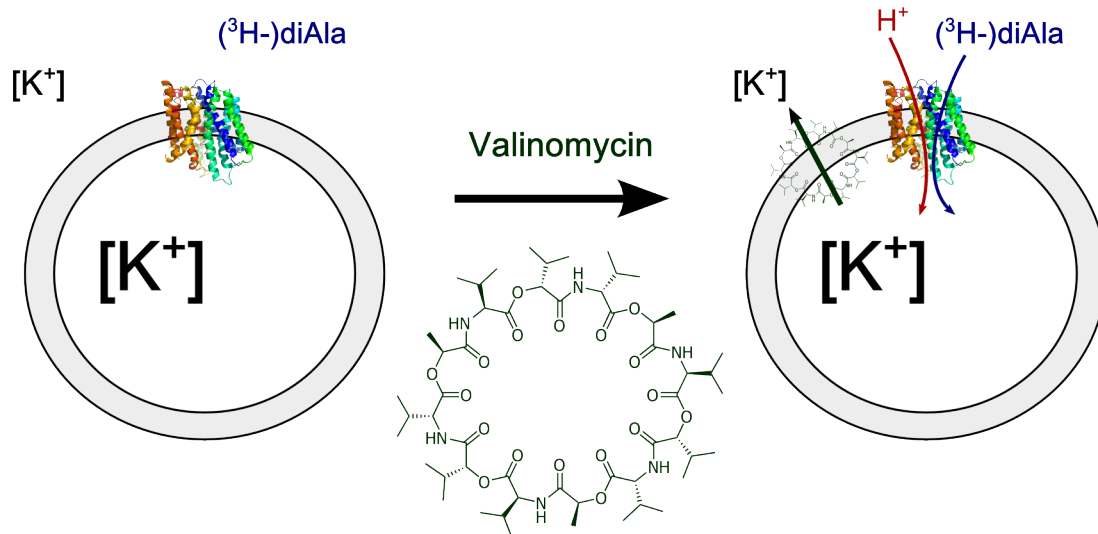
B. Substrate-driven (counterflow)
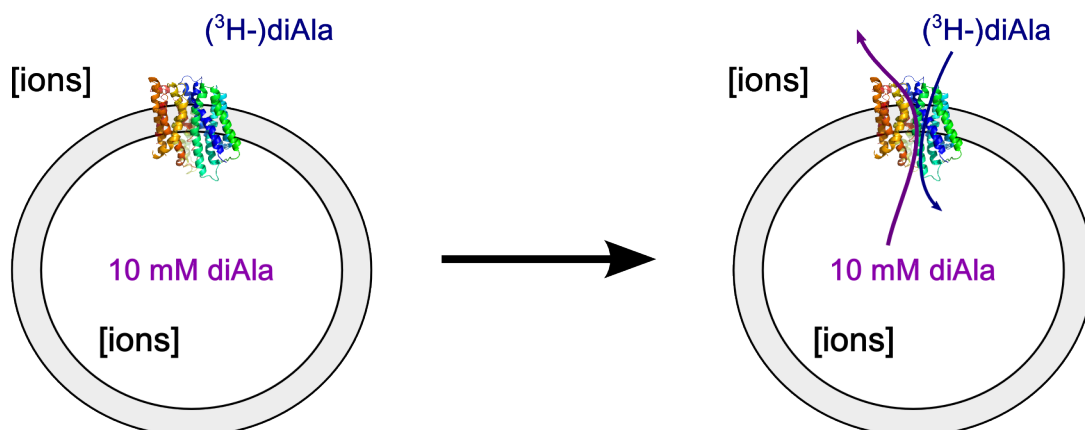
Figure 2.4: Experimental set-up for PepT$_{So}$ peptide transport. (A) ΔΨ-driven transport: the potassium ionophore valinomycin facilitates an efflux of K$^+$ ions down the K$^+$ concentration gradient created by using different internal and external liposome buffers; this creates external net positive charge, leading to protonation of the protein, and peptide transport. **(B)** Counterflow transport: in the absence of an ion gradient, liposomes were loaded with a high concentration of peptide, causing the protein to transport it out down its concentration gradient, leading to concomitant uptake of external (labelled) peptide. See also Appendix A.2.

and 3p DEER sequences (see 1.19). For both the 3p and 4p experiments the probe π and $\pi/2$ pulses were set to 32 ns, and the pump π pulse was set to 12-24 ns, to obtain complete echo inversion at maximum power (minimum ELDOR attenuation) while minimizing any proton modulation induced by pulse overlap not averaged out by varying τ_1 pulse delays. The probe frequency was set to coincide with the maximum of the nitroxide spectrum, and the pump frequency was set 65 MHz upfield. Raw data was phased using DeerAnalysis 2013

software [202], and combined by least-squares fitting using MATLAB 2013 (MathWorks) as per the DEER-Stitch method by Lovett *et al.* [197]. Distance distributions were derived from stitched data using model-free Tikhonov regularisation in DeerAnalysis 2013.

2.3   Results and discussion

Three double cysteine mutants were investigated: S141C/S432C (H4/5-H10), R201C/E364C (H6-H8/9, both cytoplasmic), and N174C/S466C (H5/H11, periplasmic, see Figure 2.3). Functional assays (Figure 2.5) performed by Nicolae Solcan, at sample conditions similar to those used in the DEER samples, showed that two of these samples were able to transport radio-labelled peptides into liposomes well above background levels (R201C/E364C and N174C/S466C), while the S141C/S432C mutant appeared to be more functionally impaired. The $\Delta\Psi$-driven assay showed that transport occurred in a valinomycin-dependent manner. This indicates that the gradient created under these sample conditions does facilitate transport, despite the small sample volume as required for the DEER samples only allowing for the creation of a modest membrane potential of roughly -30 mV, instead of -100 mV as typically used in $PepT_{So}$ transport assays (calculated as per equation A.1).

Background-corrected dipolar evolution data and the corresponding distance distributions obtained by model-free Tikhonov regularisation are shown in Figures 2.6, 2.7 and 2.8. The distributions were subjected to Gaussian deconvolution to obtain peak centres and widths (Table 2.1 and Appendix C). To be able to assess the distances observed in terms of protein conformation, we can compare the distances found to those expected from the available structures of the transporter in different stages of the transport cycle; the crystal structure in an inward-occluded state (2XUT), the repeat-swapped model (RSM) in an outward-open state, and an inward-open model based on the structure of the related POT transporter $PepT_{St}$ (Fowler *et al.*, submitted). Cα-Cα distances from these structures are given in Table 2.2. Some agreement is found between the distances observed in the DEER experiments (Table 2.1) and the distances expected from the Cα-Cα separation in crystal structure and models of the transporter (Table 2.2), with shortest distances expected and found for the S141/S432 pair, and longer distances for the other two pairs. The ~32-33 Å distance found for S141/S432 is longer than the expected distances of 21-24 Å, which is likely due to contributions of the spin label tether. Similarly, the unexpectedly short ~19-21 Å distances found for N174/S466 could be a result of spin label rotamers. Alternatively, the different environments for the protein (*i.e.* protein crystallised in detergent *vs.* reconstituted in liposomes) could contribute to these discrepancies. The distances found for R201/E364 agree very well with those expected (45 Å compared to $\gtrsim$ 43.5 Å), although the short distance expected from the RSM (26.5 Å) is not observed in most conditions. As spin-label tethers can only
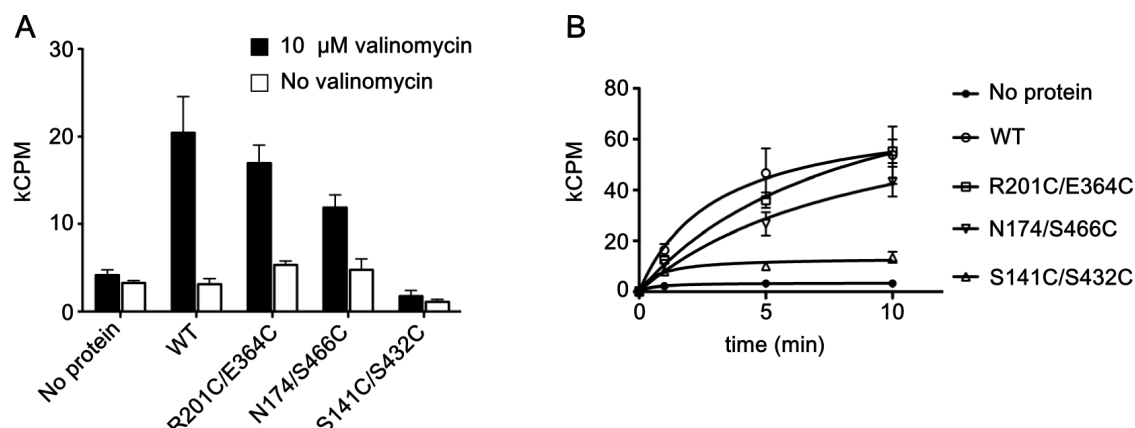
Figure 2.5: Transport activity of double Cys PepT$_{So}$ mutants for DEER. Activity assays were performed by Nicolae Solcan on the Cys mutants used in DEER under conditions similar to those used in the final DEER samples. **(A)** $\Delta\Psi$-driven assay: 5 μL proteoliposomes containing internal buffer (20 mM KPi, 100 mM KAc and 2 mM MgSO$_4$) were resuspended in 10 μL external buffer (120 mM NaPIPES and 2 mM MgSO$_4$) containing 15 μM ^{3}H-diAla in the presence and absence of valinomycin (to induce K$^+$ flow, to create an $\Delta\Psi$), to a final protein concentration of 250 μM. Uptake was measured at pH 6.5 and 30 °C after 10 min. The Y-axis shows uptake of the ^{3}H label in 1000 counts per minute (kCPM). (B) Counterflow assay: 5 μL proteoliposomes containing internal buffer (50 mM KPi pH 6.5, 2 mM MgSO$_4$) and 10 mM diAla were resuspended in 10 μL of external buffer (50 mM KPi pH 6.5, 2 mM MgSO$_4$) containing 5 mM ^{3}H-diAla, to a final protein concentration of 250 μM. Peptide-driven uptake was measured over time at 30 °C.

extend to 10 Å at most, giving a maximum spread of 20 Å, the wide distance distributions found for mutants S141/S432 and N174/S466 (and for R201/E364 "$\Delta\Psi$+diAla") spanning 25 and 45 Å, respectively, cannot solely be an effect of spin label rotamer contributions, and are thus indicative of the presence of multiple conformations.

To gain more insight into whether the distance distributions observed by DEER correspond to different conformational states of the transporter, spin label rotamer analyses were performed by Philip Fowler, in which the contribution of the spin label tether to the predicted distances is taken into account; here, a library of possible MTSL rotamer conformations is introduced into the available protein structure/model for each of the residues of a given DEER pair, discarding rotamers that would give steric clashes (as described in [232]). From the remaining rotamers that are sterically allowed, distance distributions are calculated from all the possible spin-spin distances. The resulting predicted distance distributions for the inward- and outward-facing transporter conformations are shown in Figure 2.6C, 2.7C, and 2.8C.

For the S141/S432 the Cα-Cα distances vary only ~2-3 Å for the different transporter states, and the rotamer library approach also predicts largely overlapping distance distributions. So, although the width of the distribution is clearly indicative of multiple conformations, the individual peaks cannot confidently be ascribed to a specific transporter state. Together
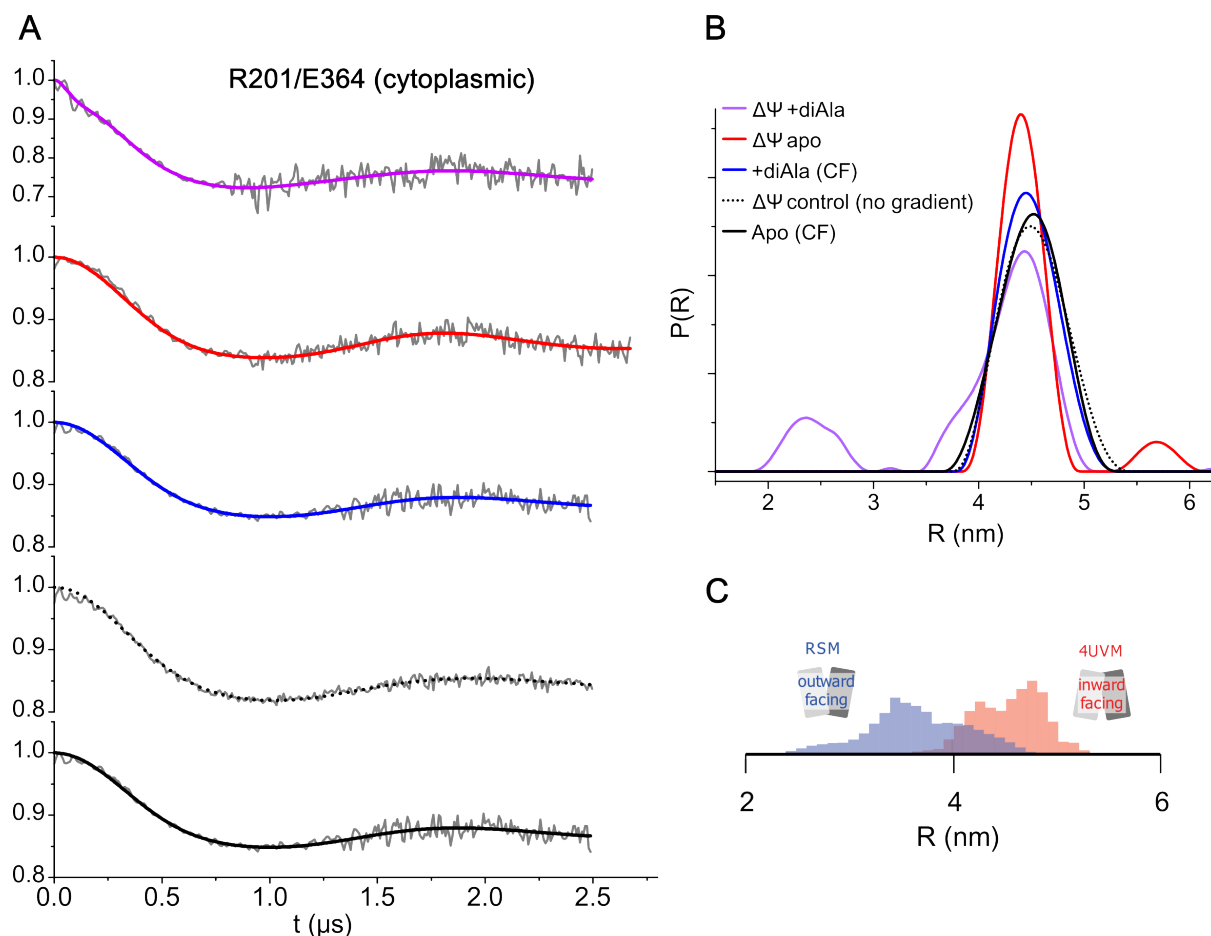
Figure 2.6: R201/E364: Fitted DEER traces and distance distributions. DEER experiments were performed in the presence of a valinomycin-induced electrochemical gradient ($\Delta\Psi$) with or without di-alanine peptide present (+diAla or apo, respectively); or under counterflow conditions (CF), *i.e.* no chemical gradient, but with high concentrations of peptide in the +diAla sample to induce transport. A "$\Delta\Psi$ control" sample was measured under the same conditions as "$\Delta\Psi$ apo" but without valinomycin, to ensure the difference in buffer compared to counterflow conditions had no effect. **(A)** Form factor (grey) obtained by background correction of the dipolar evolution function, and fit of thereof are shown. Lower S/N at longer evolution time compared to shorter evolution time is due to the difference in noise on the 4p and 3p trace. **(B)** Distance distributions derived from the fitted form factors. **(C)** Distance distributions derived from MTSL rotamer analysis (by Philip Fowler) on the inward facing crystal structure (4UVM) and the outward-facing repeat-swapped model (Fowler *et al.*, submitted).

with the poor transport capability observed, this makes this mutant a poor reporter of PepT$_{\text{So}}$ functionality.

For the N174/S466 mutant a slightly larger Cα-Cα distance change is expected (~5-9 Å, Table 2.2), although rotamer analysis again predicts substantial overlap in the DEER distance distribution (Figure 2.8C). Similar distances are observed for the N174/S466 mutant in all buffer conditions (Figure 2.8B), although in the presence of electrochemical gradient
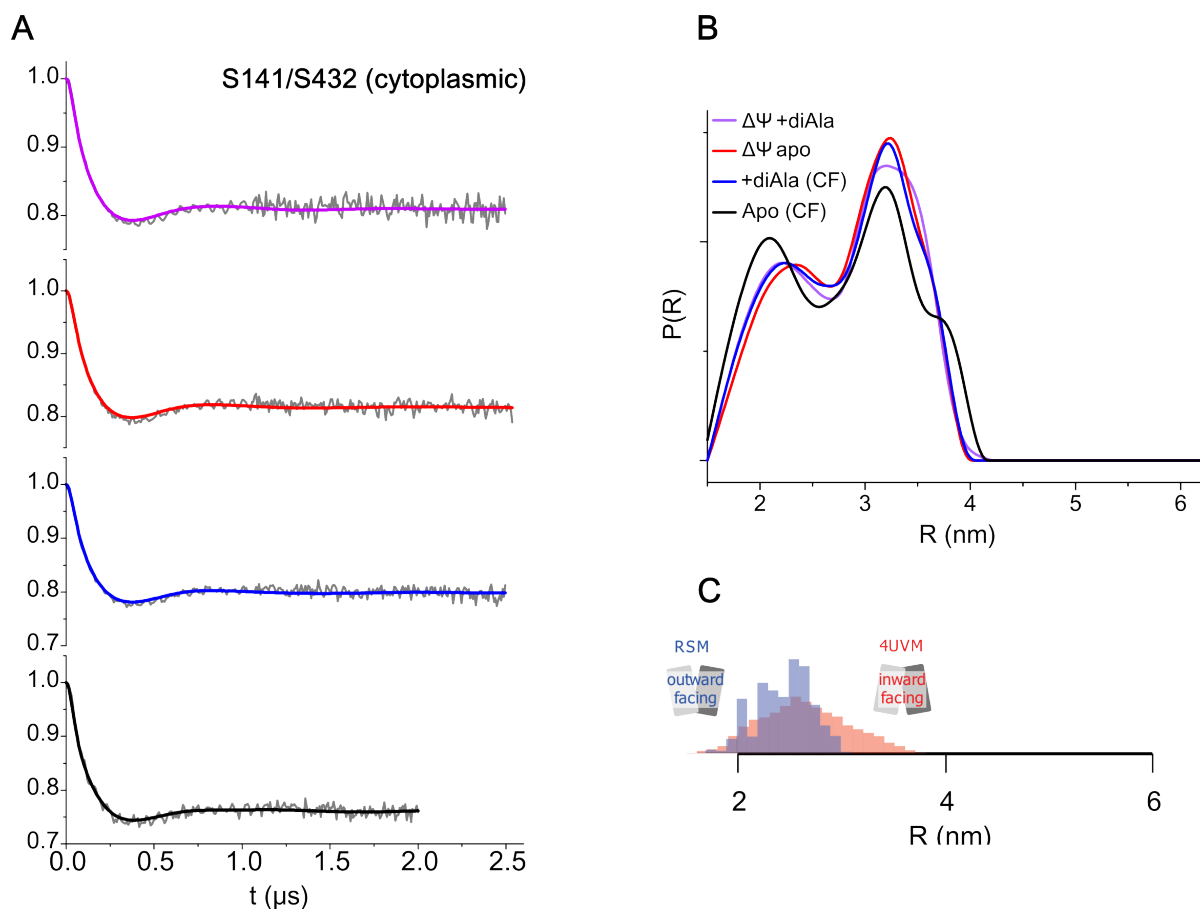
Figure 2.7: S141/S432: Fitted DEER traces and distance distributions. Same as Figure 2.6, but without the "ΔΨ control" sample.

and peptide (purple trace) a somewhat larger relative contribution of short distances was observed. The signal-to-noise ratio of the latter (3p) part of the DEER trace of the "ΔΨ apo" sample (Figure 2.8A, red trace) is too poor to distinguish the two peaks around ~40-50 Å seen in the distance distributions of the other three samples; however, visual inspection of the early part of the DEER trace shows an intermediate state between the "ΔΨ+diAla" (purple trace) and "CF" samples (blue and black traces), which is also apparent from the increased contribution of the ~20 Å peak in the distance distribution compared to CF samples (Figure 2.8B). The short distance at ~20 Å is not predicted from the Cα-Cα distances in the crystal structure and RSM (Table 2.2) or from rotamer analysis (Figure 2.8C). Although the predicted N174/S466 Cα-Cα distance is shorter for the inward-facing than the outward-facing model, rotamer analysis suggests that shorter distances (<40 Å) are more likely due to the outward-facing state of the transporter (Figure 2.8C). Considering that the rotamer analysis takes into account spin label flexibility, it is a more reliable tool to interpret DEER data than the Cα-Cα distances from the (crystal structure) models. Thus,
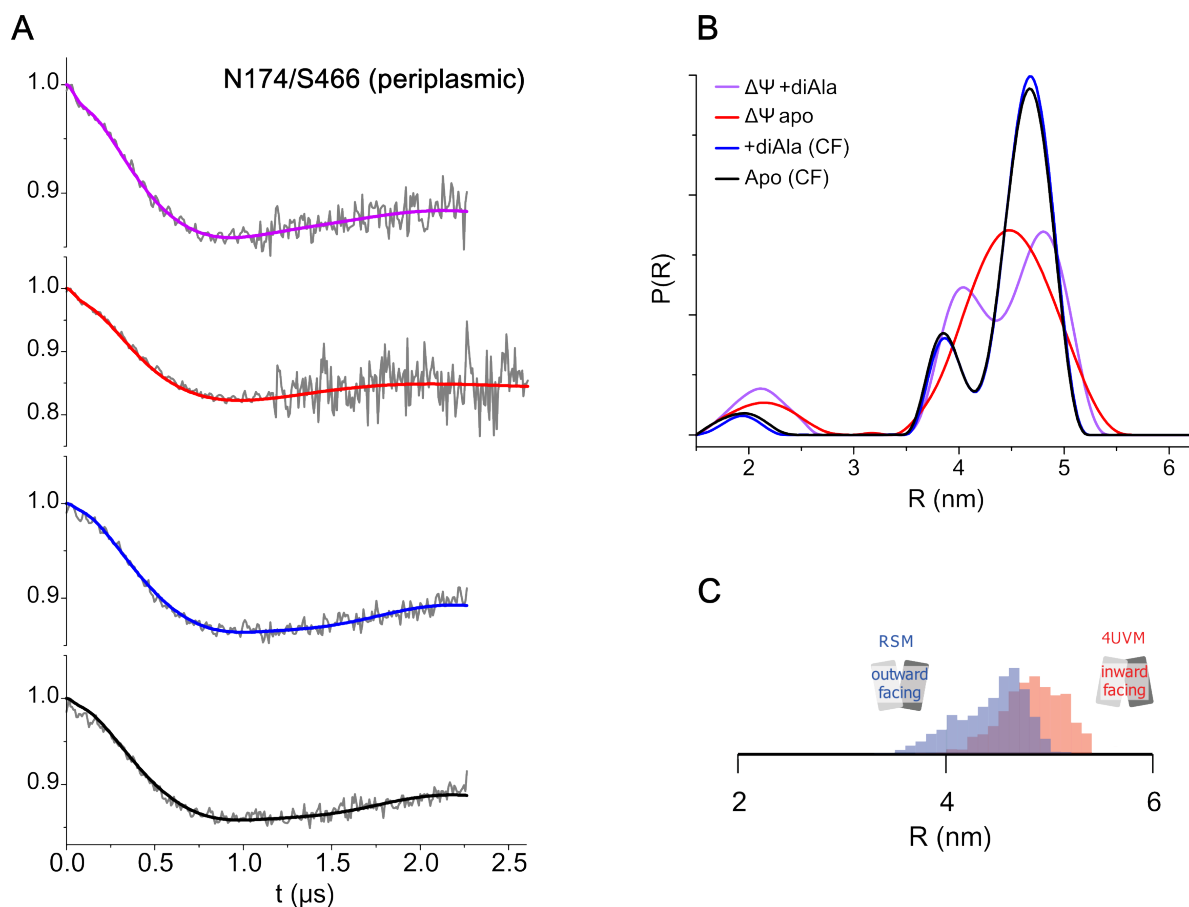
Figure 2.8: N174/S466: Fitted DEER traces and distance distributions. Same as Figure 2.6, but without the "ΔΨ control" sample.

although it is not entirely clear to what state the apparent increase in short distances in the N174/S466 mutant can be ascribed, rotamer analysis is most consistent with a bias towards the outward-facing state of the transporter in the presence of an electrochemical gradient. The R201/E364 mutant is the only sample to show a clear difference between the different sample conditions, with the "ΔΨ+diAla" sample (purple trace) showing a peak centred around 24 Å which is not present under other conditions (Figure 2.6B). Both the Cα-Cα distance (Table 2.2) and rotamer analysis (Figure 2.6C) suggest that short distances correspond to the outward-facing state of the transporter, and thus this peak can more confidently be ascribed as such. The overall width of the distance distributions seen for R201/E364 under the other experimental conditions (*i.e.* "ΔΨapo" and "CF") is much narrower (~10 Å) than observed for the other two mutants (~25-35 Å). However, the overlap in the predicted distributions for inward and outward conformational states from the rotamer analysis (Figure 2.6C) suggests that this does not exclude the possibility of this mutant also probing multiple conformations in solution, and protonation in combination with substrate binding

Table 2.1: DEER distances extracted by Gaussian deconvolution. Distance distributions obtained from DEER measurements on the three mutants (Figures 2.6, 2.7 and 2.8) were subjected to Gaussian peak-fitting in OriginPro 8.5 (OriginLab). The centre of each of the fitted Gaussian peaks (R) is given ($\pm$ the half-width at half-height) as well as the relative contribution to the total area (A). See also Appendix Appendix C.

		N174/S466		S141/S432		R201/E364	
		R (Å)	**A (%)**	**R (Å)**	**A (%)**	**R (Å)**	**A (%)**
CF	*apo*	19 ± 2	5	21 ± 4	41	45 ± 4	100
		39 ± 2	17	32 ± 4	53		
		47 ± 3	78	38 ± 1	6		
	+diAla	19 ± 2	3	22 ± 4	42	45 ± 3	100
		39 ± 1	16	33 ± 4	58		
		47 ± 3	81				
ΔΨ	*apo*	21 ± 4	10	23 ± 4	41	45 ± 2	93
		45 ± 5	90	33 ± 4	59	57 ± 3[1]	7
	+diAla	21 ± 3	12	22 ± 4	41	24 ± 3	12
		41 ± 2	35	33 ± 4	59	39 ± 3	35
		48 ± 3	53			45 ± 43	53
	control	-	-	-	-	45 ± 4	100

[1] Distance most likely a fitting artefact (not stable with variable background subtraction).

Table 2.2: Cα-Cα distances between DEER residues in PepT$_{So}$. For each residue pair the expected Cα-Cα distance was determined from the crystal structure (2XUT) in an inward-occluded state, the repeat-swapped model in an outward-open state, and an inward-open model based on the structure of the related POT transporter PepT$_{St}$ [267] built by Lucy R. Forrest and Sebastian Radestock (Fowler *et al.*, submitted).

	Cα-Cα distances (Å)		
	Inward-Occluded	**Outward-open**	**Inward-open**
N174/S466	39.4	42.8	33.6
S141/S432	24.4	20.7	22
R201/E364	$\gtrsim 43.5$[1]	26.5	43.5

[1] E364 is not resolved in the crystal structure (loop between H8 and 9 is partially missing), but overlay of the inward-open model and 2XUT shows that the Cα-Cα distance for the latter is likely to be similar or slightly larger based on the helix tilt of the resolved portion of H8.

stabilising another, more outward-open conformational state.

2.4   Conclusions

The study presented here is the first EPR study on a gradient-driven transporter that exploits liposomes to create an electrochemical gradient, thus more closely mimicking native

conditions compared to what can be achieved in isotropic conditions. While further study is required to draw robust conclusions about the transport mechanism of PepT$_{So}$, preliminary results indicate the importance of the electrochemical gradient for ligand-induced conformational changes in the transporter. The broad DEER distance distributions obtained suggest that the transporter probes a variety of conformations even in the absence of substrate, as previously observed for other MFS transporters [273–276, 278]. As previously argued for EmrE [279], this could reflect the need for a dynamic apo state to allow binding of a wide variety of structurally different substrates. Only in the presence of a gradient did the substrate appear to induce a conformational change in the receptor (for R201/E364, Figure 2.6), or perhaps at least a shift in the equilibrium of the probed conformations (for N174/S466, Figure 2.8), suggesting that protonation is required to trigger conformational changes associated with transport. Previous studies of MFS transporters (as discussed in section 2.1.2) showed that ion coupling alone could shift the conformational equilibrium [274, 275, 277, 278], or induce a different intermediate state [276]. Substrate alone in the absence of gradient was also shown to shift the conformational equilibrium in LacY [273]. As already mentioned by Hänelt *et al.*, conformational-shuttling of transporters in response to ions only, would lead to substrate-uncoupled leaks, which would be disadvantageous to transporter function *in vivo*. Indeed, another study on LacY, using transport assays on proteoliposomes containing pH-sensitive dyes, showed that protonation precedes substrate binding, and D_2O exchange studies showed that transport kinetics were dependent on protonation [280]. There, however, different results were obtained for another (non-MFS) transporter, EmrE, suggesting that functional mechanisms cannot be generalised to all transporters.

Why only the R201/E364 and not the N174/S466 spin pair reported clear conformational changes in PepT$_{So}$ is unclear, as both pairs contain residues on TM domains which are thought to be involved in transport gating (Fowler *et al.*, submitted); similar discrepancies have been observed in other DEER studies [274–276], and the rotamer analysis suggest that spin label flexibility could lead to overlapping distances, obscuring conformational changes. The distance distributions obtained for the S141/S432 mutant was largely unaffected by the presence of substrate and/or gradient (Figure 2.7), which could either reflect the small predicted change in conformation along the transport cycle, or that it transported poorly in activity assays (Figure 2.5). As all sites were chosen with analogy to a previously published LacY SDSL study [273], and an outward-facing model was only available after DEER experiment were performed, this pair was included in the study, although it now appears to have been a poor reporter. This underlines the importance of using knowledge available from other techniques, such as crystallography and modelling, in experimental design, and future

studies could exploit the information gained from spin label rotamer analysis in choosing informative labelling sites.

3 | Purification and labelling of neurotensin receptor 1 for biophysical study

3.1 Introduction

3.1.1 Production of GPCRs for structural studies

Most GPCRs, excluding rhodopsin, are naturally expressed at low levels, making their direct purification from natural sources for structural biology studies not feasible. As a result, they must be overexpressed in heterologous systems. Difficulties in overexpression of GPCRs are most likely due to several factors, such as the complex folding mechanism of these proteins, problems of insertion into host membranes, inappropriate lipid environment of the host membrane, and incorrect post-translational modifications [281]. Expression in inclusion bodies is also complicated, as refolding strategies are very difficult to optimize. Purification of GPCRs requires solubilisation of the receptor using detergents; choosing the right detergent is important to be able to purify the protein in an unaggregated, stable and active state, but it is difficult to identify the best detergents *a priori* [282].

Crystallisation of GPCRs is greatly compromised by the detergents that are required for their solubilisation; these mild detergents are typically long-chained, and the large size of the micelle interferes with the formation of inter-protein interactions required for crystal formation [283]. Additionally, the inherent flexibility of GPCRs forms a major entropic barrier to crystallisation [155]. Consequently, despite their clinical relevance, the first GPCR crystal structure was only solved in 2000 for rhodopsin (which is inherently more rigid than other GPCRs as it is covalently bound to its inverse agonist) after which it took another seven years for the next GPCR structure to be solved in 2007 for the β_2-adrenergic receptor. However, technical advances in recent years have lead to a flurry of new crystal structures of GPCRs, with high resolution structures for 25 unique receptors published to date (August 2014: 21 family A, 2 family B, 2 family C, and 1 frizzled-taste family; see Table B.1). The

use of lipidic-cubic-phase for the crystallisation of GPCR has been a major contributor, providing a membrane-mimetic matrix closer to native bilayers than traditional detergents, thus stabilising labile proteins while allowing the formation of crystal contacts between both polar and non-polar parts of the protein, contributing to better order and diffraction [152]. GPCR crystallographic has further benefited from great efforts to improve receptor expression and stability as discussed in section 1.4.1. Common strategies to improve GPCR stability for structural studies, include the deletion of flexible loops (typically intracellular loop 3, IC3), and/or the addition of stable globular proteins to these loops (typically T4-lysozyme, T4L), which is thought to aid folding and reduce flexibility [284, 285]. Soluble fusion proteins also increase hydrophilic contact surfaces to promote crystal lattice packing. Additionally, "thermostabilised" mutants of GPCRs are now routinely used to obtain crystal structures [155]. Thermostabilisation entails a process of finding point mutations that increase the thermal stability of receptors, so that they become sufficiently stable to crystallise in short-chain detergents. This is commonly achieved through alanine scanning, in which all residues of a given GPCR are sequentially mutated, and the thermostability of the resulting mutant is assessed [286]. Alternatively, an approach using so-called "directed-evolution" in which all residues are mutated to all other possible residues can also be applied [287, 288]. This approach uses FACS (fluorescence-activated cell sorting) to select well-expressing mutants and relies on the weak correlation between improved expression and improved thermostability. In both techniques, single thermostabilising mutations are combined, resulting in a final mutant with approximately 5-10 point mutations, with a significantly increased half-life compared to wild-type (WT) receptor. Thermostabilisation is usually performed in the presence of a ligand (agonist or antagonist). This results in a mutant whose stability and affinity are biased towards the ligand used, and which is said to be conformationally stabilised in a certain state, *i.e.* "active" or "inactive", depending on its preference for agonists or antagonist, respectively [289]. Small antibodies such as FABs, and especially cameloid antibodies known as nanobodies, have also been employed to obtain GPCR crystal structures where they help to stabilize specific receptor states [153]. Nanobodies are much smaller than FABs, as they only contain the light chain, and thus add less bulk to the final complex. Most notably, nanobodies were used to stabilise the complex in the crystal structure of the agonist-bound β_2-adrenergic receptor interacting with a G protein [104].

Although very valuable for obtaining well-diffracting crystals and thus crystal structures, such protein engineering approaches are not without caveats. Roughly 40% of the solved structures are agonist-bound structures. Of these agonist-bound structures, ~60% is in a so-called "active-like" state, *i.e.* an agonist-bound state which shows no or little conformational

changes compared to the basal state of the receptor. It has been argued that receptors require the presence of G protein to undergo (full) conformational changes upon ligand binding [104]. This was however not seen for rhodopsin, where substantial conformational changes were observed even in the absence of G protein [290]. Rhodopsin is the only GPCR that has been crystallised in its native form, *i.e.* without globular fusion proteins, large deletions of critical loops, or thermostabilising mutations, thus it could also be argued that the modifications made to the receptors to facilitate crystallisation alter the receptor so that its native function is impaired to some extent. Indeed, T4L is typically inserted into IC3, which is thought to be involved in G protein activation; this impairs the ability of resulting construct to activate G protein [155, 291, 292], as was also observed for several of the thermostabilised mutants [293–296]. More generally, the concern remains that the determined structures of receptors in different activation states may be influenced by the crystal lattice and/or the membrane mimetic used, and that they do not accurately represent the behaviour of the receptors in their native membrane [159], or at least, provide an oversimplified picture of GPCR activation. Proteins, and especially GPCRs, are dynamic and flexible, and will be present in many intermediate conformations not represented by the crystal structures. Indeed, NMR studies suggest that GPCRs are present in many functional states and that ligand binding shifts the equilibria between these states [297]. Studying GPCR activation for a more native, active receptor, in a membrane environment is therefore of great interest.

3.1.2 Neurotensin receptor 1

Neurotensin receptor 1 (NTS1) is a 424 amino acid (47 kDa) class A GPCR, and one of the few GPCRs that can be expressed in *E. coli* and purified in a functional, ligand-binding form, making it amenable for biophysical studies due to its relative ease of expression (Figure 3.2) [298]. Its mRNA is found heterogeneously distributed in the central nervous system and in the intestine, both in rats [299] and humans [300]. Its ligand, the tridecapeptide neurotensin (NT; ELYENKPRRPYIL), which is synthesized as part of a 170 amino acid precursor [301], has a dual role, as a neuromodulator in the brain, and as a local hormone in the periphery. NTS1 has been shown to bind NT with high affinity ($K_d \approx 1$ nM) in various cell types, and NT binding is sensitive to sodium ions and GTP [299, 300, 302, 303]. Only the last six amino acids of NT (NT$_{8\text{-}13}$, RRPYIL) are required for binding to NTS1, and NT$_{8\text{-}13}$ has been shown to bind more strongly to the receptor than the full-length NT peptide [303]. There are two other proteins known to interacted with NT, neurotensin receptor 2 (NTS2) [304] and 3 (also known as sortilin) [305]. NTS2 is also a GPCR and the rat receptors share 43% amino acid identity and 64% amino acid homology [306], while sortilin is

structurally distinct and binds a variety of additional ligands [307]. Major effects of NT include analgesia, hypothermia, modulation of dopaminergic systems, modulation of pituitary hormone secretion, inhibition of food intake, and regulation of digestive function (reviewed in [306, 308, 309]). Antipsychotic drugs also appear to influence the NT system, and it has been shown that NT-containing circuits mediate some of the rewarding properties linked to drug abuse [310]. Furthermore, studies suggests that the upregulation of NT and/or NTS1 expression is involved in the development and progression of several types of cancer, including colon, breast, lung and pancreatic cancer (reviewed in [311]). While NTS2 plays a role in the analgesic effect of NT, the role of NTS3/sortilin in NT mediated physiological effects is unclear [307], and NTS1 appears to mediate most of the pharmacological and physiological effects of neurotensin [308]. Consequently, NTS1 has been proposed as a potential target for treatment of schizophrenia, Parkinson's disease, obesity and drug addiction, and as a biomarker for certain cancers. This enormous pharmaceutical potential makes NTS1 an interesting system for structural and functional studies.

3.1.3 Production and protein engineering of NTS1

Two crystal structures of thermostabilised mutants of NTS1 have been published in recent years. Firstly, an agonist-bound crystal structure of NTS1 with six stabilising mutations and T4L introduced into IC3 was published in 2012 (PDB ID: 4GRV) [294]. This mutant was produced using a insect cell-baculovirus expression system, crystallised in lipidic-cubic phase, and is only stable in the presence of agonist. Secondly, another agonist-bound crystal structure of NTS1 expressed in *E. coli* and crystallised in detergents was published in 2014 (PDB ID: 3ZEV) [295]. This study also employed a thermostabilised mutant, although the direct-evolution technique rather than alanine-scanning was used, yielding eleven stabilising mutations (with two sites in common with 4GRV). This construct did not have T4L introduced into IC3, but the loop was truncated (residues 280-295) to decrease flexibility to aid crystallisation. This deletion, together with the mutations (especially of the conserved R267$^{3.50}$ to Leu) greatly impaired G protein coupling (5-fold reduction in G protein activation) compared to WT [295].

Other biophysical and biochemical studies have typically employed expression in *E. coli* using a fusion construct of NTS1, with N- and C-terminal fusion partners, leaving the receptor itself intact, except for the first 43 residues which are omitted as they are prone to proteolytic degradation (Figure 3.1) [302]. These fusion proteins are based on the construct NTS1A, with fusion partners being the *E. coli* maltose binding protein (MBP, N-terminal), and *E. coli* thioredoxin (TrxA, C-terminal). The fusion partners are included to aid protein

folding and insertion into the *E. coli* inner membrane, through the periplasmic targeting sequence of MBP [281]. Modified versions of the original construct include tobacco etch virus (TEV) protease cleavage sites flanking the NTS1 sequence, to allow proteolytic removal of the fusion proteins (NTS1B) [298, 312]; and fusions to fluorescent proteins have also been reported (NTS1-YFP/CFP) [206]. *E. coli* expression of NTS1B has been optimised, so as to avoid overloading of the *E. coli* translocation machinery while allowing the sustained accumulation of functional receptor at the cell membrane [298] by using a low copy number plasmid (pRG/III-hs-MBP [302]), with the weak *lac* promotor, and long, low-temperature induction periods [313].
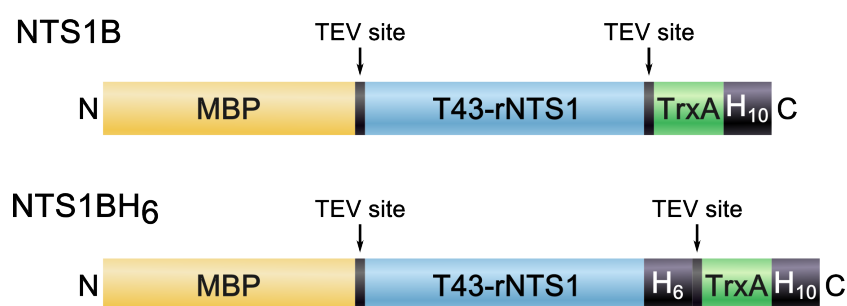
Figure 3.1: NTS1 constructs. Two constructs of NTS1 were used in this thesis: NTS1B [312] and NTS1BH$_6$. NTS1B (101 kDa) is a fusion construct of rat NTS1, with *E. coli* maltose binding protein (MBP, N-terminal) and *E. coli* thioredoxin (TrxA, C-terminal), and an C-terminal deca-His-tag (H$_{10}$). NTS1 is N-terminally truncated (residues 1-43; T43-rNTS1) in this construct as the N-terminal region, which contains three putative glycosylation sites, is sensitive to proteolytic degradation. NTS1 is flanked by two TEV protease recognition sites to allow removal of the fusion partners, by TEV cleavage, yielding NTS1. This construct was adapted to contain an extra hexa-His-tag (H$_6$) at the C-terminus of NTS1 before the TEV protease recognition site, NTS1BH$_6$, to facilitate IMAC on the cleaved receptor.

3.1.4 Aim

Having demonstrated the successful application of DEER to study the structure and function of a more stable membrane protein system, the prokaryotic peptide transporter PepT$_{So}$ (Chapter 2), the rest of this thesis will focus on to the biophysical investigation of a more challenging mammalian system. This chapter is aimed at adapting and improving the current expression and purification protocol of the non-thermostabilised NTS1B construct in order to obtain samples of sufficient quality and concentration to be amenable to FRET, EPR, and other biophysical techniques. Furthermore, to be able to site-directedly label the receptor for EPR and FRET studies with small labels, cysteine mutants of the receptor need to be produced, their activity verified, and an efficient labelling protocol needs to be established.

3.2   Materials and method

3.2.1   NTS1 construct

The NTS1B fusion construct of rat neurotensin receptor 1 was used; rat NTS1 has 84% amino acid identity and 92% similarity with human NTS1, and is thus thought to exhibit similar pharmacological properties, making it a good model for the human receptor [300]. The fusion protein has a deca-His-tag attached to the C-terminus to facilitate immobilised metal affinity chromatography (IMAC) purification. Another construct, NTS1BH$_6$, was made containing an additional His$_6$-tag at the C-terminus of NTS1 before the TEV protease recognition site facilitating IMAC on the TEV-cleaved receptor (Figure 3.1).
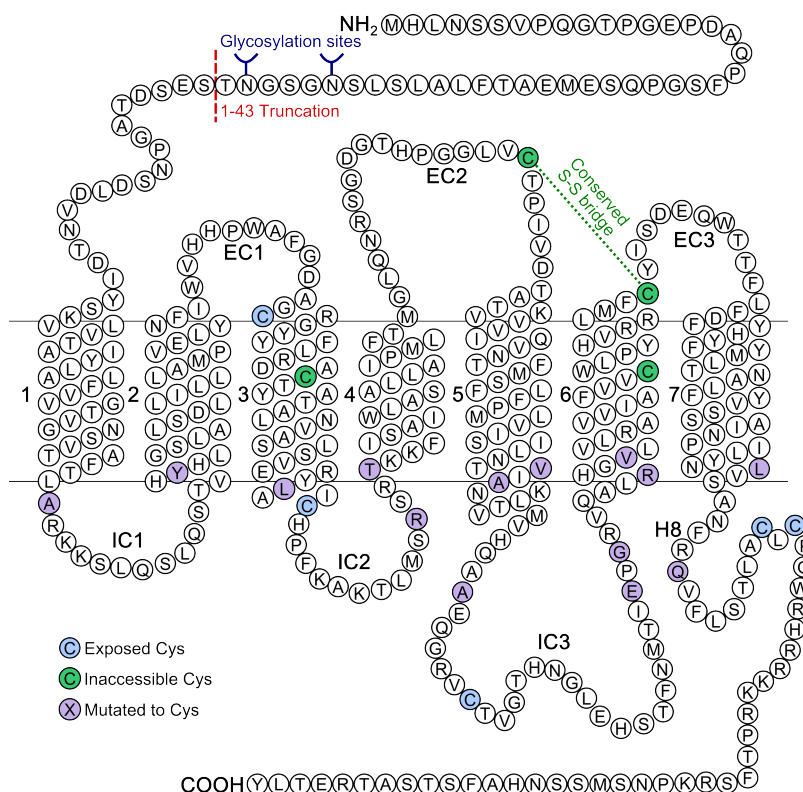
Figure 3.2: Serpentine representation of NTS1 with labelling sites highlighted. Amino acid sequence of NTS1 is shown in a snake plot. Helices are as in the 4GRV and 3ZEV crystal structures (TM7 as in 3ZEV). The extracellular loops (EC), intracellular loops (IC) and transmembrane helices are numbered. N-terminal glycosylation sites, which are absent in the NTS1B constructs, are indicated. Native cysteines that have been mutated to serine/alanine in the ΔC-NTS1B background mutant are highlighted in blue. The remaining native cysteines are inaccessible for labelling (highlighted green), as they are buried or engaged in a conserved disulfide bond. Sites where cysteines were introduced for site-directed labelling are highlighted in purple, except for all the H8 residues (374-393) that were sequentially mutated to Cys for an EPR secondary structure scanning experiment.

3.2.2 Site-directed mutagenesis

For site-directed labelling of cysteines with fluorophores or spin labels, a Cys-depleted background mutant (ΔC-NTS1B) was used, in which native accessible cysteines are mutated to alanine or serine (see Appendix A.5.1).[1] Cysteine-mutations were introduced into ΔC-NTS1B on the helix/loop interfaces of all TMs (see Table 3.1). As this work was carried out before the publication of the first NTS1 crystal structure, residues were chosen based upon alignment with successful labelling sites in a previous SDSL study of rhodopsin [314]. Other sites were also tried and/or used for a number of TMs: for TM3 C172$^{3.55/\text{IC2}}$ was employed more often than L169$^{3.52}$ to make use of the naturally occurring cysteine; for TM4 T186$^{4.42}$ was used more often than R183$^{4.39}$, as it was a more conservative mutation; for TM5 initially A272$^{\text{IC3}}$ was used more often as it was further down the helix and thus potentially better exposed for labelling, but after labelling procedures were improved, A261$^{5.52/\text{IC3}}$ was employed in later studies as it is more likely to be in a less flexible position on the helix rather than in IC3; for the same reasons E296$^{\text{IC3}}$ was initially used and later V307$^{6.34}$ in TM6; in H8 sequential cysteine mutants of all residues were made for EPR secondary structure scanning experiments, and typically Q378$^{8.52}$ was used in other experiments as it is in the middle of the putative helix. The superscript (X.Y) for each residue number represents its Ballesteros-Weinstein numbering, where X is the TM segment and Y the number of the residue with respect to the most conserved residue of the segment which is given number 50 [315]. Residues that do not fall within predicted TM segments (or H8) are labelled with the corresponding protein region. Residues with both a number and IC segment, are on the edge of TM segments and fall within the TM for some topology predictions.

3.2.3 NTS1 expression and purification

NTS1B and its derivatives were expressed in *E. coli* and purified by IMAC and ligand affinity chromatography, as described in [313], with a few modification described in this chapter and summarized in detail in Appendix A.5.2.3. Briefly, the NTS1B construct, and mutants thereof, were expressed in BL21 (DE3) cells. The cell pellet from typically 10-20 L of cell culture was homogenised, lysed by addition 1 mg/mL lysozyme, and left stirring for ~6 h after addition of detergents DDM, CHAPS and CHS (final concentration of 1%, 0.5% and 0.1% (w/v), respectively) to solubilise the membranes. Unsolubilised material was removed by centrifugation and the receptor was purified by IMAC on a 5 mL HisTrap nickel column. The IMAC eluate could then be cleaved by TEV protease if required, and was further purified by ligand affinity chromatography using NT-funtionalized resin, eluting the receptor

---

[1]The ΔC-NTS1B construct was made by me under the supervision of Marcella Orwick-Rydmark, during an internship in the group of Prof. Anthony Watts.

Table 3.1: NTS1 cysteine mutants used in site-directed labelling. Cysteine-mutations were introduced into ΔC-NTS1B on the helix/loop interfaces of all TMs. Residues were chosen based upon alignment with successful labelling sites in a previous SDSL study of rhodopsin [314], and additional mutants were created for some TMs, and in some cases used instead of the rhodopsin-based site. Ballesteros-Weinstein numbering is given for each residue (X.Y), where X is the TM segment and Y the number of the residue with respect to the most conserved residue of the segment which is given number 50. Residues that do not fall within predicted TM segments (or H8) are labelled with the corresponding protein region (IC, intracellular loop; C-term, C-terminus beyond the predicted H8).

TM/H	Rhodopsin residue	Corresponding residue in NTS1	NTS1 residues used
1	$V63^{1.58}$	$A90^{1.58}$	$A90^{1.58}$
2	$Y74^{2.41}$	$Y104^{2.41}$	$Y104^{2.41}$
3	$V137^{3.52}$	$L169^{3.52}$	$L169^{3.52}$, $C172^{3.55/IC2}$
4	$N151^{4.40}$	$R183^{4.39}$	$R183^{4.39}$, $T186^{4.42}$
5	$Q225^{5.50}$	$V259^{5.50}$	$V259^{5.50}$, $A261^{5.52/IC3}$, $V266^{IC3}$, $A272^{IC3}$
6	$A241^{IC3}$, $R252^{6.35}$	$G298^{IC3}$, $L308^{6.35}$	$E296^{IC3}$, $G298^{IC3}$, $R304C^{6.31/IC3}$, $V307^{6.34}$
7	$M308^{7.55}$	$L371^{7.55}$	$L371^{7.55}$
8	$N326^{C\text{-term}}$	$P389^{C\text{-term}}$	Whole helix: A374-H393

with high salt buffer (1 M NaCl). The final sample was concentrated, initially using centrifugal concentrators, although this approach was later abandoned as it negatively affected the specific activity of the sample as discussed below; later a 1 mL HisTrap nickel column was used to concentrate large volumes of NT column eluate, followed by either simple dilution to lower imidazole concentrations or gel filtration. The amount of functionally active (*i.e.* ligand-binding) receptor was initially measured using a saturation radio-ligand binding assay (see Appendix A.5.6), and was assumed to be similar for subsequent purifications employing ligand-affinity columns that would retain only ligand-binding, and thus functional protein. DDM concentrations were determined by a colorimetric assay for glycosidic detergents as described by Urbani *et al.* [316].

Ligand binding affinities of WT and cysteine mutant NTS1 were tested by MST (see appendix A.10). MST data was analysed in NTAnalysis software (NanoTemper Technologies) and binding curves were fitted in OriginPro 8.5 (OriginLab) using a one-site binding model based on the law of mass action (taking into account ligand-depletion, see section 6.2.5).

3.2.4 NTS1(B) labelling

Labelling conditions were initially tested by electrophoretic mobility shift assays. NTS1(B) was incubated with varying concentrations of DTT or TCEP for 1 h at room temperature

(RT) or 3-4 h at 4 °C, and reducing agent was removed using a P30 biospin spin column (Bio-Rad). Receptor was then incubated with a 5 to 20-fold molar excess of cysteine-reactive polyethylene glycol maleimide (PEGm, 5 kDa, dissolved at 5 mg/mL in DMSO), and subsequently analysed by SDS-PAGE. Gels were either stained with silver stain, or used for western blotting (see section A.7), and relative band intensities were analysed using ImageJ [317]. Incubation time, temperature, and reductant concentration were varied to find optimal conditions. Fluorophore and spin labelling was performed as described in Appendix A.5.3.

3.3 Results and discussion

3.3.1 Cysteine mutants

Expression levels of NTS1B cysteine mutants in large-scale expression ($>$8 L) and purification tests were found to be approximately half that of WT by radio-ligand binding assays, with WT-NTS1B yielding 0.7 ± 0.4 mg of active receptor per 60 g of cell pellet (typical preparation size, see Figure 3.3). Western blotting of small-scale extracts of mutant receptor together with WT controls suggested lower overall expression levels (Figure 3.4), indicating that the lower amounts of functional protein are more likely due to impaired expression, than due to reduced ligand-binding activity; using an antibody against MBP, WT-NTS1B samples show more intense bands corresponding to the receptor than the mutant samples, while expression levels of MBP, a native *E. coli* protein, and thus a control marker for total protein concentration, are similar for all samples.

Native-like activity of cysteine mutants in detergent was verified by ligand and G protein binding experiments using MST. Cysteine-depleted NTS1 was shown to bind fluorescent NT (NT-Cy5) with an affinity similar to that observed for WT, giving affinity dissociation constants $K_d \leq 2$ nM and $K_d \leq 10$ nM, respectively (Figure 3.5). K_d values are given as an upper limit, as the symmetric error distribution assumed by the fitting procedure would give rise to negative values, but the K_d can thus also be lower. These values are in good agreement with previously reported low-nanomolar (1-2 nM) values [318, 319]. Radio-ligand binding assays showed that spin labelling with MTSL also did not affect ligand-binding in NTS1B, with 100 ± 20 % activity retained (n=6, for two double TM5-6 cysteine mutants). G protein (Gα_{i1}) binding to cysteine mutants was tested for Alexa Fluor 488-labelled T186C (TM4) and V307C (TM6), compared to WT-NTS1, labelled through the native cysteines (see Figure 3.6). G protein binding affinities of T186C and V307C were lower than those observed for WT ($K_d = 1.0 \pm 0.2$ µM for both mutants, and 220 ± 90 nM for WT), Nevertheless, binding affinity was reduced in the presence of GTPγS (non-hydrolysable analogue
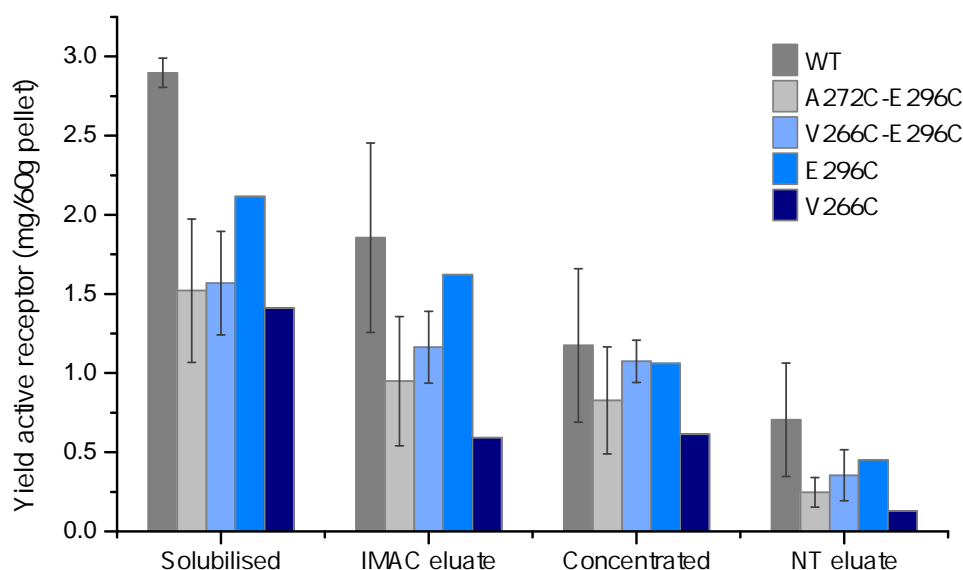
Purification step	Active receptor (mg/60 g pellet)	Relative yield (%)
Solubilised, before IMAC	2.9±0.1	100±3
IMAC eluate	1.9±0.6	60±20
Concentrated IMAC eluate	1.2±0.5	40±20
NT-column eluate	0.7±0.4	20±10

Figure 3.3: Yield of active receptor for tested cysteine mutants compared to WT NTS1B. The relative amount of active mutant NTS1B compared to WT obtained by large scale (10-25 L) expression in BL21 cells, normalised to 60 g cell pellet as determined by radio-ligand activity assay is given. Yield is given for different stages of the purification: solubilised material before IMAC, after IMAC, after dilution and concentration after IMAC, and after the NT-column step. The table also gives the relative yield (%) at the different stages for WT-NTS1B. Error bars give standard deviations calculated using data from different expression and purification batches where available (n=3 for WT, n=5 for A272C-E296C and n=2 for V266C-E296C).

of GTP) by at least and order of magnitude, proving the specificity of the interaction for both WT and mutants. It is possible that although G protein can still interact specifically with the receptor the position of the relatively large fluorophores in the mutants interferes with the G protein interaction. It can however not be excluded that the labels on WT-NTS1 (also) affect the observed K_d; while exact labelling sites for WT are not known, the most likely exposed cysteines are in the IC3 and the C-terminus, which have both been implicated in G protein coupling [320]. No K_d values for $G\alpha_{i1}$ binding to NTS1 could be found in the literature, but it has been shown by radioactivity assays that detergent-solubilised NTS1 catalyses GTP exchange at the $G\alpha_q\beta_1\gamma_2$ heterotrimer with an apparent EC_{50} of ~145 nM, which is of the same order of magnitude as the values found here [321].
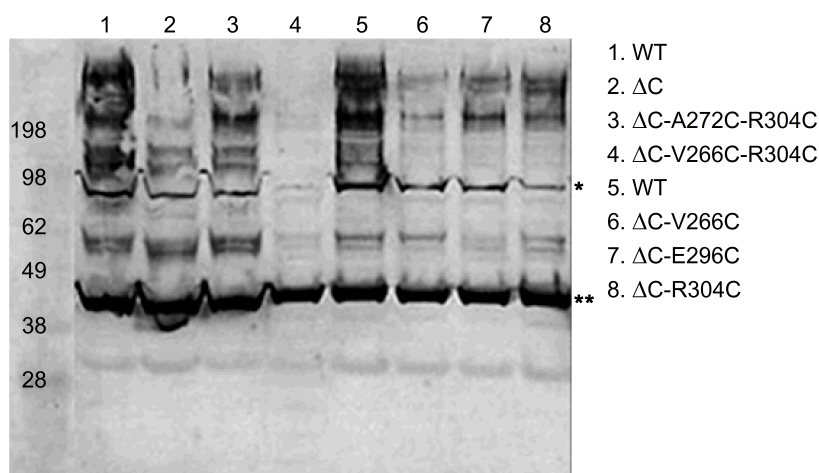
Figure 3.4: Relative expression levels of NTS1B mutants. Western blot (antibody against MBP) of small-scale extract from *E. coli* cells of the final ΔC mutant and the cysteine NTS1B mutants, V266C, E296C, R304C and two double mutants, A272C-R304C and V266C-R304C. Control WT-NTS1B samples expressed simultaneously on a small scale for each mutant trial expression are also included. Expression levels of MBP (42.5 kDa, lower band, **) are similar for WT and mutants, while the expression levels of NTS1B (upper band, *) are lower for mutants compared to WT.

3.3.2 NTS1(B) purification

3.3.2.1 Detergent concentration *vs.* receptor activity

NTS1(B) sample preparation for biophysical applications typically involves one or more concentration steps using a centrifugal concentrator [206]. However, a significant drop in the fraction of functional receptor for was observed after centrifugal concentration, concomitant with an increase in the DDM concentration (see Table 3.2), even when using devices with a MWCO of 100 kDa (with micellar size DDM being ~70 kDa). This suggests that such high detergent concentrations are deleterious to native protein activity and/or folding. To avoid this loss of sample activity, another method for concentrating NTS1(B) in detergent was tested; the NT column eluate of one or multiple NTS1(B) preparations is loaded onto a 1 mL Ni^{2+}-column, which can easily be eluted in a narrow band, giving a more concentrated sample. In an initial test, a WT-NTS1B sample was concentrated approximately 18-fold on the nickel column, after which the sample was further concentrated 20-fold using a centrifugal concentrator. The sample after IMAC contained a higher proportion of active receptor (~5-7× increase) than samples concentrated in centrifugal concentrators (Table 3.2). The detergent concentration was determined to be 0.11±0.01% (w/v) after the IMAC concentration step, rising to 1.1±0.4% after the final concentration step accompanied by a drop in ligand-binding activity. Consequently, the use of centrifugal concentrators was abandoned, and samples were only concentrated by small-volume IMAC, combining multiple preparations where concentrated detergent samples were required, and membrane reconstituted
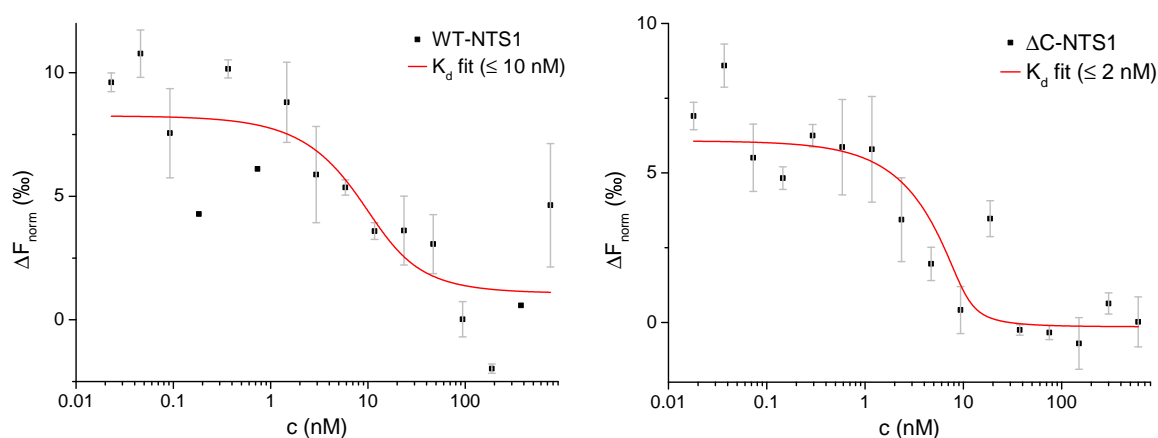
Figure 3.5: ΔC-NTS1 NT binding affinity compared to WT. Binding affinity of the cysteine depleted mutant of NTS1 was tested by MST; 10 nM NT-Cy5 was added to a dilution series of WT or ΔC-NTS1 (0.02-750 and 0.02-600 nM, respectively), in duplicate for WT and triplicate for mutant NTS1 (error bars represent standard error). Control with denatured protein showed no binding (not shown). Fitted dissociation constants (K_d) are shown.

samples were used when possible.

Final sample concentration was further optimised by inverting the flow during elution of the 1 mL Ni^{2+} column, as most protein bound to the top of the column. Further, when high protein concentration was required (*e.g.* for nanodisc production, see chapter 6) salt-exchange spin columns, instead of gel filtration columns attached to a pump, were used to remove imidazole after the final IMAC concentration step, as these give better yields and lower dilution factors; in this manner NTS1 detergent samples of ~5-10 μM could be obtained.

3.3.2.2   TEV cleavage of NTS1

For proteolytic cleavage of NTS1B to remove the fusion partners MBP and TrxA, TEV protease was produced expressed and purified as described in Appendix A.3 giving a yield of 5.5±0.7 mg/L cell culture (see Figure 3.7). The receptor was cleaved after IMAC purification of the cells lysate, and cleavage efficiency was gauged from SDS-PAGE analysis (Figure 3.8). From the relative intensities of the MBP and NTS1 band after cleavage, which should be near 1 to 1, it is apparent that NTS1 understains compared to MBP. This was observed both for Coomassie Brilliant Blue staining (~4× understained) and, more dramatically, for silver staining (~10×). This understaining leads to an underestimation of protein concentration by comparing intensities of gel bands to simultaneously run BSA standards. Thus to avoid the further use of radioactive material, protein was assumed to be active after ligand-affinity
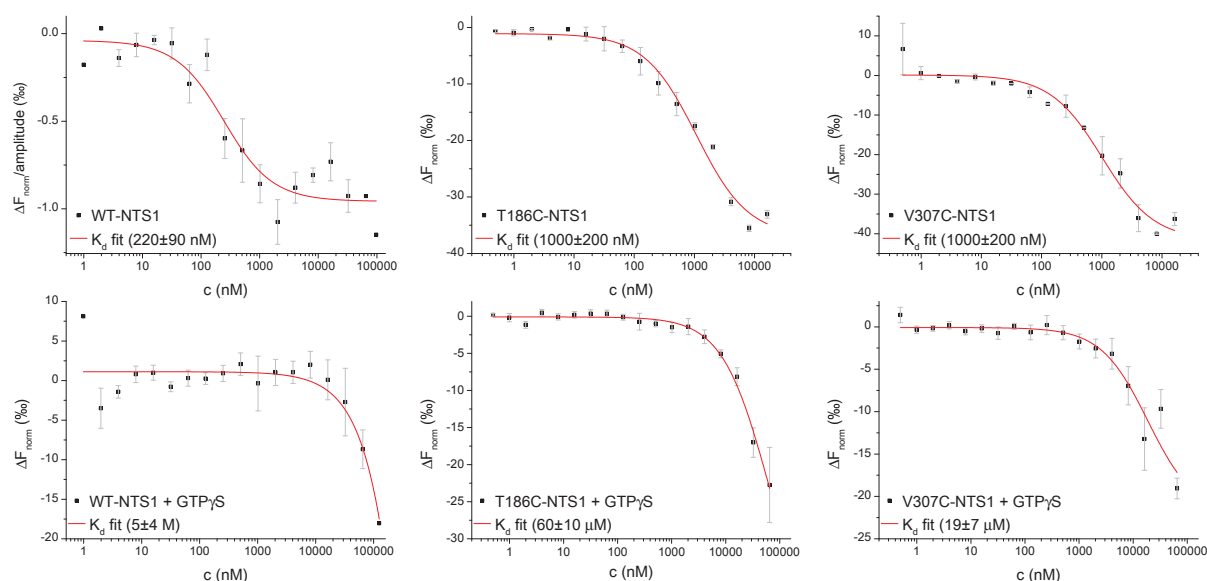
Figure 3.6: Cys-mutant NTS1 Gα$_{i1}$ binding affinity compared to WT. Binding affinity of WT-NTS1 (left), T186C (middle), and V307C (right) and was tested by MST; 40 nM of labelled NTS1 was incubated with a dilution series of Gα$_{i1}$ (0.5 nM to 62.5 μM), in the presence of 5 μM NT$_{8\text{-}13}$ (top panels), or 5 μM NT$_{8\text{-}13}$ and 0.5 mM GTPγS (negative control, bottom panels). Error bars represent standard errors of at least two experiments (n=8 for WT+NT, n=6 WT+GTPγS, n=2 for T186C+NT, n=5 for T186C+GTPγS, n=2 for V307C, n=5 for V307C+GTPγS). Fitted dissociation constants (K_d) are shown.

purification, and the absorption at 280 nm (OD280) was used to determine purified NTS1 concentrations.

TEV cleavage did result in lower final yields of ~60% compared to uncleaved WT receptor (9 ± 3 and 15 ± 2 nmol per 60 g of solubilised cell pellet, respectively, see Figure 3.9). The yield reported here for WT-NTS1B is approximately double the yield originally obtained (Figure 3.3), due to the omission of centrifugal concentrators. Yields of cleaved receptor are approximately half of those for uncleaved receptor after the NT column. Yields for cleaved and uncleaved mutants after the 1 mL Ni^{2+} column are similar however, as in later purifications with cleaved receptor the flow-through of the Ni^{2+} column was reloaded, which was not done for earlier purifications with uncleaved receptor, resulting in lower losses in this step.

3.3.2.3   Optimising ligand-affinity purification

The NT column protocol [322] was optimised to yield cleaner samples, by testing higher NaCl washing concentrations ($>$70 mM, see Figure 3.10). A persistent low molecular weight contaminant could only be removed with 150 mM NaCl (subsequent testing with 100 and 125 mM NaCl, not shown, gave similar results). Thus in future purifications NT150 was used as a washing buffer, while incubation and elution conditions were kept the same.

Table 3.2: NTS1B activity during purification *vs.* detergent concentration. Yield is given for different stages of the purification (concentration in μg/mL and total amount of receptor in mg): after dilution and concentration after IMAC (IMAC), after the NT-column step (NT), after concentration using a centrifugal concentrator (Conc), after concentration on a 1 mL Ni^{2+} column (1mL IMAC), and after salt-exchange by gel filtration after the 1 mL Ni^{2+} column concentration step (SE). The total amount of protein is determined by comparing the density of gel bands to BSA standards, and the amount of active receptor is determined by radio-ligand binding assay. The table also gives the relative amount of functional receptor (ratio of active receptor to total receptor in %). DDM concentrations were determined by colorimetric assay. Standard deviations, where given, were calculated by performing the ligand binding or detergent assay in triplicate.

	Total (μg/mL)	(mg)	Active (μg/mL)	(mg)	Functional receptor (%)	[DDM] (%)
A272CE296C						
IMAC	125	1.7	38±1	0.62±0.02	36	-
NT	15	0.31	14±1	0.29±0.04	93	0.13±0.02
Conc	500	0.06	34±1	0.004±0.001	7	5.5±0.6
V266C						
IMAC	210	3	68±4	1.0±0.2	33	-
NT	35	0.7	11±2	0.22±0.03	31	0.13±0.01
Conc	1000	0.2	56±6	0.008±0.002	5	5.6±0.9
WT						
IMAC	150	1.8	40±1	0.48±0.01	27	-
NT	10	0.3	11±5	0.3±0.1	100	0.17±0.08
1mL IMAC	180	0.2	60±5	0.060±0.005	33	0.11±0.01
SE	15	0.02	2.1±0.1	0.0031±0.0002	13	0.19±0.08
Conc	300	0.02	21±2	0.0017±0.0002	7	1.1±0.4

3.3.3 Optimising site-directed labelling

Labelling conditions were initially tested by electrophoretic mobility shift assays using PEGm. Pegylation of cysteines on the receptor through the maleimide functional group of PEGm (5 kDa) results a band shift on an SDS-PAGE, allowing easy visualisation of the labelling efficiency [323]. NTS1B was initially incubated with PEGm at 4 °C for 20-48 h showing negligible labelling (Figure 3.11), while the receptor readily labelled at room temperature (Figure 3.15).[2] Titration of reductant concentration suggested an optimal concentration of reductant of 0.2 mM and 0.5 mM TCEP and DTT, respectively (Figure 3.15).[3] Higher concentrations appeared to be detrimental to labelling efficiency, potentially because the reductant could not be removed completely by the spin columns, and thus interfered with the labelling [324]. Thus other strategies to remove reductant were used for FRET and EPR samples (see Appendix A.5.3), *e.g.* extensive washing of the protein bound to an

---

[2] These tests were carried out by me during an internship in the group of Prof. Anthony Watts, under the supervision of Marcella Orwick-Rydmark, and by Alan Goddard.

[3] Results were kindly provided by Alan Goddard.
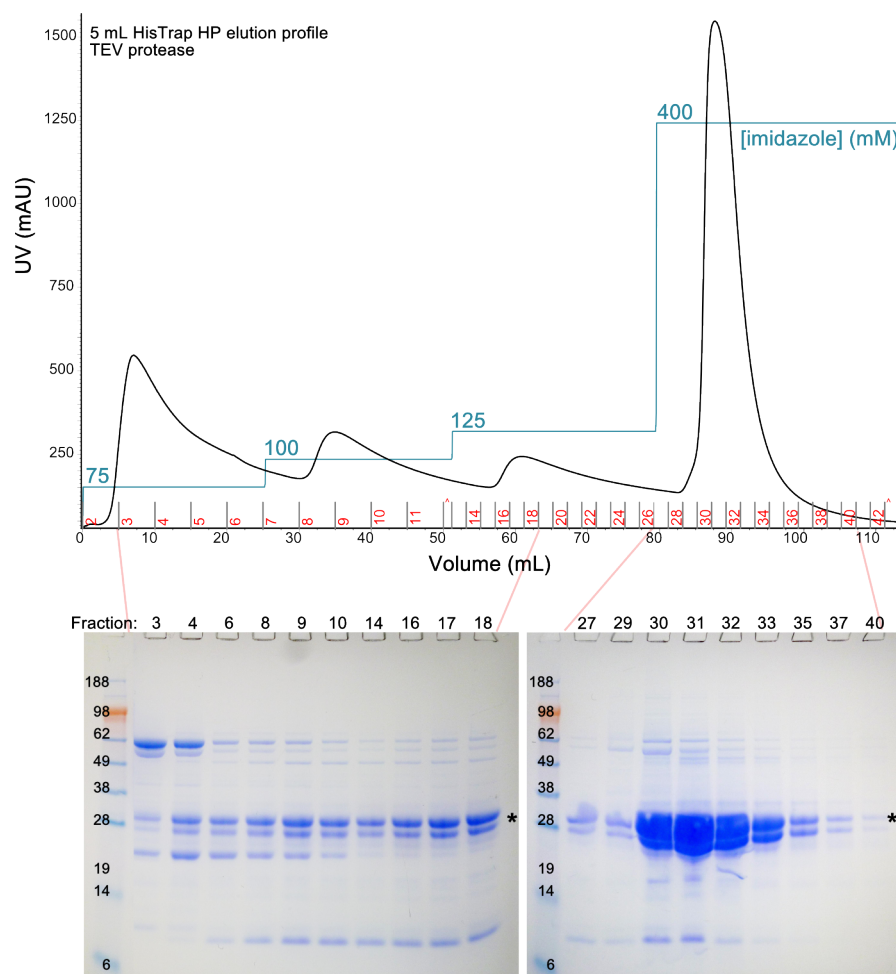
Figure 3.7: Purification of TEV protease. TEV protease was expressed as described in Appendix A.3. Protein was purified from cell lysate by IMAC on a 5 mL Ni^{2+} column (HisTrap HP, GE Healthcare). Elution protocol was optimised to obtain a cleaner sample; specifically, an imidazole step gradient (75, 100, 150, and 400 mM) was employed as indicated. Fractions were analysed by SDS-PAGE (bands corresponding to TEV are marked with *), and fractions 27-40 were pooled.

affinity column, or salt exchange using a larger desalting column (5 mL HiTrap Desalt, GE Healthcare) as shown in Figure 3.13. As labelling efficiency is easier to determine for fluorophores than for spin labels, the former were used in further optimisation of the labelling procedure. Labelling was tested after the NT column step, and after the 1 mL Ni^{2+} column (Figure 3.14); protein was incubated at room temperature with maleimide fluorophores, after which excess dye was removed and the labelling efficiency was gauged from the relative absorption of the dye and the protein (using equation A.2). Labelling after the 1 mL Ni^{2+} column concentration step was found to be most efficient. Higher protein concentrations typically give better labelling efficiencies presumably as the likelihood of protein-label collisions is increased; receptor concentrations can be as much as ten to twenty-fold higher after the 1 mL Ni^{2+} column concentration step (6-fold in Figure 3.14), explaining the increase in
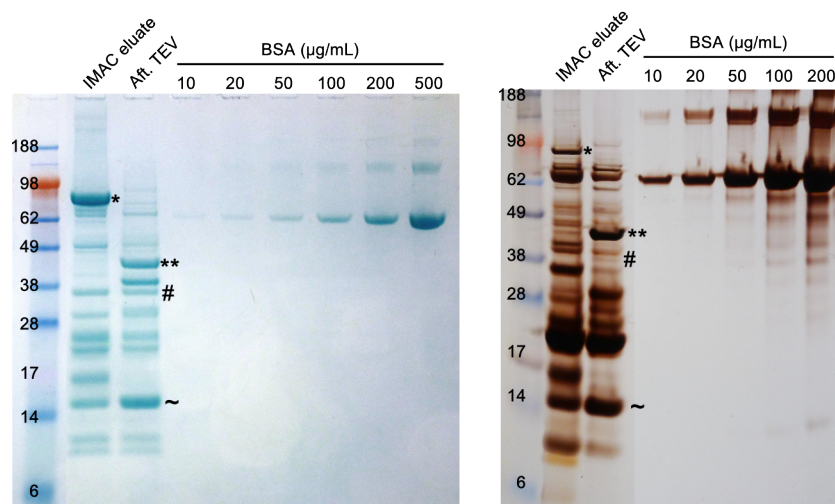
Figure 3.8: TEV Cleavage of NTS1. NTS1B IMAC eluate was incubated with a molar excess of TEV protease overnight (recommended TEV:NTS1 ratio is 1:1 [312]), aliquots from before (IMAC eluate) and after (Aft. TEV) cleavage were analysed by SDS-PAGE. Here two examples are given stained with Coomassie Brilliant Blue (left) and Silver Stain Plus (Bio-Rad). Bands corresponding to NTS1B are indicated with *, MBP with **, NTS1 with #, and TrxA with ~. NTS1 bands should theoretically be as intense as MBP bands, but NTS1 appears to understain. This is also visible in Figure 3.10.
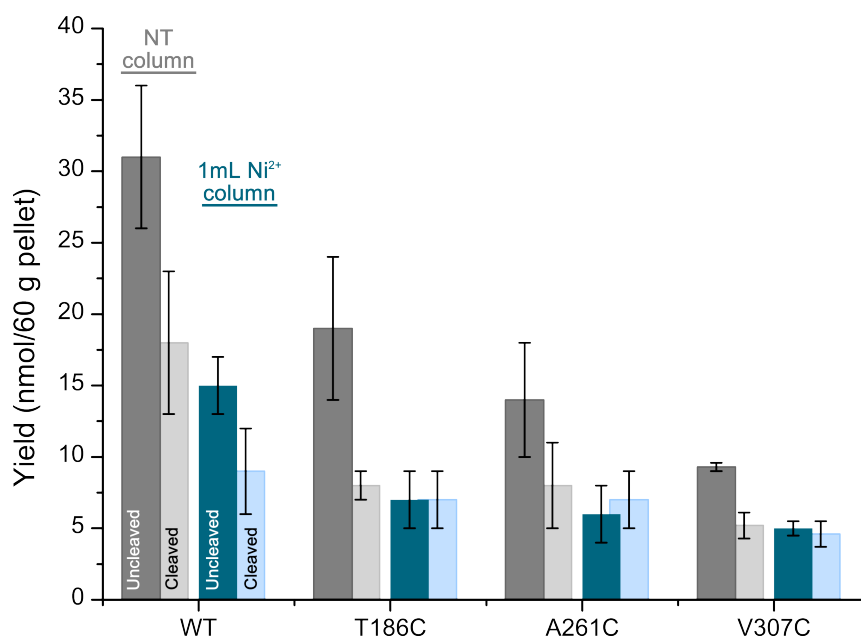
Figure 3.9: Yields cleaved and uncleaved NTS1B. Yields of total NTS1(B) in nmol per 60 g of solubilised cell pellet are given for the final stages of the purification (after the NT affinity column, grey bars, and the 1 mL Ni^{2+} column concentration step, blue bars) as determined by absorbance at 280 nm. Yields are given for WT receptor and a number of cysteine mutants, with dark-coloured bars for the uncleaved receptor, and light-coloured for cleaved receptor. Error bars give the standard error (n=4 WT-NTS1B, n=6 WT-NTS1, n=2 T186C-NTS1B, n=5 T186C-NTS1, n=3 A261C-NTS1B, n=2 A261C-NTS1, n=3 V307C-NTS1B, and n=7 V307C-NTS1).
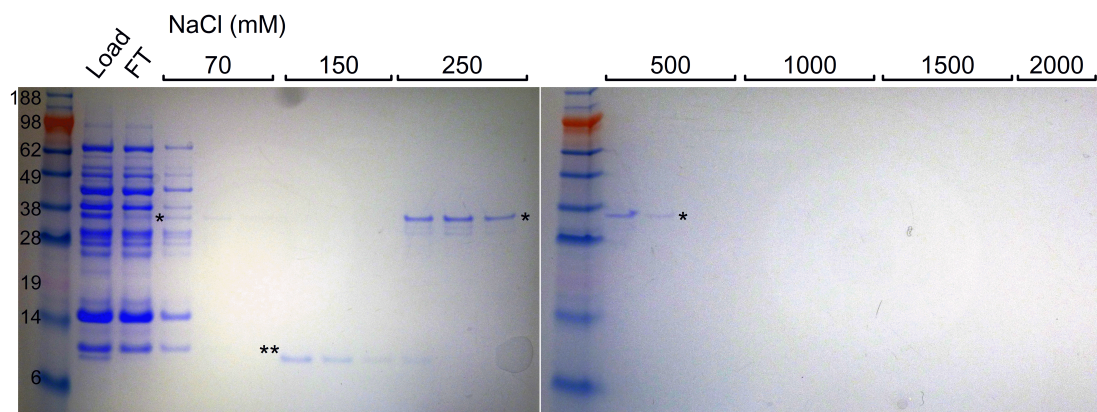
Figure 3.10: Optimizing wash step NT affinity column. NTS1 Cys mutant L371C (after TEV cleavage, Load) was incubated with NT resin (3 h at 4 °C). The flow-through (FT) was collected and the resin was washed with NT column buffer with increasing concentrations of NaCl (5 mL fractions of the wash were collected). Most contaminants (and a small amount of NTS1, marked with *) could be washed off with 70 mM NaCl. A low molecular weight contaminant (marked with **) was only washed off with 150 mM NaCl. NTS1 eluted with 250-500 mM NaCl. No further elution of NTS1 was observed when using higher NaCl concentrations (1-2 M).

labelling efficiency. Indeed to rule out dye or buffer effects, labelling of T186C after the 1 mL Ni^{2+} column was performed for the same protein preparation and the same dye at 1.2 μM and diluted to 0.4 μM (Figure 3.14B); even this modest three-fold increase in concentration greatly improved labelling efficiency, while requiring lower dye-excess and a shorter incubation period. Thus, in further experiments, the 1 mL Ni^{2+} column eluate was labelled, after which excess label and imidazole was removed by gel filtration.

To determine the amount of non-specific labelling, the ΔC mutant was incubated with PEGm. For low protein concentrations (0.15 μM) using high molar excess of PEGm (20×) and long incubation times (1 h) no non-specific pegylation was observed (Figure 3.12A). Similar labelling conditions were used in CW-EPR experiments to study NTS1 dynamics (Chapter 4), as labelling efficiency does not affect these experiments. However, for FRET and DEER experiments, high labelling efficiency is required and thus protein was labelled at higher concentrations; at receptor concentrations of 0.8 μM non-specific labelling (~50% singly labelled) was observed under the same conditions, which was reduced to ~20% at lower labelling excess (5×). Thus, label excess and time were minimised (typically 2 to 5-fold molar excess, labelling for 5-30 min) for labelling NTS1 at high concentrations to reduce non-specific labelling, relative to the more readily occurring specific cysteine labelling.
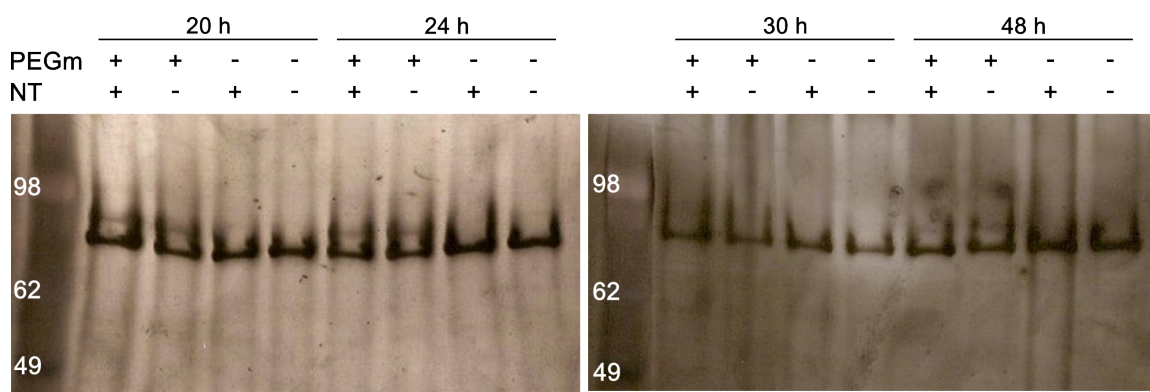
Figure 3.11: Electrophoretic mobility shift assay for labelling efficiency at 4 °C. NTS1B (0.15 µM) was incubated with a 20× excess of PEGm for 48 hours, and aliquots were taken after 20, 24, 30, and 48 hours to check the extent of labelling. The influence of adding a 10× excess of NT to the labelling efficiency was also tested. Controls with no PEGm and/or no NT were performed. Aliquots were run on a 4-12% Bis-Tris gradient gel and protein was stained using silver staining.
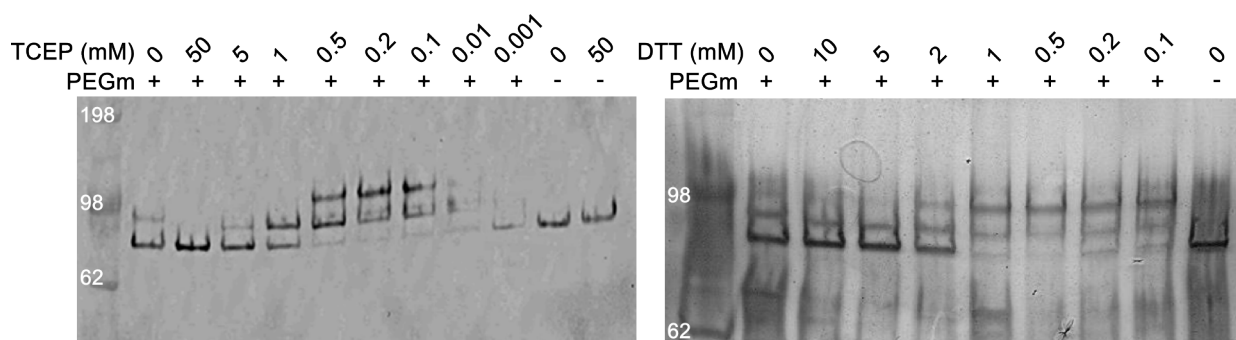
Figure 3.12: Titration of reductant by electrophoretic mobility shift assay for labelling at room temperature. NTS1B (0.2 µM) was incubated with either TCEP (0-50 mM) or DTT (0-10 mM) for 1 h at room temperature. Reductant was removed using a P30 spin column and the protein was incubated with a 20× excess of PEGm for 1 h at room temperature. Samples were run on a 4-12% Bis-Tris SDS-PAGE gel and protein was detected by western blotting with antibody against His-tag (left) or using silver staining (right). Results were kindly provided by Alan Goddard.

3.4 Conclusions

Expression and purification of WT-NTS1, and cysteine mutants thereof for FRET and EPR studies, were optimized to purify the receptor to near-homogeneity, and to relatively high protein concentrations (several micromolar), without having to use centrifugal concentrators as those proved to be deleterious for protein activity. Final yields per litre are still low (210 ± 30, 50 ± 20, and 40 ± 10 µg/L, for WT-NTS1B, WT-NTS1 and cysteine mutants of NTS1(B), respectively), compared to literature values for some other GPCRs (*e.g.* 1.5 mg/L for the β_2-adrenergic receptor expressed in *Sf9* insect cells [325]), but this probably reflects the poor stability of NTS1 in detergent compared to other GPCRs [293]. The origin thereof is unclear, but indicative of the importance of the membrane in the study of membrane
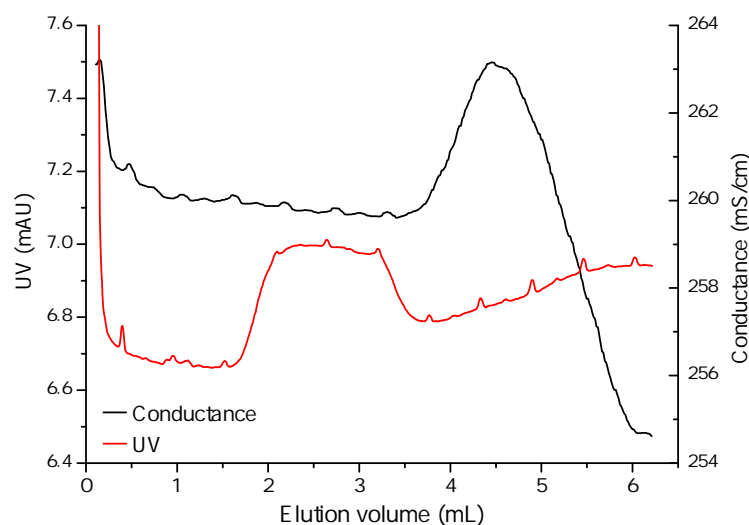
Figure 3.13: Removing reductant using salt-exchange column. Reductant (here 1 mM DTT) can be separated from the protein by salt-exchange chromatography (5 ml HiTrap Desalt, GE Healthcare). The UV trace corresponds to the protein, and the conductance trace to the reductant. Columns were connected in tandem for larger volumes, using one column per 1.4 mL of sample, or to obtain better separation for larger molecules *e.g.* MTSL.

proteins. Indeed, NTS1 was found to be more stable when incorporated into lipid bilayers, *e.g.* during early CW-EPR trials at room temperature, spectra of NTS1 reconstituted in liposomes remained unchanged over the course of the experiment (~1 h), while spectra of detergent solubilised receptor were altered (not shown). Therefore, the rest of this thesis will aim to study the receptor in an as native a system as possible, *i.e.* liposomes or nanodiscs. Labelling of cysteine mutants was optimised to give good labelling efficiency. Tests on the background Cys-less mutant showed that labelling was specific at low protein concentrations, while some non-specific labelling was observed at high protein concentration in label excess-dependent manner. Thus lower dye excess and shorter labelling times were used in subsequent FRET studies, so as to yield overall labelling efficiency of 100%. Although non-specific labelling at high protein concentration cannot be excluded, this component is likely to be the similar for all samples, as labelling conditions were kept similar throughout. Thus, analyses of relative differences between samples (*e.g.* relative FRET efficiencies, or relative average distances from DEER) should not be compromised.

The cysteine mutations did not appear to hamper NTS1 ligand-biding in detergent giving affinities similar to those observed for WT, and fluorescently labelled cysteine mutants could still couple specifically to G protein in a GTP-dependent manner, albeit with reduced affinity compared to labelled WT receptor. Furthermore, radio-ligand activity assays showed that spin labelling did not detrimentally affect ligand-binding activity. Although not all mutants were tested, the inclusion of a ligand-affinity column step in all purifications, ensures that
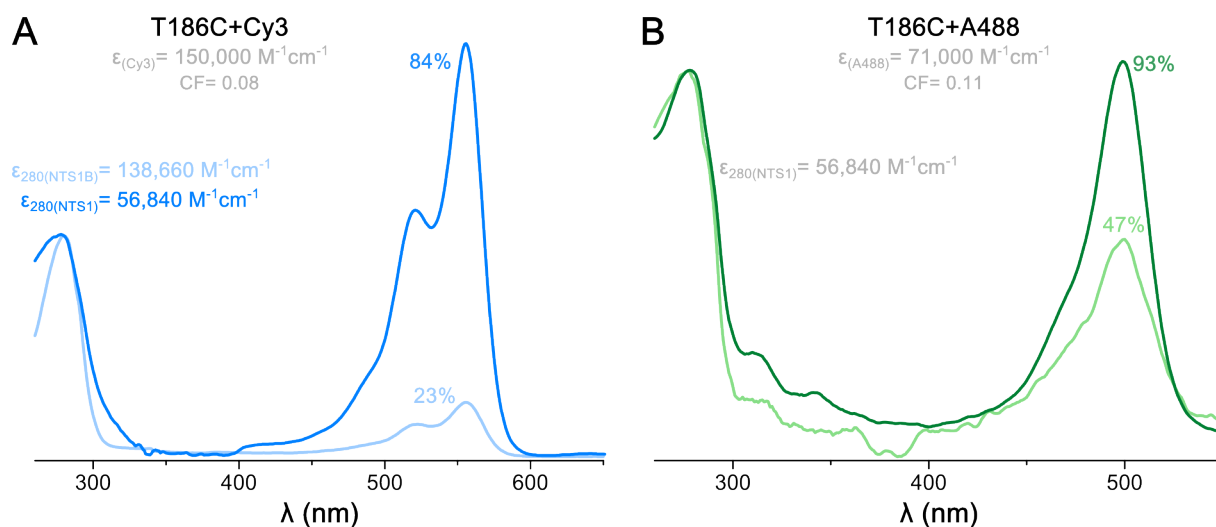
Figure 3.14: Optimizing fluorophore labelling of T186C-NTS1. NTS1 mutant T186C was incubated with maleimide fluorophores and labelling efficiency was calculated from the relative intensity of the dye (555 or 490 nm) and protein (280 nm) peaks using equation A.2 (percentage shown). **(A)** Labelling with Cy3 before (light blue, 0.2 μM T186C, 1 h at RT with 10× molar excess dye) or after the 1 mL Ni^{2+} column concentration step (blue, 1.2 μM T186C, 1 h at RT with 5× molar excess dye). **(B)** Labelling with Alexa Fluor 488 (A488) after after the 1 mL Ni^{2+} column concentration step for protein at 1.2 μM (green, 30 min, 3× molar excess dye) or for the same sample diluted to 0.4 μM (light green, 1 h, 20× molar excess dye). Absorption spectra have been normalised to the peak at 280 nm for clarity.
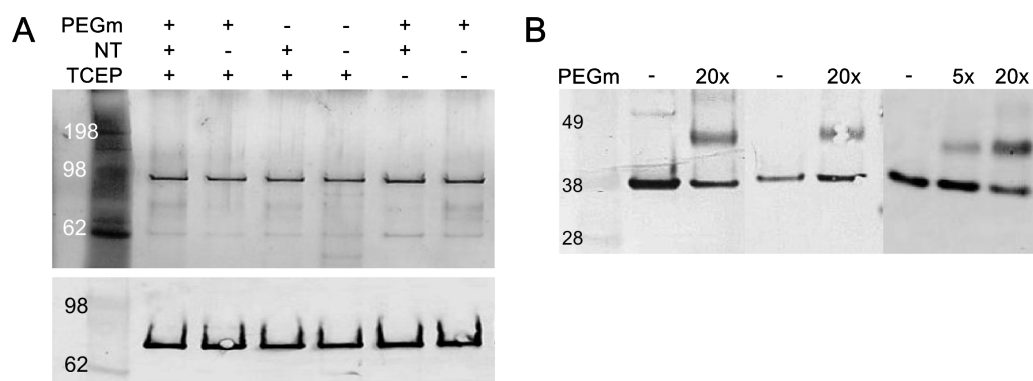
Figure 3.15: Incubation of ΔC-NTS1B with PEGm. (A) ΔC-NTS1B (0.15 μM) was incubated with either TCEP (0.2 mM) for 4 h at 4 °C. TCEP was removed with a P30 spin column and the protein was incubated with a 20× excess of PEGm for 1 h at room temperature. Samples were run on a 4-12% Bis-Tris SDS-PAGE gel and protein was detected by silver staining (top) and western blotting with antibody against MBP (bottom). The influence of ligand (NT), and omission of TCEP was also tested. **(B)** Repeat test at 0.8 μM ΔC-NTS1; protein was incubated with 5 or 20× excess PEGm.

non-functional protein is discarded. This work provides a good basis for further FRET and EPR studies.

4 | CW-EPR study of NTS1 structure and dynamics

4.1 Introduction

4.1.1 GPCR activation

GPCR activation through binding of ligands is a topic that has been, and still is, under much investigation. As crystallisation of GPCRs only became feasible relatively recently, a wide range of other biochemical and biophysical techniques, such as EPR, NMR, FRET, computer modelling, disulfide cross-linking, and mutagenesis, has been applied to the question of how ligand binding affects GPCR conformation. Studies on class A GPCRs *e.g.* rhodopsin [290, 314, 326–328], the β-adrenergic receptors [297, 329–334], the M3 muscarinic acetylcholine receptor [335, 336], and the A_{2A} adenosine receptor [337] suggest that upon ligand binding, TM6 undergoes the largest movement, and that IC3 must undergo some conformational change (reviewed in [99, 338, 339]). Mutagenesis studies of NTS1 have shown that IC3 is implicated in activation of G_q [340]. A growing number of agonist-bound GPCR crystal structures have been published over the past few years, namely for rhodopsin, the $β_1$- and $β_2$-adrenergic receptors, the A_{2A} adenosine receptor, the M2 muscarinic acetylcholine receptor, the $5HT_{1B}$ and $5HT_{2B}$ serotonin receptors, the purinergic $P2Y_{12}$ receptor, and NTS1 (recently reviewed in [99, 341], and see also Table B.1 for PDB IDs and individual references). These structures agreed with the consensus that TM6 undergoes the largest conformational change upon agonist binding, opening up a cavity to accommodate G protein interaction (Figure 4.1). Atomistic insight into the mechanism of activation has come mostly from mutagenesis studies, high-resolution crystal structures, and molecular dynamics simulations (reviewed in [99]). These studies have revealed conserved motifs that have a role as functional microdomains [342]. The most important of these motifs/domains are: (1) the "ionic lock", (2) the hydrophobic Arg cage, (3) the NPxxY motif in TM7, and (4) the "rotamer toggle switch". The ionic lock describes the interaction between the conserved $Arg^{3.50}$ of the (D/E)R(Y/M) motif on TM3, with $D/E^{3.49}$ and the partially conserved $D/E^{6.30}$ on TM6. The disruption of this salt bridge by protonation of $D/E^{6.30}$ is thought to play a role in
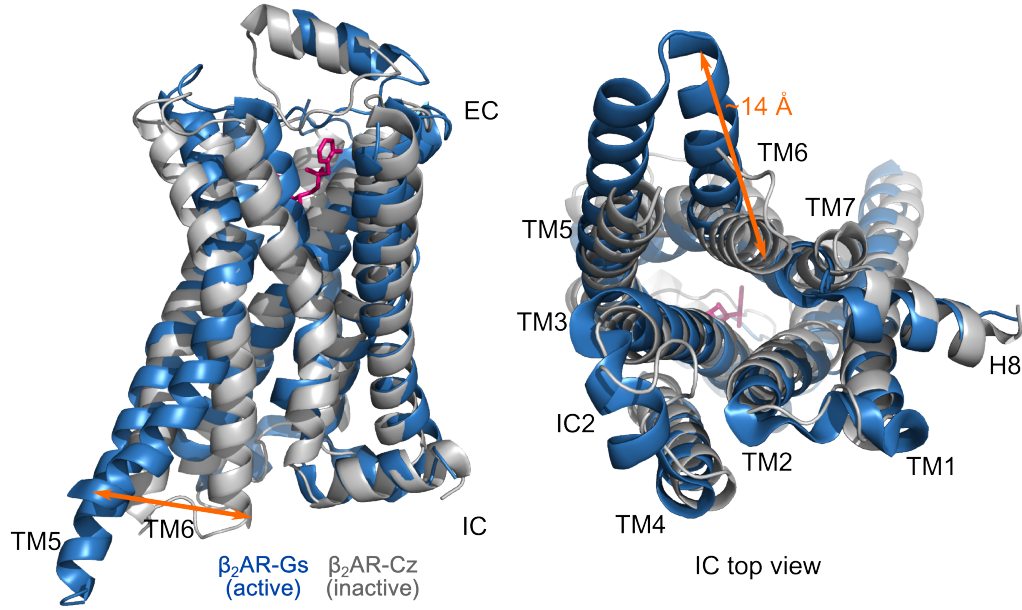
Figure 4.1: Conformational changes in β₂-adrenergic receptor activation. The activated structure of the agonist-bound β₂-adrenergic receptor (β₂AR)-G$_s$ complex (blue, PDB ID: 3SN6, ligand shown in magenta) is compared to inactive inverse-agonist (carazolol)-bound β₂AR (grey, PDB ID: 2RH1, ligand not shown); a side view perpendicular to the membrane (left), with extracellular side (EC) at the top, and a top view from the intracellular side (IC, right) is shown. The activated structure reveals that TM5 extends on the cytoplasmic face by 2 helical turns, and TM6 moves outwards by ~14 Å compared to the inactive state. Modelled on figure from [104].

GPCR activation, allowing the outward movement of TM6, although MD simulations have shown that it can also break and form spontaneously, suggesting that it is a dynamic process [334, 343]. The second motif is composed of conserved hydrophobic amino acids at positions 3.46 and 6.37 (L, V, I, and M) that form a cage restraining the conserved Arg$^{3.50}$ of the ionic lock, aiding appropriate salt bridge formation [344]. The conserved NPxxY motif found in TM7 is involved in interaction with H8 (through Y$^{7.53}$ to F$^{8.50}$) or with TM2 (through Y$^{7.53}$, via a water molecule to R$^{2.40}$); the positioning of the Y residue is thought to either allow or block movement of TM6, an thus receptor activation [345]. Lastly, the rotamer toggle switch describes the interactions of aromatic residues in the vicinity of a conserved Pro on TM6 (of the CWxP motif) that are thought to undergo ligand-induced rotamerisations, affecting the ionic lock [346]. However, crystal structures of activated rhodopsin and β₂-adrenergic receptors did not show such rotameric transitions, suggesting that they may not be required for receptor activation [345].

Crystallography and NMR data have lead to a three-state model of GPCR activation in which in the absence of ligand the receptor is in equilibrium between inactive states and intermediate active states (Figure 4.2, reviewed in [347]); agonists favour active states, while inverse agonists push the equilibrium towards the inactive states. The fully activated states

are promoted by different signalling effectors such as G protein and β-arrestin.
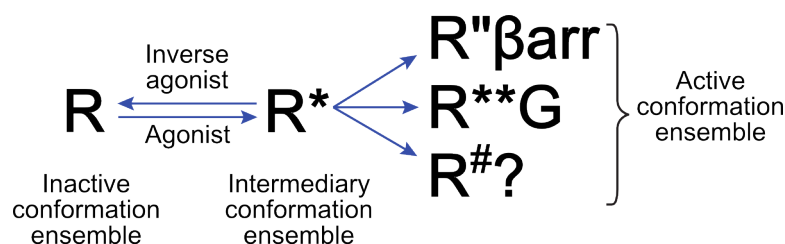
Figure 4.2: Three-state model of GPCR activation. Schematic describing a model for the transition between inactive and active states in GPCRs. In the absence of ligand the receptor is in equilibrium between inactive states (R) and intermediate active states (R*). Agonists favour R*, while inverse agonists push the equilibrium towards R. The fully activated states (R**, R", and $R^{\#}$) are promoted by different signalling effectors such as G protein (G) and β-arrestin (βarr). Figure adapted from [347].

4.1.2   GPCR structure: the eighth helix

In addition to seven transmembrane helices, many crystal structures of GPCRs seem to indicate the presence of an eighth helix (helix 8, or H8) following TM7. It has been observed in all published crystal structures for class A GPCRs, except for the CXCR4 chemokine receptor [292], the protease-activated receptor 1 [348], and one NTS1 structure (PDB ID: 4GRV) [294]. It follows the conserved NPxxY motif in TM7, and lies perpendicular to the TM helix bundle. Sequence analysis suggests that it forms an amphipathic helix, which could interact with the lipid membrane (Figure 4.3). Indeed, it is followed by a pair of semi-conserved C-terminal cysteines, which are a target for palmitoylation, anchoring the C-terminus into the membrane. The importance of the membrane for the structure of H8 has also been established by CD and NMR studies on the β_2-adrenergic receptor [350] and the CB1 cannabinoid receptor [351]. Both studies showed that a peptide corresponding to H8 was α-helical in the presence of detergent (DPC or SDS) or in membrane mimicking solvent (DMSO), whereas the sequence was unstructured in water. A computational study on class C GPCR metabotropic glutamate receptor type 2 (mGlu2) also showed that helix 8 was stabilized in the presence of cholesterol [352]. It was proposed that this could either be due to direct interaction with TM1, 7 and H8, or due to an increase in membrane thickness which allowed the helix to interact with the membrane, thus stabilizing its conformation. Physiological studies have shown H8 to be important for surface expression of GPCRs, for receptor trafficking, and for G protein activation [353–357]. For the bradykinin B_2 receptor it was reported that inserting a proline in the middle of the proposed H8 sequence reduced surface expression and receptor trafficking [358]. This effect could be overcome by the addition of an antagonist, as was also seen for the muscarinic M_1 receptor [359] and the
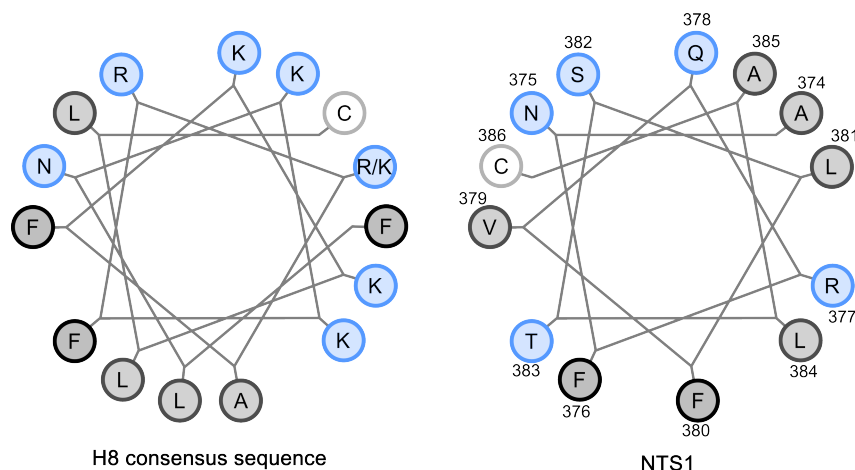
	H8 residue																	
	8.42	8.43	8.44	8.45	8.46	8.47	8.48	8.49	8.50	8.51	8.52	8.53	8.54	8.55	8.56	8.57	8.58	8.59
Consensus sequence	F 37%	L 19%	- 99%	- 99%	- 99%	N 26%	K 23%	K 15%	F 67%	R 61%	K/R 20%	A 23%	F 34%	K 19%	K 16%	L 23%	L 44%	C 17%
Apolar (%)	78	73	-	-	-	15	21	12	91	11	14	48	88	44	22	70	88	51
Polar (%)	2	24	-	-	-	64	73	83	6	86	82	45	9	52	73	25	9	41
NTS1	L	V	-	-	-	S	A	N	F	R	Q	V	F	L	S	T	L	A

Figure 4.3: H8 sequence. The consensus sequence of H8 derived from alignment of all class A GPCR sequences available from the GPCR database (GPCRDB, [349]). The table shows the percentage identity for each of the amino acid in the consensus sequence over all of the aligned sequences for each residue position, as well as the percentage of apolar or polar residues found at each residue position. The sequence of the corresponding NTS1 H8 region is also given. Percentages do not add up to 100%, as some residues are lacking for certain receptors. The consensus and NTS1 H8 sequences are also shown in a helical wheel diagram where polar residues are coloured blue, apolar residues grey, and aromatic residues black. The consensus and NTS1 sequence clearly appear to form an amphipathic helix with clustering of polar/apolar residues. The Arg in the hydrophobic cluster of the NTS1 wheel can possibly "snorkel" to a more polar environment as is common for this type amino acid.

leukotriene B$_4$ type 2 receptor [356]. This suggest that the presence of H8 might have an effect on receptor conformation, and that in the absence of a functional H8 the receptor can be stabilised in the right conformation for trafficking by antagonist. Mutation and deletion studies, and studies with GPCR chimeras where H8 was replaced by that of another GPCR showed that this part of the protein is important for G protein activation and G protein specificity [358, 359].

4.1.3 Current structural data on NTS1

As mentioned in the previous chapter, two agonist-bound crystal structures of engineered NTS1 have been published to date [294, 295]. Although the receptors are both agonist-bound, the authors speak of an 'active-like' state as the position of TM6 was not as outward as expected for a fully activated GPCR able to accommodate G protein (Figure 4.4).
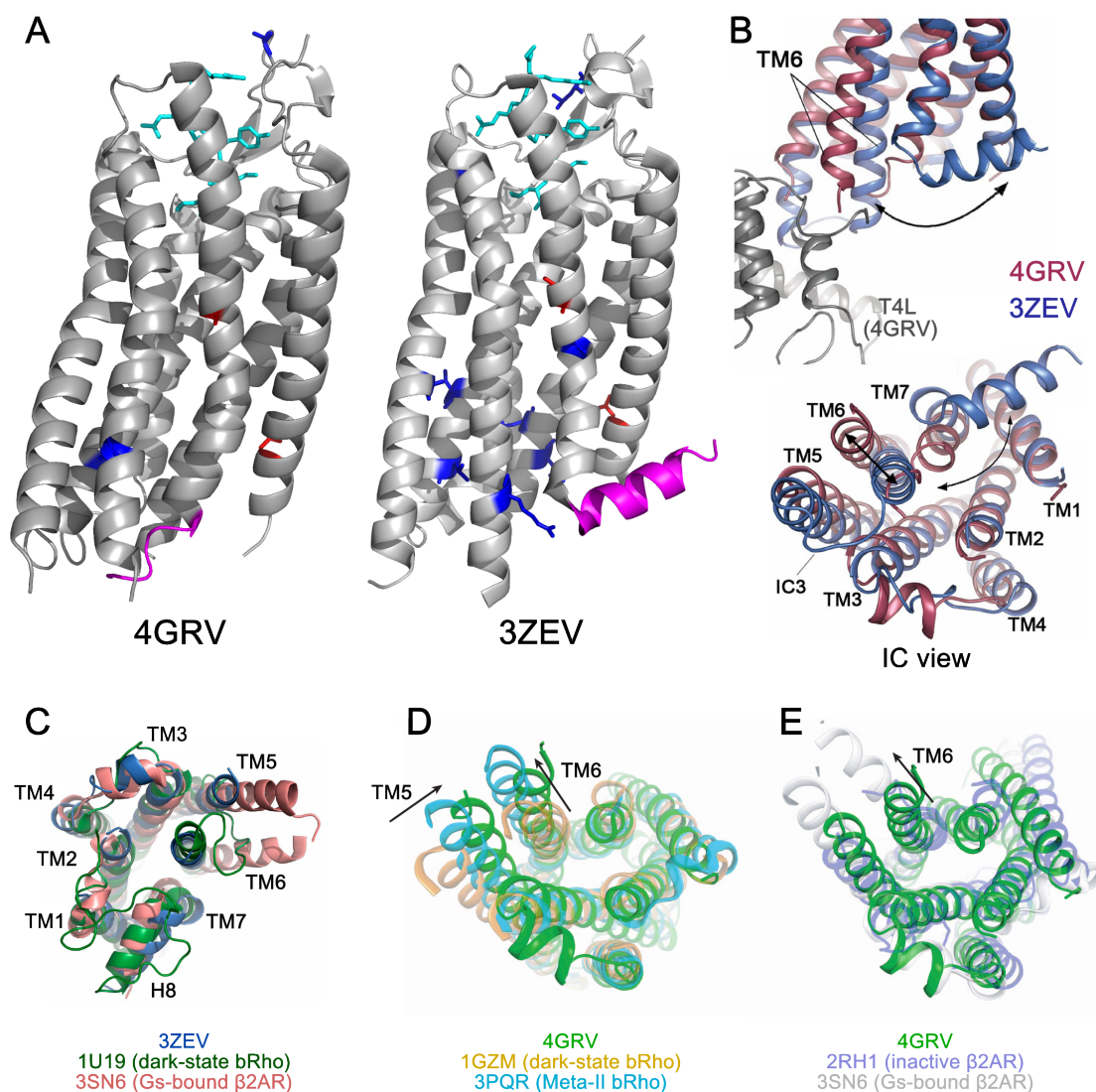
Figure 4.4: Crystal structures of NTS1. Two structures of thermostabilised NTS1 have been published to date: one with T4L introduced in IC3 (PDB ID: 4GRV), and one without T4L, but with a substantial deletion in IC3 (PDB ID: 3ZEV). **(A)** Shows both structures (with T4L removed for 4GRV), with the thermostabilising mutation sites highlighted in blue for unique mutations and red for mutations shared between the two construct, and the residues corresponding to H8 highlighted in pink. **(B)** Overlay of the two structures showing the difference in the positions of TM6 and 7 especially (adapted from [295]). **(C)** Superposition of 3ZEV (blue) with dark-state bovine rhodopsin (green) and the active structure of the G protein-bound β₂-adrenergic receptor (salmon, adapted from [295]). **(D)** Superposition of 4GRV (green) with dark-state rhodopsin (yellow) and its active meta-II state (blue), and **(E)** with the inactive (pale mauve) and active G protein-bound state (pale grey) of β₂-adrenergic receptor (adapted from [294]).

It has to be noted that both receptors were impaired in their ability to couple to G protein in functional assays, which could account for the limited outward movement observed for TM6, although there is no structure available for NTS1 in a basal state to compare to. The function and indeed the presence of H8 in NTS1 is still unclear, with only one

of the published crystal structures (3ZEV) exhibiting a H8 [295]. Both NTS1 structures were produced using different thermostabilised mutants of the receptor. 4GRV contains six mutations (A86L$^{1.54}$, E166A$^{3.49}$, G215A^{EC2}, L310A$^{6.37}$, F358A$^{7.42}$, and V360A$^{7.44}$) as well as a substitution of IC3 (residues 269-299) for T4 lysozyme. This construct was expressed in insect cells, allowing post-translational modifications such as palmitoylation, which might be important for anchoring a putative H8 to the membrane. Crystals were produced in the lipidic-cubic phase, which is a more native system than detergent micelles. Nevertheless, no H8 was observed in the crystal structure, and instead, TM7 appeared to be extended by two turns compared to the other structure. The authors briefly suggested that the lack of H8 could be a native feature of NTS1 or a result of crystallisation conditions. 3ZEV was produced without using a T4L insertion, and instead IC3 was truncated (residues 280-295) to aid crystallisation. This construct contained eleven mutations (A86L$^{1.54}$, H103D$^{2.40}$, H105Y$^{2.42}$, A161V$^{3.44}$, R167L$^{3.50}$, R213L^{EC2}, V234L^{EC2}, I253A$^{5.54}$, H305R$^{6.32}$, F358V$^{7.42}$, S362A$^{7.46}$), and was produced in *E. coli*, and thus not post-translationally modified. The receptor was crystallised in detergent supplemented with a cholesterol analogue (CHS). Despite these seemingly less native crystallisation conditions, this structure did include an α-helical H8. The authors argued that although they observed H8, the helix not very stable in NTS1 as elevated B-factors were obtained in the H8 region, and the helix is not observed in the other crystal structure of NTS1, while other GPCRs, notably the adenosine A$_{2A}$ receptor, exhibit a canonical H8 in all resolved crystal structure models [360]. They argued that H8 is more stable in the adenosine A$_{2A}$ receptor due to stabilising interactions between TM7 and H8, which are impeded in NTS1 due to neighbouring residues. The authors further argued that the presence or absence of H8 could be involved in GPCR activation. However, the role of the membrane in stabilising H8 is not taken into account, which as discussed above, has been shown to be important. The authors also pointed out that a canonical H8 perpendicular to TM7 would not be possible in the crystal lattice of 4GRV as it would clash into a neighbouring molecule, leading to the observed extension of TM7. Thus, it seems possible that H8 is a real feature of NTS1, and the lack thereof in 4GRV is due to crystallisation conditions.

4.1.4 Aim

The protein engineering typically required for obtaining high resolution structures of GPCRs often renders the resulting protein inactive/unable to couple to G protein. Furthermore, the concern remains that the changes observed in the crystal structures may not accurately represent the behaviour of the receptors in their native membrane [159], or at least, provide an oversimplified picture of GPCR activation. Studying GPCR activation for a more native,

active receptor, in a membrane environment is therefore of great interest.

This chapter aims to obtain structural and dynamic information on NTS1, and on how the receptor is influenced by ligand binding using SDSL and CW-EPR measurements. Specifically, cysteine mutants of NTS1B are spin labelled close to the intracellular loop/helix interface of each TM and reconstituted into liposomes. The EPR spectra for each of these spin-labelled mutants is recorded in the presence and absence of the agonist neurotensin, to study the effect of ligand binding on the dynamics of the different helices at the nanosecond time-scale.

In addition the presence of H8, is probed using residue scanning; a series of sequential cysteine mutants were studied by SDSL CW-EPR, to assess the secondary structure of this C-terminal stretch of the receptor reconstituted into lipid bilayers. Again, the influence of receptor activation through ligand binding on this stretch of the protein is assessed.

4.2   Materials and method

4.2.1   NTS1(B)

Cysteine mutants of NTS1B were produced, expressed, purified as described in Appendices A.5.1, A.5.2.3, and A.5.3. Cysteine mutants were labelled with MTSL ((2,2,5,5-tetramethyl-δ-3-pyrroline-1-oxyl-3-methyl)-methanethiosulfonate) as described in Appendix A.5.3. Additionally, a 1:3 (mol:mol) mix of MTSL and MTS ((1-acetoxy-2,2,5,5-tetramethyl-δ-3-pyrroline-3-methyl)-methanethiosulfonate), the NO-acetylated diamagnetic form of MTSL, was also used to label a double cysteine mutant. For the first part of the chapter (effect of ligand on TM dynamics) the intact fusion construct (NTS1B) was used, to maximize protein yields. Labelling was carried out after the NT column, and free label was removed by extensive washing during the 1 mL Ni^{2+} column concentration step. For the second part of the chapter (H8 residue scanning), the fusion partners were removed by TEV protease cleavage (see Appendix A.3), yielding NTS1, to ensure that the secondary structure would not be perturbed by the fusion partners. Labelling was carried out after the 1 mL Ni^{2+} column concentration step, removing excess label and imidazole by salt-exchange on two in tandem connected 5 mL HiTrap Desalt columns. By using a ligand affinity column in the purification, it was ensured that all mutants were indeed able to bind ligand, and thus that the final samples were active. Labelled NTS1(B) was reconstituted into liposomes (brain polar lipid), in the presence or absence of a 5$\times$ molar excess of NT, and loaded into glass capillaries flame-sealed at one end. Initial lipid-to-protein ratios were 2000:1 and 1750:1 for the TM dynamics and H8 experiments, respectively.

4.2.2 EPR

EPR spectra were recorded at 277 and 170 K, using a nitrogen cryostat on an X-band Bruker EMX spectrometer controlled by Bruker Xenon software as described in Appendix A.8.1. Microwave power was adjusted to avoid saturation. Specifically, all H8 samples were measured conservatively with 10 and 0.1 mW power at 277 and 170 K, respectively. For the less concentrated NTS1B TM samples all spectra were recorded with 20 mW power at 277 K, and the microwave power was adjusted between 1-10 mW on an individual sample basis for spectra recorded at 170 K. Between 5-125 scans per sample were collected and averaged.

4.2.3 EPR data analysis

Polynomial baseline correction, and normalisation of the EPR spectra to the integrated intensity of the absorption spectra was carried out using OriginPro 8.5.1 (OriginLab). Mobility parameters ΔH_0, A'_{zz}, and (see section 1.4.2.6) were determined from the EPR spectra recorded at 277 K. The rigid-limit parameter A^R_{zz}, and the interspin distance-dependent ratio k (equation 1.18) was determined from spectra collected at 170 K. Approximate rotational correlation times were calculated using equation 1.17b, with literature values $a = 8.52 \times 10^{-10}$ and $b = -1.16$, on the basis of the observed low field peak width ($\Delta H \approx 5 - 6$ G) of the spectra from frozen samples with immobile labels [184]. The spectral second moment was calculated from the baseline-corrected absorption spectrum $S(B)$ in MATLAB 2013 (MathWorks) by

$$\langle H^2 \rangle = \frac{\int (B - \langle H \rangle)^2 S(B) dB}{\int S(B) dB} \tag{4.1}$$

where $\langle H \rangle$ is the spectral mean

$$\langle H \rangle = \frac{\int B S(B) dB}{\int S(B) dB} \tag{4.2}$$

and B is the magnetic field. Plotting of the inverse second moment of the spectra $\langle H^2 \rangle^{-1}$ vs. ΔH_0^{-1}, is used to assess the overall mobility of residues by comparing to empirically determined ranges.

4.3 Results and discussion

4.3.1 Local TM helix dynamics

CW-EPR spectra were recorded for nine NTS1B cysteine mutants, labelled with MTSL (R1) reconstituted in brain polar lipid liposomes (Figure 4.5): singly labelled mutants A90R1$^{1.58}$ (TM1), Y104R1$^{2.41}$ (TM2), L169R1$^{3.52}$ (TM3), R183R1$^{4.39}$ (TM4), T186R1$^{4.42}$ (TM4), L371R1$^{7.55}$ (TM7), and doubly labelled mutant A272R1^{IC3}-E296R1^{IC3} (TM5-6).
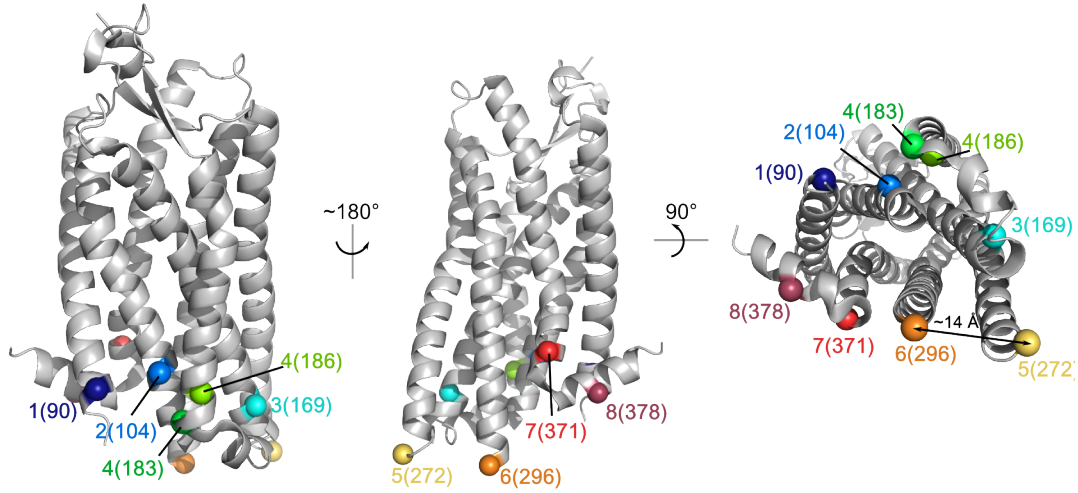
Figure 4.5: Label sites NTS1B TM helices. Mutants of NTS1B with cysteines at the IC side of each TM were labelled with MTSL: single Cys mutants $A90C^{1.58}$ (TM1), $Y104C^{2.41}$ (TM2), $L169C^{3.52}$ (TM3), $R183C^{4.39}$ (TM4), $T186C^{4.42}$ (TM4), $L371^{7.55}$ (TM7), and double Cys mutant $A272C^{IC3}$-$E296C^{IC3}$ (TM5-6). Label sites are highlighted here on the 3ZEV crystal structure. As A272C and E296C are not present on this structure, the nearest residues Q270 and P297 are highlighted instead. The expected A272R1-E296R1 distance is ~14 Å, as determined by rotamer analysis using MMM software [361].

The double cysteine mutant was labelled with either a mix of MTSL and diamagnetic MTS to examine the compounded dynamics of these sites in the absence of intramolecular interactions (spin-diluted), or with only MTSL to also examine the interactions between the labels. This double mutant was chosen as the consensus is that TM6 undergoes outward movement upon ligand binding (up to ~14 Å, Figure 4.1), which could be reflected in the TM5-6 distance which is expected to be in the CW-EPR accessible range (~7-20 Å).

EPR spectra recorded at 277 K and 170 K are shown in Figure 4.6 and D.2, respectively, and derived mobility parameters are presented in Table 4.1. All spectra were complex, containing multiple dynamic components; a more ($\tau_c \approx 30 - 200$ ns) and a less ($\tau_c \approx 2$ ns) motionally restricted component can be distinguished, labelled "1" and "2", respectively, in Figure 4.6. These two components could arise from different conformational states of the receptor, or from spin label rotamers with different interactions with their environment, making them more or less immobilised, due to a decrease in the amplitude of the motion (increased order), in the rate of motion, or both [362]. Changes in the intensity of these components reflect changes in the population of the corresponding protein states or spin label rotamers. The outer splittings ($2A'_{zz}$) reflect the mobility of the more restricted component "1", and the spectral second moment $\langle H^2 \rangle$ is dominated by this component, while the width of the central resonance line is biased by the more mobile spectral component "2" [363, 364].
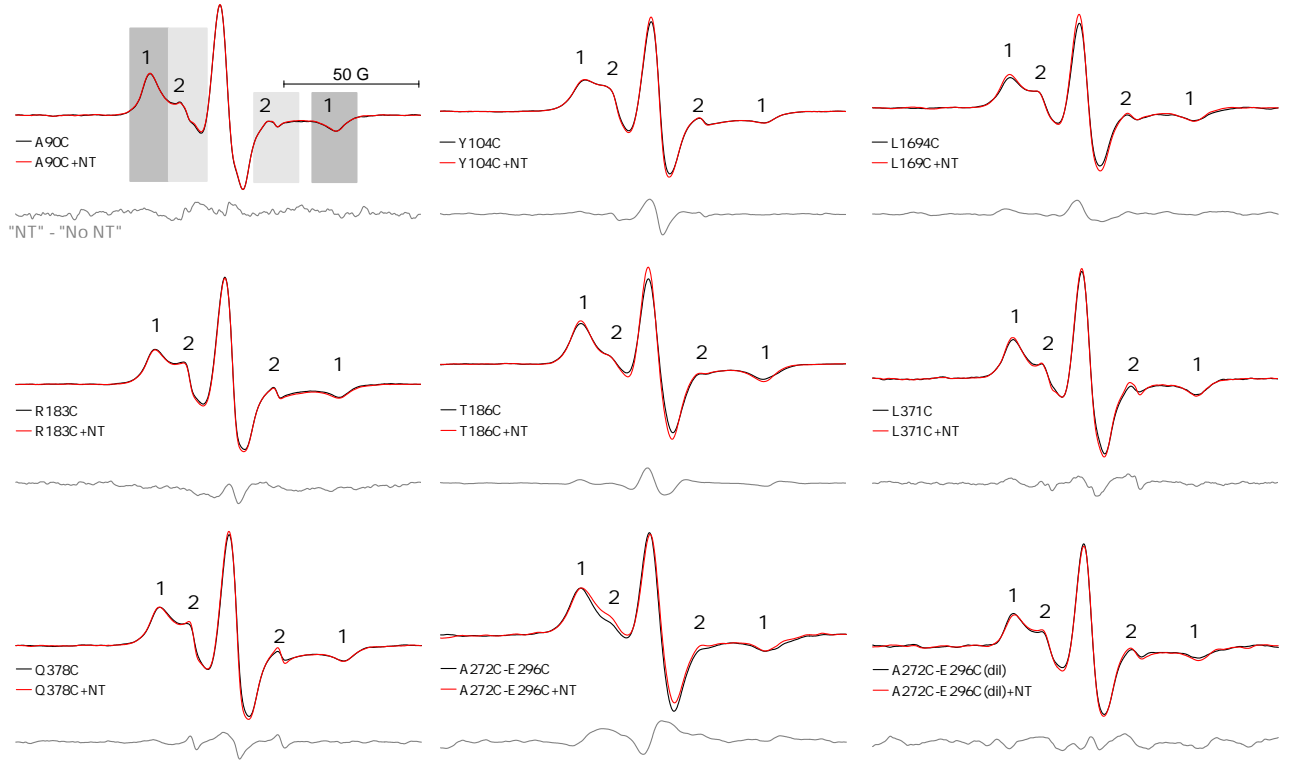
Figure 4.6: EPR spectra of NTS1B labelled on the IC side of the TMs. EPR spectra were recorded at 277 K for mutants spin labelled at the TM/loop interfaces. Spectra were recorded in the absence and presence of agonist neurotensin (+NT), and the difference spectra ("+NT" minus "no NT") are shown in grey. The spectra of the double cysteine mutant labelled with a 1:3 (mol:mol) mix of MTSL:MTS are labelled "dil". All spectra contain two components, a more and a less motionally restricted component labelled 1 and 2, respectively.

The large $2A'_{zz}$ observed for all samples suggests strong local motional restriction of the spin label (Table 4.1), which is confirmed by plotting of $\langle H^2 \rangle^{-1}$ $vs.$ ΔH_0^{-1} (Figure 4.7), where all data points fall within the "buried helix" range (see Figure 1.16) [178, 179]. The strong immobilisation of the spin label observed in this environment, could in part be due to interactions of the spin labels with the lipid bilayer. Indeed, spectra reflecting similar dynamics were previously observed for rhodopsin, both in detergent and phospholipid bilayers, in which the three measured TM-labelled samples gave rise to an immobilised spectral component that was more prominent in the membrane-reconstituted sample [363].

4.3.2 Effect of NT on local TM helix dynamics

Spectra recorded in the presence of agonist show only modest changes compared to the spectra obtained for the unliganded receptor, for a few mutants (Figure 4.6, red and black lines, respectively). For TM1 mutant A90R1, the spectrum is virtually unchanged on NT binding,
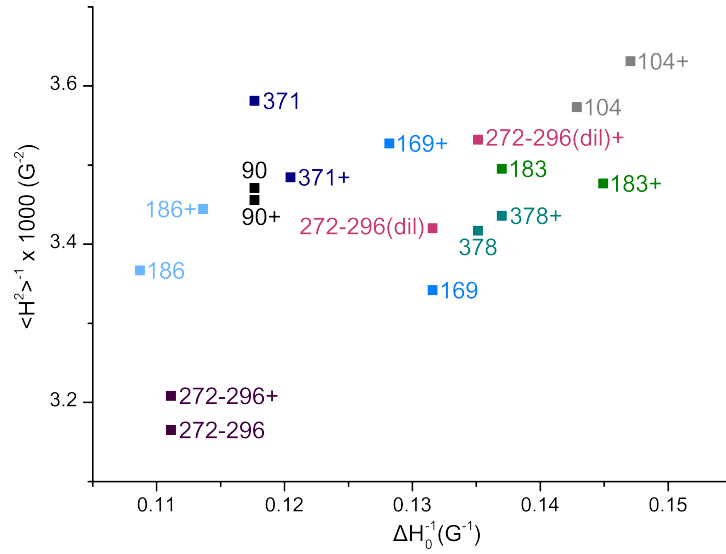
Figure 4.7: Two-dimensional mobility plot for NTS1B labelled on TMs. The inverse of the second moment is plotted against the inverse of the central linewidth for NTS1B cysteine mutants labelled at the IC end of the TM helices. Samples for the same mutant in the absence and presence (+) of NT are given the same colour to aid visual inspection. All points fall within the empirically determined topological "helix/buried" region (see Figure 1.16) [178, 179].

emphasized by the featureless difference spectrum and nearly overlapping points in the two-dimensional mobility plot (Figure 4.7), suggesting little conformational rearrangement of the helix. Similarly, the spectrum of L371R1 (TM7) shows little change, except for the region of the mobile component, which is most likely due to subtraction of a small free spin label component (~0.5% of total integrated intensity) that was present in the raw data (Figure D.1). For the two TM4 mutants, binding of NT has a smaller effect on the spectrum of R183R1, which is located in the IC2, than on that of T186R1 which is located on the edge of the helix (Figure 4.5). For both, the overall mobility of the spin label appears to modestly increase on NT binding, as evidenced by a small decrease in ΔH_0 (-0.4 G for both, Table 4.1), although the relative contributions of the two spectral components does not change. The same is observed for Y104R1 (TM2), where the change in ΔH_0 is even smaller (-0.2 G). For the TM3 mutant L169R1, a clear increase in the population of the more motionally restricted component is observed on NT binding, as well as an increase in the outer splitting (+0.6 G), while the more mobile spectral component remains largely unchanged. For Q378R1 (H8), the opposite is observed, with a slight increase of the mobile component, although ΔH_0 and $2A'_{zz}$ remain virtually unchanged (-0.1 and -0.2 G, respectively). For the double mutant A272R1-E296R1, more significant differences are observed: firstly, in the MTSL (doubly) labelled sample upon addition of NT the intensity of mobile spectral component increases, accompanied by a small decrease in the maximum outer splitting $2A'_{zz}$, suggesting an overall increase in spin label mobility. The same is observed, albeit to a lesser degree, for the spin-

Table 4.1: Mobility parameters from CW-EPR spectra of NTS1B labelled on TMs.
Outer splittings of $(2A'_{zz})$ were determined for the two distinguishable dynamic components of each spectrum recorded at 277 K ((1) the more and (2) the less immobilised component), as well as the width of the central resonance line ΔH_0. Approximate rotational correlation times (τ_c) were calculated using the rigid-limit value $2A^R_{zz}$, determined from the spectra recorded at 170 K. The interspin distance-dependent ratio k (equation 1.18) was determined from spectra collected at 170 K.

Residue		$2A'_{zz}(1)$ (G)	$2A'_{zz}(2)$ (G)	ΔH_0 (G)	$2A^R_{zz}$ (G)	$\tau_c(1)$ (ns)	$\tau_c(2)$ (ns)	k
90	-	68.8	36.3	8.5	69.8	120	2.0	0.36
	+NT	68.9	36.3	8.5	69.8	140	2.0	0.34
104	-	66.4	37.8	7.0	69.2	35	2.1	0.39
	+NT	66.4	37.4	6.8	69.8	28	2.1	0.39
169	-	67.7	37.2	7.6	69.2	71	2.1	0.37
	+NT	68.3	37.4	7.8	69.3	110	2.1	0.37
183	-	68.3	35.9	7.3	70.2	54	2.0	0.33
	+NT	68.1	36	6.9	70.1	51	2.0	0.35
186	-	67.6	36.1	9.2	69.7	49	2.0	0.37
	+NT	67.8	35.7	8.8	69.2	78	2.0	0.36
371	-	67.6	36.2	8.5	68.2	210	2.1	0.33
	+NT	68.1	36.4	8.3	68.9	150	2.0	0.34
378	-	68.1	36.6	7.4	68.9	130	2.0	0.36
	+NT	67.9	35.6	7.3	68.7	150	2.0	0.36
272-296	-	68.4	38.3	9.0	69.7	83	2.1	0.37
	+NT	68.0	37.3	9.0	69.3	84	2.1	0.38
272-296 (dil)	-	68.7	36.9	7.6	70.9	47	2.0	0.34
	+NT	67.9	37.1	7.4	70.9	33	2.0	0.34

diluted MTS/MTSL-labelled A272R1-E296R1 sample; these spectra show a larger mobile component, and overall increase in mobility of both components (larger $\langle H^2 \rangle^{-1}$ and ΔH_0^{-1}, see Figure 4.7) compared to the MTSL-only labelled sample. This suggests that a degree of the line-broadening observed originated from interspin interactions. Indeed, the peak ratio k which correlates with interspin interactions is larger for the doubly labelled (0.38) than for the spin-diluted A272R1-E296R1 sample (0.34, Table 4.1). Thus the observed increase in mobility upon NT binding could be due to a portion of the motionally restricted interacting spin labels moving apart due to movement of TM5 and or 6, as is expected from studies of other GPCRs. This is however not reflected in the value for k (0.38 for the doubly labelled A272R1-E296R1 +NT sample), suggesting that the interspin distance is not affected by the addition of NT, or that only a minor population of the receptor is affected.
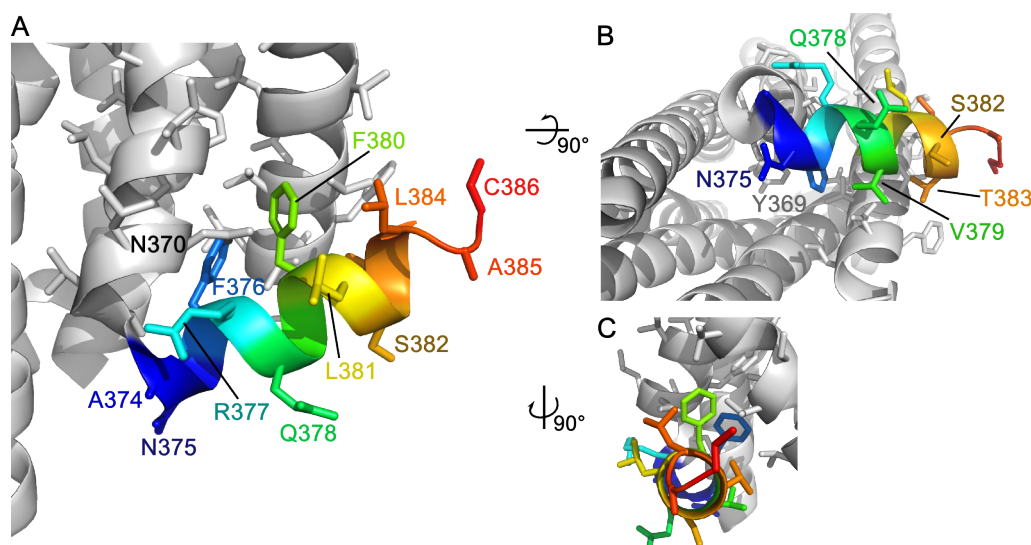
Figure 4.8: Label sites on H8 of NTS1. H8 is shown viewed **(A)** perpendicular to the plane of the membrane, **(B)** from the IC side, and **(C)** from the end of the helix in the plane of the membrane. Sequential cysteine mutants of NTS1 with mutations introduced in the C-terminus from residue 374 to 393 were labelled with MTSL. Here residues 374-386 are indicated on the 3ZEV crystal structure (later residues are not resolved). TM7 residue $Y369^{7.53}$ is thought to stabilise H8 in other GPCRs, through π-π stacking with $F376^{8.50}$, but cannot do so in the NTS1 3ZEV structure due to steric hindrance of $N370^{7.54}$.

4.3.3   H8 sequence scanning

CW-EPR spectra were recorded for sequential cysteine mutants of the C-terminal residues 374 to 393 (Figure 4.8) reconstituted in brain polar lipid liposomes, at 277 and 170 K (Figure 4.9 and D.3, respectively). The good signal-to-noise ratio of the EPR spectra indicates that all mutants labelled well, with the exception of V379C, which gave poor spectra for two separate sample preparations, suggesting that this residue is not as accessible as the others, and possibly in an relatively buried position.

The secondary structure of the probed sequence can be assessed by plotting the inverse central linewidth ΔH_0^{-1} *vs.* residue number (Figure 4.10). Figure 4.10A shows that a sine function with a period of 3.6, corresponding to the periodicity of an α-helix, can only be properly fitted to the first half of the probed stretch, running from residue 374 to 385, after which the periodicity in the data is lost. This periodicity implies that NTS1 does have an α-helical H8, in agreement with the 3ZEV crystal structure, for which H8 stretches from residues 374 to 384. The polarity of the local environment of spin label influences the maximum outer splitting ($2A_{zz}^{R}$, see section 1.4.2.3), with larger splitting corresponding to a more polar environment. Plotting $2A_{zz}^{R}$ against residue number again reveals a pattern with a periodicity of roughly 3.6 for residues 374-384 (Figure 4.10B). This periodicity is consistent with an amphipathic helix lying along the membrane, where some residues will be buried

Figure 4.9: EPR spectra H8 and C-terminus. EPR spectra were recorded at 277 K for residues along the C-terminal stretch after TM7, encompassing the putative H8. Spectra were recorded in the absence and presence of agonist neurotensin (+NT).
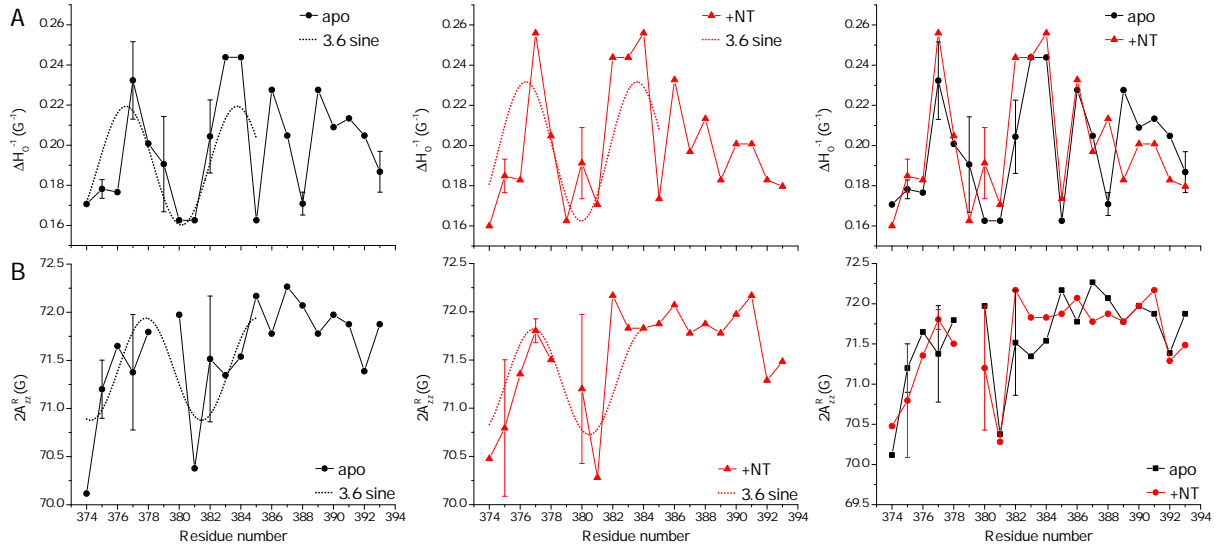
Figure 4.10: CW-EPR analysis of H8 periodicity. (A) ΔH_0^{-1} was determined from spectra recorded at 277 K, plotted against residue number and found to roughly fit a sine with a periodicity of 3.6, corresponding to α-helical structure for residues 374 to 385, after which the periodicity is lost. This pattern was similar for samples including agonist (+NT). Overlay of data for NTS1 in the absence (apo) and presence (+NT) of agonist is shown in the right panel. **(B)** Similar analysis is shown for the polarity parameter A_{zz}^R determined from spectra recorded at 170 K. Error bars are given for residues for which multiple samples were measured (n=2 for all except 377[apo] for which n=3) and represent the standard error of the mean; all other data points represent single experiments.

in the phospholipid headgroup region, and others more water exposed. Residues A374R1 and L381R1 show the smallest $2A_{zz}^R$, consistent with a membrane-buried conformation, as would be expected for the native apolar Ala and Leu residues. This observation is also consistent with the position of these residues in the middle of the apolar patch of the helical wheel prediction for NTS1 (Figure 4.3). By extension, this observation suggests that the spin labelling did not disturb the naturally expected conformation and orientation of the helix. The later C-terminal residues (385-393) show larger $2A_{zz}^R$, consistent with an extramembranous environment.

4.3.4   Effect of NT on helix 8

The effect of agonist on H8 structure was also investigated by measuring the spectra in the presence of saturating amounts of NT. Periodicity of the mobility parameters was retained in the presence of NT (Figure 4.10), suggesting that the overall conformation of H8 remains unaltered. Indeed, the overlaid spectra for each mutant in the presence and absence of ligand show little difference, suggesting that overall the local effect of NT on R1 dynamics is small (Figure 4.9). A few exceptions, out of the twenty positions monitored, are residues

R377R1, F380R1, S382R1, C388R1, and P389R1, with the first four showing an increase in the mobile component, and the last one showing a decrease of the mobile component of the EPR spectrum. The first three sites are part of the helix, as demonstrated above, but are not all expected to be on the same side of the helix (i, i+3, i+5, Figure 4.3). It is thus difficult to assign the observed effect of agonist to an overall structural change, such as a rigid body movement or rotation of H8, as this would be not be expected to give a consistent effect over all helix interfaces. It is thus more likely that the observed increases in mobility are due to local effects. The other two residues (C388R1 and P389R1) lie in the C-terminal stretch beyond H8. C388R1 is normally palmitoylated in cells, and anchored to the membrane, and is thus not expected to undergo great dynamic changes upon ligand binding *in vivo*. The observed effect is thus more likely to originate from interactions with other residues which do normally undergo changes upon ligand binding. The neighbouring P389R1 residue shows an opposite effect, with the mobile component of the spectrum decreasing relative to the immobile component upon ligand binding. The proline-to-cysteine mutation can of course have perturbed the natural conformation of this residue, as prolines have a very distinct biochemical character. Nevertheless, as this stretch of the protein appears to be unstructured from the EPR sequence scanning data (Figure 4.10), the proline-to-cysteine mutation might not be so perturbing, and it is still possible that ligand binding affects this site *in vivo*. Indeed, from Figure 4.10B, it seems that the C-terminal stretch beyond H8 becomes overall somewhat less mobile in the presence of agonist. Figure 4.11 suggests that overall all the residues probed, including those in the seemingly unstructured C-terminal stretch beyond H8, are motionally restricted. This is most likely due to interactions of the C-terminus with the membrane.

4.4   Conclusions

In agreement with the existing consensus on GPCR activation mechanism [99, 345], addition of agonist appeared to induce the largest changes in TM5-6, with NTS1 labelled at intracellular of TM5-6 showing a more mobile CW-EPR spectrum (Figure 4.6), suggestive of either increased backbone mobility, or simply less restricted motion of the spin label due to a conformational change in the receptor. TM3, and to a lesser extent 4, were the only other TMs to display modest spectral changes upon addition of agonist, showing a decrease and increase in overall spin label mobility, respectively (Figure 4.6). This could reflect the role of the proposed "ionic-lock" between TM3 and 6 in receptor activation, leading to re-arrangement of the helix and thus different spin label environment, which could also be carried forward to the relatively close TM4. As the spectra are complex, with at least two resolved components, and the spin labels probe dynamics locally, it is hard to draw any
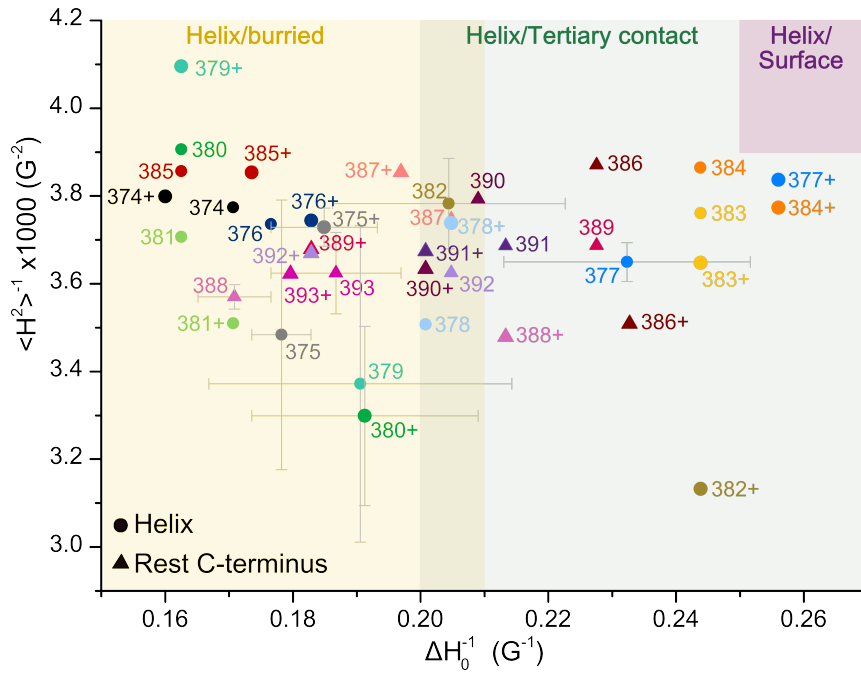
Figure 4.11: Two-dimensional mobility plot for NTS1 H8. The inverse of the second moment, $\langle H^2 \rangle^{-1}$, is plotted against the inverse of the central linewidth, ΔH_0^{-1}, for NTS1 sequential cysteine mutants labelled on the putative H8 stretch (circles) and the rest of the C-terminus (triangles) in the absence and presence ("+") of NT. Samples for the same mutant in the absence and presence of NT are given the same colour to aid visual inspection. Empirically determined topological regions of the protein [178, 179] are indicated by shaded boxes.

conclusions on overall (whole-body) protein dynamics. The previously mentioned CW-EPR study of rhodopsin showed significant spectral changes for spin labels on TM3, 5, 6 upon light activation [363]. TM6 spin-labelled rhodopsin showed strong changes at 293 K both in detergent and lipid bilayers on photo-activation, in agreement with the consensus role of this TM in GPCR activation, while for TM3 and 5 spin-labelled samples photo-activation-induced changes were greatly dampened in lipid bilayers compared to detergent. The magnitude of the effect was also shown to be temperature dependent for the TM3 spin-labelled sample, with a much more pronounced effect at 308 K compared to 293 K. The results obtained in the rhodopsin EPR study [363] are in agreement with the suggestion that GPCR activation is a dynamic process, where the energy barriers and/or energy differences, and thus the equilibrium between different states is influenced by ligand binding (see Figures 4.2 and 4.12); therefore, an increase in kinetic energy due to higher temperature makes activation more likely, leading to more pronounced effects in the EPR spectra. The effects seen here for NTS1 were more modest than those observed in the rhodopsin study. This could be due to the combined effect of the lipid bilayer and the relatively low temperature (277 K) at
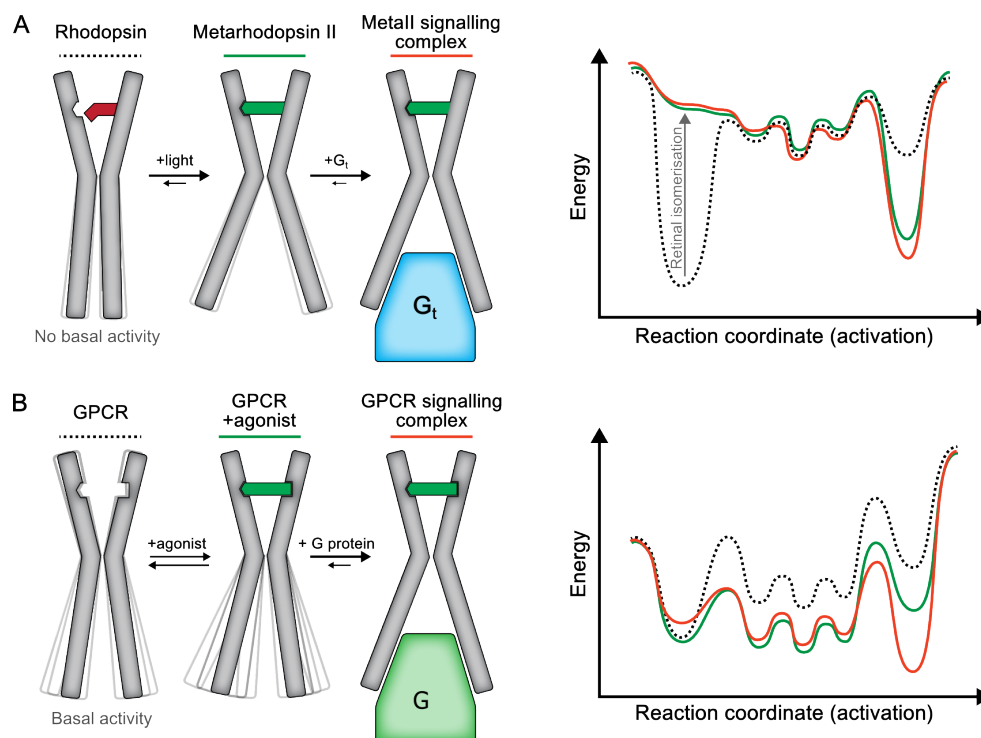
Figure 4.12: Energy landscape of GPCR activation. A schematic showing the differing models for activation of rhodopsin and other GPCRs. **(A)** Rhodopsin shows no basal activity as it is naturally covalently bound to its inverse agonist 11-*cis*-retinal, meaning the energy barrier to activation is relatively high. Light-induced isomerisation of the retinal lowers the energy barrier to the active conformation of the receptor, leading to the transducin (G_t) bound signalling complex. **(B)** Other class A GPCRs, such as the β₂-adrenergic receptor (and NTS1) do show basal activity and have been proposed to be more conformationally dynamic, due to smaller energetic differences between the different activation states (inactive, intermediate, and active) of the receptor. Agonist and G protein binding decreases the energy levels of intermediate and active states, respectively, effectively lowering the energy barrier and shifting the equilibrium towards the activation of the receptor. Figure adapted from [365].

which the experiments had to be performed, due to the poor thermal stability of NTS1[1], dampening protein motion. Furthermore, it has been argued that rhodopsin has a somewhat different mode of activation compared to other GPCRs as it is covalently bound to its inverse agonist 11-*cis*-retinal, and shows no basal activity (Figure 4.12A) [365]. Most other GPCRs, including NTS1, do show basal activity, and have thus been proposed to be more conformationally dynamic, due to smaller energetic differences between the various activation states (inactive, intermediate, and active) of the receptor (Figure 4.12B). Agonist and G protein binding decreases the energy levels of intermediate and active states, respectively, and/or lower the energy barrier between states, thus shifting the equilibrium towards the energetically more favourable active state of the receptor. Thus, the changes between the

---

[1]NTS1 has a melting temperature of ~24 °C in detergent [293] compared to ~72 °C for rhodopsin in native membranes [366].

unliganded and agonist-bound ensemble averages for diffusible ligand-binding GPCRs are expected to be smaller than those observed on photo-activation of rhodopsin, which might contribute to the lack of large changes in the CW-EPR spectra of NTS1B upon addition of agonist.

CW-EPR sequence scanning confirmed the presence of the α-helical C-terminal segment H8, for the non-thermostabilised, lipid bilayer-reconstituted receptor. Unlike proposed by Egloff *et al.* [295], the overall structure of H8 does not appear to change in the presence of agonist, and thus the lack of an H8 in the 4GRV structure appears to be a crystallographic artefact. The two-dimensional mobility plot (Figure 4.11) suggest residues in H8 and the C-terminal stretch beyond are motionally restricted, which could reflect tertiary contacts with the protein, and the bilayer as expected for H8, and as previously observed for rhodopsin [367]. Indeed, polarity analysis is consistent with an amphipathic helix along a membrane surface (Figure 4.10B). Since NTS1 samples were produced in *E. coli*, the protein was not post-translationally modified. Thus, palmitoylation of the C-terminus, as present *in vivo*, does not appear to be required for H8 helicity, although it might have a stabilising effect. The presence of ligand does not affect the overall structure of H8 (Figure 4.10), although it has some local effects, with spin labels at certain positions within the helix becoming more mobile (Figure 4.9). It is thought that interactions between the $\text{Tyr}^{7.53}$ of the conserved NPxxY motif and H8 are broken upon activation (as discussed in section 4.1.1), and this interaction is not observed in the "active-like" 3ZEV crystal structure (Figure 4.8). It is thus possible that such a change in the interaction between TM7 and H8 leads to an increase in local dynamics of H8 as observed in the EPR spectra. C-terminal residues beyond H8 appear to become more motionally restricted in the presence of agonist, although the over-all polarity of the local environment is not affected (Figure 4.10). Although no secondary structure formation is evident this could reflect propagation of conformational changes in the overall receptor required for G protein binding; indeed, residues 372-401 of the C-terminus of NTS1 have been shown to be involved in coupling to G_s and G_i-mediated pathways [368]. The work presented here suggests that, despite the agonist-bound crystal structures of NTS1 only showing an "active-like" receptor state, binding of agonist alone already has an effect on NTS1 structure and/or dynamics, and consequently that thermostabilised crystals do not necessarily reflect the structure of the receptor in solution. This conclusion stresses the importance of studying membrane proteins in a more native environment to obtain an accurate picture of their function *in vivo*, and this study forms a good starting point for future work in the presence of G protein to shed more light on the activation mechanism of NTS1.

5 | Oligomerisation of NTS1 studied by FRET and DEER

5.1 Introduction

5.1.1 GPCR oligomerisation

Over the past few decades, evidence for GPCR oligomerisation has been accumulating that challenges the idea that GPCRs function as isolated monomeric receptors in the cell membrane (reviewed in *e.g.* [369–371], see also Table 5.1). It is now widely accepted that for class C GPCRs constitutive dimerisation is essential for receptor activity [372–375]. For example co-expression of the GABA$_{B1}$ with the GABA$_{B2}$ receptor is required for GABA$_{B1}$ to reach the plasma membrane, where the two receptor isoforms form a functional heterodimer in which the GABA$_{B1}$ subunit binds the ligand and the GABA$_{B2}$ subunit couples to the G protein [374, 376]. Using a variety of techniques, such as resonance energy transfer (RET), chemical cross-linking, co-immunoprecipitation [377], a large number of class A GPCRs have also been observed to oligomerise *in vitro* and *in vivo*, *e.g.* the β$_1$- and β$_2$-adrenergic receptors, the dopamine D$_2$ and D$_3$ receptors, the δ-, κ- and μ-opioid receptors, and CXCR4, CCR2 and CCR5 chemokine receptors (reviewed extensively in *e.g.* [369–371, 378]). The function, and indeed the existence of class A GPCR oligomers *in situ*, however remains controversial, as studies with monomeric GPCRs reconstituted into nanodiscs (*e.g.* the β$_2$-adrenergic receptor [380], rhodopsin [381], and the μ-opioid receptor [382]) or monomeric receptors in detergent (*e.g.* rhodopsin [383] and NTS1 [321]) have shown that monomeric receptors can efficiently couple to G proteins. However, while these studies show that GPCRs can function as monomers *in vitro*, they do not exclude the existence of functional oligomers *in vivo*. Indeed, other studies have suggested that receptor oligomerisation might be necessary in receptor trafficking to the plasma membrane [384, 385], provides means for regulation of ligand binding [386–388] and G protein activation [389–392], and/or is involved in receptor internalisation [393, 394] (Figure 5.1).

Numerous observations of cooperativity in ligand-binding studies have strengthened the case
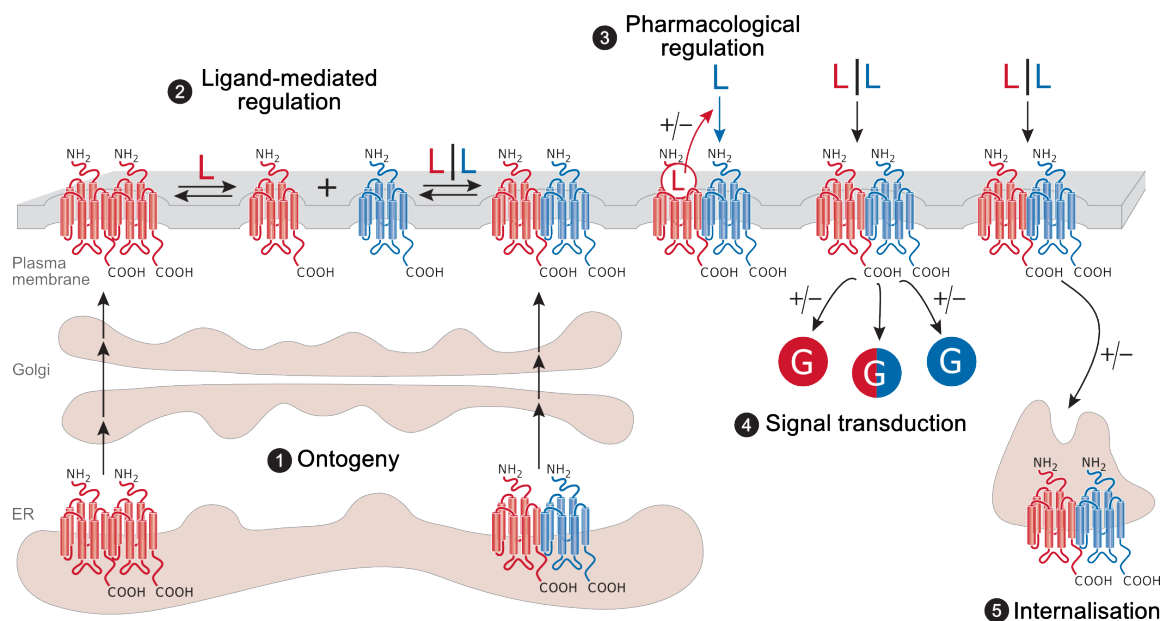
Figure 5.1: Potential functional implications of GPCR oligomerisation. GPCR homo- and hetero-oligomerisation has been observed to influence (1) maturation of receptors and trafficking to the cell surface. (2) Ligand-controlled oligomerisation has been observed, as well as (3) negative or positive cooperativity in ligand binding to the second protomer when the first is ligand occupied (here shown for heterodimers, but also observed for homodimers). (4) Stimulation/attenuation of G protein activity, or G protein selectivity has also been documented. Finally, (5) hetero- and homo-oligomerisation has been shown to influence ligand-induced internalisation of GPCRs. Figure adapted from [379].

for functional oligomerisation (reviewed in [395]). For example, for the adenosine A_3 receptor expressed in CHO cells it was found that the dissociation rate of a fluorescent agonist was affected by the presence of the unlabelled agonist which is not consistent with ligand dissociation from a monomer, and was thus interpreted as evidence for crosstalk within receptor dimers [386]. The same was observed for the adenosine A_1 receptor, albeit to a lesser extent [386]. Another example of cooperativity is given by an *in vitro* study on detergent-solubilised leukotrine B_4 (LTB_4) receptor (BLT_1) [396]; using a mixture of wild-type receptor and a ligand-binding-deficient form of the receptor that contained only one tryptophan that could report on conformational changes of the receptor, it was shown that addition of agonist LTB_4 induced conformational changes in the binding-deficient (thus apo) protomer. Allostery was also shown in native tissue using time-resolved FRET with fluorescent ligands [388]; FRET signals were detected for the oxytocin receptor in mammary gland patches (but not in brain) consistent with receptors with a quaternary structure. Results further showed a stoichiometry of one agonist molecule per dimer, consistent with negative cooperativity (which was not observed for labelled antagonists) [388]. Functional crosstalk between receptors has also been shown *in situ* [397]; in a study of the luteinizing hormone receptor, mice expressing

only a ligand-binding deficient or G protein-coupling deficient form of the receptor were crossed to produce co-expression of the two individually inactive forms, in the absence of wild-type receptor. This resulted in rescue of function, implying intermolecular functional complementation between the two forms and by extension their dimerisation [397]. This interpretation was however challenged by Zhang *et al.*, who argued that the lack of function of the mutants could also have been due to lack of cell-surface delivery [398].

Despite the earlier mentioned observation that monomeric GPCRs can couple to G protein, modulation of G protein activity ascribed to oligomerisation has also been observed; *e.g.* leukotrine BLT_2 dimers were shown to activate purified G protein less efficiently than monomers [390]; for serotonin $5\text{-}HT_{2C}$, it was observed that binding of agonist to both protomers of a dimer is needed to generate maximal function [392]; and for the related serotonin $5\text{-}HT_4$, it was shown that activation of both protomers in a dimer results in greater activation of G protein, than activation of a single protomer in a dimer does [391].

Hetero-oligomerisation of different GPCR subtypes has also been observed, with functional implications for ligand binding and G protein selectivity (reviewed in *e.g.* [399–402]), but will not be further discussed here.

The apparent role of GPCR oligomerisation in the fine-tuning of GPCR function provides therapeutic potential for targeting GPCR oligomers to regulate receptor activity [403].

5.1.2 Morphology of GPCR oligomers

5.1.2.1 Oligomerisation interface

Part of the controversy surrounding GPCR oligomerisation is due the lack of consensus on morphological aspects, such as the receptor interfaces involved in oligomerisation, the size of the oligomers (dimers or higher-order oligomers), and their possible dynamic nature (constitutive *vs.* transient, *e.g.* ligand-induced, oligomers).

While class C GPCR oligomers are believed to be relatively stable due to disulfide bonds between the extracellular segments of the protomers and/or intracellular coiled coils [369], class A GPCRs do not have the large N-termini found in class C GPCRs, and oligomerisation is thus believed to occur primarily through (hydrophobic) interactions between the TM domains [404]. Given the structural homology found in the TM domain of class A GPCRs, a common structural mechanism for dimerisation of receptor protomers might be envisaged. Detailed structural data of class A GPCR dimers however remains largely elusive, and often conflicting (see Table 5.1). Crystal structures of GPCRs have included parallel dimers in the crystal lattice, which have in some instances been interpreted as revealing a potential dimerisation interface for these receptors. The β_2-adrenergic receptor was crystallized with interprotomer contacts mediated through H8 stabilised by hydrophobic interactions with

six cholesterol and two palmitic acid molecules located between the monomers [284]. This observation was speculated to play a role in dimerisation *in vivo*, although the authors recognized conflicting studies in cell membranes where TM6 was found to be the likely dimerisation interface [405]. A later publication of a crystal structure for the β_1-adrenergic receptor speculated more freely that the crystallisation interfaces found, namely TM1-2-H8-EC1 an TM4-5-IC2-EC2, could represent oligomeric interfaces of the receptor [406]. Other crystallographic evidence comes from the CXCR4 chemokine receptor (TM5-6) [292], the κ-opioid receptor (TM1-2-H8) [407], and the μ-opioid receptor (TM1-2-H8 and TM5-6) [408]. Whether these crystallographic dimers accurately reflect the (dynamic) situation in membranes, or are simply due to non-specific crystal packing is uncertain.

Other structural data on GPCR dimer structure comes largely from mutagenesis, chemical cross-linking, RET and TM helix competition studies (see Table 5.1). The data do not show a clear consensus, with every receptor segment being implicated thus far in different studies, and even different studies on the same receptor subtype giving varying results.

5.1.2.2   Oligomeric state

Besides no clear consensus existing on the oligomerisation interface, different oligomeric states have also been found; although many studies report dimers (*e.g.* based an analytical ultracentrifugation [321] or FRET saturation experiments [206] for NTS1), higher-order oligomers have also been found. For example for the β_2-adrenergic receptor, FRET studies on the purified receptor in liposomes showed predominantly tetramers [409]. The same was found for muscarinic M_2 acetylcholine receptor in live cells [433]. The muscarinic M_3 acetylcholine receptor was found to be present as both dimers and tetramers in HEK cells, and co-immunoprecipitation showed dynamic interchange between these species [434]. The range within which expression levels could be varied in this these studies was insufficient to determine whether the proportion of tetramers relative to dimers varied with receptor density at the membrane, as would be expected from the law of mass action [370]. Another study however suggested stable oligomerisation could be detected for the dopamine D_2 receptor over a 100-fold range of expression levels [418].

5.1.2.3   Oligomerisation dynamics

The dynamics of oligomerisation are also matter of debate. Studies using ensemble tools such FRET, cross-linking an co-immunoprecipitation, generally suggested that oligomerisation is constitutive [435]. More recent studies however, using single-molecule imaging techniques (reviewed in [204]), have revealed a potential transient nature for GPCR oligomers. Recently, the stability of GPCR oligomerisation was assessed in two cell-based studies in which

Table 5.1: Class A GPCR dimerisation interfaces. A (non-extensive) list of reported structural elements of class A GPCRs implicated in oligomerisation is presented here. Abbreviations: Ref., references; AFM, atomic force microscopy; ECD, extracellular domain.

Receptor	Implicated elements	Techniques	Ref.
β_1-adrenergic	TM1-2-H8 and TM4-5-IC2	Crystallography; cross-linking	[406]
β_2-adrenergic	TM6	TM/peptide competition	[405]
	H8 + cholesterol	Crystallography	[284]
	H8, not TM6	FRET	[409]
Rhodopsin	TM4-5	Cross-linking; AFM; modelling	[410]
	TM4-5	Cross-linking; FRET	[411]
M_3 muscarinic	TM3-EC2	Mutagenesis	[412]
acetylcholine	TM1-5-7	Mutagenesis; BRET	[413]
	TM5-IC3	Cross-linking; computational modelling	[414]
dopamine D_2	TM6-7	TM/peptide competition	[415]
	TM4 (and other unidentified)	Mutagenesis	[416]
	TM4	Cross-linking	[393, 417]
	TM4-5	Cross-linking	[393]
	TM1-4	Cross-linking; RET	[418]
CCR5 chemokine	N-terminus-TM1	Mutagenesis; yeast two-hybrid	[419]
	TM1-4	Mutagenesis; TM/peptide competition	[420]
CXCR4 chemokine	TM5-6 and TM3-4	Crystallography	[292]
	TM4 + cholesterol	TM/peptide competition; cholesterol depletion	[421]
Bradykinin B_2	ECD	Mutagenesis	[422]
	N-terminus (not EC loops)	TM/peptide competition; cross-linking	[423]
α-factor	TM1-2	Mutagenesis; FRET	[424]
	TM1-4	Cross-linking	[425]
	N-terminus	Cross-linking	[426]
δ-opioid	C-terminus	Mutagenesis	[427]
κ-opioid	TM1-2-H8	Crystallography	[407]
μ-opioid	TM1-2-H8 and TM5-6	Crystallography	[408]
NTS1	TM1-2-4	Computational modelling	[428]
Serotonin $5HT_{2C}$	TM1-4-5	Cross-linking	[429]
Adenosine A_{2A}	TM5	Mutagenesis; TM peptide study	[430]
Adenosine A_{1B}	TM4	Mutagenesis; FRET	[431]
BLT1 leukotrine	TM6	TM/peptide competition	[432]

a portion of the expressed receptor was immobilised by interaction with specific antibodies, and the mobility of the remainder was probed by FRAP (fluorescence recovery after photobleaching) [436, 437]. Contrary to the previously observed stable dimerisation for the dopamine D_2 receptor [418], the FRAP study showed transient interactions between protomers, which could be stabilised by cross-linking at TM4, suggesting that the lifetime of the oligomers was short compared to the time scale of macroscopic diffusion [437]. While FRAP studies were consistent with stable β_2-adrenergic receptor higher-order oligomers containing at least 4-5 protomers, they showed transient oligomerisation of the β_1-adrenergic receptor on the time scale of seconds that could be stabilised by chemical cross-linking [436]. For both adrenergic receptors no effect of agonist or inverse agonist was observed [436]. Expres-

sion levels for the β_1 receptor were higher than those for the β_2 receptor, suggesting that the difference was probably not due to crowding, although the authors note that expression levels could still be well above native levels [436]. Single-molecule imaging studies on the M_1 muscarinic acetylcholine receptor using (slowly-dissociating) fluorescent ligand showed that the receptor formed homomers with a lifetime of ~0.5 s and no more than ~30% of the receptor was dimeric at a given time [438]. The authors used the fluorescence intensity of a single spot, and the number of steps in which this photobleached to show the presence of multiple ligands within one spot (*i.e.* of receptors within less than 200 nm of each other, the spatial resolution being limited by the diffraction limit). However, the assumption made that each protomer within an oligomer would bind ligand might not be valid, as there are numerous examples of negative cooperativity of ligand binding within GPCR dimers (reviewed in [395]), although this has not been studied for this receptor subtype. It could thus be that the results reflect a dimer-tetramer rather than a monomer-dimer equilibrium. Kasai *et al.* also used single-molecule imaging with fluorescent ligands to study the oligomerisation equilibrium of *N*-formyl peptide receptor (FPR) in live cells at physiological expression levels; FPR was found to form transient dimers with a lifetime of 91 ms, with 41% of the receptor population present as dimers [439]. Direct receptor labelling with SNAP-tags was also used in a single-molecule study of the β_1- and β_2-adrenergic receptor, again using spot intensity and photobleaching steps to infer oligomeric state [440]; this study showed longer homodimer lifetimes of ~4 s, which was speculated to be due to the lower temperature used in this study (20.5 °C) compared to the study of Kasai *et al.* (37 °C) and Hern *et al.* (23 °C), or to be a receptor subtype-specific effect [439]. Further, as seen in the earlier FRAP study [436], the β_2-adrenergic receptor showed a higher proportion of dimers relative to monomers than the β_1-adrenergic receptor, with 60% dimeric species at low densities (0.15-0.3 particles/μm^2) compared to 30%, respectively [440]. Higher-order oligomers were observed for both subtypes with the extent of oligomerisation increasing with particle density [440].

These studies provide compelling evidence for the possibility that GPCR oligomers are dynamic species. The observed interactions are not necessarily random as the stability of membrane protein quaternary structures varies from very stable interactions as seen for oligomeric ion-channels such as KcsA, to transient interactions as seen for receptor tyrosine kinases that are thought to exist in a monomer-dimer equilibrium at the membrane, showing that biologically significant protein-protein interactions can be transient [441]. It has been proposed that transient oligomerisation might facilitate the exchange of protomers during receptor activation, potentially contributing to signal amplification, providing scope for physiological or pharmacological regulation [371].

5.1.3 NTS1 dimerisation

Biophysical studies on the oligomerisation behaviour of NTS1 have thus far been limited. The receptor has been shown to heterodimerise with other neurotensin receptors (NTS2 and 3) in cell-based studies, with functional consequences for receptor trafficking and NT-mediated receptor activity [442–444]; NTS1 surface expression was shown to be downregulated by co-expression of NTS2, and NTS1 signalling through adenylyl cyclase and phospholipase C was suppressed [442–444]. NTS1 has also been shown to heterodimerise with dopamine receptors (D_2 and D_3), where NT-induced activity of NTS1 was observed to have antagonistic effect on dopamine release in *in vivo* studies in rats, and in cell-based studies [445–447].

Homodimerisation of NTS1 has thus far only been investigated *in vitro* and *in silico*. Co-immunoprecipitation studies on NTS1 showed that the receptor homodimerises in HeLa cells, but the functional implications were not studied [444]. A FRET study with purified NTS1 fused to fluorescent proteins (CFP/YFP) showed that the receptor can dimerise in lipid bilayers but not in detergent concentrations typically used in GPCR purifications (0.1 % DDM, w/v) [206]. Competition with untagged receptor verified the specificity of the interaction. FRET saturation experiments, in which the ratio of acceptor-to-donor-labelled NTS1 was varied, indicated that the receptor was predominantly present as a dimer rather than a higher-order oligomer [206]. Dimerisation was further shown to be independent of agonist binding, consistent with a constitutive dimer [206]. However, using SEC-MALS (size exclusion chromatography multi-angle light scattering) White *et al.* found that the receptor could dimerise at lower detergent concentrations (0.01% DDM, w/v) and in a receptor concentration dependent manner [321]. This suggests that NTS1 does not form a constitutive dimer, but rather is present in a monomer-dimer equilibrium, for which a K_d for dimerisation of ~2-20 nM was determined [321]. Dimeric NTS1 further showed positive cooperativity in ligand binding, and catalyzed G protein nucleotide exchange with lower affinity than monomeric receptor [321].

The only published data on the possible dimerisation interface of NTS1 homodimers comes from *in silico* studies by Casciari and co-workers [428]. Using an approach based on rigid-body docking of an homology model based on rhodopsin, the authors generated dimer models which were in agreement with the expected free energy of dimerisation (as calculated from the K_d obtained by White *et al.* [321]). The highest-ranking dimer model from this study showed a dimerisation interface comprising TM1, 2, and 4, stabilised by hydrophobic and electrostatic interactions (Figure 5.2) [428].

An unpublished TM competition study, in which the effect of single TM segments of NTS1
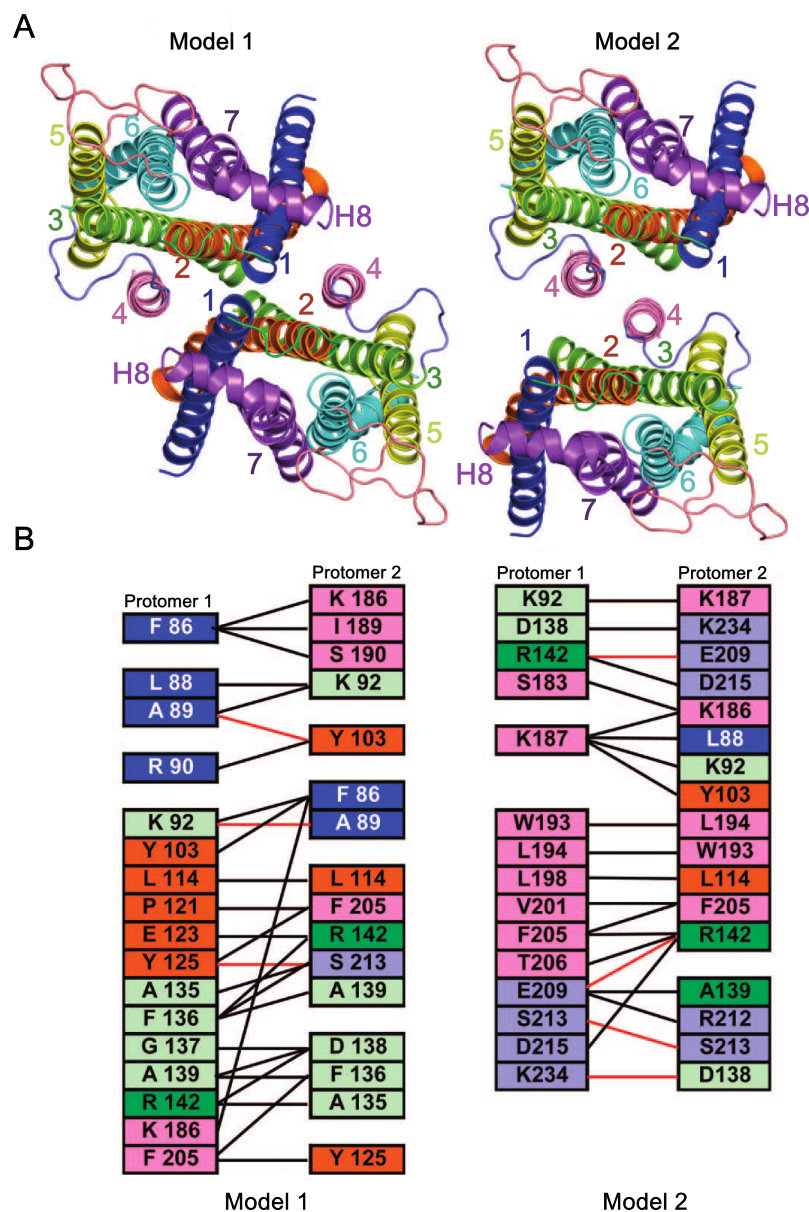
Figure 5.2: Model of NTS1 dimer from computational study. (A) Cartoon representing the two highest ranking models for the NTS1 dimerisation interface from a computational study based on rigid body docking, viewing the dimers from the intracellular side [428] **(B)** Residues that contribute to the dimer interface are indicated, coloured in accordance with their TM location as in **(A)**. Figure adapted from [428].

on the observed FRET efficiency between CFP/YFP-tagged NTS1 reconstituted into lipo-somes was studied, is presented in Figure 5.3 (Attrill, Verdurmen, Oates *et al.*, unpublished results). Disruption of the NTS1-CFP-NTS1-YFP oligomers would result in a reduction of the relative FRET efficiency (as demonstrated by a positive control in which unlabelled NTS1 was included). Most of the tested TM-peptides could not reduce the observed relative FRET efficiency to greater extent than a non-related TM peptide (walp, negative control),
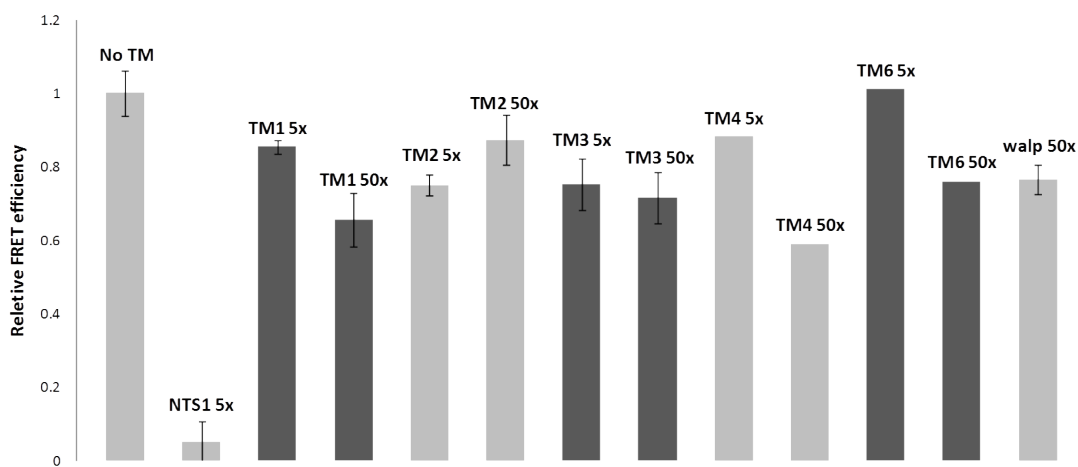
Figure 5.3: TM competition study of NTS1. Results form an TM competition study are presented here (Attrill, Verdurmen, Oates *et al.*, unpublished results); the effect of single TM segments of NTS1 on the observed FRET efficiency between CFP/YFP-tagged NTS1 reconstituted into liposomes was studied. FRET efficiency is normalized to the efficiency observed in the absence of single TM peptides. A positive control including a $5\times$ molar excess of unlabelled NTS1 showed strongly reduced FRET efficiency, due to disruption of the NTS1-CFP-NTS1-YFP oligomers. Peptides corresponding to individual TM segments of NTS1 were added at a $5\times$ and $50\times$ molar excess. A negative control testing the effect of an unrelated TM peptide (walp) was also included.

although the strongest effect was seen for a peptide corresponding to TM4 at high ($50\times$) molar excess (Figure 5.3). This suggests that NTS1 dimerisation does not critically depend on the intermolecular interactions of one specific TM domain (although the effect of TM5 was not studied here).

5.1.4 Aim

This chapter aims to elucidate the dimerisation interface of NTS1 dimers in membrane bilayers. To this end, spin-labelled or fluorescently labelled NTS1 is reconstituted into liposomes and interlabel distances are measured by FRET or DEER. By measuring apparent interprotomer FRET efficiencies for NTS1 labelled with fluorophores on different TMs, the relative proximity of each TM to its analogue in the other protomer within the NTS1 dimer can be determined, and thus its proximity to the dimer interface compared to the other TMs (Figure 5.4). DEER distance measurements are preformed to provide insight into the conformational heterogeneity of NTS1 dimers. This represents the first detailed study into GPCR dimer structure in a membrane bilayer exploiting the benefits of site-directed labelling with small probes and DEER. Furthermore, in collaboration with Mark Wallace (Department of Chemistry, University of Oxford) and Oliver Castell (previously Department of Chemistry, University of Oxford, now University of Cardiff), single-molecule FRET studies on NTS1

dimerisation were set up using fluorescently labelled NTS1 as used in the bulk FRET studies, reconstituted in a model bilayer system. These single-molecule experiments should provide additional information on the dynamics of NTS1 oligomerisation, and the oligomerisation state equilibrium which is not accessible by the ensemble techniques. Single-molecule FRET has the benefit over single-molecule studies using co-localisation and spot intensity (as discussed in section 5.1.2.3) that it can probe interactions on shorter distance ranges (3.5-14 nm), overcoming to some extent the limitations imposed by the diffraction limit, providing stronger evidence for direct protein-protein interactions.
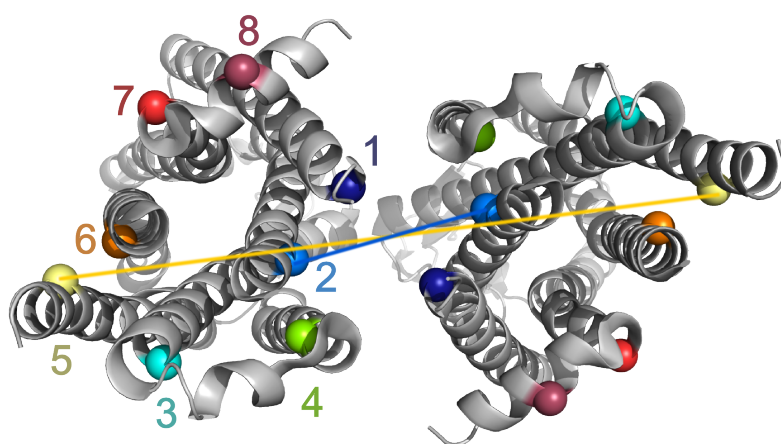
Figure 5.4: Label sites on NTS1. A cartoon of an NTS1 dimer (3ZEV crystal structure, dimer based on the proposed interface in [428]) is shown with numbered TM/H segments. Single cysteine mutants of NTS1 with cysteines at the IC side of each TM were labelled with fluorescent dyes or spin label for FRET and DEER studies, respectively: $A90C^{1.58}$ (TM1), $Y104C^{2.41}$ (TM2), $S(C)172C^{3.55}$ (TM3), $T186C^{4.42}$ (TM4), $A261C^{5.52}$ (TM5), $V307C^{6.34}$ (TM6), $L371^{7.55}$ (TM7), and $Q378C^{8.52}$ (H8) are highlighted in the structure. If a TM segment is present in the dimer interface, the interlabel distances will be shorter (*e.g.* blue line for TM2) than if a TM segment is at the distal side of the dimer (*e.g.* yellow line for TM5), thus (average) interlabel distances can be used to probe the dimerisation interface.

5.2 Materials and method

5.2.1 FRET

Cysteine mutants of NTS1 were fluorescently labelled with Alexa Fluor dyes as described in Appendix A.5.3. Eight single cysteine mutants were used for site-directed labelling, with cysteines introduced at the helix/loop interface on the intracellular side of NTS1: $A90C^{1.58}$ (TM1), $Y104C^{2.41}$ (TM2), $S(C)172C^{3.55}$ (TM3)[1], $T186C^{4.42}$ (TM4), $A261C^{5.52}$ (TM5), $V307C^{6.34}$ (TM6), $L371C^{7.55}$ (TM7), and $Q378C^{8.52}$ (H8) (Figure 5.4). Each mutant was labelled with Alexa Fluor 488 (A488), and Alexa Fluor 555 (A555), to serve as

---

[1]Native Cys, reintroduced into the cysteine-depleted background mutant where it is mutated into a Ser.

the donor and acceptor, respectively. Protein stock concentrations were determined through absorption measurements and bicinchoninic acid colorimetric assays against bovine serum albumin standards. Per sample 0.15-0.2 nmol of donor and/or acceptor (each) was used, and the final sample was resuspended in 110-200 μL of liposome buffer giving a maximal final concentration of ~1 μM. Samples were reconstituted in brain polar lipid (BPL, Avanti polar lipids) liposomes, using Bio-Beads (Bio-Rad) for detergent removal as described in Appendix A.5.4. Donor and acceptor were reconstituted together at a 1:1 molar ratio for FRET samples, as well as separately for donor-only, and acceptor-only controls. The receptor was reconstituted at high lipid-to-protein ratio to avoid crowding artefacts. The donor and acceptor only samples were reconstituted at an initial lipid-to-protein ratio of 12,000:1 (mol:mol), while 6,000:1 was used for the mixed samples as they contained twice the amount of protein, keeping total amount of lipid in each sample constant to maintain light scattering at the same level. Samples were prepared in triplicate (or more) where possible, for at least two individual sample preparations. Fluorescence emission spectra were recorded at room temperature on a Perkin-Elmer LS-50B fluorimeter (slit widths 4.5 nm for excitation and 5 nm for emission, to optimize the signal-to-noise ratio). For FRET samples (containing both donor and acceptor), and acceptor-only samples emission spectra with excitation at the donor (490 nm) and acceptor (555 nm) wavelength were recorded (over 495-600, and 560-600 nm, respectively). For donor-only samples only the emission spectrum with excitation at the donor wavelength was recorded. A background sample consisting of empty liposomes was also prepared and measured to correct for any background fluorescence and scattering effects from the sample spectra. The FRET data was processed as discussed in [448]. First, the background spectrum (empty liposomes) was subtracted from all spectra. Spectra were smoothed using Savitzky-Golay filtering (10 nm window, 2nd order polynomial) using OriginPro 8.5 to minimize noise artefacts in the determination of spectral maxima. Then, the FRET spectrum (mixed sample at donor excitation) was corrected for bleedthrough by subtracting the donor-only spectrum, scaled to the donor peak in the FRET spectrum (Figure 5.5A), and the uncorrected FRET ratio (A) was then calculated

$$A = \frac{F_{ex:D}^{em:A}}{F_{ex:A}^{em:A}} \tag{5.1}$$

where $F_{ex:D}^{em:A}$ is the fluorescence intensity of bleedthrough-corrected FRET spectrum at the acceptor emission maximum, and $F_{ex:A}^{em:A}$ the intensity of the FRET sample at the acceptor maximum upon acceptor excitation (Figure 5.5B). The crosstalk ratio was determined from the acceptor-only sample (ratio A_0),

$$A_0 = \frac{F_{ex:D}^{em:A}}{F_{ex:A}^{em:A}} \tag{5.2}$$
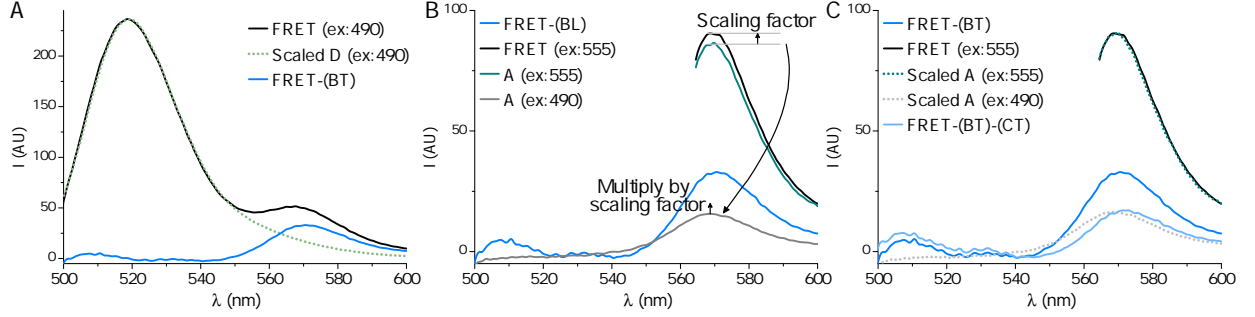
Figure 5.5: Processing of FRET data. (A) After correction for liposome scattering (not shown), FRET data is corrected for bleedthrough (BT), by subtracting the donor-only spectrum (D), scaled to the donor peak in the FRET spectrum (at excitation wavelength 490 nm). **(B)** Data is corrected for crosstalk (CT) using the ratio of the emission intensity (I) of the acceptor-only sample (A) excited at 490 nm and 555 nm, and this ratio is used to calculate the corrected FRET ratio as described in the text. **(C)** Subtraction of the scaled crosstalk contribution of the acceptor from the bleedthrough-corrected FRET spectrum, gives the effective FRET spectrum (FRET-(BT)-(CT)).

where $F_{ex:D}^{em:A}$ and $F_{ex:A}^{em:A}$ are the fluorescence intensity for the acceptor-only sample at the acceptor emission maximum upon excitation at the donor or acceptor wavelength, respectively (Figure 5.5B). The bleedthrough-corrected FRET ratio (FR) was calculated (Figure 5.5C)

$$FR = \frac{A}{A_0} \tag{5.3}$$

from which the apparent FRET efficiency (E_{app}) was calculated,

$$E_{app} = (FR - 1)\frac{\varepsilon_A^{490\,nm}}{\varepsilon_D^{490\,nm}} \tag{5.4}$$

correcting for the extinction coefficient ratio of the acceptor (ε_A) and the donor (ε_D) fluorophores at the donor excitation wavelength used, which in the case for Alexa Fluor 555 (5.5a) and 488 (5.5b), corresponds to 15.2% and 81.7% of the maximum extinction coefficients, respectively:

$$\varepsilon_A^{490\,nm} = 0.152 \times \varepsilon_{A,max}$$
$$= 0.152 \times 150,000\,M^{-1}cm^{-1} \tag{5.5a}$$
$$\varepsilon_D^{490\,nm} = 0.817 \times \varepsilon_{D,max}$$
$$= 0.817 \times 71,000\,M^{-1}cm^{-1}. \tag{5.5b}$$

The apparent FRET efficiency was further corrected for the donor-to-acceptor ratio (r_{DA}) in the FRET samples. The r_{DA} was determined from the fluorescence emission spectra, correcting for quenching of the donor emission due to FRET as described in [449]:

$$F_D = F_{ex:D}^{em:D} + F_{FRET,cor}\frac{\Phi_D}{\Phi_A} \tag{5.6}$$

where $F_{FRET,cor}$ is the FRET signal (so $F_{ex:D}^{em:A}$ for the mixed donor-acceptor sample) corrected for bleedthrough and crosstalk as described in Figure 5.5, and Φ_D and Φ_A the fluorescent quantum yield of the donor and acceptor fluorophores, respectively, and were taken to be 0.92 and 0.10, respectively, as specified by the manufacturer. As the fluorescence emission is proportional to the sample concentration, multiplied by the quantum yield and the extinction coefficient, the donor-to-acceptor ratio r_{DA} can be calculated using

$$r_{DA} = \frac{F_D}{F_A} \frac{\Phi_A \varepsilon_A}{\Phi_D \varepsilon_D} \tag{5.7}$$

where $F_A = F_{ex:A}^{em:A}$, *i.e.* the emission of acceptor in the mixed FRET sample, upon excitation at the acceptor maximum. The corrected FRET efficiency E_{cor} is calculated from E_{app} and r_{DA}:

$$E_{cor} = E_{app} \frac{(1 + r_{DA})}{r_{DA}} \tag{5.8}$$

as derived in [214], assuming random association of donor- and acceptor-labelled NTS1. This correction accounts for the dimerisation of like fluorophore-tagged receptors (*i.e.* NTS1-A488-NTS1-A488 and NTS1-A555-NTS1-A555 dimers), which leads to an underestimation of the FRET efficiency.

The corrected FRET efficiencies from multiple FRET samples were then averaged, and subjected to statistical analysis using R in RStudio software (RStudio, Inc.) and the BEST method [450], which is a Bayesian alternative to the two-sample *t*-test, to test the difference between the samples, and the influence of agonist.[2] More details on the Bayesian data analysis can be found in Appendix E.

5.2.2 DEER

Cysteine mutants of NTS1 were spin labelled with maleimide PROXYL as described in Appendix A.5.3. Spin-labelled receptor was reconstituted at a lipid-to-protein ratio of 1500:1 (mol:mol). DEER samples were reconstituted in POPC:POPE:cholesterol (15:15:10 molar ratio), which supports NTS1 ligand binding activity, and dimerisation to the same extent as BPL [40, 448]. A lower lipid-to-protein ratio than in the FRET samples was used to reduce the volume of the lipid pellet and thus maximize the concentration of the final sample as DEER is less sensitive than FRET (100s μM required at X-band), and the final sample was resuspended in 30 μL of liposome buffer. Spin-diluted samples were prepared to allow for short-distance determination by second moment analysis (see below): spin-labelled receptor was reconstituted together with unlabelled receptor at a 1:3 molar ratio, to reduce the amount of dimers with two labelled protomers compared to those with only one labelled

---

[2]R script for statistical analysis was set up with help from Stijn van Weezel (Department of Economics, Royal Holloway, University of London).

protomer (the dimers with two unlabelled protomers are EPR silent), thus giving an overall spectrum close to that of dimers without intradimeric dipolar interactions. DEER traces (3p and 4p) were recorded and stitched as described in Appendix A.8.2. Briefly, samples were loaded into 3 mm quartz tubes, flash-frozen in liquid nitrogen, and measured at X-band on an ELEXYS E580 (Bruker), at 50 K, using a 3 mm split-ring resonator (ER-4118X-MS3, Bruker). The samples were later transferred to 1.6 mm quartz tubes and measured at Q-band (~33.4 GHz) on an ELEXYS E580 equipped with a SuperQ-FT bridge (Bruker)[3], at 50 K, using a 2 mm split-ring resonator (EN-5107D2, Bruker).

The average relaxation time T_2 of the samples was estimated (as described in Appendix A.8.2) to be 780±60 ns (ranging between 660-1020 ns, data not shown). DEER experiments were performed using both 4-pulse and the 3-pulse DEER sequence (see 1.19). Resulting DEER traces were phase-corrected using DeerAnalysis 2013 [202] and then stitched together using MATLAB 2013 (MathWorks) by least-squares fitting as per the DEER-Stitch method described by Lovett *et al.* [197]. Distance distributions were derived from stitched data using DeerAnalysis 2013.

5.2.3 Second moment analysis

Second moment analysis was used to calculate short-range internitroxide distances (<2 nm) using field-swept X-band absorption spectra recorded for the DEER samples (see Appendix A.8.2). The spectral second moment ($\langle H^2 \rangle$) was calculated from the baseline-corrected absorption spectrum, as described in section 4.2.3, for a spectrum with interacting nitroxides (reconstitution of only spin-labelled NTS1), $\langle H^2 \rangle_D$, and for a spectrum corresponding to non-interacting nitroxides (reconstitution of spin-labelled NTS1 together with non-labelled NTS1 at a molar ratio 1:3 of to dilute the internitroxide interactions), $\langle H^2 \rangle_S$. The internitroxide distance (r in nm) is calculated using the relation

$$r = \frac{2.32}{(\langle \Delta H^2 \rangle \cdot 10^8)^{1/6}} \tag{5.9}$$

where

$$\langle \Delta H^2 \rangle = \langle H^2 \rangle_D - \langle H^2 \rangle_S \tag{5.10}$$

in T^2. Absorption spectra were collected at 50 K on a Bruker Elexys E580 and baseline corrected using OriginPro 8.5, after which the second moment and internitroxide distance was calculated using MATLAB 2013 (MathWorks).

---

[3]Courtesy of Mark Newton, University of Warwick.

5.2.4 Single-molecule FRET[4]

Single-molecule FRET experiments on NTS1 were conducted in collaboration with Oliver Castell (Department of Biochemistry, University of Oxford, now University of Cardiff)—see footnote 4 of this chapter for details. NTS1 Cys-mutant T186C (TM4) was labelled with Cy3 (donor) and Cy5 (acceptor) dyes (GE Healthcare) in the same manner as for the bulk FRET experiments. Donor- and acceptor-labelled receptor were then reconstituted together by Oliver Castell into droplet-interface bilayers (DIBs) to be imaged by total internal reflection fluorescence (TIRF) microscopy as described in [451] (Figure 5.6). DIBs were made with 1,2-diphytanoyl-*sn*-glycero-3-phosphocholine (DPhPC) in which NTS1 had been shown to be able to dimerise and bind ligand (personal communication Alan Goddard). Receptor was reconstituted at a protein density of ~2.4 molecules/μm^2. Fluorescence emission from the donor (NTS1-Cy3, 550-615 nm) and acceptor (NTS1-Cy5, 650-750 nm), were registered side by side by a CCD sensor. The two images were translated if required to spatially register the two images. Spots corresponding to donor (D) and acceptor (A) were tracked in time and then cross-correlated, correcting for background, bleedthrough and crosstalk. The intensities of the D and A were extracted from the corrected images, and used to calculate apparent FRET efficiencies for every detected track, and tracks were filtered to only include those with an acceptor signal significantly above background.

5.2.5 Lipid-to-protein ratio

Sucrose density gradients were used to determine the lipid-to-protein (L:P) ratio after reconstitution. A sucrose density gradient with concentrations steps of 5% from 35 to 5% sucrose (w/v) added to reconstitution buffer was prepared. The reconstituted sample was layered on top of the gradient, and the gradients were centrifuged overnight in a swing-out rotor (SW41, Beckman Coultier) at 28,500 rpm (~100,000×g). The sucrose gradient was then fractionated and the presence of reconstituted receptor, verified by SDS-PAGE analysis. The position of the proteoliposome band on the gradient was used to estimate the density and thus the L:P ratio of the samples using the equation derived by Barber [452]

$$\rho(T) = (B_1 + B_2 T + B_3 T^2) + (B_4 + B_5 T + B_6 T^2)Y + (B_7 + B_8 T + B_9 T^2)Y^2 \quad (5.11)$$

---

[4]For this work, I only produced the labelled NTS1 and was involved in the discussion on the design of the experiment. Reconstitution into the DIB was initially optimized by Alan Goddard (Department of Biochemistry, University of Oxford, now University of Lincoln) and Oliver Castell (Department of Chemistry, University of Oxford, now University of Cardiff) with NTS1 produced by Alan Goddard, using NTS1 Cys-mutants produced by me. Under supervision of Mark Wallace (Department of Chemistry, University of Oxford), Oliver Castell reconstituted the final labelled NTS1 samples (produced by me) into DIBs, performed single-molecule FRET experiments and analysed the data.
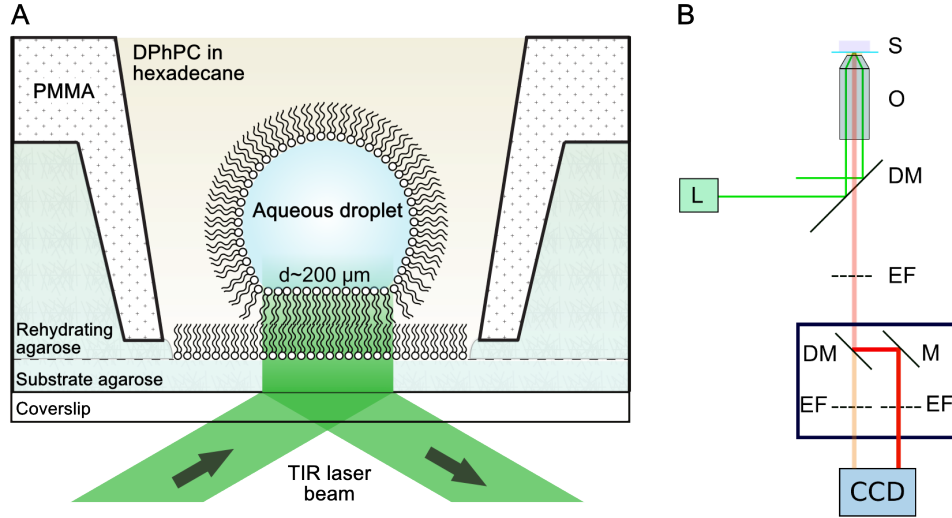
Figure 5.6: Set-up single-molecule FRET experiments. (A) Schematic of a droplet-interface bilayer (DIB); agarose is spin-coated on top of a coverslip on which a lipid monolayer (in hexadecane) is deposited. Addition of receptor in aqueous solution to the lipid-hexadecane mix results in the formation of a lipid monolayer around the aqueous droplet. The settled droplet fuses with the monolayer on the agarose, forming a lipid bilayer into which the receptor inserts. The size of the bilayer (and thus receptor density) can be controlled by mechanical manipulation of the droplet. More details are given in [451]. The receptor fluorescence is imaged by total-internal reflection (TIR) fluorescence microscopy. **(B)** Experimental set-up of the TIRF microscope. The laser beam (L) at the donor wavelength is focussed on the sample (S) through the objective (O), using a dichroic mirror (DM). The emitted fluorescence passes the DM and an emission filter (EF), after which it is split by a second DM, separating the emission from the donor (Cy3, 550-615 nm) and acceptor (Cy5, 650-750 nm), which are registered side by side by a CCD sensor. Images were adapted from figures provided by Oliver Castell.

where ρ is the density (kg/dm^3), T the temperature (°C), Y the fraction of sucrose in solution and B_{1-9} are constants ($B_1 = 1.00037$, $B_2 = 3.96805 \times 10^{-5}$, $B_3 = -5.85133 \times 10^{-6}$, $B_4 = 0.389824$, $B_5 = -1.05789 \times 10^{-3}$, $B_6 = 1.23928 \times 10^{-5}$, $B_7 = 0.1700976$, $B_8 = 4.75301 \times 10^{-4}$, $B_9 = -8.92397 \times 10^{-6}$). The partial specific volume ($\overline{v}$ in mL/g) which follows from that (as the reciprocal of the density) can be used to estimate the L:P ratio (w/w) by solving

$$\overline{v}_{proteoliposomes} = x\overline{v}_{lipid} + (1-x)\overline{v}_{protein} \qquad (5.12)$$

for x (fraction of lipid). The $\overline{v}_{proteoliposomes}$ is the partial specific volume of the sample determined from the sucrose gradient, $\overline{v}_{lipid}$ is the contribution of the lipid and can be determined by running a lipid-only sample on a sucrose gradient (~0.986 mL/g for BPL was determined in our laboratory), and $\overline{v}_{protein}$ is the contribution of the protein and can be calculated from its amino acid composition using the relation derived by Cohn and Edsall [453] modified for the effect of temperature [454]

$$\overline{v}_{protein,T} = \overline{v}_{25} + 4.25 \times 10^{-4}(T - 25) = \frac{\sum n_i M_i \overline{v}_i}{\sum n_i M_i} + 4.25 \times 10^{-4}(T - 25) \qquad (5.13)$$

where $\overline{v}_{protein,T}$ is the partial specific volume at temperature T, and $\overline{v}_{25}$ that at 25 °C, calculated from the number of moles (n_i) for each particular amino acid (i) with molecular weight M_i and partial specific volume $\overline{v}_i$. The fraction of lipid x in w/w can then be used to calculate a molar L:P ratio using the molecular weight of the lipid and protein.

5.3 Results and discussion

5.3.1 Lipid-to-protein ratio

Discontinuous (5-35%) sucrose-density gradients were run of liposome-reconstituted NTS1 to estimate the lipid-to-protein ratio as described in section 5.2.5. Samples were reconstituted at initial lipid-to-protein ratios of 1500:1 and 6000:1 (mol:mol) for the DEER and FRET samples, respectively. The density of the proteoliposomes was taken to be the same as the density of the sucrose solution with which the sample aligned on the gradient (with a resolution of 5% (w/v) as a step-gradient was used); the observed density for three separate gradients for the FRET samples, and four for the DEER samples was averaged. The FRET samples ran as a single band, while for the DEER samples a second band corresponding to empty liposomes was observed (as verified by SDS-PAGE analysis). The final lipid-to-

Table 5.2: Estimation of lipid-to-protein ratio from sucrose density gradients. The density ρ_{PL} of proteoliposome samples prepared for FRET and DEER experiments was estimated by running the samples on a sucrose density gradient, using equation 5.11, from which the partial specific volume $\overline{v}_{PL}$ of the proteoliposomes was calculated. The lipid-to-protein ratio (L:P, w/w) was calculated using equation 5.12, using $\overline{v}_{lipids}$ =0.986 mL/g [206] and $\overline{v}_{protein}$ =0.735 mL/g (equation 5.13). The weight ratio was converted to a molar ratio assuming an average molecular weight of 650 g/mol for BPL.

Initial L:P (mol:mol)	ρ_{PL} (kg/dm^3)	$\overline{v}_{PL}$ (mL/g)	Final L:P (w/w)	Final L:P (mol:mol)	Receptors/ vesicle	Density (10^3 copies/μm^2)
FRET						
6000:1	1.03±0.2	0.97±0.2	12±2	840±20	90±20	1.6±0.3
DEER						
1500:1	1.05±0.2	0.95±0.2	6±1	410±10	180±40	3.1±0.6

protein ratios were substantially lower than the initial ratios used in the reconstitution, with estimated ratios of 840±20 (6000:1 initial) and 410±10 (1500:1 initial) for the FRET and DEER sample, respectively (Table 5.2). The origin hereof is unclear, but it has been observed earlier for detergent-mediated reconstitution of NTS1 [206], and could in part be due to absorption of lipids by the hydrophobic Bio-Beads used in the reconstitution procedure [455], and due to not all liposomes incorporating protein (as a band corresponding to empty liposomes was seen on the sucrose gradients of NTS1 DEER samples).

The lipid-to-protein ratio can be used to estimate the receptor density in the proteoliposomes

as described in [206]. Assuming the vesicle radius to be 500 Å (as unilamellar liposomes were created by extrusion through 100 nm filters), and the internal radius as 460 Å (subtracting a bilayer thickness of 40 Å), the total surface area of the liposome bilayer is estimated at 5.8×10^6 Å^2 (including both surfaces of the bilayer). Using the total area (A_T), the number of receptor molecules (n_R) per vesicle can be estimated from

$$A_T = n_L A_L + 2 n_R A_R \tag{5.14a}$$

and with lipid-to-protein ratio $r = n_L/n_R$ it follows that

$$n_R = \frac{A_T}{r A_L + 2 A_R} \tag{5.14b}$$

where A_R and A_L are the surface area of the receptor and the lipid molecules, which were taken to be 71.1 Å^2 (area of a POPC molecule [456]) and 1350 Å^2 (protein size estimated from crystal structure ~30×45Å [295]), and n_L is the number of lipids. The factor 2 for A_R in equation 5.14a accounts for the contribution of NTS1 to the surface area on both sides of the membrane. Thus, the number of receptors per vesicle were estimated to be 90 ± 20 and 180 ± 40, corresponding to a receptor density of $1.6 \pm 0.3 \times 10^3$ and $3.1 \pm 0.6 \times 10^3$ molecules/μm^2 for the FRET and DEER samples, respectively (Table 5.2). This is similar to receptor densities reported in the literature for cell studies based on heterologous over-expression of the β$_2$-adrenergic receptor [457], but is similarly well above expected physiological densities of ~6000 copies/cell (~2 molecules/μm^2) [439]. However, the BRET efficiency due to β$_2$-adrenergic receptor dimerisation in the cell-based study was constant over the same density range as used here, suggesting that bystander BRET (or FRET) due to crowding is minimal under these conditions [457]. Indeed, a previous FRET study on NTS1 under similar conditions did not see dependence of the apparent FRET efficiency on the lipid-to-protein ratio [206].

5.3.2   Ensemble FRET

5.3.2.1   Interprotomer FRET efficiency for different TMs

Interprotomer resonance energy transfer efficiencies (E_{cor}) for each TM and H8 were calculated as described in section 5.2.1. As E_{cor} relates to the distance between fluorophores (see section 1.4.4.1) it can be used to gauge spatial proximity. A high E_{cor} for a certain TM (relative to the other TMs) would mean that it is relatively close to its counterpart on the other protomer within the dimer; for a symmetric dimer this translates to it being closer to the dimer interface, on average, than the other TMs (see Figure 5.4). All of the different label positions seem to give a significant amount of FRET (Table 5.3). The data suggests

that certain TMs (TM1, 4 and 7) have lower average FRET efficiencies than others (TM2, 5, 6 and H8), and the differences were found to be statistically significant (see Appendix E, and Table E.1). The lowest E_{cor} was found for TM7 (0.68±0.07, Table 5.3). Using the literature

Table 5.3: Bulk interprotomer FRET efficiency for different TMs. NTS1 Cys-mutants labelled with Alexa Fluor 488 (donor) or 555 (acceptor) on TM1-7 or H8, are reconstituted at equimolar ratio in brain polar lipid liposomes, with (+NT, 5 µM) or without agonist. Data is corrected for bleedthrough, crosstalk and donor-to-acceptor ratio for n replicate experiments, and the resulting mean corrected FRET efficiency E_{cor} and standard error of the mean are given. The difference between the mean apparent FRET efficiencies ($\Delta\mu$) for each mutant in the presence and absence of neurotensin agonist is also given. Bayesian data analysis methods are used to calculate the probability (Pr) that this difference is non-zero, and the probability of $\Delta\mu$ being larger or smaller than zero is given (see Appendix E).

TM/H (Residue)	E_{cor}	n	E_{cor} (+NT)	n	$\Delta\mu$	Pr ($\Delta\mu> 0$)	Pr ($\Delta\mu< 0$)
1 (A90C)	0.73 ±0.03	13	0.77 ±0.04	9	-0.038	0.73	0.27
2 (Y104C)	0.9 ±0.1	6	0.9 ±0.1	6	0.054	0.40	0.60
3 (S172C)	1.03 ±0.05	5	1.02 ±0.02	5	0.0056	0.49	0.51
4 (T186C)	0.77 ±0.03	13	0.78 ±0.04	10	-0.010	0.57	0.43
5 (A261C)	0.98 ±0.06	6	1.05 ±0.09	6	-0.073	0.70	0.30
6 (V307C)	0.99 ±0.04	11	0.82 ±0.04	7	0.17	0.99	0.01
7 (L371C)	0.68 ±0.07	6	0.7 ±0.1	4	-0.073	0.67	0.33
8 (Q378C)	0.89 ±0.02	8	0.89 ±0.02	8	0.0047	0.43	0.57

value of 70 Å for the Förster radius (R_0) [458], that E_{cor} corresponds to an average TM7-TM7 interprotomer distance of 62±6 Å. With the diameter of a monomer being ~40 Å, this longest found average distance is shorter than what would be expected for TMs on the distal side of the dimer (*i.e.* $2 \times 40 = 80$ Å). A potential explanation is that the flexible linkers of the dyes (~15 Å) could lead to the dyes pointing towards the dimer interface, which if stabilised in such a position by (non-)specific interactions with the rest of the protein, could lead to a smaller average distance than expected from the Cα-Cα distance. No evidence for this exists however, and computational studies to calculate fluorophore rotamer libraries suggest that fluorophores with long linkers sample a great number of conformations, and thus extreme positions (pointing maximally towards or away from the dimer interface) are likely to be averaged out [231]. These calculations are conducted in the absence of explicit water and electrostatic interaction, however, which could still stabilize certain label rotamers above others, thus this possibility cannot entirely be excluded [231]. However, as ensemble FRET experiments give an average FRET efficiency of all protein conformations, and organisations, another explanation for this observed relatively short average distance is that it arises due to multiple dimer interfaces. In that scenario no single TM is at the most distal

position at all times, thus leading to a lower maximal average interprotomer distance. This also agrees with the observation of significantly higher FRET efficiencies for several TMs, namely TM2, 3, 5 and 6 (Table 5.3), which is not consistent with a single dimer interface. A dimer interface comprising TM3 and 5 could explain the high efficiency seen for TM3, 5 and 6, but not TM2 which is on the opposite side of the monomer (see Figure 5.4). Again, the average distances corresponding to these FRET efficiencies (between ~30-50 Å) are longer than would be expected for TM segments directly at the interface, and shorter than those for TMs at the periphery of the dimer. Taken together these observations support the notion of multiple dimer interfaces. The FRET efficiency observed for TM3 is significantly higher than that observed for TM2 (Tables 5.3 and E.1), suggesting that, on average, TM3 is closer to, or present more often in the dimer interface than TM2. Other differences between TM2, 3, 5 and 6 were not found to be statistically significant, suggesting equal likelihood of finding the TMs at the dimer interface.

5.3.2.2   The effect of agonist on FRET efficiency

Bulk FRET experiments were also performed in the presence of agonist, NT. Table 5.3 summarises the statistical Bayesian analysis on the effect of agonist on E_{cor} for each of the TMs, giving the probability for $\Delta\mu$ (difference in average FRET efficiency) being larger or smaller than zero (see also Appendix E). Thus for sites where $\Pr(\Delta\mu < 0)$ and $\Pr(\Delta\mu > 0)$ differ greatly (*i.e.* where a non-zero difference has a probability of at least 0.68 (one standard deviation), 0.95 (two standard deviations), or 0.997 (three standard deviations)) NT can be said to have a reasonably likely effect on E_{cor}, and the sign of $\Delta\mu$ gives the direction of the effect, that is, whether E_{cor} is lower (-) or higher (+) in the absence of NT. The analysis shows that the largest (and most probable) effect of NT is observed in TM6, with a ~99% probability that NT decreases E_{cor}, followed by smaller effects on TM1 and 5, with a small probability of ~73% and ~70%, respectively, that NT decreases E_{cor}. For all other TMs smaller effects and/or effects with lower probabilities (<0.68) were observed, implying that NT has no statistically significant effect on these TMs (within the dimer). The pattern of E_{cor} is largely unchanged for the different TMs, with TM2, 3 and 5 still giving the highest E_{cor} (Table 5.3). The main difference is seen for TM6, with a large decrease in observed mean E_{cor} upon addition of NT, reducing its statistically significant distinguishability from the "low E_{cor}" samples (TM1, 4 and 7, see Table E.1). Considering the consensus that TM6 undergoes the largest conformational change upon activation by agonist binding (see section 4.1.1, Figure 4.1), these findings suggest that agonist does not affect the dimerisation interface itself, but does affect the receptor conformation in the dimer in a similar manner as it does in the monomer.

5.3.3 DEER

5.3.4 Data processing

Distance distributions for the interprotomer distances between the different TMs (1-7) and H8 were initially determined from X-band DEER experiments. DEER-Stitch was employed to maximize t_{max} and thus the longest mean distances that can be reliably observed. A shorter 4-pulse DEER trace ($t_{max} = 800-1200$ ns) was "stitched" to a longer 3-pulse DEER trace ($t_{max} = 1600-2000$ ns), through least-square analysis. Experiments for TM1-7 were repeated at Q-band, where the increased sensitivity of the experiments allowed for longer DEER traces to be recorded ($t_{max,4p} = 1400$ ns and $t_{max,3p} = 2400-3000$ ns).

Analysis of the DEER data obtained at both X- and Q-band was complicated due to uncertainty in the background correction. Reliable background fitting requires traces to be recorded beyond the decay of the dipolar modulation, or in other words, the longest detectable distance (equation 5.15), determined by the distance between the two π probe pulses, t_{max}, must exceed the longest intramolecular distance in the sample [198].

$$r_{max,\langle r \rangle} \approx 5 \sqrt[3]{\frac{t_{max}}{2\,\mu s}} \; nm \tag{5.15}$$

As the dimer sample is likely to contain long distances (up to 9 nm can be expected), this condition can not be met as it would mean that traces of at least 11.7 μs would need to be recorded—which is practicably impossible for membrane proteins under these conditions. The improved sensitivity of Q-band *vs.* X-band did allow for significantly longer traces to be recorded, but the low-power set-up used, limited the experiments to relatively long pulse lengths (60 ns pump and 30/60 ns probe pulses *vs.* 12-24 ns and 32 ns at X-band), negatively affecting the modulation depth, and further complicating background correction.

To aid background correction, an experimental background sample was prepared and measured for one of the mutants (S172C). Fitting a stretched exponential to this sample revealed a background dimensionality of 2.3. The same dimensionality could however not be effectively used for all other samples, suggesting that there was some variation between preparations. Unfortunately, the large amount of protein required to prepare these samples (interspin contributions need to be diluted by the addition of an excess of unlabelled protein) made it impracticable to prepare experimental background samples of sufficient quality for all mutants. Furthermore, while the dimensionality for that particular mutant could be determined, the starting point for background fitting still resulted in uncertainties; examination of the Pake pattern calculated from the resulting dipolar evolution function after background correction, as typically recommended when using DeerAnalysis software,

again relies on the aforementioned assumption that the longest detectable distance exceeds the longest intramolecular distance in the sample, and could thus not be reliably used here. Indeed, using the validation tool in DeerAnalysis to systematically vary the background starting time showed that there was great uncertainty, with the goodness of fit improving significantly when later background fit starting times were used than those chosen based on Pake pattern inspection. In fact, varying the dimensionality of the background between 2.3-3.0 also affected the goodness of fit, with better fits obtained at higher dimensionalities. However, as some information on the correct dimensionality (2.3 for S172C) was known from the experimental background, a value of 2.5 was chosen for the final analysis, to accommodate all samples without biasing individual fits. Validation tests varying the background starting point were subsequently run in DeerAnalysis, to assess the uncertainty in the distance distributions.

5.3.5 Distance distributions

X- and Q-band DEER data were analysed using model-free Tikhonov regularisation; fitted dipolar evolution functions after background correction, and corresponding distance distributions are shown in Figure 5.7. At Q-band, modulation depths were poor for all samples, due to limited excitation bandwidth as discussed in the previous section. Low modulation depths were found for some samples at X-band (TM1, 3 and 5 in particular), despite the use of shorter pulse lengths, and thus greater excitation bandwidth compared to the Q-band experiments. This could be due to (1) poor labelling efficiency, (2) low dimerisation rate, and/or (3) distances outside of the observable range (both longer and shorter). Poor labelling efficiency of the maleimide spin label is not expected, given that maleimide fluorophores used in the FRET experiments reacted very readily with the same mutants. The high FRET efficiencies found here (section 5.3.2) suggest substantial dimerisation of the receptor. Indeed, the dimerisation rate of NTS1 in liposomes has been previously determined to be 89.2 % by FRET saturation experiments at higher lipid-to-protein ratios than used in for the DEER samples (initial ratios of 6000:1 *vs.* 1500:1 used here) [206], and is therefore likely to be similar, if not higher, in these experiments. Thus, it seems that the poor modulation depth for these samples at X-band is most reasonably explained by the presence of short (<1.8 nm) or long (>6 nm) distances. Indeed, comparison of the field-swept echo absorption spectra recorded for the DEER samples with those for the same mutants spin-diluted with unlabelled receptor, clearly show signs of dipolar broadening for all mutants, indicative of short distances, which can be estimated by second moment analysis (see Figure 5.8). The distance distributions derived from the background corrected data are shown in Figure 5.7B and D for X- and Q-band measurements, respectively.
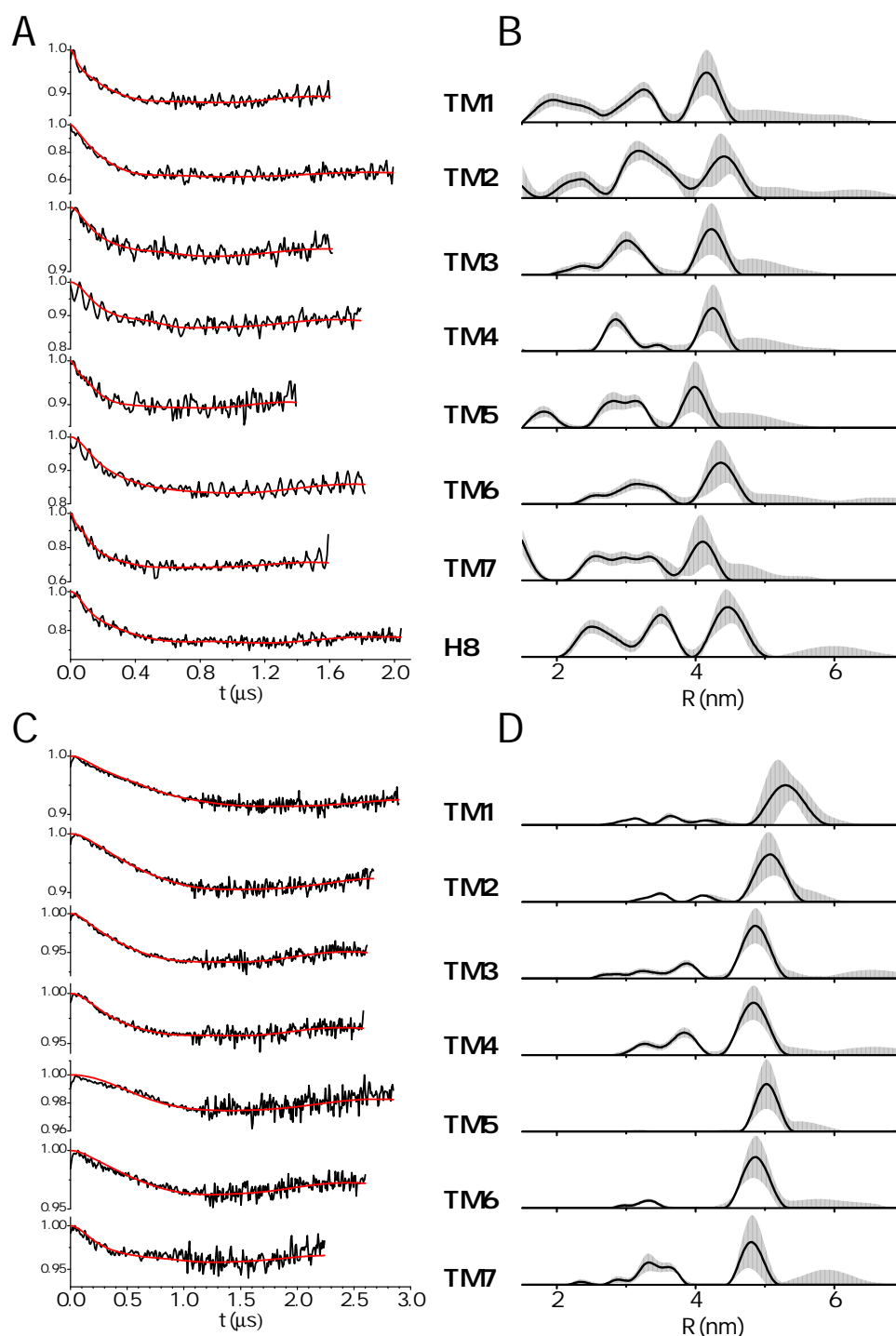
Figure 5.7: X- and Q-band DEER on NTS1 dimers. DEER traces were recorded at X-(**A, B**) and Q-band (**C, D**) for NTS1 samples spin-labelled at the intracellular side of TM1-7 and H8. The background-corrected dipolar evolution functions and fits thereof (red line) are shown (**A, C**). The corresponding distance distributions are shown (**B, D**). Grey shaded areas in the distance distributions correspond to the estimated error for the probability for each of the distances in the distribution, covering the mean value of the probability plus/minus two times its standard deviation (determined by varying the background correction starting time). The dipolar evolution functions before background correction are shown in Figure F.1.
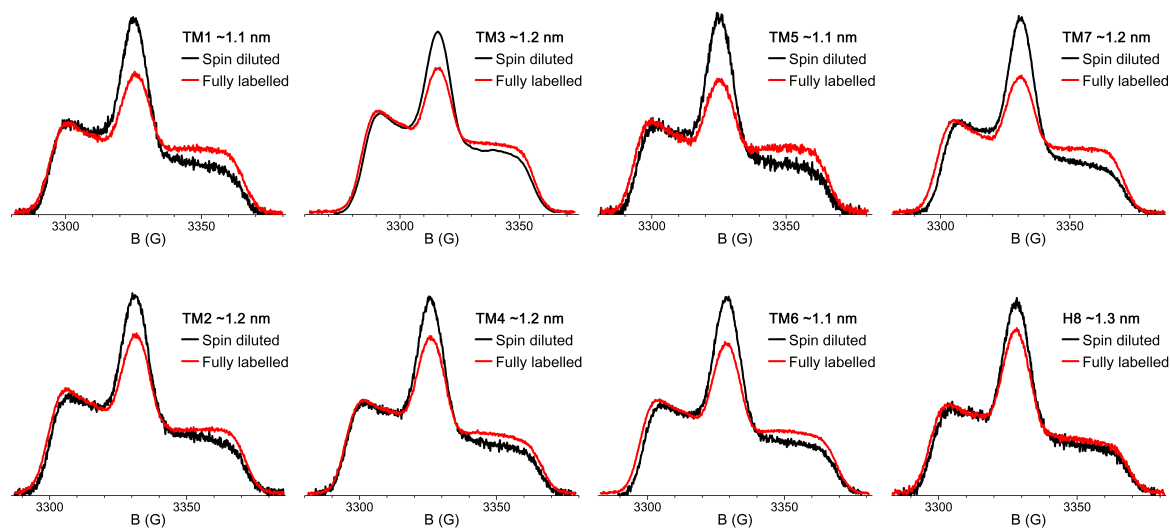
Figure 5.8: Second moment analysis of NTS1 dimer EPR absorption spectra. Field-swept echo absorption spectra were recorded for NTS1 spin-labelled at the intracellular side of TM1-7 and H8 (red line, same samples as used for DEER measurements). Dipolar broadening is observed compared to spin-labelled mutants reconstituted together with an excess (1:3) of unlabelled sample to dilute the spin-spin interaction (black line). Second moment analysis of the two spectra gives an estimate of short distances present in the samples.

The estimated error for the probability for each of the distances in the distribution is indicated by the grey shaded areas (covering the mean value of the probability plus/minus two times its standard deviation), determined by varying the background correction starting time (as discussed in section 5.3.4). The uncertainty in background correction is reflected in the large errors estimated for the found distances, especially for the longer distances (>4 nm) in the X-band dataset, which cannot be reliably determined from the short DEER traces. Wide distributions with multiple peaks are observed for all mutants, especially at X-band. The shorter distances observed at X-band are less prominent in the Q-band analysis. This is in part due to the poor modulation depth observed at Q-band, which hampered correct background subtraction, and led to less reliable fitting, especially of the early part of the DEER trace that contains information on the short distances (Figure 5.7C). Suppression of the small short-distance peaks in the Q-band distance distributions led to a very poor fit of the early part of the DEER time traces, suggesting that these contributions to the overall distribution are not artefactual. Further, the data collected at Q-band suggests the presence of longer distances than could be measured at X-band (Figure 5.7D), which is due to the fact that up to 1.4 µs longer DEER traces could be collected due to the improved sensitivity at Q-band.

Great uncertainty in correct background subtraction leading to uncertainty the determined distances, taken together with the fact that short distances which are present in the sample

(as evident from dipolar broadening of the absorption spectra, Figure 5.8) are not reflected in the distributions, and as well as the likelihood non-represented longer distances (maximum intradimer distance ~8 nm), means the respective contribution of the different peaks cannot reliable be interpreted. Nevertheless, it can be concluded from this data that broad distance distributions in Figures 5.7C and D, spanning over 3.0 nm cannot be solely due to spin label rotamers—as the tethers can only extend to 1.0 nm at most, giving a maximum spread of 2.0 nm—and must be due to multiple protein conformations. As this is seen for all mutants, this, taken together with the FRET data, provides strong evidence that NTS1 has multiple dimer interfaces.
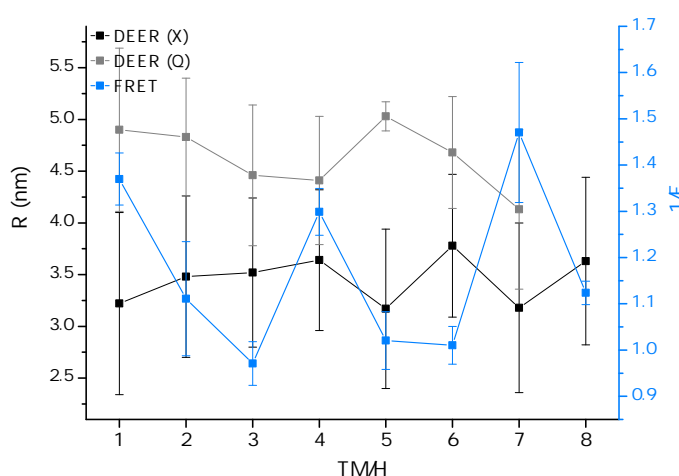
Figure 5.9: Average distances found by DEER compared to FRET efficiencies. Average distances calculated from the DEER distance distributions for data obtained at X-band (black) and Q-band (grey) are shown alongside the inverse of the FRET efficiencies for NTS1 mutants labelled on TM1-7 or H8. The inverse of the FRET efficiency is used as a proxy for the relative corresponding distances as a distance could not be determined reliably for all samples, as FRET efficiencies very close to 1 (or higher, due to uncertainties in the measurements) were found.

A comparison of the average distance obtained from the DEER experiments with the inverse of the FRET efficiencies determined for the different mutants is shown in Figure 5.9. The inverse of the FRET efficiency is a good proxy for relative corresponding distances and is used as a distance could not be determined reliably for all sites, as FRET efficiencies very close to 1 (or higher, due to uncertainties in the measurements) were found. Unfortunately, the pattern found in the FRET experiments is not mirrored in the DEER experiments (at either X- or Q-band). This is most likely due to the limited distance range that can be probed by DEER (~2-5 nm) compared to the expected distances (~0.5-8 nm), which is better suited to the distance range that can be probed by the fluorophore pair used in the FRET experiments (~3-14 nm). The DEER data is thus not as suited as the FRET data to make predictions about the (average) relative proximity of the different TM segments to

the dimer interface.

5.3.6 Single-molecule FRET

In collaboration with Oliver Castell (Department of Chemistry, University of Oxford, now University of Cardiff) and Mark Wallace (Department of Chemistry, University of Oxford, see footnote 4 of this chapter for details) single-molecule FRET experiments were conducted on fluorophore-labelled NTS1 reconstituted in artificial DPhPC bilayers, to gain insight into the dynamics of NTS1 dimerisation (see Figure 5.6 for experimental set-up). Experiments were performed at low receptor densities (~2.4 molecules/μm^2), to mimic native conditions. Preliminary results for NTS1 labelled at TM4 (T186C) are shown in Figure 5.10. TIRF microscopy was employed for imaging of the receptor in the bilayer; fluorescence emission from the donor (NTS1-Cy3, 550-615 nm) and acceptor (NTS1-Cy5, 650-750 nm), were registered side by side by a CCD sensor (Figure 5.10A). As the sample was excited at the donor-wavelength, fluorescence observed at the acceptor wavelength (after appropriate corrections) corresponded to a FRET signal, *i.e.* to a likely dimerisation event (with donor- and acceptor-labelled NTS1 within approximately one Förster radius, ~6.0 nm [459], of each other).

From the amount of donor spots *vs.* acceptor spots, it could be determined that only ~5% of the receptor population was dimeric at any given time.

Single-molecule tracking of cross-correlated donor and acceptor spots allowed following a FRET (*i.e.* dimerisation) event in real-time, with a resolution of 10 ms. Two such tracked FRET events are shown in Figure 5.10B and C; excisions of donor (D) and acceptor (A) ROIs are shown here, as well as their combined intensity (C). The figures show "filmstrips", of the fluorescence observed for each of the ROIs in time, with time-steps of 10 ms. The first event (Figure 5.10B) shows a long dimerisation event persisting for ~250 ms. The other event (Figure 5.10C) shows shorter protein association of 10 to a few 10s of milliseconds. Thus, these preliminary experiments show that, at low receptor densities, dimerisation appears to be transient with a dimer lifetime of ~10s-100s ms (exact lifetime has not yet been determined).

Interestingly, the acceptor fluorescence intensity (and thus FRET efficiency) appears to vary over time, and was not the same for all dimerisation events observed; Figure 5.10D shows a histogram compiling FRET efficiencies calculated for >3000 FRET events. A distribution of apparent FRET efficiencies can be observed with a peak centred around ~0.3, and a second peak at 1, consistent with multiple dimer interfaces. The peak at 1 corresponds to the maximum FRET efficiency that would be observed for interfluorophore distances shorter than ~0.5×R_0, *i.e.* ~3 nm.
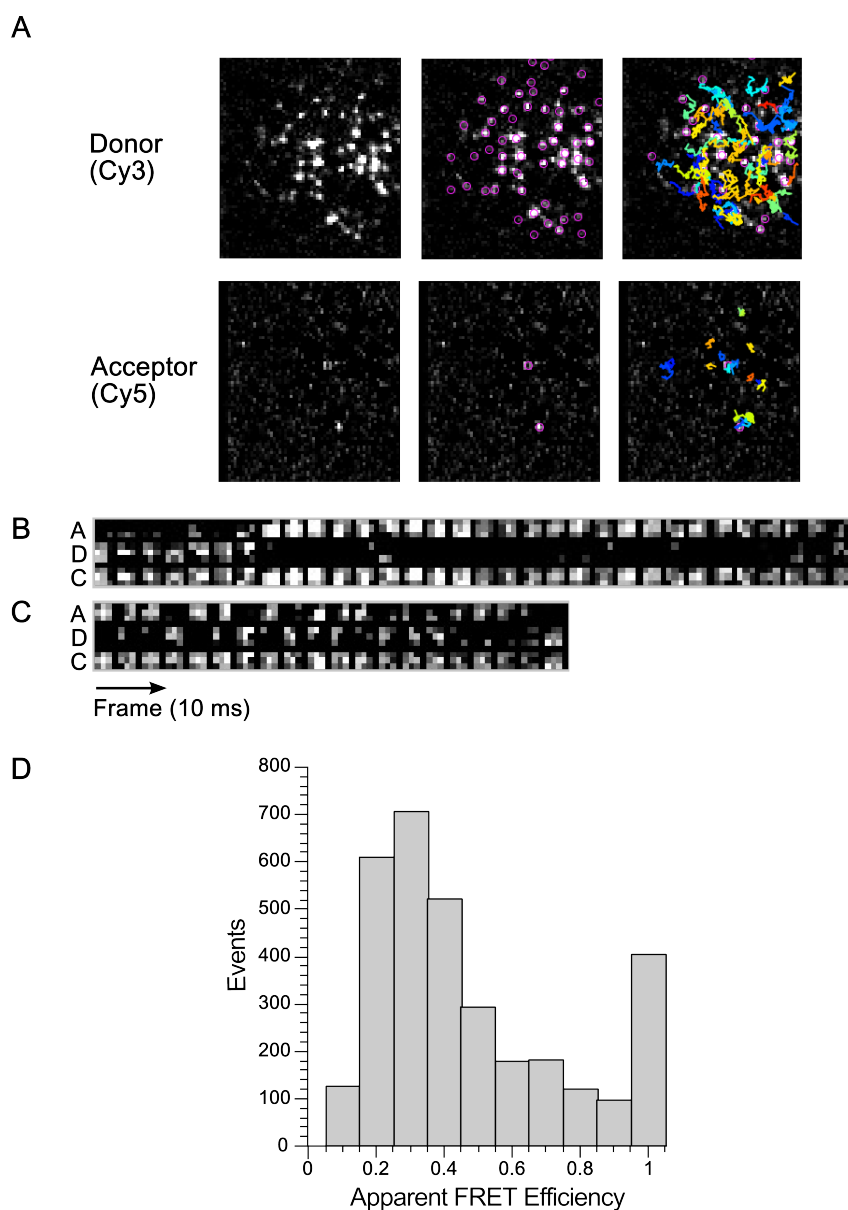
Figure 5.10: Single-molecule FRET on NTS1 dimerisation. Preliminary results on NTS1 dimerisation studied by single-molecule FRET are shown here for NTS1 labelled at T186C (TM4) with Cy3 (donor) and Cy5 (acceptor). Experiments and data analysis were performed by Oliver Castell (University of Oxford, now University of Cardiff). **(A)** Fluorescence from donor-labelled NTS1 and acceptor-labelled NTS1 are measured simultaneously (left panel). Single particles are detected (middle panel), and tracked in time (right panel). Trajectory linking of donor and acceptor tracks enables calculation of FRET efficiency (after appropriate corrections). **(B,C)** Excisions of donor (D) and acceptor (A) ROIs for two dimerisation events are shown here, as well as their combined intensity (C). The "filmstrips" show the fluorescence observed for each of the ROIs in time, with time-steps of 10 ms. **(D)** Histogram compiling FRET efficiency calculated for >3000 FRET events.

5.4   Conclusions

In agreement with recent data obtained for other GPCRs [204], the combined ensemble FRET, EPR, and single-molecule FRET data presented in this chapter supports the notion of a dynamic NTS1 dimer, with possibly some preferred dimer interfaces. Relatively high ensemble FRET efficiencies were found for TM 2, 3, 5 and 6, compared to the other TM helices, suggesting that they are closer to the dimerisation interface than the other TMs (under the assumption that NTS1 forms a symmetric homodimer, suggested from dimeric GPCR crystal structures [292, 406–408]). This result cannot be explained by a single oligomerisation interface, as TM2 faces to the opposite side of the protein compared to TM3, 5 and 6, suggesting the presence of multiple quaternary arrangements (see Figure 5.11). The notion of multiple oligomerisation interfaces is also in agreement with the earlier TM competition study on NTS1, where no single TM was able to disrupt dimerisation (see Figure 5.3). Thus,
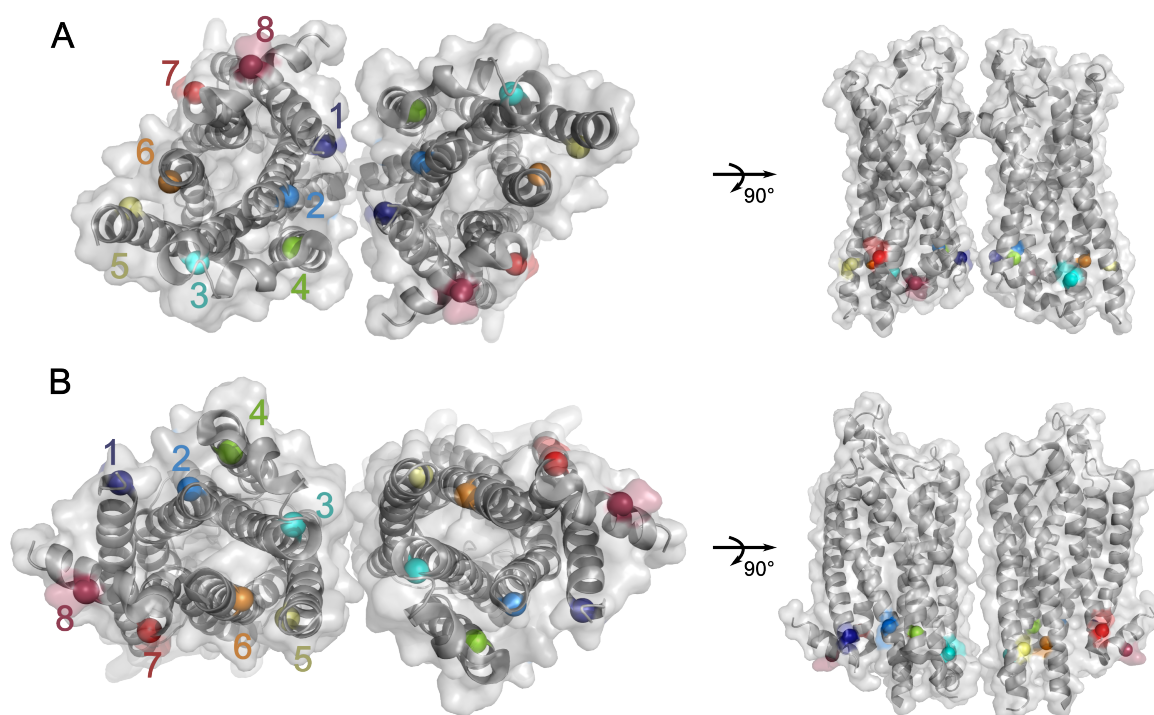
Figure 5.11: Proposed oligomerisation interfaces. Relatively high ensemble FRET efficiencies were found for TM 2, 3, 5 and 6, compared to the other TM helices, suggesting that they are closer to the dimerisation interface than the other TMs, and that NTS1 has multiple oligomerisation interfaces, *e.g.* comprising **(A)** TM2 or **(B)** TM3-5-6. Cartoon representation of possible interfaces are shown here, but these will need to be verified by molecular modelling, or protein docking approaches.

interfaces comprising TM2, 3, 5 and/or 6 are predicted from the ensemble FRET data. An interface comprising TM2 will however also lead to proximity of TM1 and 4 to the interface

(Figure 5.11A), despite relatively low FRET efficiencies being observed for NTS1 labelled at the latter TMs (Table 5.3). The average FRET efficiency for TM2 is (statistically significantly) lower than TM3 (Table E.1). It is thus possible that a TM1-2-4 interface (as previously proposed from computational modelling [428]) is also present, but that a TM3-5-6 interface is preferred. It can however not be excluded that the relatively high FRET efficiency seen for TM2 is due to flexibility in the fluorophore linker, while this is less likely for TM3, 5, and 6 as here all three neighbouring TMs show elevated FRET efficiencies. Investigation of the primary sequence of the different NTS1 TM segments shows that TM3 and 6 contain a relatively large number of residues/motifs implicated in TM-TM interactions compared to the other TMs (see Figure 5.12): (1) residues capable of acting both as an H-bond donor and acceptor, (2) Cys residues which can form disulfide bonds, and/or (3) GxxxG or GxxxxxxG-like motifs (where G can also be A, or S), which promote close interhelical packing, thus promoting interhelical van der Waals interactions [460]. Likewise,
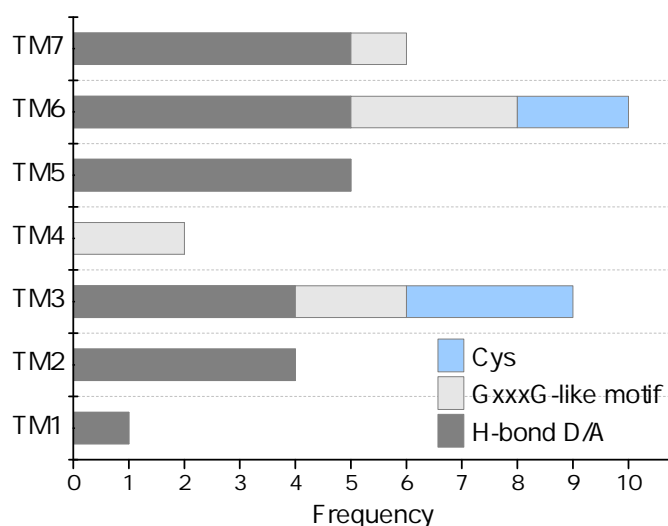
Figure 5.12: Sequence analysis of TM segments for oligomerisation propensity. The primary sequence of the different NTS1 TM segments was investigated to determine the frequency of (1, dark grey) residues capable of acting as an H-bond donor and acceptor (*i.e.* N, E, D, Q or H), (2, light grey) GxxxG or GxxxxxxG-like motifs (where G can also be A, or S), and (3) Cys residues, which can all promote TM-TM interactions, either by direct interactions (1 and 3, blue), or by promoting close interhelical packing, thus promoting interhelical van der Waals interactions (2).

TM2 and 5 contain a relatively high amount of residues capable of forming interhelical H-bonds, compared to TM1 and 4. However, TM7 also contains many H-bond donor/acceptor residues, while it showed the lowest ensemble FRET efficiency (Table 5.3). Thus more detailed modelling of dimerisation interfaces will be required to elucidate the molecular origin of the proposed TM interfaces, as has been done for the proposed interfaces of the

β-adrenergic receptors [461].

The preliminary single-molecule FRET data presented here represents the first single-molecule FRET study into GPCRs dimerisation. Previous single molecule studies have relied on co-localisation and step-photobleaching techniques [438–440], which are less reliable in determining *bona fide* protein-protein interactions compared to FRET, which requires the receptors to be within at least 1.4 nm of each other, thus providing >100-fold improved spatial resolution compared to the other diffraction-limited techniques.

The data presented here suggests that NTS1 dimerisation is transient with a dimer lifetime of 10s-100s ms. This is agreement with recent studies on other class A GPCRs, which have found transient dimers with lifetimes ranging from ~100 ms to ~5 s [438–440]. The dissociation constant of dimerisation has previously been estimated for NTS1 in detergent to be ~2-20 nM [321]. From thermodynamics, it follows that the half-time of a complex is related to its K_d as $t_{1/2} = 6.93 \times 10^7 / K_d$ [404]; a K_d of 2-20 nM, thus corresponds to a lifetime in the order of seconds (35-350 s). Although this is longer than observed in the study presented here, which might reflect different experimental conditions (*e.g.* detergent-solubilised *vs.* bilayer-reconstituted receptor), this also supports the finding that NTS1 dimers are transient.

Furthermore, a wide distribution of apparent FRET efficiencies was found for NTS1 labelled on TM4, with two apparent peaks; a main peak centred around 0.3 and a smaller peak at 1 (Figure 5.10D), corresponding to a longer and a shorter distance, respectively. This finding suggests the presence of multiple dimer interfaces. In agreement with the ensemble FRET data, the fact that the main peak for this mutant was seen at lower apparent FRET efficiencies, suggests that TM4 is not the preferred dimerisation interface, although this will need to be verified by conducting single-molecule experiments with NTS1 labelled at a different TM, *e.g.* TM6. Interestingly, only ~5% of the receptor appeared to be dimeric at any given time, which is a smaller oligomeric population than observed for other GPCRs in single-molecule studies (with oligomeric species representing ~30-60% of the receptor population [438–440]), at similar receptor densities (~2.4 *vs.* ~0.5-2 copies/μm^2), which are similar to receptor densities as found in the cell [439]. This suggests that NTS1 dimers might be less stable than dimers of other GPCRs. However, although NTS1 was seen to dimerise in DPhPC (Alan Goddard, personal communication), it cannot be excluded that the low dimerisation rate seen in the single-molecule FRET is in part due to the different lipid composition used in this study compared to the more native (BPL, or POPC/POPE/cholesterol) liposomes used in the FRET and DEER studies. DPhPC was used as preliminary trials with BPL did not lead to the formation of stable bilayers in the droplet-bilayer-interface system, and future

work will aim to produce bilayers of more native lipid-composition. Nevertheless, the observation that dimers may be transient, does not exclude their physiological relevance, as other proteins, such as receptor tyrosine kinases have been observed to exist in a monomer-dimer equilibrium, with dimerisation required for their activity [462].

The observation of multiple dimerisation interfaces in the data presented in this chapter, suggests the possibility of higher-order oligomers, specifically dimers of dimers. Although predominantly dimeric species were observed in bulk FRET saturation experiments [206], evidence for higher-order oligomers of NTS1 exists from CW-EPR studies on NTS1-lipid interactions (Bolivar Gonzalez *et al.*, unpublished results, reproduced in Figure 5.13). As
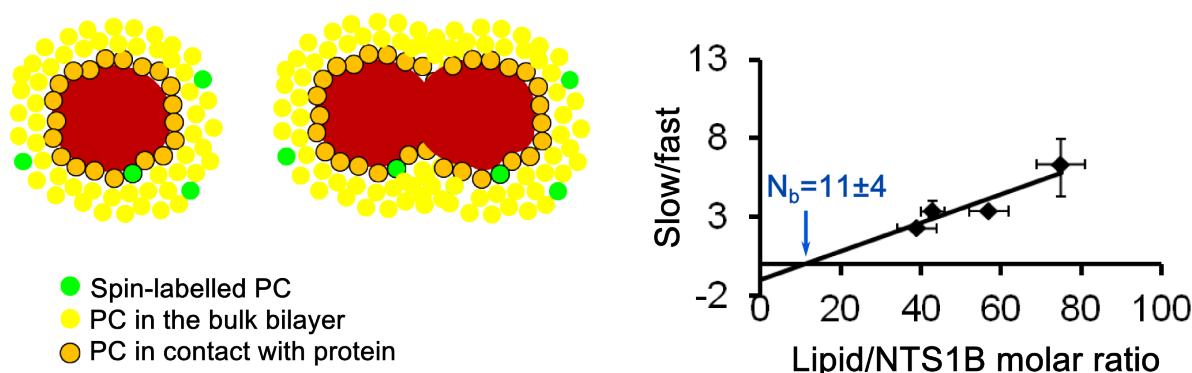
Figure 5.13: Number of lipids solvating NTS1B. The immobilisation of spin-labelled DOPC lipids (due to contact with the protein) in an unlabelled DOPC background as calculated from the amount of slow-motion component compared to fast-motion component in the EPR spectrum (slow/fast) is plotted against lipid-to-protein ratio. The results reveal that at low lipid-to-protein ratios (<80:1 molar ratio) NTS1B is solvated by 11±4 PC lipids (from the intercept, N_b, of the extrapolated data with the x-axis), and that this ratio is constant over the studied lipid-to-protein ratios (40-80 to 1). Experiments were performed by Juan Bolivar Gonzalez, unpublished results.

shown in Figure 5.13, experiments in which NTS1 was reconstituted at different lipid-to-protein ratios in a DOPC bilayer in the presence of 1%-mol of spin-labelled DOPC, revealed that, under the very high protein densities used (with molar lipid-to-protein ratios <100:1), NTS1 has an annular lipid ring of 11±4 lipids per protomer. This result is consistent with NTS1 forming higher-order oligomers, as GPCR monomers and dimers are estimated to have an annular lipid ring of ~23 and ~19 lipid molecules, respectively [45]. The fact that higher-order oligomers were not consistent with bulk FRET saturation experiments at lower receptor densities (~500-1000:1, molar lipid-to-protein ratio) [206], suggests NTS1 can form higher-order oligomers in a concentration-dependent manner, with higher-order oligomers (potentially dimers of dimers) being the predominant species at very high protein densities, dimers at intermediate protein densities (~1-3×10³ copies/μm²) [206], and monomers at the low protein densities used in the single-molecule experiments and observed in cells (~1-3 copies/μm²). Indeed, the law of mass action would predict that for transient dimers the

monomer-dimer equilibrium is biased towards dimers at higher receptor densities.

Agonist did not appear to have a pronounced effect on the overall ensemble FRET efficiency (Table 5.3). Only TM6 was significantly affected, in agreement with previous observations for other GPCRs that TM6 undergoes the largest conformational change upon receptor activation [99]. These results suggest that the overall dimer morphology is retained upon agonist stimulation, and that agonist induces similar conformational changes in the dimer as observed in the monomer, and by extension that the dimer might be signalling-competent. Indeed, NTS1 dimers have been shown to couple to G protein in detergent [321]. Although the physiological significance of NTS1 homodimerisation is as yet unknown, as NTS1 dimerisation has not yet been studied *in situ*, dimers were shown to couple less efficiently to G protein in detergent [321]. It is tempting to speculate that the apparent concentration dependency of dimerisation could be a way of regulating receptor signalling at varying expression levels, in a negative feedback mechanism, where NT-induced increased expression of NTS1 [463], leads to increased dimerisation at high receptor concentration and concomitant down-regulation of signalling. However, such a mechanism would need to be verified by *in vivo* studies.

6 | NTS1 signalling studied by microscale thermophoresis

6.1 Introduction

6.1.1 GPCR-G protein interaction

Upon ligand binding on the extracellular side of the membrane, GPCRs undergo conformational changes which lead to exchange of GDP for GTP in the α subunit of heterotrimeric G proteins on the intracellular side, and activation of downstream signalling pathways (see Figure 1.7). The specific cell response depends on the G protein subtype, and specific GPCRs can couple through one or more G protein subtypes. Different families of G proteins are associated with different pathways. Cloning studies have identified 35 human G protein genes, 16 encoding Gα, 5 Gβ and 14 Gγ subunits [464, 465]. The trimer is typically classified by the α subunit, with four families identified to date: G_s, G_i, G_q, and G_{12}. Typically signalling through Gα_s or Gα_i increases or decreases cAMP levels through stimulation or inhibition of adenylyl cyclase, respectively. Gα_q activates phospholipase C (PLC) leading to increased levels of diacylglycerol and IP$_3$ and raised calcium levels. The Gα_{12} members signal through the activation of GTP-binding proteins (*e.g.* of the Rho family), and are involved in communication between G protein-linked signalling pathways.

The Gα subunit is ~40-45 kDa in size and consists of two domains: a GTPase domain and an α-helical domain, with three switch regions that change conformation from the GDP- to the GTP-bound form. The C-terminal α-helix (α5) has been shown to convey specificity, and to bind to a crevice formed in the activated receptor by outward movement of TM5 and 6, where the G protein C-terminus forms polar and non-polar interactions with the TM core (TM3, 5 and 6) and IC2-3 [99, 104, 326, 466, 467]. Crystallography confirmed earlier EPR observations, that this leads to a large conformational change of the helical domain relative to the GTPase domain (Figure 6.1) [104, 468]. The smaller Gβ and Gγ subunits (~35 and 8-10 kDa, respectively) have also been shown to activate a wide variety of effectors, such as ion channels, lipid kinases and phospholipases. Most combinations of G$\beta\gamma$ can form functional heterodimers, and while the role of specific combinations is still not well understood,
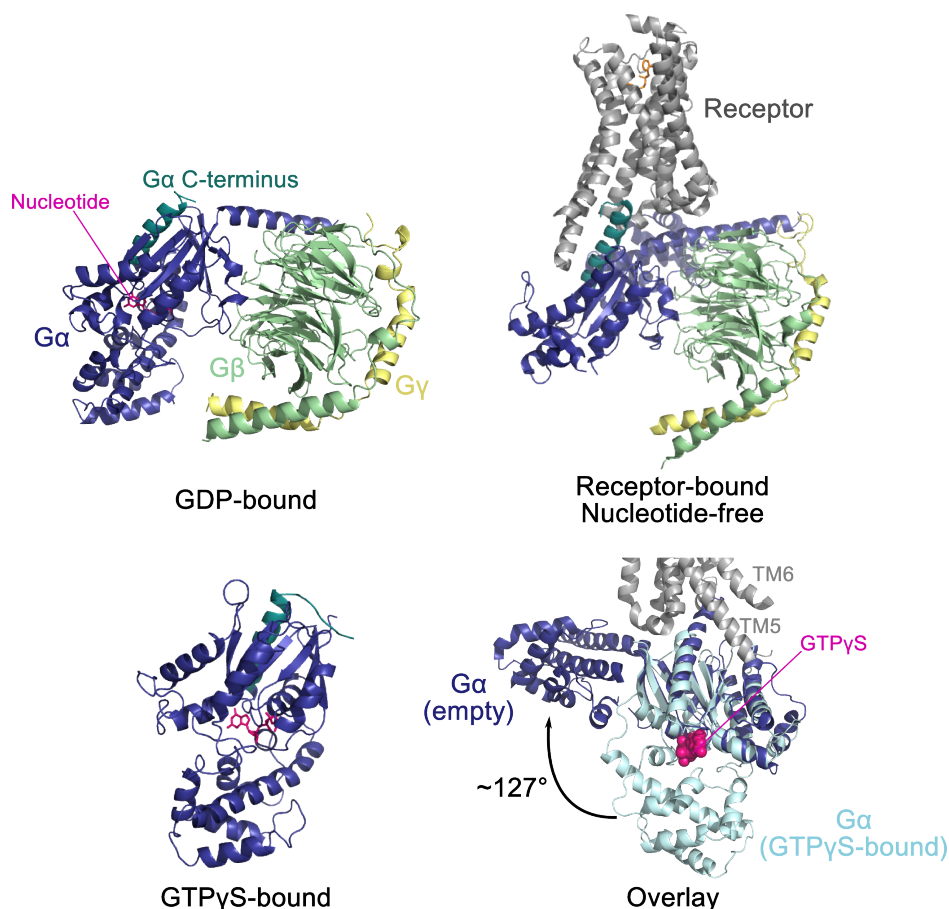
Figure 6.1: Conformational changes in the Gα subunit. Crystal structures solved for G proteins in different states illustrate the conformational changes the protein undergoes upon activation, with the α subunit shown in dark blue (with its C-terminus that interacts with the receptor highlighted in teal), the β subunit in green, the γ subunit in yellow, the receptor in grey (with its ligand in orange), and the G protein-bound nucleotide in pink. Structures are shown for a G protein heterotrimer bound to GDP (PDB ID 1GOT, $G\alpha_{t/i}\beta_1\gamma_1$); a nucleotide-free heterotrimer bound to receptor (PDB ID 3SN6, $G\alpha_s\beta_1\gamma_2$ bound to β_2-adrenergic receptor, with T4-lysozyme and stabilising nanobody not shown); and $G\alpha_t$ bound to a non-hydrolysable analogue of GTP, GTPγS (PDB ID 1TND). An overlay of the GTP bound (light blue) form and the nucleotide-free form bound to receptor (dark blue) shows the large displacement of the helical Gα domain relative to the GTPase Gα domain (~127° rotation about the junction between the domains).

it has been suggested that they convey functional selectivity (reviewed in [469]).

Ligand-GPCR-G protein interactions have been postulated to follow a cubic ternary complex model (CTC) (Figure 6.2) [470]. This model assumes that receptors have two distinct binding sites, one for ligands and one for G proteins; that receptors exists in two states with respect to their ability to activate G proteins, active (R*) and inactive (R); that the interactions between ligand, G protein and receptors are governed by the law of mass action; and that all possible interactions between ligands, G proteins, and receptor states are potentially significant and represented. Thus, in this model of G protein-GPCR interaction,

GPCRs can be in an active or inactive state, and can bind ligand and/or G proteins in both states; in addition, pre-coupled, inactive or non-ligand-bound GPCR-G protein complexes are possible, as well as basal receptor activity in the absence of ligand. Furthermore, the model describes how the apparent binding affinities of G protein to the receptor can be modulated by the binding of ligand, and vice versa.
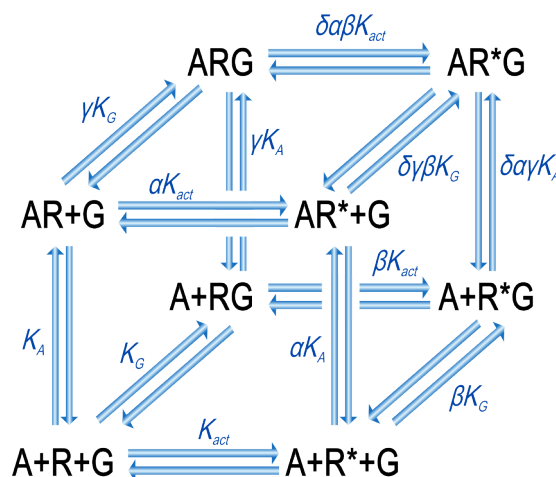
Figure 6.2: Cubic ternary complex model of ligand-GPCR-G protein interaction. Schematic of the CTC model with equilibrium association constants as defined in [470], where R and R* represent the inactive and active state of the receptor, G the G protein, and A the ligand. Factors α, β, γ, and δ describe how agonist binding affects the activation of the receptor, how G protein binding affects receptor activation, how agonist binding affects G protein coupling to the receptor, and how G protein binding affects ligand binding, respectively. If these factors are >1 then the one interaction is facilitated by the other.

6.1.2 Ligand binding and G protein coupling in NTS1

NTS1 has been shown to couple through three G protein subtypes: G_s, G_i and G_q (reviewed in [320]). Mutagenesis studies have suggested that different regions of the receptor are required for binding to the different G proteins; deletions in IC3 (residues 270-296) negatively affected NT-induced PLC activation, but not cAMP production [340], while deletions in the first half of the C-terminus (residues 372-401) had the opposite effect [368, 471]. These results suggest that interactions with IC3 are crucial for G_q activation, while G_s and G_i couple to the first half of the C-terminus.

Besides its natural ligand neurotensin, NTS1 also binds the native peptide neuromedin N, which is a six amino acid NT-like peptide (KIPYIL), originating from the same 170 amino acid precursor as NT. It binds the receptor with similar low nanomolar affinity, but has a reduced signalling potency [471]. A variety of synthetic peptidic agonists, analogues of the C-terminal NT hexapeptide NT_{8-13} which can cross the blood-brain barrier, have also been

produced [471–473]. These analogues typically bind with similar affinities and lead to generation of the same second messengers as NT. More recently, non-peptidic (partial) agonists and have been documented, although these show much lower (typically micromolar) affinity for the receptor [474, 475].
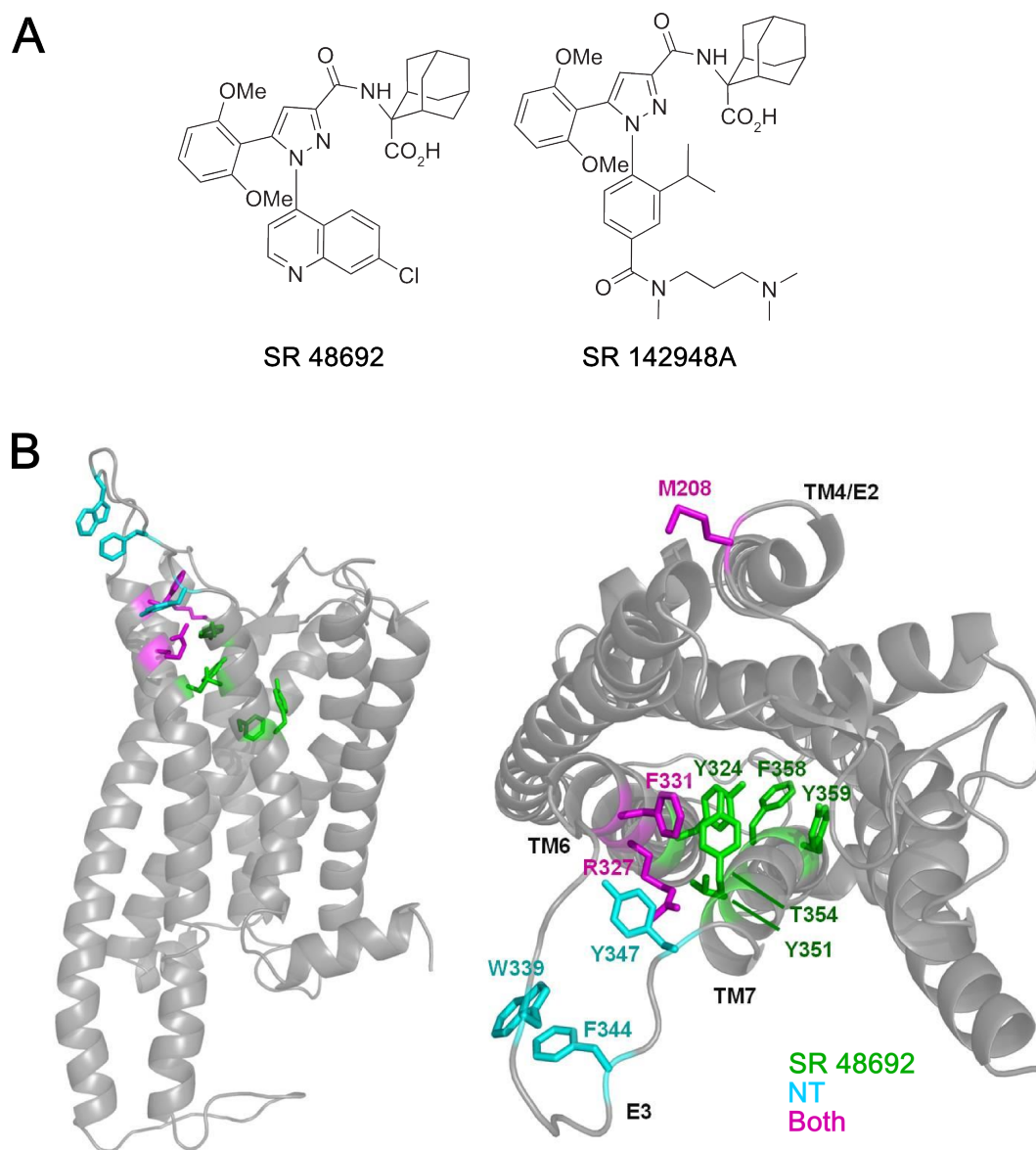
Figure 6.3: Structure of NTS1 antagonists and the NTS1 ligand binding site. (A) Chemical structure of two NTS1 antagonists is shown, SR48692 and SR142948A, both developed by Sanofi-Recherche. **(B)** Homology model of NTS1 (courtesy of S. Tapaneeyakorn) based on rhodopsin for the transmembrane regions and the β-adrenergic receptors for the loop regions viewed from the side (left) and top (right). Residues involved in binding of neurotensin (W339, F344 and Y347, cyan), inverse agonist SR48692 (Y324, Y351, T354, F358 and Y359, green) or both (M208, F331 and R327, magenta), as determined from mutagenesis studies (reviewed in [476]), are highlighted (reproduced from [166]).

Two synthetic non-peptidic antagonists developed by Sanofi-Recherche have also been described in the literature: SR48692 and SR142948A (Figure 6.3A) [477, 478]. Both show low nanomolar affinity for the receptor, and compete with NT binding [472, 479, 480]. Mutagenesis studies have been used to map out the binding site of NT and SR48692 and these studies have shown that the binding sites indeed partially overlap with each other, with both ligands binding between TM6 and 7 (Figure 6.3B, reviewed in [476]). SR48692 shows a markedly higher affinity for NTS1 over NTS2 (IC_{50} of 5.6 and 300 nM, respectively [477]), while SR142948A shows similar K_d for both receptors (3.4 and 4.8 nM, respectively [480]). SR142948A was shown to have a broader spectrum of antagonist activity in mice compared to SR48692, but this was ascribed to be potentially due to its higher affinity for NTS2 [472]. Cell studies showed that SR48692 blocks the action of both G_q and G_i [481, 482]. Other studies however suggest that its antagonist action might be cell-type specific, but this may also simply reflect the cell-type specific pharmacology of NTS1 [478, 482–484]. Data on the effect of SR142948A on specific G protein pathways is more scarce; one study suggests that SR142948A inhibits G_q-mediated effects in a cell-type specific manner [485]. In another study it was observed that SR142948A was a less potent antagonist than SR48692 in NTS1 transfected CHO (Chinese hamster ovary) cells, for the blockage of NT-induced ELK-1 expression [486], which has been linked to G_q- and G_i-mediated pathways [487].

Biased agonism has also been observed for the $NT_{8\text{-}13}$ analogue EISAI-1 ((Me)RKPW-*tert*-LL-OEt) favouring G_s/G_i- over G_q-related pathways [471], which was argued to be due to differential stabilisation of functionally different receptor conformational states [488]. Furthermore, the constitutively activating mutation of $F358^{7.42}$ in NTS1, was shown to yield elevated basal activity with respect to IP_3, but not cAMP production [489]. SR48692 acted as an inverse agonist on the F358A mutant, suggesting that TM7 is involved in conformational changes leading to G_q activation, consistent with its role in ligand binding.

6.1.3   Lipid dependence of NTS1 function

Ligand-binding to NTS1 has been shown to be sensitive to its lipid environment (see Figure 6.4) [40]. The presence of PE was found to be specifically required, with no discernible activity in POPC alone. While the presence of the cholesterol analogue CHS increased the stability of the receptor (*i.e.* increased its half-life), CHS or cholesterol were not required for ligand binding. Indeed, ligand binding to NTS1 has been shown earlier in *E. coli* membranes which lack cholesterol [302]. BPL (porcine brain polar lipid extracts, headgroup composition given in the table in Figure 6.4 as specified by the manufacturer, Avanti Polar Lipids), best supported receptor ligand-binding activity [40].

A recent study investigated ligand and G protein binding to NTS1 reconstituted into POPC

BPL (Brain Polar Lipid)	
Component	(w/w %)
PC	12.6
PE	33.1
PI	4.1
PS	18.5
PA	0.8
Unknown	30.9
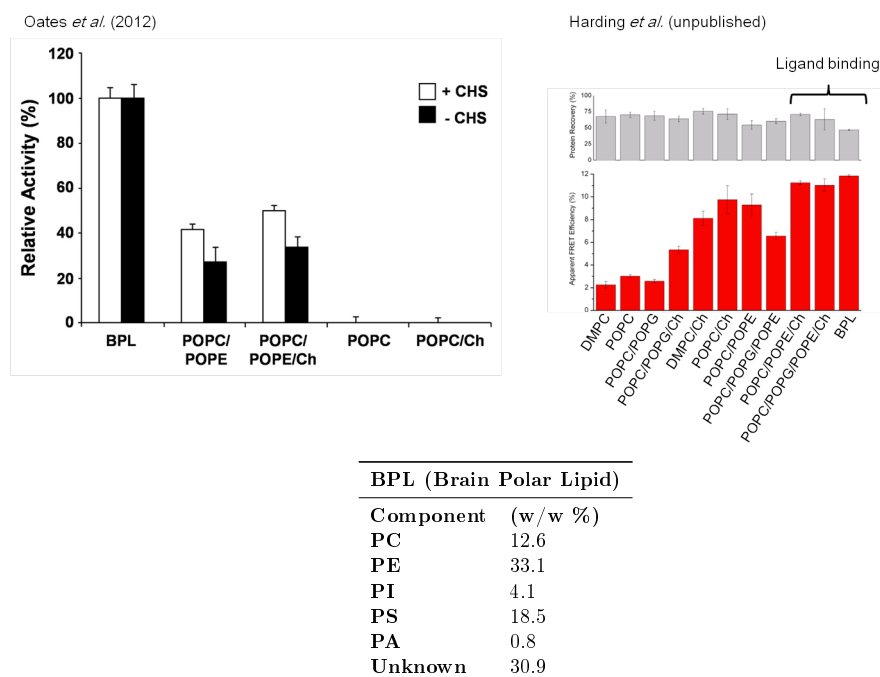
Figure 6.4: Lipid dependence of NTS1 activity. Activity of NTS1 reconstituted into liposomes of different lipid compositions was tested by radio-ligand binding assays in [40] (for NTS1 purified both with and without CHS present). Harding *et al.* (unpublished) also tested the reconstitution efficiency (top panel) and dimerisation rate (bottom panel) for different lipid compositions; they only found three compositions that supported lipid binding activity all including POPE, and cholesterol contrary to the findings in [40]. In both cases BPL (porcine brain polar lipid extracts, headgroup composition given in the table as specified by the manufacturer, Avanti Polar Lipids), best supported receptor ligand binding activity.

only, POPC/POPG (1:1), or POPG-only nanodiscs [42]. In this study, radioactivity binding assays suggested that ligand binding occurred with similar affinity for all lipid compositions, while the apparent affinity of G_q coupling increased with increasing POPG content, as gauged by higher radio-labelled GTPγS turnover. Thus, these studies show that membrane lipid composition are important for NTS1 activity.

6.1.4 Nanodiscs: practical considerations

Nanodiscs are disc-like bilayers stabilised by the belt protein MSP (membrane scaffold protein), and are a powerful method for membrane protein reconstitution, allowing access to both sides of the incorporated membrane protein (see section 1.3.5). Nanodiscs are self-assembling and can in principle be made with any bilayer-forming lipids to suit individual protein requirements. In practice however, some lipids yield better results than others, and particular empirically determined experimental conditions need to be adhered to for optimal results (see Table 6.1) [139]. Additionally, they form most efficiently at temperatures close to the phase transition of the lipids used [139]. The optimal ratio of lipid-to-MSP, and of

target protein-to-MSP needs to be determined empirically for each membrane protein and lipid composition. When choosing the MSP-to-target-protein ratio, it has to be considered that at lower ratios, the chance of incorporating more than one target protein per discs increases. Although theoretically, if a small enough MSP construct is chosen, steric constraints would make this highly unlikely, it cannot be completely excluded.

6.1.5   Aim

The aim of the study presented in this chapter is to study the G protein-GPCR interaction of NTS1 and how this is modulated by lipids and receptor-ligand interactions. While a previous study suggested that negatively charged lipids are important for this interaction [42], the effect of using more native lipid environments on G protein affinity will be tested here. To this end, NTS1 will be reconstituted into nanodiscs of different lipid compositions. Nanodiscs will be engineered so as to make them suitable for microscale thermophoresis (MST) measurements to study biomolecular interactions. Furthermore, the effect of NTS1 ligands, *i.e.* its native agonist NT, and two antagonists SR48692 and SR142948A, on G protein affinity will also be investigated, for the receptor in detergent and in nanodiscs of different lipid composition.

6.2   Materials and method

6.2.1   Gα_{i1}

G protein was expressed and purified as described in Appendix A.6. The activity of Gα_{i1} was verified by fluorescence polarisation saturation-binding experiments with guanosine 5'-O-(3-thiotriphosphate) BODIPY thioester (BODIPY-GTPγS) as also described in Appendix A.6.

6.2.2   Reconstitution of NTS1 in fluorescent nanodiscs

To produce fluorescently labelled nanodiscs for MST experiments without having to label the receptor, MSP was labelled, since this would allow better control over labelling efficiency than, for example, using labelled lipids, and thus produce a more uniform sample. MSP naturally contains a relatively large number of lysines (8% of all residues), but as these are likely to be integral to its amphiphilic nature, and thus its function, a cysteine was introduced in the MSP construct which does not contain any native cysteines (see Appendix A.4). The Cys was introduced at the N-terminus after the TEV protease recognition site, as the N-terminus of MSP is amenable to modification [138]. The new Cys-MSP construct was expressed in *E. coli* and purified by IMAC on a nickel column as previously described in [139] with a few modifications (see Appendix A.4). The TEV site was used to remove the

His$_6$-tag by proteolytic cleavage, to allow enrichment of nanodiscs loaded with NTS1-His$_6$ on a nickel affinity column, separating out the empty, non-His-tagged discs. Cleavage was done by overnight incubation with TEV at a 1:10 (TEV:MSP) molar ratio and 5 mM DTT (see Figure 6.5). Cleaved MSP was then separated from TEV and uncleaved material by
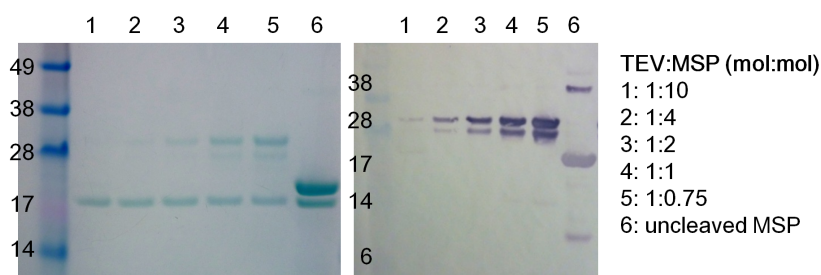
Figure 6.5: MSP test cleavage by TEV protease. MSP was incubated overnight at 4 °C with varying amounts of TEV (1 to 10, 4, 2, 1 and 0.75 TEV:MSP molar ratio). Aliquots of each reaction were analysed by SDS-PAGE alongside uncleaved MSP (apparent molecular weight of the SeeBlue Plus2 Pre-Stained Standard are indicated). The gel was stained by Coomassie blue (left) and a western blot was developed using an anti-His antibody (right). Cleavage appears to be complete even at the lowest TEV:MSP ratio (lane 1). The band at ~20 kDa corresponds to MSP, while the higher band at ~28 kDa corresponds to TEV protease (which also contains a His-tag).

a second round of IMAC, by collecting the flow-through, and labelled with Alexa Fluor 647 maleimide dye (A647) as described in Appendix A.4. The pH was controlled to ensure pH<7.5 to favour Cys labelling over Lys labelling. By comparing the absorption at 280 nm with that of the fluorophore maximum, correcting for the contribution of the fluorophore at 280 nm (see equation A.2), the labelling efficiency was determined to be 93.5%, giving roughly two fluorophores per nanodisc on average.

Nanodiscs were then prepared as described in Appendix A.5.5 (Figure 6.6). Briefly, a lipid film of the appropriate lipid (mixture) was prepared (see section A.5.4) and lipids resuspended in sodium cholate buffer (50 mM Tris-HCl pH 7.4, 50 mM NaCl, 1 mM EDTA, 100 mM sodium cholate) to give a final concentration of 20-40 mM lipid. Lipids were sonicated (3×1 min) using a bath sonicator, followed by 5-10 freeze-thaw cycles in liquid nitrogen. Lipid was added to NTS1, followed by MSP, and the sample was incubated for 1 h on a rotating wheel at 4 °C, after which Bio-Beads (Bio-Rad) were added for detergent removal overnight. The ratios at which the components (lipid, NTS1, MSP) are mixed are vital to the efficiency of nanodisc formation. These ratios have to be determined empirically for each target protein and each lipid composition, adhering to guidelines determined by Sligar and co-workers [139]. The lipid-to-MSP ratio and the MSP-to-NTS1 ratios used for the different lipid compositions are given in Table 6.1. Optimisation of the lipid-to-MSP ratio for BPL nanodiscs is shown in Figure G.1.
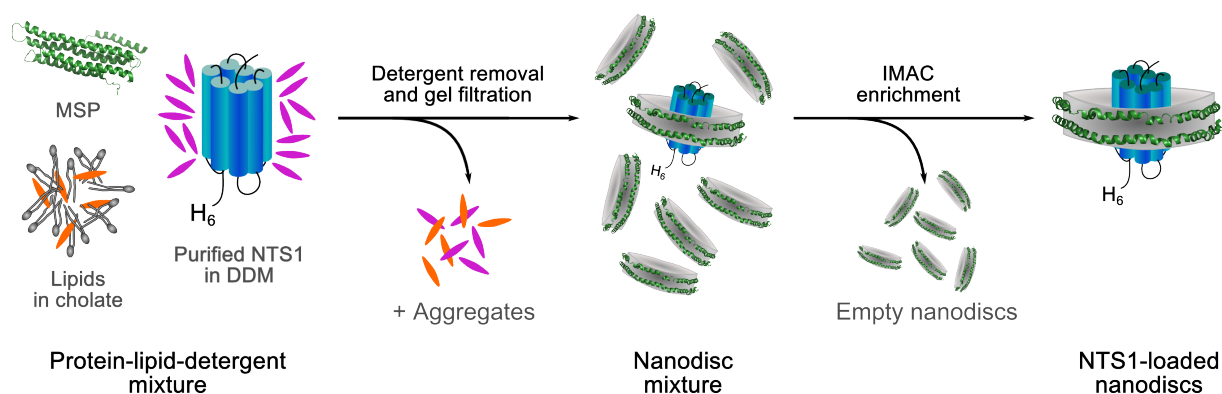
Figure 6.6: Schematic of NTS1 nanodisc production. Nanodiscs were made by mixing lipids solubilised in sodium cholate with detergent-solubilised His-tagged (H$_6$) NTS1 and the MSP belt protein. Detergent is removed by incubation with Bio-Beads overnight, after which nanodiscs are separated from larger aggregates by gel filtration. Finally, NTS1-loaded nanodiscs are separated from empty nanodiscs by IMAC facilitated by the His-tag on NTS1.

Table 6.1: Experimental conditions for nanodisc formation. Optimal conditions as determined by Sligar and co-workers are stated next to the conditions used in this chapter for nanodisc formation using three different lipid compositions, namely POPC:POPC (1:1, mol:mol), POPC:POPG:BPL (1.5:1:1.07), and BPL alone. Optimal MSP-to-lipid and target protein-to-MSP ratios have to be empirically determined for each individual lipid-protein combination.

Reagent	Optimal conditions	POPC:POPG (1:1)	POPC:POPG:BPL (1.5:1:1.07)	BPL
[NTS1] (µM)	~1	1.5-2.1	1.7-2.0	1.7-2.0
[MSP] (µM)	~120-140	120	90-120	120
[Glycerol] (%)	<4	1.9-2.6	3	2.2-2.8
[Cholate] (mM)	12-40	18-19	15-27	19-27
[Lipid] (mM)	4-18	7.3-7.5	6.0-7.8	7.8-8.3
MSP:Lipid	Empirical	1:60 (loaded)	1:65 (loaded)	1:65 (loaded)
		1:65 (empty)	1:70 (empty)	1:70 (empty)
NTS1:MSP	Empirical	1:50-80	1:50-80	1:60-80

Nanodiscs were separated from larger aggregates by gel filtration (10/30 Superdex 200 column, GE Healthcare). For NTS1 containing nanodiscs, preparations were enriched by separating empty from loaded discs by IMAC. Pooled fractions were loaded onto a 1 mL HisTrap HP column equilibrated with nanodisc gel filtration buffer, washed with 50-90 CV of gel filtration buffer supplemented with 2-4 mM imidazole, after which NTS1 containing nanodiscs are eluted with 500 mM imidazole. Peak fractions were pooled, and dialysed against 5 L of gel filtration buffer overnight at 4 °C, and the final sample concentration was determined from the absorption spectrum.

6.2.3 Fluorescent labelling of NTS1 for MST

Purified WT-NTS1 in detergent was labelled as described in section A.5.3. WT-NTS1 naturally contains five potentially exposed cysteines (*i.e.* located in a loop, or at the TM/loop interface), and was thus incubated with a 40× molar excess (*i.e.* 8× per cysteine) of Alexa Fluor 488 (A488). Free dye was removed by gel filtration and, final protein concentration (2.1 μM) and labelling efficiency (~1.15 labels per NTS1 molecule on average) were determined from the absorption spectrum.

6.2.4 MST

Microscale thermophoresis experiments were carried out on a Monolith NT.115 (NanoTemper Technologies) with blue/red filter set, using the blue filter set for A488-labelled samples and the red for A647. Samples were centrifuged (10,000×g, 10 min) and/or filtered (0.2 μm centrifugal filter) to remove any aggregates. Dilution series (12-16 points) of the unlabelled binding partner were prepared ensuring that no additional gradient (salt, glycerol, imidazole, DMSO etc.) was created by careful buffer matching. Where used, agonist (NT), antagonist (SR48692 or SR142948A), and/or GTPγS were added at saturating concentrations (5 μM, 5 μM, and 0.5 mM, respectively) to all components (fluorescent binding partner, non-fluorescent binding partner, and buffer) of the titration series. To minimize adsorption of the sample to the reaction tubes, LoBind tubes (Eppendorf) were used. Furthermore, for experiments with detergent-solubilised NTS1 0.1 mg/mL BSA was added to passivate the reaction tube surface. For nanodisc samples 0.006% Tween-20 (w/v) was included. Passivating agents were again added to all separate components to avoid creation of a gradient in the dilution series. Under these conditions the fluorescence was found to be constant (within ±10%) for all points in the titration curve. The minimum amount of fluorescent binding partner needed was determined by a capillary scan, adjusting the LED power to give fluorescence counts between 200-1500, typically using 95% LED power for samples containing 5-25 nM of the fluorescent binding partner. Dilution series were left to incubate at 4 °C for at least 30-60 min after which they were loaded into hydrophilic capillaries (NanoTemper Technologies) by capillary action. Thermophoresis was measured at varying MST power (20, 40 and 80%), with 80% usually giving the best results.

6.2.5 MST data analysis

In section 1.4.5.3 it was already shown that for a binding event
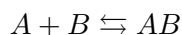
$$A + B \leftrightharpoons AB$$

the law of mass action dictates that the equilibrium dissociation constant K_d can be described by

$$K_d = \frac{([A] - [AB])([B] - [AB])}{[AB]}$$

where $[A]$ and $[B]$ are the total concentrations of A (not-observed, titrated partner) and B (fluorescent, constant partner) and $[AB]$ that of the complex AB, and that solving this equation for the fraction of bound molecules gives a direct relation between F_{norm} and the K_d which can then be obtained by fitting the MST data. This approach is to be preferred over using a simple, approximate one-site binding model for saturation binding experiments, such as

$$[AB] = B_{max}[A]/(K_D + [A]) \tag{6.1}$$

where B_{max} is the experimental estimate of the maximum binding capacity, as these models are only valid under the assumptions that $[A] \gg [B]$ and $[B]_{free} \approx [B]$ [490]. Under these approximations, the depleting effect on the free concentration of B is not taken into account, which is expected to be substantial under the experimental conditions used in MST as the fluorescent binding partner B is only added at very low (nM) concentrations. Thus, one should use the full quadratic solution to equation 1.41b for the fraction of bound fluorescent partner, $[AB]/[B]$:

$$K_d = \frac{([A] - [AB])([B] - [AB])}{[AB]} \tag{6.2a}$$

$$[AB]K_d = ([A] - [AB])([B] - [AB]) \tag{6.2b}$$

$$0 = [AB]^2 - ([A] + [B] + K_d)[AB] + [A][B] \tag{6.2c}$$

which is a quadratic equation of the type $0 = ax^2 + bx + c$ with solutions $x = \frac{-b \pm \sqrt{b^2 - 4ac}}{2a}$, thus

$$\frac{[AB]}{[B]} = \frac{[A] + [B] + K_d - \sqrt{([A] + [B] + K_d)^2 - 4[A][B]}}{2[B]} \tag{6.2d}$$

As F_{norm} linearly reports on $[AB]/[B]$ as discussed in section 1.4.5.3

$$F_{norm} = (1 - x)F_{norm,unbound} + xF_{norm,bound}$$

where $x = [AB]/[B]$ it follows that

$$x = \frac{F_{norm} - F_{norm,unbound}}{(F_{norm,bound}) - F_{norm,unbound}} \tag{6.3a}$$

which combined with equation 6.2d gives the following expression for F_{norm}

$$F_{norm} = F_{norm,unbound} +$$
$$(F_{norm,bound} - F_{norm,unbound}) \frac{[A] + [B] + K_d - \sqrt{([A] + [B] + K_d)^2 - 4[A][B]}}{2[B]}$$
$$\tag{6.3b}$$

which can be directly fitted to the MST binding isotherm where $F_{norm,unbound}$ represents the plateau at low concentrations of A where most fluorescently labelled B is free (unbound), and $F_{norm,bound}$ the plateau at high concentrations of A where binding should reach saturation.

6.3 Results and discussion

6.3.1 G protein expression and activity assay

$G\alpha_{i1}$ was purified to near homogeneity by IMAC on a nickel column (Figure 6.7), yielding 22.1 ± 0.7 mg of protein per litre of culture. Fluorescence polarisation experiments verified
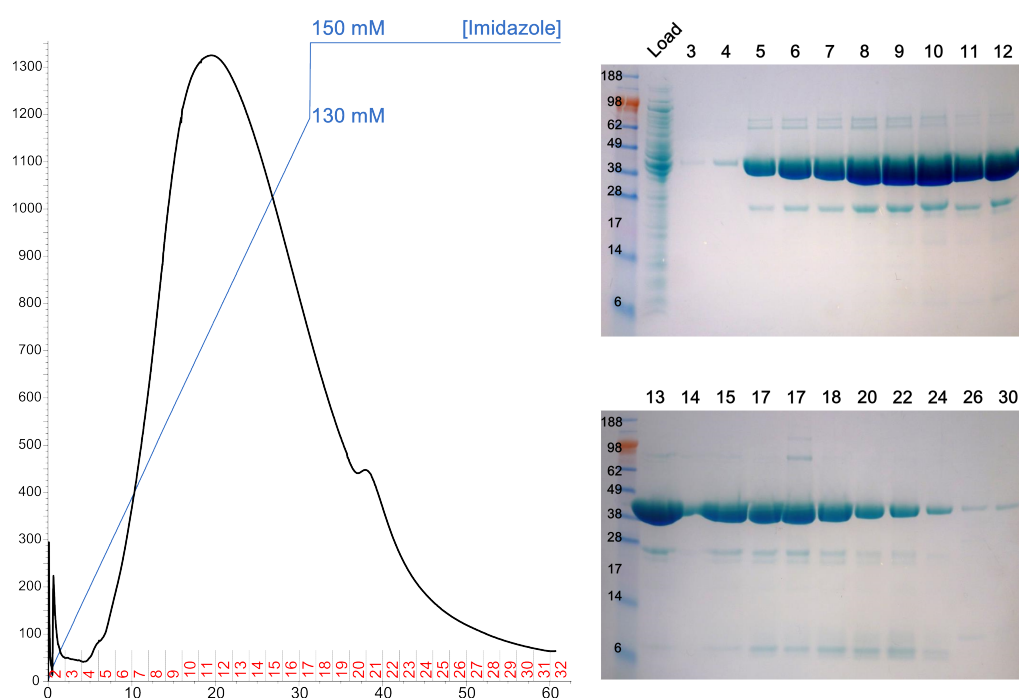
Figure 6.7: Purification of Gα_{i1}. Gα_{i1} was purified by IMAC (elution profile showed here (left)) as described in section A.6. Purity of the fractions was verified by SDS-PAGE analysis (right) to be >95%.

the activity of two separate preparations of $G\alpha_{i1}$; both were found to specifically bind fluorescently labelled GTPγS with nanomolar affinity ($K_d = 40 \pm 2$ nM and $K_d = 44 \pm 2$ nM, Figure 6.8), which close to an earlier reported value of $K_d = 150 \pm 50$ nM [491].

6.3.2 Nanodisc formation

Nanodiscs of different lipid composition were prepared to assess the effect of lipids on the GPCR-G protein interaction (Figure 6.9). POPC:POPG (1:1 molar ratio, referred to as PCPG from here onwards) discs formed most efficiently, as evident from the relatively small
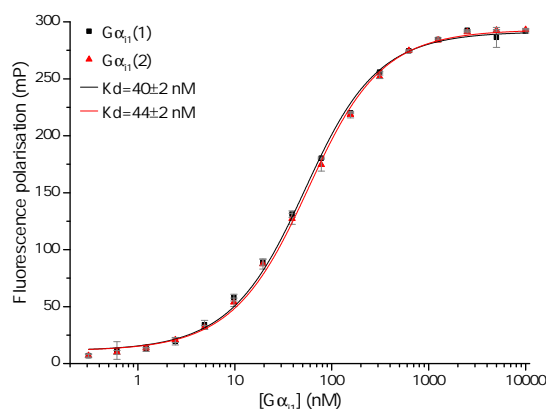
Figure 6.8: GTP binding capability of $G\alpha_{i1}$ verified by fluorescence polarisation. The activity of $G\alpha_{i1}$ was verified by fluorescence polarisation saturation-binding experiments to guanosine 5'-O-(3-thiotriphosphate) BODIPY thioester (BODIPY-GTPγS); the affinity (K_d) was determined by incubating serial dilutions (in triplicate) of $G\alpha_{i1}$ with 25 nM BODIPY-GTPγS for 1 h, and recording the endpoint fluorescence polarisation. Non-specific binding was tested by repeating the experiment in the presence of 1 mM unlabelled GTPγS. Specific binding (total minus non-specific) was fitted in OriginPro 8.5 (OriginLab) using a one-site binding model, accounting for ligand depletion. Error bars represent the standard error of three experiments.

peak at the void volume of the gel filtration column (~8 mL, Figure 6.9), containing aggregated material, compared to the void volume peaks of the other two lipid compositions. POPC:POPG:BPL (1.5:1:1.07, referred to as PCPGBPL from here onwards) nanodiscs preparations gave a slightly larger aggregate peak, but the nanodiscs had a similar elution profile and retention time to the PCPG discs, suggesting that they were not very different. The BPL nanodisc formed less efficiently. Firstly, samples were still cloudy after incubation with the Bio-Beads overnight, and thus a significant (lipid) pellet was formed upon centrifugation before the gel filtration column compared to that observed for PCPG and PCPGBPL. Indeed, whereas both the PCPG and the PCPGBPL lipid mixtures were transparent when resuspended in the sodium cholate reconstitution buffer, the BPL suspension was still cloudy after sonication and numerous freeze-thaw cycles. The BPL gel filtration chromatogram also looks markedly different from the other two; the aggregate peak (at ~8 mL) is more prominent, and the nanodisc peak is less uniform. Fractions corresponding to the early shoulder at 12.8 mL elution volume were pooled, as these were likely to contain the larger, NTS1-loaded, nanodiscs, while later fractions were more likely to contain predominantly empty discs (as confirmed by SDS-PAGE, Figure 6.9).

The hydrodynamic radius of the nanodiscs was estimated to be ~4.5-5 nm from the gel filtration elution volumes (Figure G.2). The morphology of the nanodiscs was examined by negative-stain electron microscopy (EM).[1] EM images were obtained for Alexa Fluor-labelled

---

[1]Uranyl acetate staining and transmission electron microscopy was carried out by Roslin Adamson (Department of Biochemistry, University of Oxford).
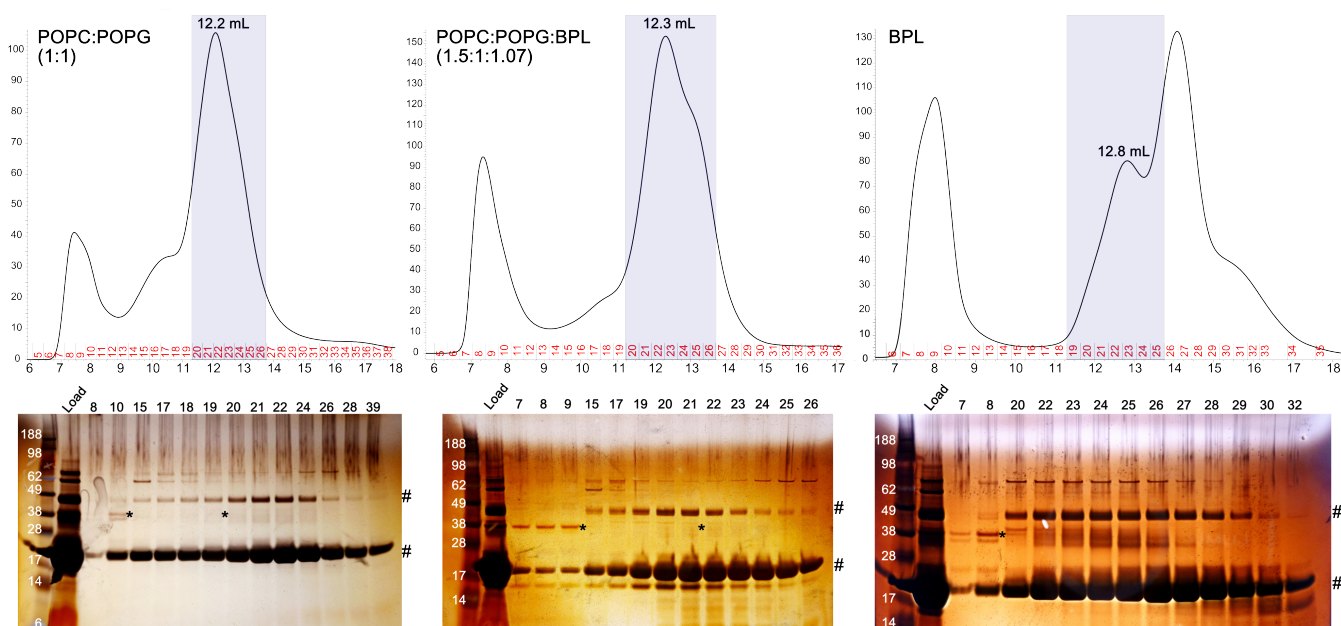
Figure 6.9: Gel filtration of nanodiscs. Nanodiscs of different lipid compositions were prepared: POPC:POPG (1:1), POPC:POPG:BPL (1.5:1:1.07), and BPL nanodiscs, with lipid ratios given in mol:mol, assuming an average molecular weight of 650 g/mol for BPL. Gel filtration traces of the separation of nanodiscs from other material are shown (top) as well as corresponding SDS-PAGE analyses of the fractions, stained with silver stain (bottom). Gel bands corresponding to MSP are marked with #, and bands corresponding to NTS1 are marked with *. Shaded area in the gel filtration traces indicate the fractions pooled for further enrichment.

PCPG and BPL discs (see Figure 6.10). Both lipid compositions appear to generate a relatively homogeneous population of discs of roughly the expected size (~10 nm diameter), showing that fluorescently tagging MSP does not affect overall nanodisc morphology. To address the question of whether the BPL nanodiscs did indeed contain all components of the initial BPL lipid mixture, thin layer chromatography (TLC) was performed.[2] To this end, nanodiscs were lyophilised, resuspended in methanol:chloroform (4:1 v:v) and run on silica-coated glass plates along reference samples (BPL, sphingomyelin, and cholesterol, see Figure 6.11 for details). The analysis of the chromatograms is complicated by the different solvents used for the sample (methanol:chloroform 4:1) and the reference samples (chloroform only), resulting in different retention on the silica for the same compounds. This is overcome to some extent by also running both samples together, through subsequent application on the same spot; thus, for all chromatograms three spots were run, from left to right (1) "unknown", (2) "unknown" and "reference" spotted on top of each other, and (3) "reference". Comparing the BPL reference to the nanodiscs, molybdenum blue spray (Figure 6.11A) shows that the phospholipid content of nanodiscs is the same as that found in

---

[2]TLC was performed with the aid of Peter Fisher (Department of Biochemistry, University of Oxford).
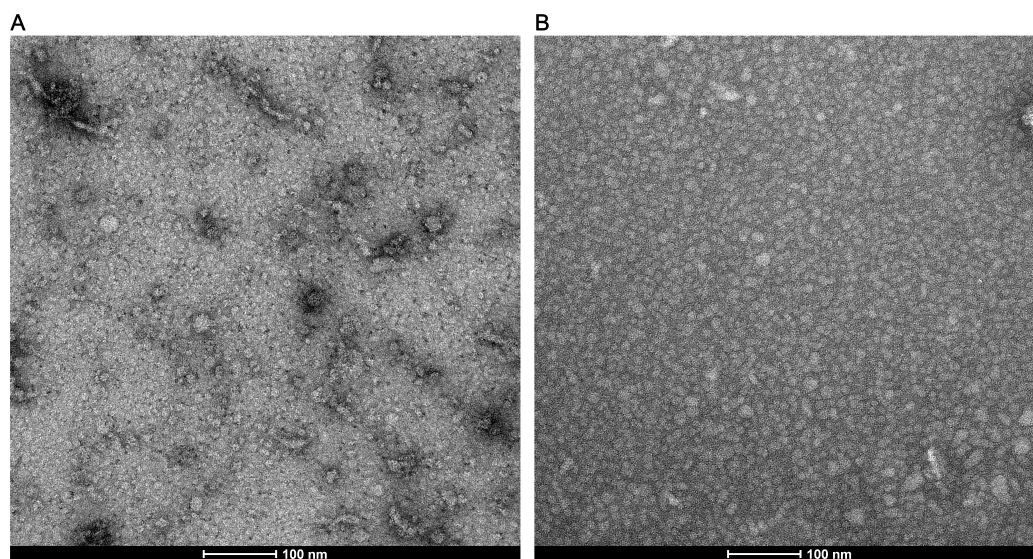
Figure 6.10: Negative stain electron microscopy on nanodiscs. Uranyl acetate staining and transmission electron microscopy were used to image **(A)** POPG:POPC and **(B)** BPL nanodiscs. Imaging was carried out by Roslin Adamson (Department of Biochemistry, University of Oxford).

BPL, with two spots appearing for both the standard and the reference. The third, lowest spot visible for the BPL reference with the molybdenum blue spray is less clear for the ND sample, which is less concentrated overall, but becomes clearly visible after charring (Figure 6.11B). Charring further reveals two higher spots on the TLC in the BPL lane, that are not phospholipids. Spots at similar height are vaguely visible for the nanodisc sample, and the spots are roughly in the same place in the middle "mixed" lane, suggesting that they should indeed be at the same height in the sample and the reference. Furthermore the spots appear to be more intense in the middle lane, than in the right lane, suggesting the ND sample is contributing to them, but it cannot be excluded that this is due to slightly different loading, and that the presumed spots in the left lane are just background charring. A separate test for the presence of sphingomyelin (Figure 6.11C) reveals that the second spot from the bottom in the BPL sample corresponds to this lipid type, and that it is indeed present in the nanodisc preparation. Surprisingly, cholesterol does not appear to have been incorporated into the nanodiscs (Figure 6.11D), despite TLC of BPL itself showing that the mixture does contain a significant amount of cholesterol (Figure 6.11E; the amount of cholesterol present in BPL is not specified by the supplier). Thus, BPL nanodiscs contain most of the components of BPL except for cholesterol.

The high MSP-to-NTS1 ratio used ensures that most of the discs contain only one receptor. Assuming a Poisson distribution, using a 50:1 MSP ratio would result in <1% of the loaded nanodiscs containing more than one NTS1 molecule, assuming multimeric insertions are
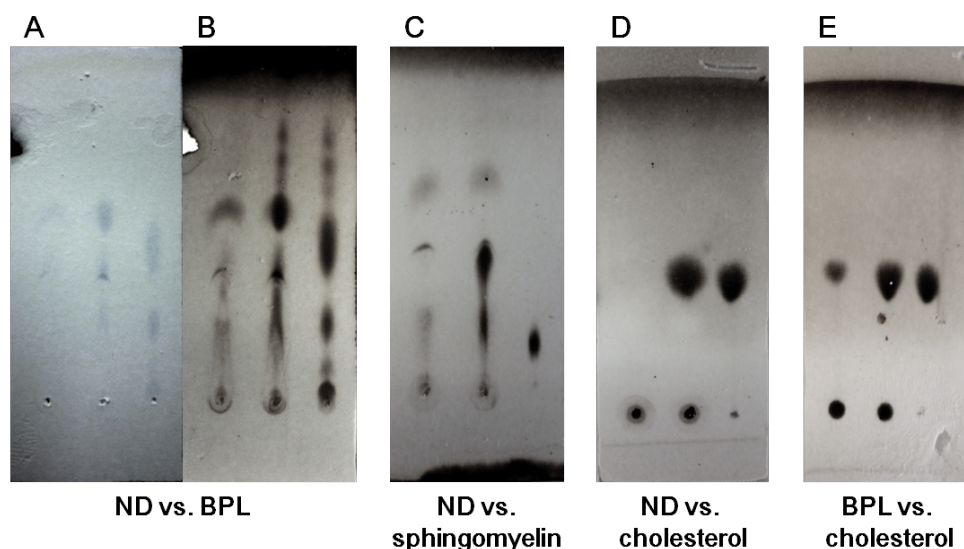
Figure 6.11: TLC of BPL nanodiscs. Lipid content of brain polar lipid (BPL) nanodiscs (NDs) was evaluated using thin layer chromatography. Lyophilised ND resuspended in methanol:chloroform (4:1 vol:vol) were run alongside reference samples in chloroform. For all chromatograms three spots were run, from left to right (1) "unknown", *i.e.* ND (**A-D**) or BPL (**E**), (2) "unknown" and "reference" spotted on top of each other, and (3) "reference". (**A**) ND run with BPL stained with molybdenum blue spray (Sigma) to visualize phospholipids only, and (**B**) then charred. (**C**) ND run with sphingomyelin and charred. (**D**) ND run with cholesterol and (**E**) BPL (standard) run with cholesterol, both charred. (**A-C**) were run using chloroform:methanol:ammonium hydroxide (65:30:3 vol:vol) as solvent, and (**D-E**) were run in hexane:ether (50:50 vol:vol).

equally likely as monomeric insertions.[3] The fixed size of the MSP belt however, imposes steric constraints on the size of the properly formed nanodiscs; thus insertion of two NTS1 molecules with an diameter of ~4 nm into discs with a diameter of ~10 nm (as determined by EM and from the elution volume on the gel filtration column, in agreement with the expected literature value [138]) is likely to be less favourable than the insertion of a single NTS1 molecule. Furthermore, the calculated probability of multimeric insertion is based on the incorporation of NTS1 and MSP with the same probability, while from SDS-PAGE analysis it is evident that a larger proportion of NTS1 is not incorporated into nanodiscs, eluting as part of larger aggregates in the early void volume fractions (Figure 6.9). This results in a lower effective NTS1-to-MSP ratio, and thus even lower, negligible proportions of multimeric nanodisc insertion. The final sample can thus be regarded as representing the monomeric receptor.

---

[3]A 1:50 NTS1-to-MSP ratio (the highest used), gives a maximum 0.04 success rate of an NTS1 loaded disc (with 2 MSP molecules per disc). Assuming a Poisson distribution the probability of one NTS1 per disc is 0.038, and more than one is 0.00078, giving a 0.99% probability for multimeric insertion.

6.3.3   NTS1 ligand binding

Agonist and antagonist binding activity of the receptor was tested by label-free MST, exploiting the native Trp fluorescence of the protein (Figure 6.12).[4] The dissociation constant of <20 nM determined for NT binding (Figure 6.12A) is in agreement with previous SPR data showing a K_d of 1-2 nM for NTS1B [319]. Interestingly, binding of the agonist reduced
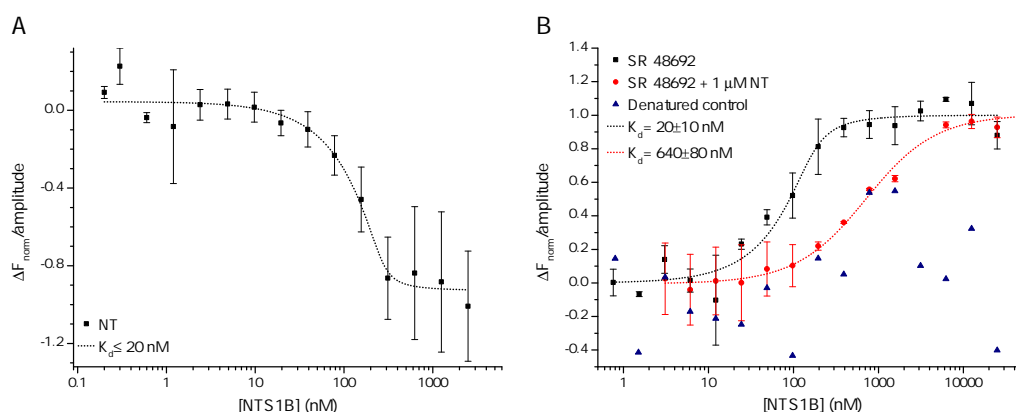
Figure 6.12: NTS1B ligand binding tested by label-free MST. (A) Neurotensin is titrated to a constant concentration of NTS1B (150 nM). **(B)** The antagonist SR48692 is titrated to a constant concentration of NTS1B (150 nM) in the absence (black) and the presence (red) of a saturating amount of NT (1 µM). Protein was thermally denatured as a control (blue), showing binding. Data was normalised to the amplitude of the sigmoidal binding isotherm and fitted with a one-site binding model accounting for ligand depletion (the corresponding K_d values are shown).

the thermophoretic mobility of the complex (ΔF_{norm} decreases with increasing receptor concentration), while the opposite was observed for the antagonist SR48692. While these opposite effects could be due to the different chemical structures of the two ligands, their small size (<2 kDa) compared to the size of the receptor (~100 kDa) makes it more likely that this difference is due to changes in the receptor itself. This observation could thus reflect the different structural effects the agonist and antagonist have on the receptor, with NT promoting an active receptor conformation, while SR48692 locks the receptor in an inactive conformation, giving rise to differences in the hydration shell and thus the thermophoretic properties of the receptor-ligand complexes.

MST experiments to determine the affinity of NT for nanodisc-reconstituted NTS1 were also attempted using Alexa Fluor 488 labelled NT (NT-A488), titrating the Alexa Fluor 647 labelled nanodiscs and detecting at the ligand wavelength. Unfortunately, due to the low concentration of the nanodisc samples (135 nM and lower), the receptor could not be

---

[4]Label-free measurements were carried out by Stefan Duhr (NanoTemper Technologies) on a Monolith NT.LabelFree (NanoTemper Technologies). Results previously published in [166].

titrated to saturation, and no clear results were obtained. The reverse experiment, titrating unlabelled NT to a constant amount of fluorescent nanodiscs did also not elicit any detectable changes, presumably due to the relatively small size of the ligand compared to the nanodisc. Binding of NT to nanodiscs-reconstituted samples has been shown before by radio-ligand binding assays [42], and by SPR (Adamson and Watts, unpublished results). Thus, despite not being able to show ligand binding by MST, samples were assumed to be active.

6.3.4   GPCR-G protein interaction and its modulation by ligand

Binding of the G protein α subunit $G\alpha_{i1}$ to fluorescent nanodisc-reconstituted and detergent-solubilised NTS1 was investigated in the presence of agonist (NT) and antagonist (SR48692 or SR142948A, which will be referred to as SR48 and SR14, respectively, in the rest of this section). The affinity of the $G\alpha_{i1}$-NTS1 interaction was determined by fitting MST-derived binding curves (Figure 6.13) with a one-site binding model accounting for ligand depletion, and the corresponding K_d values are compiled in Table 6.2. Interestingly, the affinity of the G protein appears to be dependent on the lipid composition of the nanodiscs, with highest affinity observed for BPL in the presence of agonist ($K_d = 140 \pm 60$ nM, *vs.* 700 ± 300 and 600 ± 300 nM for PCPGBPL and PCPG, respectively). For detergent-solubilised NTS1, the affinity ($K_d = 220 \pm 90$ nM) is similar to that of BPL nanodiscs, and higher than the PCPG an PCPGBPL nanodiscs, suggesting that the detergent might better support native activity than non-native lipid bilayers. In the absence of any ligand, the affinity of the G protein for the receptor decreases for the BPL nanodiscs (from $K_{d,NT} = 140 \pm 60$ nM to $K_{d,NoLig} = 300 \pm 100$ nM). Thus, although NT binding could not be directly detected by MST, this result implies that the agonist does bind to, and activates the receptor. The effect of agonist was also seen for PCPG nanodiscs (from $K_{d,NT} = 600 \pm 300$ nM to $K_{d,NoLig} = 1.9 \pm 0.8$ μM), but was not observed for PCPGBPL-reconstituted or detergent-solubilised NTS1. This could reflect the poor resolution that was obtained for the PCPGBPL sample in the absence of ligand, with rather large uncertainty in the K_d value ($K_{d,NoLig} = 700 \pm 500$ nM), masking any small difference, although the upper boundary of the determined dissociation constant is above that observed for PCPGBPL in the presence of agonist ($K_{d,NoLig} = 700 \pm 300$ nM). The resolution for the DDM/CHS detergent sample was better however, and the lack of agonistic effect suggests that the conformation of the receptor in detergent is different from that in liposomes, giving rise to different pharmacological behaviour. Addition of antagonist SR48 decreased the affinity of the G protein for NTS1 in all environments except PCPG. The largest decrease in affinity was observed for BPL and PCPGBPL nanodiscs (4.3× increase of the mean K_d for both), while the effect in detergent was more modest (1.7×

Table 6.2: Affinity of $G\alpha_{i1}$ for NTS1 determined by MST. The dissociation constants (K_d) for the interaction between $G\alpha_{i1}$ and NTS1 in the presence of different ligands, as determined from MST experiments shown in Figure 6.13, are given. Affinity was determined for NTS1 reconstituted into nanodiscs of different lipid composition (PCPG, PCPGBPL, and BPL) and for detergent-solubilised NTS1 (DDM/CHS). The interaction between $G\alpha_{i1}$ and empty nanodiscs (ND) was also studied (Figure 6.14). As a negative control the interactions were studied in the presence of GTPγS, which decouples the G protein from the receptor *in vivo*. K_d values were determined with a one-site binding model accounting for ligand depletion, using the average of n experiments, and the error estimate of the fit is given.

Interaction	PCPG	PCPGBPL	BPL	DDM/CHS
No ligand	1.9 ± 0.8 μM ($n = 3$)	700 ± 500 nM ($n = 4$)	300 ± 100 nM ($n = 3$)	140 ± 70 nM ($n = 4$)
+NT	600 ± 300 nM ($n = 4$)	700 ± 300 nM ($n = 4$)	140 ± 60 nM ($n = 4$)	220 ± 90 nM ($n = 6$)
+SR48692	500 ± 300 nM ($n = 3$)	3 ± 2 μM ($n = 4$)	600 ± 300 nM ($n = 4$)	370 ± 70 nM ($n = 2$)
+SR142948A	600 ± 300 nM ($n = 3$)	500 ± 300 nM ($n = 4$)	300 ± 100 nM ($n = 4$)	50 ± 20 nM ($n = 1$)
+NT+GTPγS	4 ± 2 μM ($n = 2$)	9 ± 5 μM ($n = 4$)	1.5 ± 0.8 μM ($n = 3$)	5 ± 4 M ($n = 2$)
(Empty ND) +NT	800 ± 600 nM ($n = 4$)	400 ± 200 nM ($n = 4$)	200 ± 100 nM ($n = 4$)	-
(Empty ND) +NT+GTPγS	5 ± 4 μM ($n = 3$)	2 ± 1 μM ($n = 3$)	30 ± 20 μM ($n = 3$)	-

increase of the mean K_d) and less certain due to overlapping error margins. Interestingly, for these three conditions the antagonist SR14 had a weaker antagonist effect than SR48 (BPL: $K_{d,SR14} = 300 \pm 100$ nM *vs.* $K_{d,SR48} = 600 \pm 300$ nM), or even slightly agonistic effect compared to NT, or the basal receptor state (PCPGBPL: $K_{d,SR14} = 500 \pm 300$ nM *vs.* $K_{d,NT} = 700 \pm 300$ nM; DDM: $K_{d,SR14} = 50 \pm 20$ nM *vs.* $K_{d,NT} = 220 \pm 90$ nM). For PCPG, neither antagonist lowered the affinity of the G protein to NTS1 with respect to the agonist-bound state, although higher affinity was observed for both the SR48 and SR14-bound receptor than for receptor in the basal state ($K_{d,SR48} = 500 \pm 300$ and $K_{d,SR14} = 600 \pm 300$ nM, respectively, *vs.* $K_{d,apo} = 1.9 \pm 0.8$ μM). This suggests that the antagonists do bind to the PCPG-reconstituted receptor, but remarkably, that their effect on the G protein-NTS1 interaction is the same as that of agonist. Whether this result is relevant to *in vivo* conditions is unclear, as the PCPG lipid composition is quite different from the native, mammalian environment of NTS1. It is thus possible, that this lipid composition does not support native NTS1 activity, as suggested by poor ligand-binding compared to BPL previously observed in liposomes (Figure 6.4).
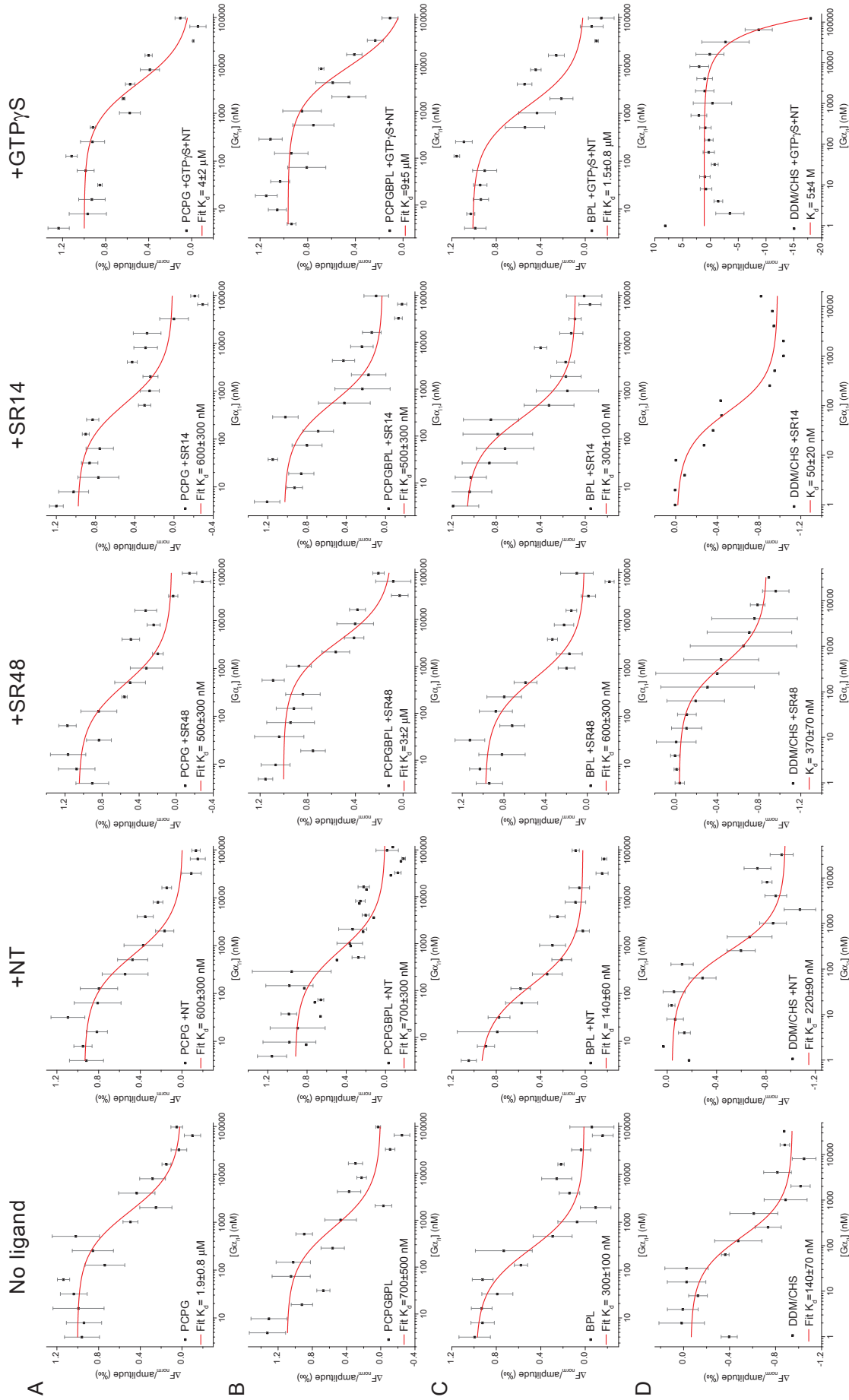
Figure 6.13: Lipid-dependence of GPCR-G protein interaction studied by MST. The affinity of $G\alpha_{i1}$ for NTS1 is determined by MST experiments in the absence of ligand, in the presence of NT, SR48, SR14, or NT and GTPγS (negative control). The effect of the lipid environment is tested by doing the experiments in nanodiscs of **(A)** PCPG, **(B)** PCPGBPL, or **(C)** BPL lipid content, or **(D)** for detergent-solubilised receptor. Data was normalised to the amplitude of the sigmoidal binding curve and fitted with a one-site binding model accounting for ligand depletion (the corresponding K_d values are shown). Error bars represent the standard error of at least two experiments (see Table 6.2).

As a negative control G protein was incubated with GTPγS, a non-hydrolysable analogue of GTP, the binding of which decouples the G protein from the receptor *in vivo*. An increase in K_d was observed under all conditions, suggesting that the G protein-NTS1 interaction is indeed specific (Table 6.2).

6.3.5   G protein interaction with lipid

G protein was also incubated with empty nanodiscs to investigate the interaction of the protein with the different bilayer compositions (Figure 6.14). Again, as a control experiment the interaction was also tested in the presence of GTPγS. As seen for the receptor in section 6.3.4,
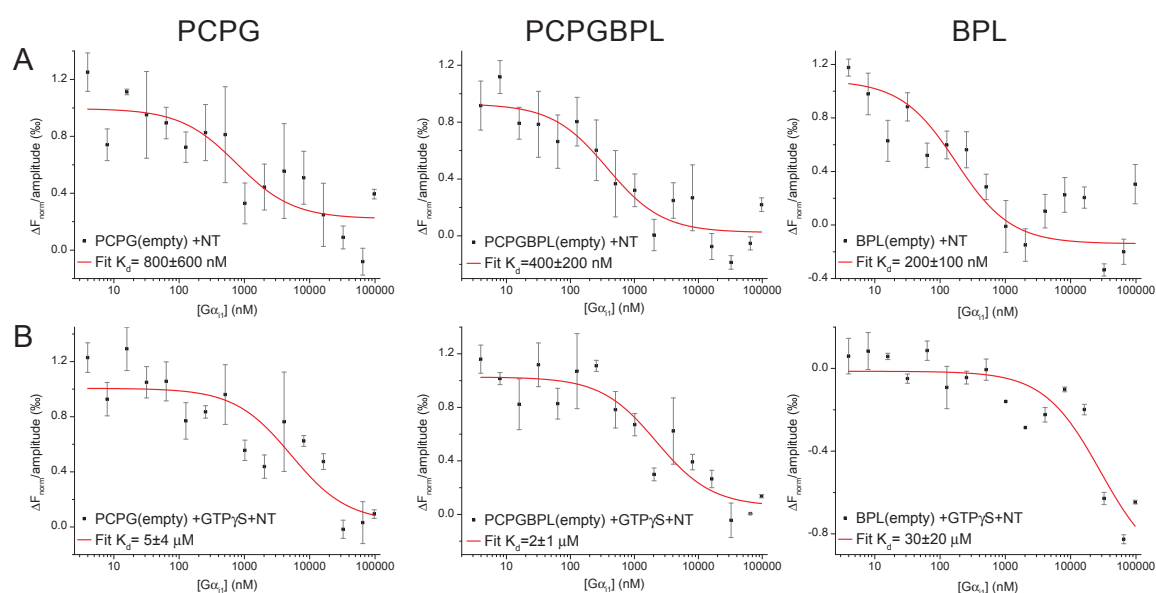
Figure 6.14: Lipid-G protein interaction studied by MST. The affinity of $G\alpha_{i1}$ nanodiscs of different lipid composition was determined by MST experiments: PCPG (left), PCPGBPL (middle), and BPL (right). Measurements were performed in the presence of **(A)** NT, and **(B)** GTPγS as a negative control. Data was normalised to the amplitude of the sigmoidal binding curve and fitted with a one-site binding model accounting for ligand depletion (the corresponding K_d values are shown). Error bars represent standard error of at least two experiments (see Table 6.2).

the affinity of $G\alpha_{i1}$ for empty nanodiscs, *i.e.* not containing NTS1, appears to be lipid composition dependent: G protein interacts with BPL nanodiscs with a K_d of 200 ± 100 nM, while lower affinity interaction with $K_d = 400 \pm 200$ nM and $K_d = 800 \pm 600$ nM is observed for PCPGBPL and PCPG discs, respectively (Table 6.2). Addition of GTPγS significantly increased the K_d for all lipid compositions, proving the specificity of the interaction. The dependence of the affinity on the lipid composition suggests that these experiments demonstrate pre-coupling of the G protein to lipid, with K_d values similar to those observed for the receptor (Table 6.2).

6.3.6   Conclusion

The use of fluorescently labelled MSP is established here as a novel method for performing MST on membrane proteins in a native environment, allowing the use of native, unlabelled receptor. The use of labelled MSP provides improved flexibility in assay set-up compared to conventional label-free MST, which is limited to systems in which only one of the two binding partners exhibits native UV fluorescence. Furthermore, as the nanodisc-reconstituted membrane protein is the fluorescent species in this approach, the experiments require only relatively small amounts of membrane protein at low concentrations (~5-25 nM), making the approach amenable to difficult systems, such as GPCRs.

The work presented here provides insight into the importance of the lipid environment in the early stages of GPCR signalling, using a minimal system of only the (lipid-reconstituted) receptor, the G protein α subunit and ligand. Firstly, the $G\alpha_{i1}$ was shown to interact with empty nanodiscs, in a GTPγS-dependent manner, implying the interaction is specific. Furthermore, the interaction was also shown to be lipid dependent, with higher affinity found for nanodiscs with higher BPL content (Table 6.2 and Figure 6.14). It has previously been shown that GDP-bound G_i heterotrimers and the $G\beta\gamma$ heterodimers preferentially interact with PE liposomes, compared to PC liposomes, in a PE-ratio dependent manner, while GTPγS-bound $G\alpha_{i1}$ showed the opposite behaviour [492]. Indeed, the affinity of GTPγS-bound $G\alpha_{i1}$ was lowest for BPL nanodiscs, which contains the highest proportion of PE lipid of the three lipid mixtures studied here. As the conformation of $G\alpha_{i1}$ in the present study in the absence of GTPγS is likely to represent the inactive conformation found in the heterotrimer, in agreement with [492], the higher affinity of the $G\alpha_{i1}$ for BPL nanodiscs observed here might thus be due to the PE content of the discs. PE is a lipid with a propensity to form non-bilayer phases, and is predominant in the membranes of the neural system, and it is thought that the curvature that it induces in membranes contributes to the dependence of protein function on the membrane lipid composition [5]. Furthermore, the PE headgroup can form much stronger, direct hydrogen-bonds than other types of lipids, which could contribute to lipid-protein interactions [4].

It has to be noted that in the work presented here, $G\alpha_{i1}$ was expressed in *E. coli*, and thus not post-translationally modified. The study by Vögler *et al.* [492] however, used myristoylated $G\alpha_{i1}$, and α subunit acylation has been shown to be important for membrane association in the absence of the $\beta\gamma$ dimer [493, 494]. Although the lack of myristoylation greatly hampered membrane association in these studies, it was not entirely abolished [493, 494]. Expression levels in these cell-based studies are likely to be in the same concentration range as the dissociation constants observed here for the lipid-G protein interaction (~100s nM,

Table 6.2 and Figure 6.14)[5]; furthermore, it is possible that the affinity determined here in this minimal system overestimates the affinity *in vivo*, due to competitive interactions with other cytosolic components or differences in viscosity due to cellular crowding, and/or pH or ionic strength [235, 236]. Thus, taking this into consideration, at expression levels that are likely to be below the K_d, indeed a large fraction of G protein would be expected to not be associated with the membrane, as observed in the cell-based studies [493, 494], while under the minimal conditions used in the work presented here the interaction can still be observed. It is thus likely that myristoylation increases the affinity of the G protein for the membrane, although the lipid specificity does not appear to be affected.

Interestingly, the same pattern of lipid dependence was observed for the G protein-GPCR interaction, with higher affinities obtained for the BPL nanodiscs, which correlates well with the previously observed lipid requirements of the receptor for NT binding (Figure 6.4) [40]. The observation that the receptor and G protein appear to favour the same lipid environment, could mean that *in vivo* this shared preference leads to locally elevated concentrations of both signalling partners, which would be beneficial for rapid cell response to ligand stimulation. In turn, the reduced affinity of activated (GTP-bound) Gα for the receptor and the lipid membrane, under all studied lipid compositions, ensures the decoupling of the α subunit, allowing it to interact with cytosolic downstream signalling targets.

In accordance with a earlier plasmon-waveguide resonance study on opioid receptors [495], the affinity of the G protein for NTS1 appeared to be ligand-dependent, which was most clear for the BPL nanodiscs where agonist increased the basal affinity, while antagonists decreased the affinity, or kept the affinity at basal levels (Table 6.2), in accordance with their pharmacological effect of stimulation or inhibition of signalling. Another interesting observation was the difference between the two antagonists, with SR48692 reducing the G protein affinity for the receptor more strongly than SR142948A (in all cases but PCPG), in accordance the study cited in section 6.1.2, which showed SR142948A to be a less potent antagonist than SR48692 [486]. However, the broad range of antagonist activity observed for SR142948A in mice [472], and cell-based studies on the inhibition of G_q [485], suggest that the lower antagonist effect of SR142948A compared to SR48692 could be G protein subtype-dependent. Future studies with other G protein subtypes could further address this possibility of biased antagonism.

Lipid-dependence of the G protein-GPCR interaction has previously been shown for other GPCRs. In agreement with the results presented here, PE lipids have been shown to be important for the activation of rhodopsin and the affinity of transducin for the receptor

---

[5]At an average cell size of ~17 μm (COS-M6, Life Technologies), high expression levels of 1^6 molecules/cell (expression levels are not specified in [493, 494]) would result in a cellular concentration of ~1 μM.

[496, 497]. However, G_t has also been shown to be associated with negatively charged PS lipids [498]. Such a preferential interaction of G protein with negatively charged lipids could explain the seemingly contradicting results observed in the study on NTS1 by Inagaki *et al.* [42], where the apparent affinity of G_q for NTS1 showed positive correlation with the POPG content relative to POPC. However, the effect of PE lipids was not investigated in that study; it is thus possible that negatively charged lipids do lead to increased G protein interaction with the membrane, compared to a zwitterionic PC background, but that PE lipids do so to a greater extent, supporting native receptor function, as observed here. However, as a different G protein subtype was studied here (G_i *vs.* G_q), it cannot be excluded that the lipid-dependence of G protein interaction is also G protein-subtype specific. Indeed, NTS1 has been shown to couple through three G protein subtypes, and it is possible that the lipid environment of the receptor plays a role in the G protein subtype selectivity.

Thus, lipid-dependence, combined with ligand-dependence of G protein affinity, provides great scope for GPCR modulation, and could play a role in biased signalling of the receptor. This study provides a good basis for future study on how GPCR signalling is further modulated by other signalling components, such as other G protein subtypes, the βγ dimer, and post-translational modification of receptor and G protein, ultimately giving a detailed insight into the regulation of the early stages of GPCR signalling.

7 | Conclusions and future work

Recent experimental progress in the field of membrane proteins, such as improved expression techniques, protein engineering strategies to improve stability and/or reduce conformational heterogeneity, the use of small antibodies to stabilise protein conformations, and the use of lipidic-cubic-phase for crystallisation, has lead to an exponential growth in the number of available high-resolution crystal structures (see section 1.4.1). The field of GPCR structural biology in particular has relied heavily on the use of protein engineering strategies, such as the use of thermostabilising mutations, deletion of flexible, but functionally important, unstructured regions of the protein (*e.g.* IC3 and C-terminus), or the insertion of soluble proteins into said regions, which has been shown to hamper receptor activity (reviewed in Chapter 3). Indeed, crystal structures of wild-type receptors have so far only been obtained for rhodopsin, which is thought to be conformationally more homogeneous than other GPCRs, due to covalent binding of its inverse agonist ligand, and it may be that crystallisation of other wild-type GPCRs is not feasible due to their inherent flexibility precluding the long-range order required in crystal formation. Consequently, other biophysical methods such as FRET, EM, AFM, NMR and EPR which do not require crystallisation provide great scope for further study on membrane protein structure and function, particularly as they are compatible with more native membrane-reconstituted preparations. This thesis presents examples of the application of a variety of biophysical techniques to the study of membrane protein structure and function, using different membrane reconstitution methods to study the proteins in a native-like environment.

Chapter 2 presents the first example of a DEER study using liposomes to create an electrochemical gradient for the study of gradient-driven membrane protein transporters. The DEER-Stitch method used proved to be highly suited to the study of membrane proteins reconstituted into liposomes, which often suffer from short relaxation times due to the high local concentrations, compared to isotropic detergent-solubilised samples [499]. While further study is required to draw robust conclusions about the transport mechanism of $PepT_{So}$, the findings reported here demonstrate the importance of the electrochemical gradient for

substrate-induced conformational changes in the transporter. However, conformational equilibria, as gauged from the DEER distance distributions, were only modestly affected by the presence of substrate and an electrochemical gradient. This observation might in part be due to the symmetric protein insertion into the liposomes which is expected to result from the reconstitution method used [500]. Although this should not hamper the purely substrate-driven experiments, for the gradient-driven experiments symmetric insertion of the transporter results in a portion of the transporters to be oriented against the generated electrochemical gradient. The effect of this random protein distribution has not yet been investigated in transport assays. Future work could aim at silencing the spin labels on the "wrongly oriented" transporters by the addition of a reducing agent, such as ascorbic acid; by adding reductant on the outside of the liposomes in samples of PepT$_{So}$ labelled on the cytoplasmic face of the transporter, signals arising from PepT$_{So}$ reconstituted in the wrong orientation with respect to the gradient, *i.e.* with the cytoplasmic side of the transporter pointing out of the liposomes, could be silenced so that these signals do not contribute to the observed distance distribution. To silence unwanted signals from PepT$_{So}$ labelled at the periplasmic face of the transporter reducing agent would have to be included in the internal liposome buffer. However, as in the current reconstitution protocol the internal liposome buffer is also present outside the liposomes before the buffer is exchanged, this strategy would be limited to silencing cytoplasmic labelled sites. Furthermore, such a strategy would be technically challenging, as it would greatly reduce the absolute signal measured, although the sensitivity issue could in part be overcome by using Q-band rather than X-band instrumentation, which greatly improves the sensitivity of the DEER experiment (see Chapter 5). Alternatively, the reconstitution procedure could be optimised so as to obtain asymmetric insertion of the transporter, as has been achieved for other membrane proteins [501].

Rotamer analysis was used to predict spin label distance distributions for different residue pairs, in an attempt to attribute observed distances to specific states of the receptor in the transport cycle. This approach showed that although distinguishable interlabel distances might be expected from Cα-Cα distances derived from structural models, the conformational flexibility of the spin label can lead to overlapping distance distributions, which cannot be readily distinguished in the DEER experiment. Therefore, future work will aim at using the knowledge gained from rotamer analysis in choosing informative labelling sites. Furthermore, if by such an approach residue pairs can be found that report on the conformational state of the transporter, *i.e.* residue pairs with DEER distance distributions in which peaks can clearly be attributed to different conformational states, then DEER measurements on such samples can be used in future functional studies of the transporter, where not only the effect of substrate and/or gradient can be investigated, but also the functional implications

of different receptor mutants might be linked to transporter structure.

The rest of this thesis focuses on an experimentally more challenging membrane protein system, the GPCR NTS1. Various structural and functional aspects of the receptor are investigated including receptor activation, G protein binding, and receptor oligomerisation. The NTS1 purification protocol was further optimised, and a labelling protocol for site-directly labelling of NTS1 cysteine mutants was established in order to obtain samples of sufficient quality amenable to FRET, EPR and other biophysical techniques (Chapter 3). CW-EPR was then used to study the effect of agonist on the local dynamics of spin probes at the intracellular side of the protein (Chapter 4). Observed effects of agonist were relatively modest with the largest changes occurring in TM5-6, in agreement with the consensus model of GPCR activation. Improvements in sample preparation that have been made since the execution of these early CW-EPR studies mean that shorter EPR measurement times would now possible, opening up the possibility of repeating the measurements at slightly higher temperatures, which could lead to more pronounced effects as previously observed for rhodopsin [363]. Furthermore, it would be interesting to study the effect of G protein on the EPR spectra, as it has been postulated that the presence of G protein is required to stabilise the active state of the receptor [345, 365]. In addition, a CW-EPR sequence scanning study presented in Chapter 4 confirmed the presence of an α-helical C-terminal H8 segment for the non-thermostabilised, membrane-reconstituted receptor, settling the controversy raised by conflicting crystallographic results of two different thermostabilised NTS1 mutants. The helical structure was observed both in the presence and absence of agonist, suggesting that H8 secondary structure is not involved in receptor activation. Some modest changes in spin label dynamics were however observed upon addition of agonist. Again, it would be interesting to study how the presence of G protein affects the agonist-induced changes in H8 dynamics observed by EPR. Circular dichroism studies on a peptide corresponding to H8 are planned in order to determine the effect of the membrane environment on H8 secondary structure, by measuring peptide helicity in the presence and absence of liposomes. Furthermore, molecular dynamics simulations on the receptor embedded in lipid bilayers of different lipid compositions are under way in order to obtain more detailed insight into the molecular interactions between H8 and the rest of the protein, and the lipid bilayer, and how these relate to its stability.

In Chapter 5 ensemble and single-molecule FRET were combined with DEER to investigate the oligomerisation interface and oligomerisation dynamics of NTS1. Whereas previous research had suggested that NTS1 forms constitutive dimers [206], the work presented here is

consistent with more recent single-molecule studies on GPCR oligomerisation, showing that oligomerisation is transient (with a dimer lifetime of ~10s-100s ms) and that the interface of the dimer is dynamic. The data is consistent with the presence of multiple dimerisation interfaces, and revealed a concentration dependence of the extent of oligomerisation, in agreement with the law of mass action. Agonist did not appear to affect the overall extent of oligomerisation observed in the ensemble FRET experiments, nor the proposed dimerisation interfaces, and only significantly affected the FRET efficiency observed for NTS1 labelled on TM6. This result is in agreement with the CW-EPR data (Chapter 4) and the consensus on GPCR activation, that TM6 undergoes the largest conformational change upon ligand binding, suggesting that agonist induces similar conformational changes in the dimer as observed in the monomer, and by extension that the dimer might be signalling competent. The physiological significance of NTS1 homodimerisation is as yet unknown, although detergent studies have shown that dimers couple less efficiently to G protein in detergent [321]. Future studies using the *in vitro* systems established here, and in particular the single-molecule FRET system, could further study the effect of agonists, antagonists and/or the presence of G proteins on the dynamics of NTS1 dimerisation. Furthermore, *in vivo* studies of NTS1 oligomerisation at varying expression levels, combining single-molecule FRET techniques to look at the extent of dimerisation, with functional assays, could shed light the role of dimerisation on receptor signalling, and test the negative feedback mechanism proposed in Chapter 5 (*i.e.* that NT-induced increased expression of NTS1 [463], leads to increased dimerisation at high receptor concentration and concomitant down-regulation of signalling).

While the DEER studies presented here suggested the presence of multiple dimerisation interfaces, the quality of the data (*i.e.* limited t_{max} at X-band, and poor modulation depth at Q-band due to the limited excitation bandwidth) was not sufficient to use confidently in determining which helices participate in the oligomerisation interface. This could be greatly improved by performing Q-band DEER measurements using higher-power equipment, which would improve the excitation bandwidth of the experiment. However, the information on preferred oligomerisation interfaces gained by FRET could already be used in a molecular modelling, or protein docking approaches, to gain more insight on the molecular origin of the proposed TM interfaces, as has been done for the proposed interfaces of the β-adrenergic receptors [461].

In Chapter 6, the signalling mechanism of NTS1, was investigated using the novel biophysical method of microscale thermophoresis (MST) to assess the affinity of the receptor to G protein *in vitro* in the absence of ligand, or in the presence of agonist or antagonist. To

assess the influence of the lipid environment on the receptor function, MST measurements were preformed in detergent and in nanodiscs of different lipid compositions. Nanodiscs in which the MSP belt protein, surrounding the lipid bilayer of the nanodisc, was fluorescently tagged were successfully formed, and their disc morphology was confirmed by EM. Thus, the use of fluorescently labelled nanodiscs is established here as a novel, general method for performing MST on membrane proteins in a native environment, allowing the use of native, unlabelled receptor. Using NTS1 reconstituted into labelled nanodiscs, it was shown that G protein has a higher affinity for the receptor in lipid mixes closer to native conditions (*i.e.* lipid mixes with higher BPL content), suggesting an important role for the lipids in receptor activity. Furthermore, the possibility of biased antagonism was raised, as while one of the tested antagonists (SR48692) increased the K_d of the G protein-receptor interaction compared to agonist, the other (SR142948A) only showed a modest effect on the K_d. Tests with empty nanodiscs also suggested preferential interaction of the G protein with BPL over POPC-POPG lipid mixtures. This work provides a good basis for future study on how GPCR signalling is further modulated by other signalling components; *e.g.* experiments with other G protein subtypes and/or other ligands could further explore the possibility of biased-signalling. In addition, the effect of the G protein βγ subunits could be tested, as well as post-translational modifications of the receptor and G protein, or interactions with β-arrestins, and other regulatory components [502].

In summary, this work represents the first CW-EPR (Chapter 4), pulsed EPR (Chapter 5), single-molecule FRET (Chapter 5), and MST (Chapter 6) studies on a lipid-embedded GPCR binding a diffusible ligand. As well as providing considerable insight into a variety of functional aspects of NTS1, this thesis opens up several promising lines of research for future study of NTS1 and other membrane proteins in physiologically relevant environments.

A | Materials and methods

Brief material and methods are provided in each chapter. This appendix provides a more detailed overview of the experimental conditions for the work presented in this thesis.

A.1 Buffers

Note: Temperature-sensitive buffers (*e.g.* Tris-HCl buffers) are adjusted to the required pH at the temperature that the buffers will be used.

A.1.1 Growth media

Luria-Bertani (LB): Bought from BD (Per litre: 10 g bacto-tryptone, 5 g yeast extract, 10 g NaCl) for DH5α cells; supplemented with 1% glucose (w/v) for BL21 cells.
LB Agar: Bought from BD (Per litre: 10 g bacto-tryptone, 5 g yeast extract, 10 g NaCl, 15 g agar) for DH5α cells; supplemented with 1% glucose (w/v) for BL21 cells.
SOC medium: Per litre: 20 g bacto-tryptone, 5 g yeast extract, 0.5 g NaCl, 2.5 mM KCl, 10 mM MgCl$_2$, 20 mM glucose, adjusted to pH 7.0.
2×YT: Per litre: 16 g peptone, 10 g yeast extract, 5 g NaCl, adjusted to pH 7.0. Supplemented with 0.2% glucose (w/v) for NTS1 expression.
TB medium for MSP expression: Per 900 mL, 12 g peptone, 24 g yeast extract, 4 mL glycerol, to which is added 100 mL 0.17 M KH$_2$PO$_4$, 0.72 M K$_2$HPO$_4$ (sterilised separately from rest of the medium).

A.1.2 NTS1B purification

Protease inhibitors: Leupeptin, pepstatin A, aprotinin, at a final concentration of respectively 2 µg/mL, 2 µg/mL and 3 µg/mL.
2× Solubilisation buffer: 100 mM Tris-HCl, pH 7.4, 400 mM NaCl, 60% glycerol (v/v), protease inhibitors.
NiA: 50 mM Tris-HCl, pH 7.4, 200 mM NaCl, 10% glycerol (v/v), 0.5% CHAPS (w/v), 0.1% DDM (w/v), 0.1% CHS (w/v), 50 mM imidazole, protease inhibitors.

NiB: 50 mM Tris-HCl, pH 7.4, 200 mM NaCl, 10% glycerol (v/v), 0.5% CHAPS (w/v), 0.1% DDM (w/v), 0.1% CHS (w/v), 500 mM imidazole, protease inhibitors.

NT0: 50 mM Tris, pH 7.4, 10% glycerol, 0.1% DDM (w/v), 0.01% CHS (w/v).

NT70, NT150, NT1: Same as NT0, supplemented with 70, 150 or 1000 mM NaCl, respectively.

NiA^0 for 1 mL Ni^{2+} column concentration: 50 mM Tris-HCl, pH 7.4, 200 mM NaCl, 10% glycerol (v/v), 0.1% DDM (w/v), 0.01% CHS (w/v).

NiB$^-$ for 1 mL Ni^{2+} column concentration: Same as NiA^0, supplemented with 500 mM imidazole.

SE buffer: 50 mM Tris-HCl pH 7.4, 10% glycerol (v/v), 50 mM NaCl, 0.1% DDM (w/v), 0.01% CHS (w/v), 1 mM EDTA.

Assay buffer for detergent samples: 50 mM Tris-HCl pH 7.4, 0.1% DDM (w/v), 0.01% CHS (w/v), 1 mM EDTA, 0.1 mg/mL BSA.

Liposome buffer: 50 mM Tris-HCl pH 7.4, 50-200 mM NaCl (depending on end use), 1 mM EDTA, saturate buffer with N_2 before use.

Nanodisc lipid buffer: 50 mM Tris-HCl pH 7.4, 50 mM NaCl, 1 mM EDTA, 100 mM sodium cholate.

Nanodisc GF buffer: 50 mM Tris-HCl pH 7.4, 50 mM NaCl, 5 mM $MgCl_2$.

A.1.3 TEV purification

Sample buffer: 50 mM Tris-HCl pH 7.4, 300 mM NaCl.

Wash buffer: 50 mM Tris-HCl pH 7.4, 300 mM NaCl, 30 mM imidazole.

Elution buffer: 50 mM Tris-HCl pH 7.4, 300 mM NaCl, 500 mM imidazole.

Dilution buffer: 50 mM Tris-HCl pH 7.4, 300 mM NaCl, 50% glycerol (v/v).

A.1.4 MSP purification

Resuspension buffer: 20 mM phosphate buffer, pH 7.4, protease inhibitors.

Wash buffer 1: 40 mM Tris-HCl pH 8.0, 0.3 M NaCl, 1% Triton X-100 (v/v).

Wash buffer 2: 40 mM Tris-HCl pH 8.0, 0.3 M NaCl, 50 mM sodium cholate, 20 mM imidazole.

Wash buffer 3: 40 mM Tris-HCl pH 8.0, 0.3 M NaCl, 50 mM imidazole.

Elution: 40 mM Tris-HCl pH 8.0, 0.3 M NaCl, 0.4 M imidazole.

Dialysis buffer: 20 mM Tris-HCl pH 7.4, 0.1 M NaCl, 0.5 mM EDTA.

A.1.5 Gα_{i1}

Equilibration buffer: 50 mM Tris-HCl pH 8.0, 20 mM β-mercaptoethanol, protease inhibitors.

Wash buffer: 50 mM Tris-HCl pH 8.0, 20 mM β-mercaptoethanol, 0.5 M NaCl, 10 mM imidazole, protease inhibitors.

Elution buffer 1: 50 mM Tris-HCl pH 8.0, 20 mM β-mercaptoethanol, 100 mM NaCl, 10 mM imidazole, 10% glycerol.

Elution buffer 2: 50 mM Tris-HCl pH 8.0, 20 mM β-mercaptoethanol, 100 mM NaCl, 500 mM imidazole, 10% glycerol.

Dialysis buffer: 50 mM Tris-HCl pH 7.4, 50 mM NaCl, 10% glycerol (v/v), 5 mM $MgCl_2$.

A.1.6 SDS-PAGE and western blotting

2× Sample buffer: 200 mM Tris-HCl (pH 8.8), 20% glycerol (v/v), 5 mM EDTA, 0.02% bromophenol blue (w/v). To a 700 μL aliquot, 200 μL 20% SDS (w/v) and 100 μL 0.5 M DTT is added before use.

Tris-Glycine SDS running buffer: 25 mM Tris pH 8.3, 192 mM Glycine, 0.1% SDS (w/v).

MES running buffer: 20× stock bought from Invitrogen (50 mM Tris base, 50 mM MES (2-(N-morpholino)ethanesulfonic acid), 1 mM EDTA, 0.1% SDS at pH 7.3).

Tris-Glycine transfer buffer: 12 mM Tris-HCl pH 8.3, 96 mM Glycine.

Coomassie Brilliant Blue staining solution: Coomassie Brilliant Blue R250 (0.25% w/v), methanol (45% v/v), MilliQ H_2O (45% v/v), glacial acetic acid (10% v/v).

Coomassie destain solution: Methanol (45% v/v), MilliQ H_2O (45% v/v), glacial acetic acid (10% v/v).

A.2 PepT_{So}

PepT_{So} cysteine mutants were expressed and purified by Simon Newstead and Nicolae Solcan (Department of Biochemistry, Oxford), as described previously [254]. Purified samples were reduced for one hour at room temperature (RT) in 10 mM TCEP in buffer (20 mM Tris-HCl, pH 7.5, 150 mM NaCl, 0.03% DDM (w/v), 30% glycerol (v/v)). The solution was diluted to a final volume of 1.5 mL and reductant was removed by size-exclusion chromatography (5 mL HiTrap Desalt, GE Healthcare; two columns were connected in tandem for larger sample volumes) on an ÄKTA purification system (GE Healthcare - all column chromatography reported in this thesis was performed on an ÄKTA system unless stated

otherwise). Spin label, (1-oxyl-2,2,5,5-tetramethylpyrroline-3-methyl)-methanethiosulfonate (MTSL), was obtained from Toronto Research Chemicals. MTSL was dissolved in DMSO (10 mg/mL) and added at a tenfold molar excess over each cysteine labelling site, and incubated with the sample for three hours at RT. The sample was concentrated to 500 μL using a vivaspin500 concentrator with a 50 kDa molecular weight cut-off (Sartorius Stedium), and run on a Superdex 200 10/30 gel filtration column (GE Healthcare) pre-equilibrated with reconstitution buffer (50 mM KPi, 150 mM KCl, 0.3 % (w/v) n-decyl-β-D-maltoside (DM) at pH 7); this was done to remove excess spin label, and to exchange the detergent DDM for DM as the latter has a ~10-fold higher CMC and is thus easier to remove for lipid reconstitution. Samples were reconstituted by Nicolae Solcan into liposomes of acetone-ether washed $E.$ $coli$ total lipid extract and POPC (Avanti Polar Lipids) at a 3:1 ratio (w/w) by rapid dilution (see also [267]). Lipids were resuspended in liposome buffer (50 mM Kpi at pH 7), and added to the protein at a 1000:1 molar ratio, followed by rapid (150-fold) dilution into liposome buffer, to dilute the DM concentration below its CMC, and ultracentrifugation (130,000×g) to pellet proteoliposomes. Pellets were resuspended in storage buffer to ~0.4 mg/mL, followed by five freeze-thaw cycles to scramble the protein orientation in the membrane [500]. To have the desired internal and external buffer for transport assays and DEER experiments, samples were extruded, as that breaks open the liposomes, allowing for replacement of the internal buffer. To this end proteoliposomes were pelleted (50,000 rpm, TLA 100.2 rotor, Beckman Coultier, 30 min at 4 °C), resuspended in the desired internal buffer, and extruded through 400 nm polycarbonate filters (Avanti Polar Lipids) 11 passes using a mini-extruder (Avanti Polar Lipids). Proteoliposomes were then again pelleted (as before but at 15 °C to prevent membrane fusion) and resuspended in 15 μL of the desired external buffer.

Transport was either initiated in a electrochemically (ΔΨ) driven manner, or substrate-gradient-driven manner (counterflow). For the ΔΨ-driven experiment, liposomes were created with a high concentration of K^+ ions in the internal buffer (120 mM) and resuspended in external buffer without K^+ (but otherwise balanced in charge, by 120 mM Na^+) containing the K^+-ionophore valinomycin (10 μM). Valinomycin-mediated K^+ efflux from the liposomal lumen creates an electrical potential, ΔΨ, across the membrane (positive out, negative in), as described by Viitanen et $al.$ [503]

$$\Delta\Psi(\text{mV}) = -59\log\left(\left[K^+\right]_{in} / \left[K^+\right]_{out}\right) \tag{A.1}$$

where $\left[K^+\right]_{in}$ and $\left[K^+\right]_{out}$ are the concentrations of K^+ ions inside and outside of the liposomes. The excess of positive charge outside the liposomes leads to protonation of the transporter, facilitating transport of di-alanine (di-Ala, ^{3}H-labelled for the transport assay,

unlabelled in the DEER experiments). For transport assays, radio-ligand accumulated in-side the liposome is quantified by scintillation counting (Perkin Elmer, Wallac 1409 DSA liquid scintillation counter).

In counterflow conditions, internal and external buffer have the same ion concentrations, and instead 10 mM of di-Ala is added to the internal buffer. This leads to transport of the unlabelled diAla down its concentration gradient, and concomitant uptake of ^{3}H-diAla which is included at low concentrations (5 µM) in the external buffer for activity assays, until the di-Ala gradient is equilibrated, after which accumulated radio-ligand is quantified. This latter transport mechanism is uncoupled from proton transport. Internal and external buffers for both experimental set-ups are given in Table A.1.

Table A.1: PepT$_{So}$ buffer conditions for transport. Internal and external liposome buffer was adjusted to initiate substrate (diAla) transport in a electrochemically driven manner ($\Delta\Psi$) or by a substrate gradient (counterflow) as discussed in the text. All buffers were adjusted to pH 6.5. The amount of peptide added to the external buffer (tritium labelled for transport assays, unlabelled in the DEER experiments) is also given.

Buffer	Experimental set-up	
	$\Delta\Psi$-driven	Counterflow
Internal	20 mM KPi, 100 mM Kac, 2 mM MgSO$_4$	20 mM KPi, 2 mM MgSO$_4$, 10 mM (cold) diAla
External	120 mM NaPIPES, 2 mM MgSO$_4$, 10 µM valinomycin	20 mM KPi, 2 mM MgSO$_4$
(^{3}H-)diAla	15 µM	5 µM

Thus, DEER samples were prepared in 4 conditions: with electrochemical gradient and substrate ($\Delta\Psi$+diAla), with electrochemical gradient, without substrate ($\Delta\Psi$ apo), without gradient with substrate (counterflow, CF+diAla), and without gradient without substrate (CF apo). A fifth condition was tested for one mutant, where the same buffers as for the $\Delta\Psi$ samples were used, but without valinomycin, to control for any buffer effects ($\Delta\Psi$ control). As transport assays show that transport of added substrate completes within ~5-15 min, 10 µL of the external buffer was added shortly before transfer into high-precision 3 mm quartz tubes (Wilmad-LabGlass) to initiate transport. Samples were then quickly flash-frozen in liquid nitrogen to trap the protein in a transporting state, and to avoid water crystallisation.

A.3   TEV protease

Starter cultures (7.5 mL LB, 50 µg/mL kanamycin) were inoculated with a single culture of TEV plasmid-transformed BL21(DE3) each, and incubated overnight at 37 °C and 200 rpm. In 2 L conical flasks, aliquots of 500 mL 2×YT medium supplemented with 50 µg/mL

kanamycin were inoculated with 5 mL of starter culture each, and incubated at 37 °C at 120 rpm, usually growing 10 L of culture at a time. When the culture reached an OD_{600} of 0.25 the temperature was lowered to 20 °C. Expression was induced at an OD_{600} of 0.6 by addition of IPTG to a final concentration of 0.4 mM, and cells were grown overnight. Cells were harvested by centrifugation (7,000×g, 4 °C, 15 min) and stored at -80 °C or used directly. Cell pellet (~40-60 g) was resuspended in a minimal volume (~1:1) of TEV sample buffer supplemented with protease inhibitors. Cells were incubated on ice with DNase I (~1 mg) and lysozyme (1 mg/mL) for 20 min and then lysed using a French press (3 rounds at 1,000 psi). Cell debris was separated from lysate by centrifugation (70,000×g, 50 min, 4 °C). Supernatant was filtered through a 0.2 μm syringe filter and imidazole was added to a final concentration of 30 mM, before loading the sample onto a 5 mL HisTrap HP column (GE Healthcare), pre-equilibrated with sample buffer supplemented with 30 mM imidazole. The sample was washed with ~50 CV of 30 mM imidazole sample buffer and then eluted with an imidazole step gradient of 100 mM for 4 CV, 150 mM for 4 CV, 200 mM for 2 CV, and 350 mM for 6-8 CV. Fractions were analysed by SDS-PAGE and the cleanest fractions were pooled and concentrated using a centrifugal concentrator (vivaspin20, 10,000 MWCO, Sartorius Stedium Biotech) and diluted in sample buffer with 50% glycerol (v/v) to dilute the imidazole concentration below 100 mM. Final TEV concentration was determined by A_{280} ($\epsilon_{280} = 32,290$ $M^{-1}cm^{-1}$).

A.4   Membrane scaffold protein (MSP)

The membrane scaffold protein (MSP) construct MSP1D1 was altered to include a cysteine at the N-terminus after the TEV protease recognition site for labelling purposes, yielding the construct CysMSP.[1] The cysteine was introduced by QuickChange site-directed mutagenesis as described in section A.5.1 using primers listed in Table A.2 (all primers used in this thesis were purchased from Sigma-Aldrich). MSP was expressed and purified as previously described in [139] with minor modifications. Briefly, starter cultures (7.5 mL LB, 50 μg/mL kanamycin) were inoculated with a single culture of CysMSP plasmid-transformed BL21(DE3) each, and incubated overnight at 37 °C and 200 rpm. In 2 L conical flasks, aliquots of 500 mL TB medium supplemented with 50 μg/mL kanamycin were inoculated with 5 mL of starter culture each, and incubated at 37 °C at 200 rpm, usually growing 10 L of culture at a time. When the culture reached an OD_{600} of 1.4-1.6 expression was induced by addition of IPTG to a final concentration of 1 mM. Cells were harvested 3 h

---

[1]The primers were designed by myself, but the PCR was carried out by Alan Goddard (Department of Biochemistry, University of Oxford, now University of Lincoln) and Adriana Cherskov (Department of Biochemistry, University of Oxford, visiting student from Princeton University).

Table A.2: Primers for Cys mutation to MSP1D1. A cysteine was introduced at the N-terminus after the TEV protease recognition site for labelling purposes, to avoid labelling the numerous lyseines which are likely important for function.

Primers	
For:	**5' G TAT TTT CAG GGT TCT ACC TGC TTC AGT AAA CTT CGC GAA C 3'**
Rev:	**5' G TTC GCG AAG TTT ACT GAA GCA GGT AGA ACC CTG AAA ATA C 3'**

post-induction by centrifugation (7,000×g, 4 °C, 15 min) and stored at -80 °C. Thawed cell pellet (~40-60 g) was resuspended in 100 mL of 20 mM phosphate buffer pH 7.4, supplemented with protease inhibitors and ~1 mg of DNase I. Triton X-100 (Sigma-Aldrich) was added to a final concentration of 1% (v/v), and the cells were lysed by sonication (3×1 min) with a probe sonicator. Cell debris was separated from the lysate by centrifugation (30,000×g, 30 min). Imidazole was added to the supernatant (20 mM), and the lysate was loaded on an 5 mL HisTrap HP column (GE Healthcare), equilibrated with 40 mM phosphate buffer pH 7.4. The column was washed with 50-70 CV of each of the washing buffers: (1) 40mM Tris-HCl pH 8, 0.3 M NaCl, 1 % Triton-X (v/v); (2) 40mM Tris-HCl pH 8, 0.3 M NaCl, 50 mM sodium cholate, 20 mM imidazole; and (3) 40mM Tris-HCl pH 8, 0.3 M NaCl, 50 mM imidazole. MSP was then eluted with 400 mM imidazole. Cleanest fractions (as determined by SDS-PAGE) were pooled and concentrated in centrifugal concentrators (vivaspin20, 10,000 MWCO), and diluted in and/or dialysed against 20 mM Tris-HCl pH 7.4, 0.1 M NaCl, 0.5 mM EDTA at 4 °C. Final MSP concentration was determined by A$_{280}$ (ϵ_{280} =21,430 M^{-1}cm^{-1}).

If required, the N-terminal His$_6$-tag was cleaved off by overnight incubation with TEV protease at a 10:1 (MSP:TEV) molar ratio in the presence of 5 mM DTT. Cleaved MSP was separated from TEV protease, any uncleaved MSP and cleavage products by IMAC. MSP was dialysed or diluted so that the imidazole concentration was below 20 mM. The sample was passed over a 1 mL HisTrap HP column (GE Healthcare), and flow-through was collected, followed by a 20 mM imidazole wash to remove non-specifically bound cleaved MSP. Fractions of flow-through and wash were inspected by SDS-PAGE, pooled and re-concentrated it if needed in a centrifugal concentrator. Final cleaved MSP concentration was determined by A$_{280}$ (ϵ_{280} =18,450 M^{-1}cm^{-1}).

For MST experiments with fluorescent nanodiscs, the cleaved MSP was labelled with Alexa Fluor 647 (A647, Life Technologies). The concentrated sample was reduced with 10 mM DTT for 1 h at room temperature, after which the reductant was removed by gel filtration using two 5 mL HiTrap Desalt columns (GE Healthcare) connected in tandem, equilibrated

with MSP dialysis buffer. The freshly reduced sample was then incubated with a small excess (1.7:1 mol:mol) of A647 for 3 h at room temperature. The pH was controlled to ensure pH <7.5 to favour Cys labelling over Lys labelling. Excess dye was then removed by gel filtration on a 10/30 Superdex 75 column (GE Healthcare), equilibrated with MSP dialysis buffer. Labelling efficiency was determined by comparing the absorption at 280 nm with that of the fluorophore maximum, correcting for the contribution of the fluorophore at 280 nm:

$$E_{labelling} = \frac{[\text{Label}]}{[\text{Protein}]} = \frac{A_{Fluor}/\epsilon_{Fluor}}{(A_{280} - CF \times A_{fluor})/\epsilon_{Protein}} \tag{A.2}$$

where A_{Fluor} and A_{280} are the maximum absorption of the fluorophore and the absorption at 280 nm, respectively, ϵ_{Fluor} the extinction coefficient of the fluorophore at its maximum, and $\epsilon_{Protein}$ that of the protein at 280 nm. CF is a correction factor to account for the contribution of the fluorophore at 280 nm which is determined from the excitation spectrum of the free fluorophore in solution as the percentage absorption at 280 nm compared to its maximum absorption.

A.5   Neurotensin receptor 1

A.5.1   Site-directed mutagenesis

For site-directed labelling of cysteines with fluorophores or spin labels, a Cys-depleted background mutant (ΔCys-NTS1B) was used, in which native accessible cysteines are mutated to alanine or serine. The existing NTS1B construct naturally contains two cysteines in the TrxA stretch and nine cysteines in the NTS1 stretch, of which seven are putatively exposed (*i.e.* not buried in the transmembrane region). The exposed TrxA cysteines (C32 and C35 in native TrxA) and five of the exposed NTS1 cysteines (C172$^{3.55}$, C278^{IC3}, C332$^{6.59}$, C386$^{C\text{-term}}$, and C388$^{C\text{-term}}$ in NTS1) were mutated to serines, and one alanine for C388. The two remaining "exposed" NTS1 cysteines (C142$^{3.25}$ and C225^{EC2}) were not mutated, as they are likely to form a disulfide bridge that is conserved in family A GPCRs, and mutating either cysteine results in an inactive complex.[2] However, when treated with reductant the receptor remains active (*i.e.* ligand-binding), suggesting that these disulfide bridge cysteines are inaccessible for spin labelling. Similar results were obtained in a fluorescence labelling study of the β_2-adrenergic receptor, where the corresponding disulfide bond cysteines were also left unmutated [409]. New cysteine mutations at selected sites were introduced in this background mutant, for site-directed labelling (see Tables A.4 and A.5).

In addition to Cys mutants, a new NTS1 construct based on NTS1B, NTS1BH$_6$, was made

---

[2]Unpublished results, H. Attrill.

Table A.3: ΔCys mutants of NTS1B. Native accessible cysteines are replaced by serines and one alanine. The C388A mutation was made after the C386S mutation, and thus includes this mutation in the primer sequence. Ligand-binding activity of the individual mutants was previously shown to be similar to WT (unpublished results).

Residue	Primers	
C172S	For:	**5'** GTG GAG CGC TAC TTG GCC ATC AGC CAT CCC TTC AAG GCC AAG ACC **3'**
	Rev:	**5'** GGT CTT GGC CTT GAA GGG ATG GCT GAT GGC CAA GTA GCG CTC CAC **3'**
C278S	For:	**5'** GAG CAG GGC CGA GTG AGC ACC GTG GGC ACA CAC **3'**
	Rev:	**5'** GTG TGT GCC CAC GGT GCT CAC TCG GCC CTG CTC **3'**
C332S	For:	**5'** CGA CGC CTG ATG TTC AGC TAT ATC TCG GAT GAA **3'**
	Rev:	**5'** G TTC ATC CGA GAT ATA GCT GAA CAT CAG GCG TCG **3'**
C386S	For:	**5'** CTG TCC ACG CTG GCC AGC CTT TGT CCT GGG TGG **3'**
	Rev:	**5'** CCA CCC AGG ACA AAG GCT GGC CAG CGT GGA CAG **3'**
C388A	For:	**5'** ACG CTG GCC AGC CTT GCG CCT GGG TGG CGC CAC **3'**
	Rev:	**5'** GCG GCG CCA CCC AGG CGC AAG GCT GGC CAG CGT **3'**
C32STrx & C35STrx	For:	**5'** TTC TGG GCA GAG TGG AGC GGT CCG AGC AAA ATG ATC GCC CCG **3'**
	Rev:	**5'** CGG GGC GAT CAT TTT GCT CGG ACC GCTCT CCA CTC TGC CCA GAA **3'**

that has an additional His$_6$-tag at the C-terminus of NTS1 between the TEV recognition sites. This construct was created to allow IMAC on cleaved NTS1B (*i.e.* NTS1), and specifically, the use of a 1 mL nickel column to combine and concentrate several batches of NT column eluate (see section A.5.2.3). The primers used to do this (designed by Alan Goddard) are shown in Table A.6. This mutation was also introduced in the ΔCys-NTS1B mutant, and cysteine mutants thereof. These NTS1BH$_6$ mutants were all exclusively used when cleaved NTS1 was the desired end-product. All work with the full-length fusion construct was performed using the original NTS1B construct.

Site-directed mutagenesis was performed based on the QuickChange II protocol (Stratagene). 2.5 U of *Pfu*Ultra HF DNA polymerase (2.5 U/µL) was added to the PCR reaction mixture (Table A.7). The temperature was cycled according to Table A.8. The annealing temperature and number of cycles were varied if required. Parental DNA was digested for 1 hour at 37 °C by addition of 10 U DpnI restriction enzyme (10 U/µL, Life Technologies). All mutations were verified by gene sequencing (SourceBioscience).

A.5.2 Expression and purification

A.5.2.1 Transforming *E. coli*

A 50 µL aliquot of DH5α (for site-directed mutagenesis) or BL21(DE3) (for expression) competent cells (Novagen), was incubated on ice with ~250 ng of plasmid DNA stock for 30 min. Cells were heat shocked (90 s at 42 °C) and placed on ice for 2 minutes. 500 µL

Table A.4: Cysteine mutants of NTS1. Residues on the helix/loop interfaces were chosen based on alignment with successful labelling sites in previous SDSL studies of rhodopsin. Cysteines were introduced at the chosen sites by site-directed mutagenesis using the primers listed here.

Residue			Primers
TM1	A90	For:	**5'** GCC TTC ACT CTA TGC CGG AAG AAG TCA CTG C **3'**
		Rev:	**5'** G CAG TGA CTT CTT CCG GCA TAG AGT GAA GGC **3'**
TM2	Y104	For:	**5'** CAG AGC ACT GTG CAT TGC CAC CTG GGC AGC CTG **3'**
		Rev:	**5'** CAG GCT GCC CAG GTG GCA ATG CAC AGT GCT CTG **3'**
TM3	L169	For:	**5'** AGT GTG GAG CGC TAC TGC GCC ATC AGC CAT CCC **3'**
		Rev:	**5'** GGG ATG GCT GAT GGC GCA GTA GCG CTC CAC ACT **3'**
	C172	For:	**5'** CGC TAC TTG GCC ATC TGC CAT CCC TTC AAG GCC **3'**
		Rev:	**5'** GGC CTT GAA GGG ATG GCA GAT GGC CAA GTA GCG **3'**
TM4	R183	For:	**5'** ACC CTC ATG TCC TGC AGC CGC ACC AAG **3'**
		Rev:	**5'** CTT GGT GCG GCT GCA GGA CAT GAG GGT **3'**
	T186	For:	**5'** TCC CGC AGC CGC TGC AAG AAA TTC ATC **3'**
		Rev:	**5'** GAT GAA TTT CTT GCA GCG GCT GCG GGA **3'**
TM5	V259	For:	**5'** TCC ATC CTA AAC ACC TGC ATT GCC AAC AAA CTG **3'**
		Rev:	**5'** CAG TTT GTT GGC AAT GCA GGT GTT TAG GAT GGA **3'**
	A261	For:	**5'** CTA AAC ACC GTG ATT TGC AAC AAA CTG ACA GTC **3'**
		Rev:	**5'** GAC TGT CAG TTT GTT GCA AAT CAC GGT GTT TAG **3'**
	A272	For:	**5'** ATG GTG CAC CAG GCC TGC GAG CAG GGC CGA GTG **3'**
		Rev:	**5'** CAC TCG GCC CTG CTC GCA GGC CTG GTG CAC CAT **3'**
TM6	E296	For:	**5'** TTC AAC ATG ACC ATC TGC CCG GGT CGT GTC CAG **3'**
		Rev	**5'** CTG GAC ACG ACC CGG GCA GAT GGT CAT GTT GAA **3'**
	G298	For:	**5'** ATG ACC ATC GAG CCG TGT CGT GTC CAG GCC CTG **3'**
		Rev:	**5'** CAG GGC CTG GAC ACG ACA CGG CTC GAT GGT CAT **3'**
	R304	For:	**5'** CGT GTC CAG GCC CTG TGC CAC GGA GTC CTC GTC **3'**
		Rev:	**5'** GAC GAG GAC TCC GTG GCA CAG GGC CTG GAC ACG **3'**
	V307	For:	**5'** GCC CTG CGC CAC GGA TGC CTC GTC TTA CGT GCT **3'**
		Rev:	**5'** AGC ACG TAA GAC GAG GCA TCC GTG GCG CAG GGC **3'**
TM7	L371	For:	**5'** CCC ATC CTC TAC AAC TGC GTC TCC GCC AAC TTC **3'**
		Rev:	**5'** GAA GTT GGC GGA GAC GCA GTT GTA GAG GAT GGG **3'**
H8	Q378	For:	**5'** TCC GCC AAC TTC CGC TGC GTC TTT CTG TCC ACG **3'**
		Rev:	**5'** CGT GGA CAG AAA GAC GCA GCG GAA GTT GGC GGA **3'**

of SOC medium was added and the cells were subsequently incubated at 37 °C for 1 h. The culture was then plated onto LB agar plates supplemented with 100 µg/mL ampicillin (Sigma-Aldrich), and 1% glucose (w/v) for the BL21 cells, and incubated overnight at 37 °C.

A.5.2.2 Expression in *E. coli*

Starter cultures (7.5 mL LB, 1% (w/v) glucose, 100 µg/mL ampicillin) were inoculated with a single culture of NTS1B(H$_6$) plasmid-transformed BL21(DE3) each, and incubated

Table A.5: Cysteine mutants helix 8 NTS1. Individual cysteine mutants were made for the sequence predicted to form H8 in NTS1, for secondary structure analysis by SDSL CW-EPR.

Residue	Primers	
A374C	For:	5' TAC AAC CTG GTC TCC TGC AAC TTC CGC CAG GTC 3'
	Rev:	5' GAC CTG GCG GAA GTT GCA GGA GAC CAG GTT GTA 3'
N375C	For:	5' AAC CTG GTC TCC GCC TGC TTC CGC CAG GTC TTT 3'
	Rev:	5' AAA GAC CTG GCG GAA GCA GGC GGA GAC CAG GTT 3'
F376C	For:	5' CTG GTC TCC GCC AAC TGC CGC CAG GTC TTT CTG 3'
	Rev:	5' CAG AAA GAC CTG GCG GCA GTT GGC GGA GAC CAG 3'
R377C	For:	5' GTC TCC GCC AAC TTC TGC CAG GTC TTT CTG TCC 3'
	Rev:	5' GGA CAG AAA GAC CTG GCA GAA GTT GGC GGA GAC 3'
Q378C	As in Table A.4	
V379C	For:	5' GCC AAC TTC CGC CAG TGC TTT CTG TCC ACG CTG 3'
	Rev:	5' CAG CGT GGA CAG AAA GCA CTG GCG GAA GTT GGC 3'
F380C	For:	5' AAC TTC CGC CAG GTC TGT CTG TCC ACG CTG GCC 3'
	Rev:	5' GGC CAG CGT GGA CAG ACA GAC CTG GCG GAA GTT 3'
L381C	For:	5' TTC CGC CAG GTC TTT TGC TCC ACG CTG GCC AGC 3'
	Rev:	5' GCT GGC CAG CGT GGA GCA AAA GAC CTG GCG GAA 3'
S382C	For:	5' CGC CAG GTC TTT CTG TGC ACG CTG GCC AGC CTT 3'
	Rev:	5' AAG GCT GGC CAG CGT GCA CAG AAA GAC CTG GCG 3'
T383C	For:	5' CAG GTC TTT CTG TCC TGC CTG GCC AGC CTT GCG 3'
	Rev:	5' CGC AAG GCT GGC CAG GCA GGA CAG AAA GAC CTG 3'
L384C	For:	5' GTC TTT CTG TCC ACG TGC GCC AGC CTT GCG CTT 3'
	Rev:	5' AAG CGC AAG GCT GGC GCA CGT GGA CAG AAA GAC 3'
A385C	For:	5' TTT CTG TCC ACG CTG TGC AGC CTT GCG CCT GGG 3'
	Rev:	5' CCC AGG CGC AAG GCT GCA CAG CGT GGA CAG AAA 3'
S(C)386C	For:	5' CTG TCC ACG CTG GCC TGC CTT GCG CCT GGG TGG 3'
	Rev:	5' CCA CCC AGG CGC AAG GCA GGC CAG CGT GGA CAG 3'
L387C	For:	5' TCC ACG CTG GCC AGC TGT GCG CCT GGG TGG CGC 3'
	Rev:	5' GCG CCA CCC AGG CGC ACA GCT GGC CAG CGT GGA 3'
A(C)388C	For:	5' ACG CTG GCC AGC CTT TGC CCT GGG TGG CGC CAC 3'
	Rev:	5' GTG GCG CCA CCC AGG GCA AAG GCT GGC CAG CGT 3'
P389C	For:	5' CTG GCC AGC CTT GCG TGT GGG TGG CGC CAC CGC 3'
	Rev:	5' GCG GTG GCG CCA CCC ACA CGC AAG GCT GGC CAG 3'
G390C	For:	5' GCC AGC CTT GCG CCT TGC TGG CGC CAC CGC CGA 3'
	Rev:	5' TCG GCG GTG GCG CCA GCA AGG CGC AAG GCT GGC 3'
W391C	For:	5' AGC CTT GCG CCT GGG TGC CGC CAC CGC CGA AAG 3'
	Rev:	5' CTT TCG GCG GTG GCG GCA CCC AGG CGC AAG GCT 3'
R392C	For:	5' CTT GCG CCT GGG TGG TGC CAC CGC CGA AAG AAG 3'
	Rev:	5' CTT CTT TCG GCG GTG GCA CCA CCC AGG CGC AAG 3'
H393C	For:	5' GCG CCT GGG TGG CGC TGC CGC CGA AAG AAG AGG 3'
	Rev:	5' CCT CTT CTT TCG GCG GCA GCG CCA CCC AGG CGC 3'

Table A.6: Primers for inserting His$_6$-tag in NTS1B between TEV recognition sites. An additional His$_6$-tag was inserted into NTS1B at the C-terminus of NTS1 between the TEV recognition sites. This construct was created to allow IMAC on cleaved NTS1B (*i.e.* NTS1).

Primers	
For:	**5'** C ACC AGC GCC ACC CGG CAT CAT CAT CAT CAT CAT GAG AAC CTG TAC TTC C **3'**
Rev:	**5'** G GAA GTA CAG GTT CTC ATG ATG ATG ATG ATG ATG CCG GGT GGC GCT GGT G **3'**

Table A.7: PCR reaction mixture.

Volume	Component
5 µL	10× *Pfu*Ultra Buffer
0.5 µL	template DNA (~5-50 ng)
x µL	125 ng of forward primer
x µL	125 ng of reverse primer
1 µL	dNTP mix (10 mM each)
1 µL	*Pfu*Ultra DNA polymerase (2.5 U/µL)
$50 - (7.5 + 2x)$ µL	ddH$_2$O (to bring final volume to 50 µL)

Table A.8: PCR temperature cycling scheme.

Segment	Cycles	Temperature	Time	
1	1	95 °C	60"	
2	15[1]	95 °C	30"	*melt*
		55 °C[2]	60"	*anneal*
		68 °C	10'	*extend*
F	1	68 °C	10'	
	1	4 °C	∞	

[1] The number of cycles in segment 2 was increased to 18 if 15 cycles appeared to be insufficient.
[2] The annealing temperature was varied between 50 to 63 °C if required.

overnight at 37 °C and 200 rpm. In 2 L conical flasks, aliquots of 500 mL 2×YT medium supplemented with 0.2% glucose, and 100 µg/mL ampicillin were inoculated with 5 mL of starter culture each, and incubated at 37 °C at 200 rpm, usually growing 10 L of culture at a time. When the cultures reached an OD$_{600}$ of 0.3 the temperature was decreased to 26 °C, until the cultures reached an OD$_{600}$ of 0.5, at which point expression was induced by addition of IPTG (Sigma-Aldrich) to a final concentration of 0.25 mM. Cells were harvested by centrifugation (7,000×g, 4 °C, 15 minutes) after overnight expression and either solubilised directly or flash-frozen in liquid nitrogen and stored at -80 °C.

A.5.2.3 Purification

All purification steps were carried out at 4 °C unless stated otherwise. For receptor solubilisation, cell pellet was resuspended in 2 mL 2× solubilisation buffer (supplemented with protease inhibitors as described in Appendix A.1) per gram of pellet using a hand-held blender (Breville). Cells were incubated for 20 min with 1 mg DNase I and lysozyme (both Sigma-Aldrich) at a final concentration of 1 mg/mL under gentle stirring. DDM, CHAPS (both Melford) and CHS (Sigma-Aldrich) were added drop-wise to a final concentration of 1%, 0.5% and 0.1% (w/v), respectively. MilliQ H_2O was added to give a final volume of 4 mL per gram of pellet, and the cells were left to stir for 6 h. Unsolubilised material was pelleted by centrifugation (70,000×g, 4 °C, 60 min). The solubilised fraction (supernatant) was filtered through a 0.2 µm syringe filter (Millipore) and imidazole (Merck) was added to a final concentration of 50 mM, before loading the sample onto a freshly charged, 5 mL HisTrap HP column (GE Healthcare), pre-equilibrated with NiA buffer. The column was washed with 35-40 CV of NiA buffer and the protein was eluted by step gradient (67% for NTS1B, 100% for $NTS1BH_6$) with buffer NiB, giving an effective imidazole concentration of 350 mM for NTS1B, or 500 mM for $NTS1BH_6$. A_{280} was monitored and the peak fractions were pooled, concentrated if needed using a centrifugal concentrator (vivaspin20, 100,000 MWCO, Sartorius Stedium Biotech), and diluted five-fold with NT0 buffer. The receptor was further purified by ligand affinity chromatography, using resin funtionalized with neurotensin (NT): either (1) biotinylated NT immobilized on Tetralink tetrameric avidin resin (Promega), or (2) N-terminally Cys-derived NT (Cys-NT) immobilized on Ultralink iodoacetyl resin (Pierce, Thermo Scientific). Biotinylated NT had been synthesised in-house using standard solid phase synthesis techniques, and Cys-NT (CELYENKPRRPYIL) was purchased from Alta Bioscience; each was bound to the resin as directed by the manufacturer's instructions. For NT column purification, the diluted IMAC eluate was incubated with approximately 1-2 mL of resin for 2-3 h at 4 °C on a rotating wheel. NT resin was washed with 50-70 CV of NT70 buffer (70 mM NaCl), followed by an optional 50 CV wash with NT150 buffer (150 mM NaCl), after which the sample was eluted with NT1 buffer (1 M NaCl). Apart from a high level of purity, the ligand affinity column ensures only active, *i.e.* ligand-binding, receptor is retained. The NT column eluate was concentrated using a 1 mL HisTrap Ni^{2+}-column (GE Healthcare). The sample was loaded onto the column at 0.5-1 mL/min. Flow-through was collected and optionally re-applied to the column. The column was washed with NiA^0 buffer (30-100 CV, depending on whether reductant/unreacted label needed to be removed), and eluted with an 80% step gradient of NiB^- (400 mM imidazole). The eluate thereof was either diluted 3-5× in NT0 buffer (to lower the imidazole concentration to <100 mM and the sodium chloride concentration to ~50 mM in the final

sample to allow salt-sensitive ligand binding), or desalted using a 5 mL HiTrap Desalt column (GE Healthcare), or multiple columns in tandem for larger sample volumes (roughly 1.4 mL/column can be loaded), pre-equilibrated with SE buffer to remove the imidazole and lower the NaCl concentration to 50 mM. Alternatively, Zeba Spin Desalting Columns, MWCO 7K (Pierce, Thermo Scientific) equilibrated with SE buffer were used to buffer exchange the sample.

If required, NTS1B fusion partners MBP and TrxA were removed by cleavage with TEV protease: 5 mM DTT was added to the IMAC eluate before the NT column. Previously, a 1:1 NTS1B:TEV molar ratio was determined to be sufficient for full cleavage [312]. As the receptor was not pure at this stage of the purification, exact NTS1B concentrations were hard to determine; thus, typically 80-150 nmol of TEV protease was added, which is well in excess over typical NTS1B yields at that stage of the purification. The sample was then incubated 6-12 h at 4 °C on a rotating wheel, after which it was filtered and incubated with the NT resin as per usual to purify the receptor from remaining contaminants, cleaved fusion partners and TEV.

The final receptor concentration was determined from A_{280} (ϵ_{280} 138,660 and 56,840 $M^{-1}cm^{-1}$ for NTS1B and NTS1, respectively), gel electrophoresis against BSA standards, and/or BCA (bicinchoninic acid) colorimetric protein assays against BSA standards (Pierce, Thermo Scientific). The amount of functionally active (*i.e.* ligand-binding) receptor was initially measured using a saturation radio-ligand binding assay (see section A.5.6). Purified samples were flash-frozen in liquid nitrogen and stored at -80 °C.

A.5.3   NTS1 labelling

Fluorescent labels used were Alexa Fluor dyes (Molecular Probes, Life Technologies), namely Alexa Fluor 488 and Alexa Fluor 555 (A488 and A555 respectively), and Amersham CyDye Fluors (GE Healthcare), namely Cy3 and Cy5. For spin labelling either MTSL ((2,2,5,5-tetramethylpyrroline-1-oxyl-3-methyl)methanethiosulfonate, Toronto Research Chemicals) or maleimido-PROXYL (3-Maleimido-2,2,5,5-tetramethyl-1-pyrrolidinyloxy, Sigma-Aldrich) was used. Cysteine mutants of NTS1 were labelled with fluorophores or with spin labels using one of two labelling protocols. Labelling was either (1) carried out after NT column purification after which the sample was concentrated and excess label was removed by IMAC (1 mL HisTrap HP), or (2) after concentration of the NT column eluate by IMAC, after which excess label was removed by size-exclusion chromatography. In the first scenario, receptor was reduced with 5-10 mM DTT or TCEP during incubation with the NT resin.

Reductant was removed by washing the resin as normal. The NT column eluate was then labelled at room temperature for maximally 1 h.[3] The sample was then bound to the 1 mL nickel column (1 mL HisTrap HP), and washed extensively (70-100 CV) to remove excess label, after which the labelled NTS1 was eluted. In the second scenario, 5-10 mM DTT was added to the NT column eluate, which was then concentrated on a 1 mL nickel column as per usual, washing extensively (70-100 CV) to remove reductant prior to labelling. The 1 mL nickel eluate was then labelled at RT for maximally 1 h, after which free label was removed by size-exclusion chromatography, using 1-3 5 mL HiTrap Desalt columns (GE Healthcare) connected in tandem, depending on the size of the label to be separated and the volume of the sample. Alternatively, Zeba Spin Desalting Columns, MWCO 7K or 40K (Pierce, Thermo Scientific) were used to remove excess label.

The pH was controlled to ensure efficient and specific labelling. For labelling with maleimides, the pH was kept between 7-7.4 (to avoid labelling of lysines which is more favourable at pH 8). For labelling with MTSL (more favourable at pH ~8) the pH was kept at 7.4. As Tris buffer was used, the pH at RT (and thus during labelling) was higher than the pH at 4 °C (during the rest of the purification). Thus, buffers to be used in labelling procedures were pH-adjusted at RT. For spin labelling, the sample was incubated with a 20× molar excess of spin label (using A_{280} to determine protein concentration) for 1 h at RT. For fluorophore labelling the sample was incubated with 2-20× molar excess of label for 5-60 min at RT. Label excess and labelling time was optimised for each mutant using absorption spectroscopy to gauge the labelling efficiency (equation A.2).

A.5.4   Reconstitution into liposomes

Lipids were purchased from Avanti Polar Lipids, either in powder-form or dissolved in chloroform. For powdered lipids, the appropriate amount of lipid was dissolved chloroform:methanol (50:50), or chloroform only to approximately 10-25 mg/mL in a round-bottom flask. The lipid solution was dried down to a lipid film either under nitrogen, or using a rotary evaporator. The film was dried further overnight in a desiccator under vacuum and stored at -20 °C until needed or used immediately. The lipid film was suspended in liposome buffer to give a final concentration of 5 mg/mL, and sonicated (3×1 min) using a bath sonicator, followed by 10 freeze-thaw cycles using liquid nitrogen. The liposomes were then extruded through a 100 nm polycarbonate filter using a mini-extruder, for at least 11 passes to obtain a homogeneous distribution of liposomes of 100 nm in diameter. DDM was added to the lipid suspension at a final concentration of 0.025 % (w/v) and the lipids

---

[3]Labelling protocol optimisation showed that NTS1 does not label efficiently at 4 °C, but readily labels at RT.

were gently stirred for 1-3 h. The detergent-liposome mix was then added to the receptor at the desired lipid-to-protein ratio, and incubated for 1 h at 4 °C. Bio-Beads (Bio-Rad), washed with methanol, followed by MilliQ water, and equilibrated with liposome buffer, were then added at 0.3 g/mL (wet weight) and the sample was left to incubate overnight on a rotating wheel at 4 °C. Bio-Beads were then removed, and proteoliposomes were harvested by centrifugation (~100,000×g, 3 h, 4°C). The supernatant was removed and the pelleted proteoliposomes resuspended in liposome buffer adjusting the volume to satisfy the concentration requirements for the end-use of the sample. Proteoliposomes samples were either used directly, or stored at -80 °C (or in liquid N_2 for spin-labelled DEER samples).

A.5.5   Reconstitution into nanodiscs

A lipid film was prepared as described in section A.5.4, and MSP was produced and purified as described in section A.4. The lipid film was suspended in nanodisc lipid buffer containing 100 mM sodium cholate to give a final concentration of 20-40 mM lipid, and sonicated (3×1 min) using a bath sonicator, followed by 5 freeze-thaw cycles in liquid nitrogen. Lipid was added to NTS1, followed by MSP, and the sample was incubate for 1 h on a rotating wheel at 4 °C. Bio-Beads were equilibrated in liposome buffer and added to the sample (~1 g of wet Bio-Beads for a preparation with 1-4 nmol of NTS1), which was incubated overnight on a rotating wheel at 4 °C. After overnight incubation, the Bio-Beads were exchanged (0.5-1 g) and the sample was incubated for an additional 2 h, after which the sample was taken off the Bio-Beads and concentrated to 500 μL using a vivaspin6 concentrator with a 50 kDa molecular weight cut-off (Sartorius Stedium) Aggregates were removed by centrifugation (10,000×g, 10 min, 4 °C) and the supernatant was filtered (Nanosep MF low-volume 0.2 μm centrifugal filter, PALL Corporation). Samples were run on a gel filtration column (10/30 Superdex 200 column, GE Healthcare) to separate nanodiscs from larger aggregates. Fractions were analysed by SDS-PAGE and peak fractions were pooled. If required, NTS1 containing nanodiscs were separated from empty discs by IMAC (which required to use of cleaved MSP, *i.e.* without the His-tag, described in section A.4): the pooled fractions were loaded onto a 1 mL HisTrap HP column equilibrated with nanodisc GF buffer, washed with 50 CV of GF buffer supplemented with 2-4 mM imidazole, after which NTS1 containing nanodiscs were eluted in GF buffer with 500 mM imidazole. Peak fractions were pooled, and dialysed against a total of 5 L of GF buffer overnight at 4 °C.

The ratios in which the components (lipid, NTS1, MSP) are added during nanodisc formation are vital to its efficiency. These ratios have to be determined empirically for each target protein and each lipid composition, adhering to guidelines determined by Sligar and

co-workers [139] as detailed in Table A.9 (also shown in Chapter 6). The lipid-to-MSP ratio and the MSP-to-NTS1 ratios for the different lipid mixes used in this work are also given in Table 6.1.

Table A.9: Experimental conditions for nanodisc formation. Optimal conditions as determined by Sligar and co-workers are stated next to the conditions used in this thesis for nanodisc formation using three different lipid mixes, namely POPC:POPC (1:1, mol:mol), POPC:POPG:BPL (1.5:1:1.07), and BPL alone. Optimal MSP-to-lipid and target protein-to-MSP ratios have to be empirically determined for each individual lipid-protein combination.

Reagent	Optimal conditions	POPC:POPG (1:1)	POPC:POPG:BPL (1.5:1:1.07)	BPL
[NTS1] (μM)	~1	1.5-2.1	1.7-2.0	1.7-2.0
[MSP] (μM)	~120-140	120	90-120	120
[Glycerol] (%)	<4	1.9-2.6	3	2.2-2.8
[Cholate] (mM)	12-40	18-19	15-27	19-27
[Lipid] (mM)	4-18	7.3-7.5	6.0-7.8	7.8-8.3
MSP:Lipid	Empirical	1:60 (loaded)	1:65 (loaded)	1:65 (loaded)
		1:65 (empty)	1:70 (empty)	1:70 (empty)
NTS1:MSP	Empirical	1:50-80	1:50-80	1:60-80

A.5.6 Radio-ligand biding assay

A ^{3}H-neurotensin radio-ligand binding assay was used to quantify amounts of active (*i.e.* ligand-binding) receptor. Reaction samples were prepared in triplicate by mixing buffer, unlabelled NT, ^{3}H-NT(New England Nuclear), and receptor as summarised in Table A.10, in that order on ice. Samples were diluted in assay buffer and incubated with 9 nM ^{3}H-NT peptide (specific activity of 3.33 TBq/mmol, PerkinElmer) for 1 hour at 4 °C (see Table A.10). Non-specific binding was assayed by competition with excess (4 μM) unlabelled peptide. Receptor-bound ligand was separated from unbound ligand by gel filtration using P30 spin columns (Bio-Rad). Scintillation vials were filled with 5 mL scintillation fluid (ScinitSafe 3 Liquid Scintillation Cocktail, Fischer Scientific), to which the gel filtration eluate was added, and the samples were mixed by vortexing. The number of counts for each sample was measured on a scintillation counter (Perkin Elmer, Wallac 1409 DSA Liquid Scintillation Counter), and used to calculate the amount of bound ligand, and thus the amount of active receptor, in the sample [313]. Specific binding was determined by subtracting non-specific cpm from total cpm.

Table A.10: Reaction mixture radio-ligand activity assay for NTS1 in detergent.
Reaction samples were prepared in triplicate by mixing activity assay buffer, unlabelled NT,
^{3}H-NT and receptor in that order on ice.

	^{3}H-NT (µL)[1]	Assay buffer (µL)[2]	NTS1 (µL)[3]	NT (µL)[4]
Total	5	30	25	–
Non-specific	5	28	25	2

[1] 100× dilution of ^{3}H-NT stock, in assay buffer vortexed thoroughly ensure homogeneous distribution.
[2] 50 mM Tris-HCl pH 7.4, 0.1% DDM, 0.01% CHS (w/v), 1 mM EDTA, 0.1 mg/mL BSA.
[3] Dilute sample to nanomolar concentrations such that cpm~1000-5000.
[4] Unlabelled NT stock added is 120 µM, giving a final concentration of 4 µM.

A.6   Gα_{i1}

The construct for Gα_{i1} was kindly donated by Renaud Wagner (University of Strasbourg,
France). Gα_{i1} was expressed and purified as described in [504]), with minor modifications.
Starter cultures (7.5 mL LB, 100 µg/mL ampicillin) were inoculated with a single culture
of Gα_{i1} plasmid-transformed BL21(DE3) each, and incubated overnight at 37 °C and 200
rpm. In 2 L conical flasks, aliquots of 500 mL enriched medium (see Appendix A.1) supple-
mented with 100 µg/mL ampicillin were inoculated with 5 mL of starter culture each, and
incubated at 30 °C at 200 rpm, usually growing 10 L of culture at a time. When the culture
reached an OD$_{600}$ of 0.5-0.7, expression was induced by addition of IPTG to a final concen-
tration of 0.1 mM, and cells were grown overnight. Cells were harvested by centrifugation
(7,000×g, 4 °C, 15 min) and stored at -80 °C or used directly. Cell pellet (~40-60 g) was
resuspended in a minimal volume (~1:1) of equilibration buffer (20 mM Tris-HCl pH 8, 20
mM β-mercaptoethanol) supplemented with protease inhibitors. Lysozyme was added to 1
mg/mL, and cells were incubated on ice for 30 min, after which MgSO$_4$ (5 mM) and DNase
I (~1 mg) were added, and cells were lysed either using a French press (3 rounds at 1,000
psi), or by sonication with a probe sonicator (4-7×1 min). Cell debris was separated from
lysate by centrifugation (70,000×g, 30 min, 4 °C). Supernatant was filtered through a 0.2
µm syringe filter, before loading the sample onto a freshly charged, 5 mL HisTrap column
(GE Healthcare), pre-equilibrated with equilibration buffer. The sample was washed with
~70 CV of wash buffer (10 mM imidazole, 0.5 M NaCl) and then eluted with an imidazole
gradient of 10-150 mM (over ~8 CV), followed by ~4 CV of 150 mM imidazole, and ~8 CV
of 500 mM imidazole elution buffer to ensure all protein was eluted. Fractions were analysed
by SDS-PAGE and the cleanest fractions were pooled, concentrated using a centrifugal con-
centrator (vivaspin20, 10,000 MWCO), and dialysed overnight against 2 L of dialysis buffer
(50 mM Tris-HCl pH 7.4, 10% glycerol (v/v), 50 mM NaCl, 5 mM MgCl$_2$) at 4 °C. The
sample was further dialysed for 4 h against 2 L of dialysis buffer, followed by another 1 L

for 3 h, after which the sample was recovered and the final concentration was determined by A_{280} (ϵ_{280} =35,780 $M^{-1}cm^{-1}$).

G protein activity was tested by saturation-binding experiments to guanosine 5'-O-(3-thiotriphosphate) BODIPY thioester (BODIPY-GTPγS, Molecular Probes, Life Technologies); the affinity (K_d) was determined by incubating serial dilutions (in triplicate) of Gα_{i1} (0.3 nM to 10 µM final concentrations) with 25 nM BODIPY-GTPγS for 1 h, and recording the endpoint fluorescence polarisation at 520 nM using a Pherastar fluorescence plate-reader (BMG). Non-specific binding was tested by repeating the experiment in the presence of 1 mM unlabelled GTPγS. Data was fitted in OriginPro 8.5 (OriginLab) using a one-site (total minus non-specific) binding model, accounting for ligand depletion.

A.7   SDS-PAGE and western blotting

Proteins were separated using a X-cell Surelock minicell and pre-cast Tris-Glycine (12%, or 4-12%), or NuPAGE Bis-Tris (12%, or 4-12%) gels (Invitrogen), using either Tris-Glycine running buffer (150 V, 60 min) or MES running buffer (200 V, 35 min). Protein samples were mixed 1:1 with 2× sample buffer, and denatured at ~100 °C for 3-5 minutes. For Coomassie staining, gels were incubated for 1 h Coomassie Brilliant Blue staining solution, and destained overnight with destaining solution. For silver staining, gels were stained using Silver Stain Plus (Bio-Rad). For western blotting, proteins were separated on an SDS-PAGE gel and transferred to a nitrocellulose or PVDF membrane (GE Healthcare) by semi-dry transfer (Trans-Blot, Bio-Rad) for 1-2 h at 100 mA. NTS1B was detected using a mouse anti-His or anti-MBP antibody (Sigma-Aldrich) using WesternBreeze Chromogenic Western Blot Immunodetection (Invitrogen). NTS1 was detected using a polyclonal goat anti-NTS1 antibody and a mouse anti-goat secondary antibody (NTR-20, Santa Cruz Biotechnology).

A.8   EPR

A.8.1   CW-EPR

For CW-EPR experiments, approximately 10-40 µL of spin-labelled NTS1(B) was loaded into a ~0.5 mm glass capillary (Blaubrand intraMARK disposable glass micropipettes, BRAND, or Sigma-Aldrich capillaries) flame-sealed at one end. Spectra were recorded on an X-band CW spectrometer (Bruker EMX, controlled by Bruker Xenon software) at ~9.2-9.8 GHz, using a X-band Super High Sensitivity Probehead (Bruker). The temperature was controlled (277 or 170 K) using a nitrogen cryostat coupled to a variable temperature unit (Oxford Instruments). Spectra were typically collected with a sweep width of 200 G (centre field set to coincide with the central peak), at 45-70 s per scan, and the time constant was

adjusted to ~1/10 of the conversion time to maximize the signal-to-noise ratio. The modulation amplitude was set at 2 or 3-4 G for spectra recorded at 277 or 170 K, respectively. Receiver gain was set at 40-60 dB, and microwave power was adjusted to avoid saturation (10-20 mW at 277 K, and 0.1-2 mW at 170 K). Between 5-125 scans were collected and averaged.

A.8.2 DEER

Approximately 30 µL of spin-labelled sample was loaded into a high-precision 3 mm quartz tube (Wilmad-LabGlass). Pulsed EPR experiments (T_2-measurements, field-swept absorption spectra, and DEER) were performed on an X-band pulsed spectrometer (Bruker Elexys 680) at 30-70 K using a helium cryostat controlled by a variable temperature unit (Oxford Instruments), and a 3 mm split-ring resonator (ER-4118X-MS3, Bruker).

T_2-measurements were performed by a two-pulse echo experiment ($\pi/2 \rightarrow T_0 + \tau \rightarrow \pi \rightarrow T_0 + \tau \rightarrow$ Echo, where $T_0 = 200$ ns, $\pi = 32$ ns and $\pi/2 = 16$ ns) detecting the echo amplitude as a function of the interpulse delay τ (varied by 8 ns steps). Exponential fit of the decay gave the T_2 relaxation time.

Field-swept absorption spectra (used for short distance determination by second moment analysis) were recorded by applying a Hahn echo sequence ($\pi/2 \rightarrow \tau \rightarrow \pi \rightarrow \tau \rightarrow$ Echo, where $\tau = 200$ ns, $\pi = 32$ ns and $\pi/2 = 16$ ns), and detecting the echo amplitude at varying magnetic field position (sweep width 150 G).

DEER experiments were performed using 4-pulse (4p) and 3-pulse (3p) DEER sequences (see Figure 1.19). The start time t_0 for the pump pulse was to 0 (for 3p) or 80 ns (for 4p) after the first π observer pulse and incremented by 8 ns. The first $\pi/2$ pulse was phase-cycled (+x/-x, 8 steps) to eliminate receiver offsets. At X-band, for both the 3p and 4p the probe π and $\pi/2$ pulses were set to 32 ns, and the pump π pulse was set to 12-24 ns, so as to obtain complete echo inversion at maximum power (minimum ELDOR attenuation) while minimizing any proton modulation induced by pulse overlap not averaged out by varying τ_1 pulse delays. The probe frequency was set to coincide with the maximum of the nitroxide spectrum, and the pump frequency was set 65 MHz upfield.

For Q-band (~33.4 GHz) DEER, samples were transferred to high-precision 1.6 mm quartz tubes (Wilmad-LabGlass), and measured on an ELEXYS E580 equipped with a SuperQ-FT bridge (Bruker)[4], at 50 K using a helium cryostat controlled by a variable temperature unit (Oxford Instruments), and a 2 mm split-ring resonator (EN-5107D2, Bruker). The same pulse sequences were applied as at X-band, except probe pulses were set at 30 and 60 ns ($\pi/2$ and π, respectively), positioning the pump pulse at the nitroxide maximum, and the

---

[4]Courtesy of Mark Newton, University of Warwick.

probe pulse ~55 MHz downfield. The exact frequency difference between the probe and pump pulse was calculated for each sample from the positions of the spectral maximum and highfield local maximum as determined from the field-swept absorption spectra. Pump pulse length was set to 58-64 ns so as to obtain complete echo inversion at maximum power (minimum ELDOR attenuation).

The τ_1 pulse delay was set to 200 ns for all experiments, while the τ_2 pulse delay (or τ' in the 3p pulse scheme, Figure 1.19) was adjusted per sample, depending on its (T_2) relaxation rate, finding a compromise between high signal-to-noise ratio and maximum dipolar evolution time t_{max} (and thus maximum observable distance). Typically, a shorter 4-pulse DEER trace ($t_{max} = 800-1600$ ns) and a longer 3-pulse DEER trace ($t_{max} = 1600-3500$ ns) were recorded. The shot-repetition time was set between 1-2 ms to minimize saturation.

Raw data was phased using DeerAnalysis 2013 software [202], to correct for any experimental data acquired in the imaginary channel. Distorted data points were removed from the end of the 4p and the beginning of the 3p trace, and each trace was background-corrected simultaneously assuming a homogeneous, spatially confined background,

$$B(t) = \exp{-kt^{d/3}} \tag{A.3}$$

where k is inversely related to the spin concentration, and d is the background dimension (typically set between 2-2.5 for liposomal samples). k is varied so that the differences between the background decay of the two traces is minimized, to obtain the best fit between the 3p and 4p data, by least-squares fitting using MATLAB 2013 (MathWorks) as per the DEER-Stitch method by Lovett *et al.* [197]. Distance distributions were derived from stitched data using DeerAnalysis 2013.

A.9   Ensemble FRET

Cysteine mutants of NTS1 were fluorescently labelled with Alexa Fluor dyes as described in Appendix A.5.3. Alexa Fluor 488 was used as the donor fluorophore and Alexa Fluor 555 as the acceptor. Donor and acceptor were reconstituted together at a 1:1 ratio for FRET samples, as well as separately for donor-only, and acceptor-only control samples. Receptor was reconstituted in brain polar lipid at 6,000:1 lipid-to-protein ratio (mol:mol) for the mixed FRET sample, or at 12,000:1 for the control samples, to keep the total amount of lipid in each sample constant to keep light scattering at the same level. Per sample 0.15-0.2 nmol of donor and/or acceptor (each) was used, and the final sample was resuspended in 110-200 μL of liposome buffer giving a maximal final concentration of ~1 μM. Samples were prepared in triplicate where possible, for at least two individual preparations per mutant.

A background sample consisting of empty liposomes was also prepared and measured to be able to subtract any background fluorescence and scattering effects from the sample spectra. Fluorescence emission spectra were recorded at room temperature on a Perkin-Elmer LS-50B fluorimeter (slit widths 4.5 nm for excitation and 5 nm for emission, to optimize signal-to-noise ratio). For FRET, acceptor-only, and liposome background samples emission spectra with excitation at the donor (490 nm) and the acceptor (555 nm) wavelength were recorded (over 495-600, or 560-600 nm, respectively). For donor-only samples only the emission spectrum with excitation at the donor wavelength was recorded. The FRET data was processed as discussed in [448] (see also Chapter 5).

A.10   MST

Fluorescently labelled NTS1 detergent and nanodisc samples were prepared as described in sections A.5.3, A.4 and A.5.5. $G\alpha_{i1}$ was prepared as described in section A.6. Labelled NT was produced by Alan Goddard and Eleanor Healey (University of Oxford) by labelling a N-terminal cysteine derivative of neurotensin (Alta Bioscience) with Alexa Fluor 488 (Sigma-Aldrich) or Cy5 (GE Healthcare) by mixing the dye with a threefold excess of the peptide, adjusting the pH to 7 and incubating for 1 h at RT. Labelled NT was purified by HPLC (20-60% acetonitrile gradient, semi-preparative C18 column), and labelling and purity were verified by mass spectrometry. Labelled NT was lyophilised and subsequently stored in 50 mM Tris pH 7.4.

Samples were centrifuged prior to use to remove any large particles ($10,000 \times g$, 10 min) and/or filtered (Nanosep MF 0.2 μm centrifugal filter, PALL Corporation). Dilution series (12-16 points) of the unlabelled binding partner were prepared ensuring that no additional gradient (salt, glycerol, imidazole, DMSO etc.) was created by careful buffer matching. To test their effect on G protein binding, agonist (NT_{8-13}, Sigma-Aldrich), antagonist (SR48692 or SR142948A, both Sanofi-Aventis), and/or GTPγS (Roche) were added at saturating concentrations (5 μM, 5 μM, and 1 mM, respectively) to all components (fluorescent binding partner, non-fluorescent binding partner, and buffer). To minimize adsorption of the sample to the reaction tubes, LoBind tubes (Eppendorf) were used. Furthermore, for experiments with detergent-solubilised NTS1 0.1 mg/mL BSA was added to passivate the reaction tube surface. For nanodisc samples 0.006% Tween-20 (w/v) was included. Passivating agents were again added to all separate components to avoid creation of a gradient in the dilution series. The minimum amount of fluorescent binding partner needed was determined by a capillary scan adjusting the LED power to give fluorescence counts between 200-1500, typically using 95% LED power for samples containing 5-25 nM of the fluorescent binding partner. Dilution series were left to incubate at 4 °C for 30-60 min, after which they

were loaded into hydrophilic capillaries (NanoTemper Technologies) by capillary action. Thermophoresis was measured on a Monolith NT.115 (NanoTemper Technologies), using the blue filter set for A488 or the red for A647, at varying MST power (20, 40 and 80%), with 80% usually giving the best results. Ligand binding affinity was also tested by label-free MST on a Monolith NT.LabelFree (NanoTemper Technologies)[5], with 20% LED and 40% MST power (as described in [166]). Laser on- and off-times were set at 30 and 5 s, respectively, for all measurements. Data analysis procedures are detailed in Chapter 6.

---

[5]Label-free MST measurements were performed by Stefan Duhr (NanoTemper Technologies) at NanoTemper Technologies in Munich, Germany.

B | GPCR structures

Table B.1: Published high-resolution GPCR structures Table lists GPCRs for which structures have been solved, grouped per GPCR family. Where a ligand was bound to the receptor it is listed, as well as the state the receptor appeared to be in: R, inactive/basal state; R*, (fully) active state; R*I, intermediate, "active-like" state; G/n indicates that the receptor was bound to a G protein or C-terminal peptide of the Gα subunit, or to a G protein-mimicking antibody; O* is an activated state of rhodopsin, like R* but without any retinal present. Structures are of human receptors unless indicated otherwise. Abbreviations: IA, inverse agonist; Ant, antagonist; A, agonist; pA, partial agonist; bA, biased agonist; AM, allosteric modulator; G-CT, C-terminal peptide of the Gα subunit; G-Nb, G protein-mimicking nanobody.

Receptor	State	Ligand/Complex	PDB codes	References
Class A				
Rhodopsin				
Bovine	R	11-*cis*-retinal	1F88, 1HZX, 1L9H, 1GZM, 1U19, 2I35, 2I36, 2J4Y, 3C9L, 3C9M	[505–512]
	R	11-*cis*-retinal (IA) + beta-ionone (AM)	3OAX	[513]
	R	9-*cis*-retinal (IA)	2PED	[514]
	O*	No retinal	3CAP, 4BEZ[1]	[290, 515]
	O*G	No retinal + G-CT	3DQB, 2X72[1,] 4J4Q	[326, 516, 517]
	R*	all-*trans*-retinal (A)	2G87, 2HPY, 23I7, 4BEZ[2]	[510, 515, 518, 519]
	R*I	all-*trans*-retinal (A; MetaII state)	3PXO	[520]
	R*IG	all-*trans*-retinal (A; MetaII state) + G-CT	3PQR	[520]
	R*G	all-*trans*-retinal (A) + G-CT	4A4M[1]	[521]
Squid	R	11-*cis*-retinal (IA)	2ZIY, 2Z73	[522, 523]
	R	9-*cis*-retinal (IA)	3AYN	[524]
	R*I	all-*trans* retinal (A; Batho intermediate)	3AYM	[524]
Adrenergic recepors				
β₂	R	Carazolol (IA)	2RH1, 2R4R, 2R4S, 3KJ6[3,] 4GBR	[284, 525, 526]
	R	Timolol (IA)	3D4S	[527]
	R	ICI 118,551 (IA)	3NY8, 3NY9	[528]
	R	Alprenolol (Ant)	3NYA	[528]
	R*I	FAUC50 (irreversible A)	3PDS	[529]
	R*In	BI-167107 (A) + G-Nb	3P0G, 4LDE	[530, 531]

(Table B.1 Continued)

Receptor	State	Ligand/Complex	PDB codes	References
	R*G	BI-167107 (A) + Heterotrimeric G protein	3SN6	[104]
	R*In	Hydroxybenzylisoproterenol (A) + G-Nb	4LDL	[531]
	R*In	Adrenaline (A) + G-Nb	4LDO	[531]
	R*In	FAUC50 (irreversible A) + G-Nb	4QKX	[532]
Turkey β_1	R	Cyanopindolol (Ant)	2VT4, 2YCX, 2YCY, 4BVN	[533–535]
	R	Dobutamine (pA)	2Y00,[4] 2Y01[4]	[329]
	R	Carmoterol (A)	2Y02[4]	[329]
	R	Isoprenaline (A)	2Y03[4]	[329]
	R	Carazolol (IA)	2YCW	[534]
	R	Iodocyanopindolol (Ant)	2YCZ	[534]
	R	Bucindolol (bA)	4AMI	[536]
	R	Carvedilol (bA)	4AMJ	[536]
	R	No ligand	4GPO	[406]
	R	4-methyl-2-(piperazin-1-yl) quinoline (Ant)	3ZPR, 3ZPQ	[537]
A_{2A} adenosine receptor	R	ZM241385 (Ant)	3EML, 3PWH, 4EIY[5]	[291, 296, 538]
	R*I	UK-432097 (A)	3QAK	[360]
	R*I	Adenosine (A)	2YDO	[539]
	R*I	NECA (A)	2YDV	[539]
	R	xhantine XAC (Ant)	3REY	[296]
	R	caffeine (Ant)	3RFM	[296]
	R	1,2,4-triazine isomers (Ant)	3UZA, 3UZC	[540]
	R	ZM241385 + allosteric IA Nb	3VG9, 3VGA	[541]
Chemokine recpetors				
CXCR4	R	CVX15 (Ant)	3OE0	[292]
	R	IT1t (Ant)	3OE6, 3OE8, 3OE9, 3ODU	[292]
CXCR1	R	No ligand	2LNL[6]	[542]
CCR5	R	Maraviroc (AM-Ant)	4MBS	[543]
Muscarinic acetylcholine receptors				
M2	R	3-quinuclidinyl-benzilate (Ant)	3UON	[544]
	R*n	iperoxo (A) + G-Nb	4MSQ	[545]
	R*n	iperoxo (A) + LY2119620 (AM) + G-Nb	4MQT	[545]
M3	R	tiotropium (IA)	4DAJ	[336]
Opioid receptors				
κ	R	JDTic (Ant)	4DJH	[407]
μ	R	β-funaltrexamine (Ant)	4DKL	[408]
δ	R	Naltrindole (Ant)	4EJ4	[546]
	R	Naltrindole (Ant)+Na$^+$ (AM)	4N6H	[547]
Serotonin 5HT receptors				
2B	R*I	Ergotamine (A)	4IB4, 4NC3[7]	[548, 549]

(Continued on next page)

<div align="center">(Table B.1 Continued)</div>

Receptor	State	Ligand/Complex	PDB codes	References
1B	R*	Ergotamine (A)	4IAR	[550]
	R*	Dihydroergotamine (A)	4IAQ	[550]
D3 dopamine	R	Eticlopride (Ant)	3PBL	[551]
H1 Histamine	R	Doxamine (Ant)	3RZE	[552]
Nocicpetin/ orphanin FQ receptor	R	Peptide mimetic C24 (Ant)	4EA3	[553]
Protease-activated receptor 1	R	Vorapaxar (Ant)	3VW7	[348]
rat Neurotensin receptor 1	R*I	Neurotensin (A)	4GRV, 3ZEV, 4BUO, 4BV0, 4BWB	[294, 295]
Spingosine 1-phosphate receptor	R	Sphingolipid mimic ML056 (Ant)	3V2W, 3V2Y	[554]
Purinergic P2Y$_{12}$ receptor	R	AZD1283 (Ant)	4NTJ	[555]
	R*I	2MeSADP (A)	4PXZ	[556]
	R*I	2MeSATP (ATP-derivative of A)	4PY0	[556]
Free fatty acid receptor 1	R	TAK-875 (AM A)	4PHU	[557]
Class B				
Corticotropin releasing factor receptor 1	R	CP-376395 (Ant)	4K5Y	[558]
Glucagon receptor	R	NNC0640 (Ant)	4L6R	[559]
Class C				
Metabotropic glutamate receptors				
mGlu1	R	FITM (AM Ant)	4OR2	[560]
mGlu5	R	mavoglurant (AM Ant)	4OO9	[561]
Frizzled/Taste Family				
Smoothened receptor	R	LY2940680 (Ant)	4JKV	[562]
	R	Cyclopamine (Ant)	4O9R[7]	[563]
	R	ANTA XV (Ant)	4QIM	[564]
	R	SANT-1 (Ant)	4N4W	[564]
	R*I	SAG1.5 (A)	4QIN	[564]

[1] Structure carrying G90C disease mutation.
[2] Structure of constitutively active mutant.
[3] Structure of methylated receptor.
[4] Structure of agonist-bound receptor, but thermostabilised in the R (inactive) state.
[5] Chimera of A_{2A} and BRIL
[6] NMR structure of receptor backbone in phospholipid bilayers of native receptor.
[7] Structure determined using free electron laser x-ray serial femtosecond crystallography.

C | DEER data PepT$_{So}$

C.1 DEER data

Dipolar evolution time domain data corresponding to the background-corrected data in Figures 2.6, 2.7, and 2.8 is shown here. The fitted stretched exponential background is also shown (background dimensionality was varied between 2 and 3 to obtain the best fit shown here). The dipolar spectra (Fourier transformation of the background-corrected dipolar evolution data) are presented alongside the raw data.

C.2 Gaussian deconvolution of distance distributions

The distance distributions obtained from the DEER data by Tikhonov regularisation were subjected to Gaussian deconvolution (see Figures C.4, C.5, and C.6) to obtain peak centres and widths summarised in Table C.1 (also reported in Chapter 2).
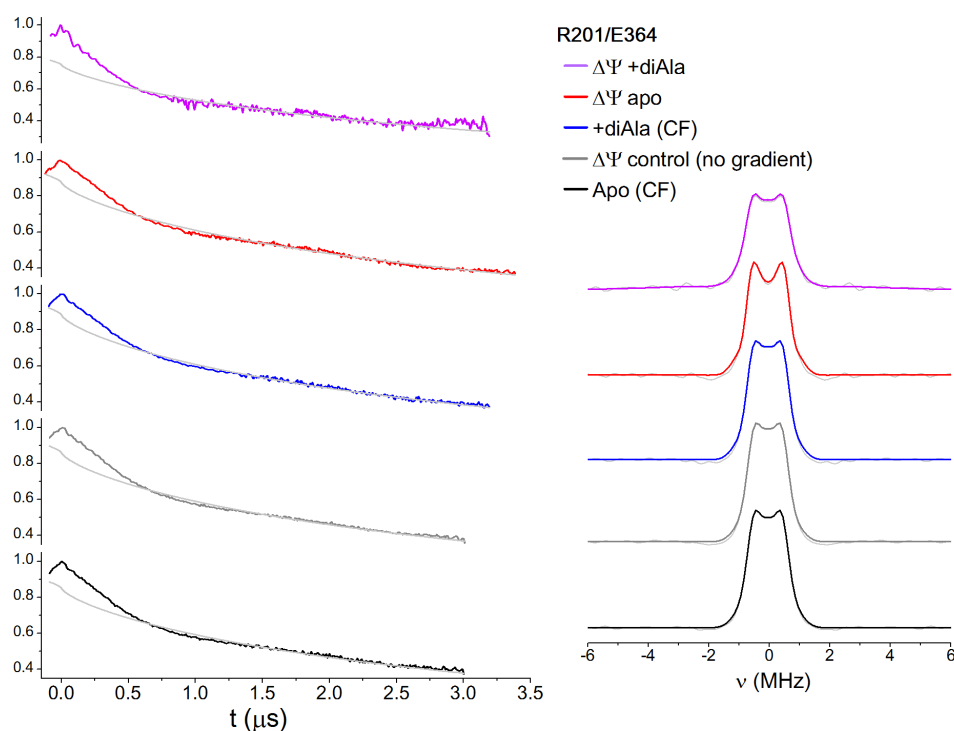
Figure C.1: R201/E364: Dipolar evolution time domain data and dipolar spectra. Raw DEER data, and the fitted background (grey, d=2.2 for all) are shown (left), as well as the dipolar spectra (right) for experiments performed in the presence of a valinomycin-induced electrochemical gradient ($\Delta\Psi$) with or without di-alanine peptide present (+diAla or apo, respectively); or under counterflow conditions (CF), *i.e.* no chemical gradient, but with high concentrations of peptide in the +diAla sample to induce transport. A "$\Delta\Psi$ control" sample was measured under the same conditions as "$\Delta\Psi$ apo" but without valinomycin.
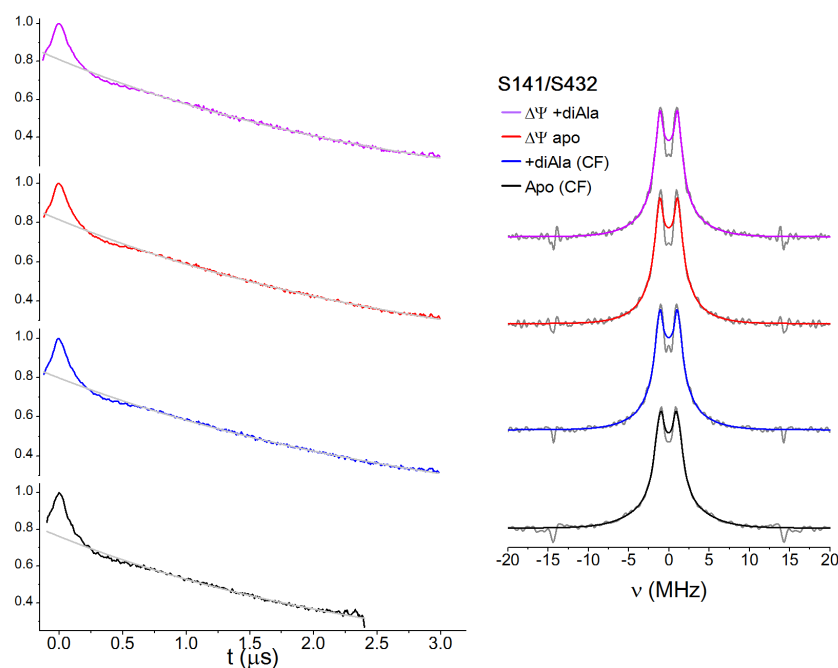
Figure C.2: S141/S432: Dipolar evolution time domain data and dipolar spectra. Same as Figure C.1, but without the "ΔΨ control" sample. Background dimensionality was 3 in this case. Dimensionalities closer to the theoretically expected 2 gave very poor fits.
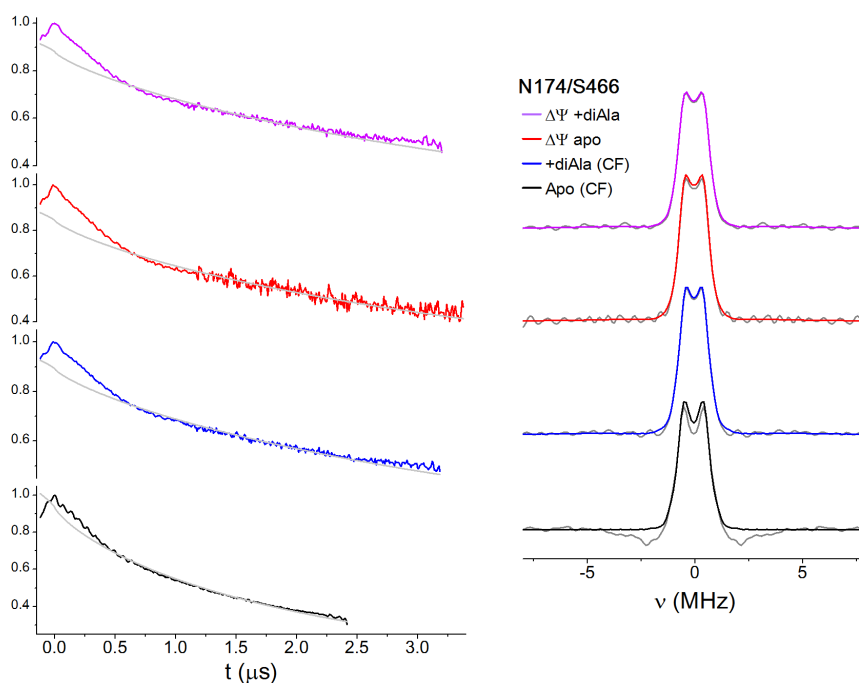
Figure C.3: N174/S466: Dipolar evolution time domain data and dipolar spectra. Same as Figure C.1, but without the "ΔΨ control" sample. Background dimensionality was 2.4 in this case.

Table C.1: DEER distances extracted by Gaussian deconvolution. Distance distributions obtained from DEER measurements on the three mutants were subjected to Gaussian peak-fitting in OriginPro 8.5 (OriginLab). The centre of each of the fitted Gaussian peaks (R) is given ($\pm$ the half-width at half-height) as well as the relative contribution to the total area (A).

		N174/S466		S141/S432		R201/E364	
		R (Å)	**A (%)**	**R (Å)**	**A (%)**	**R (Å)**	**A (%)**
CF	*apo*	19 ± 2	5	21 ± 4	41	45 ± 4	100
		39 ± 2	17	32 ± 4	53		
		47 ± 3	78	38 ± 1	6		
	+diAla	19 ± 2	3	22 ± 4	42	45 ± 3	100
		39 ± 1	16	33 ± 4	58		
		47 ± 3	81				
ΔΨ	*apo*	21 ± 4	10	23 ± 4	41	45 ± 2	93
		45 ± 5	90	33 ± 4	59	57 ± 3^{1}	7
	+diAla	21 ± 3	12	22 ± 4	41	24 ± 3	12
		41 ± 2	35	33 ± 4	59	39 ± 3	35
		48 ± 3	53			45 ± 43	53
	control	-	-	-	-	45 ± 4	100

[1] Distance most likely a fitting artefact (not stable with variable background subtraction).

R 201/E 364
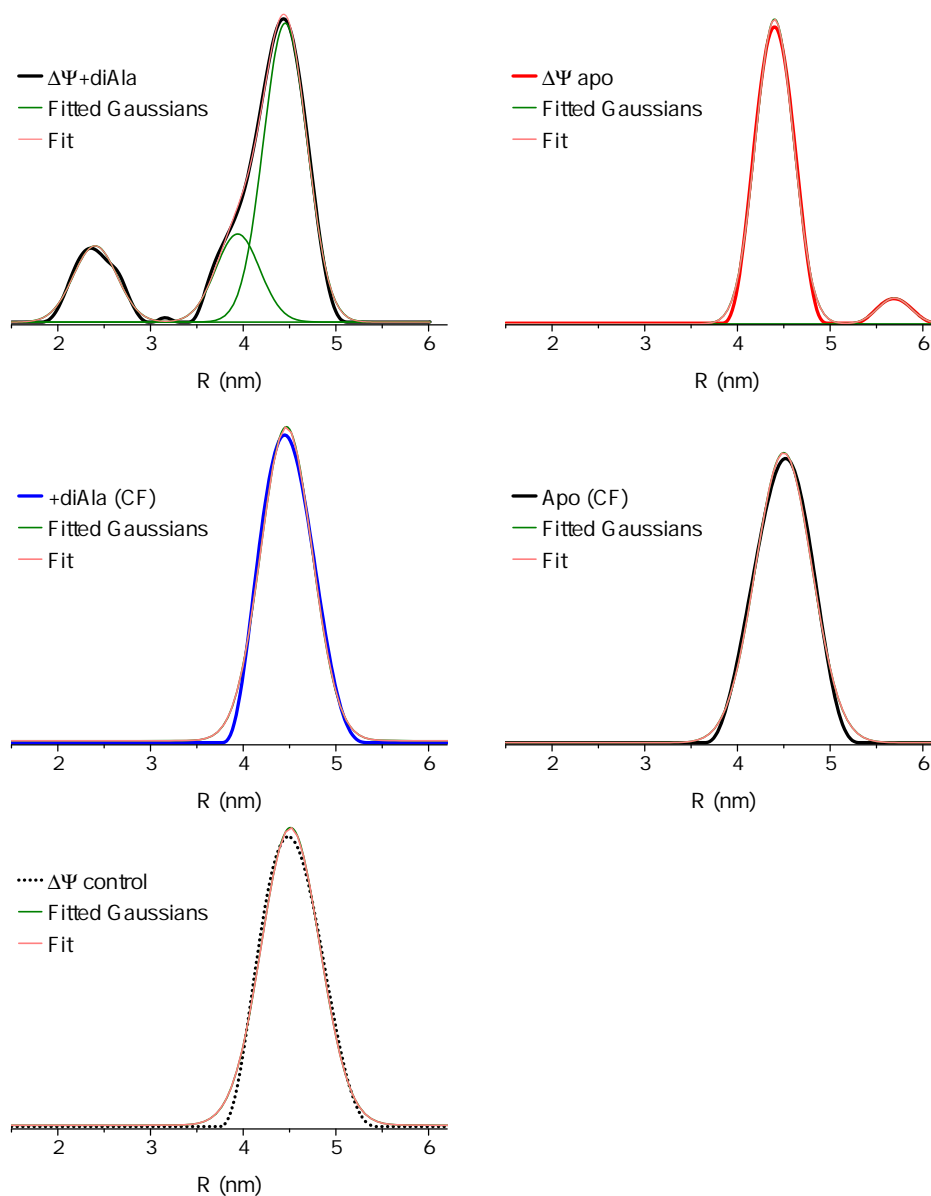
Figure C.4: R201/E364: Gaussian peak fitting of distance distribution. Distance distributions obtained from DEER measurements were subjected to Gaussian peak-fitting in OriginPro 8.5 (OriginLab), for experiments performed in the presence of a valinomycin-induced electrochemical gradient ($\Delta\Psi$) with or without di-alanine peptide present (+diAla or apo, respectively); or under counterflow conditions, *i.e.* no chemical gradient, but with high concentrations of peptide in the +diAla sample to induce transport. A "$\Delta\Psi$ control" sample was measured under the same conditions as "$\Delta\Psi$ apo" but without valinomycin..
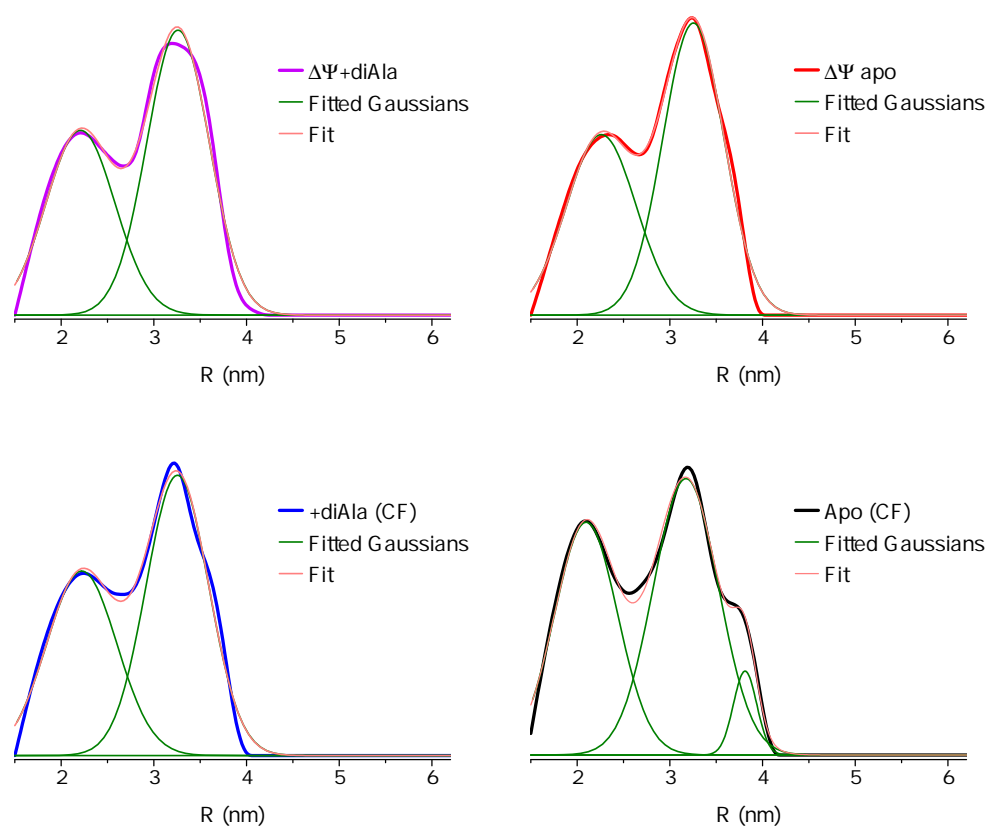
Figure C.5: S141/S432: Gaussian peak fitting of distance distribution. Same as Figure C.4, but without the "ΔΨ control" sample.

N174/S 466
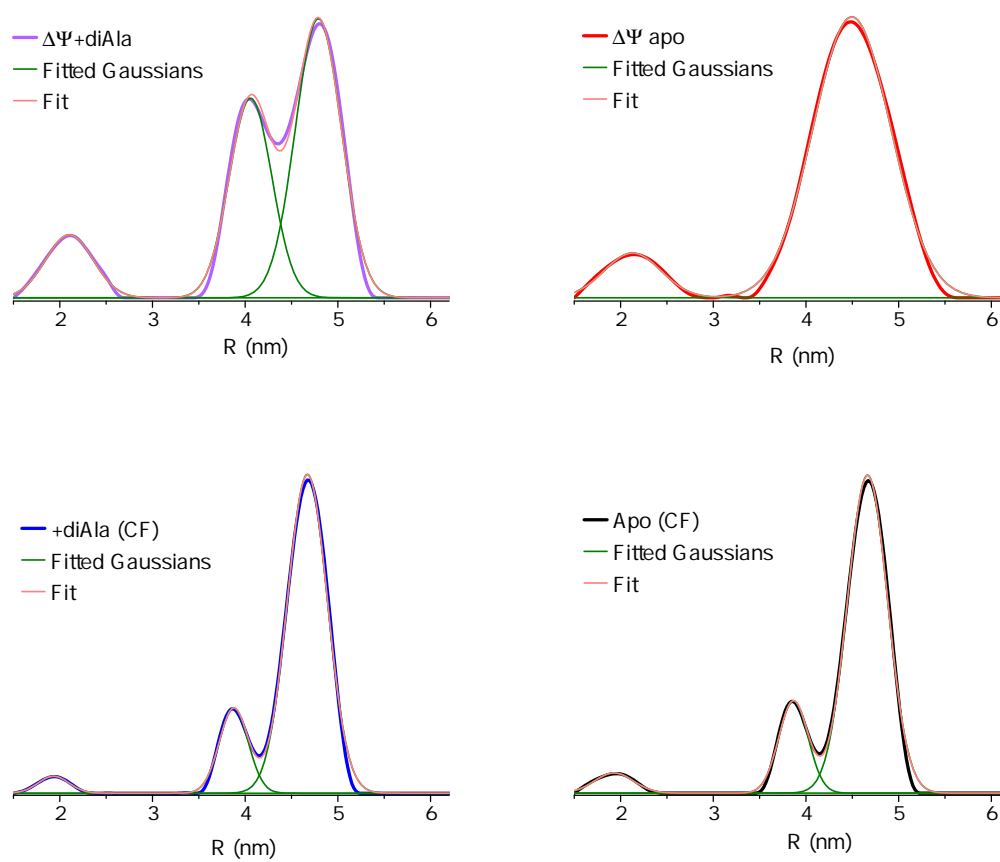
Figure C.6: N174/S466: Gaussian peak fitting of distance distribution. Same as Figure C.4, but without the "ΔΨ control" sample

D | CW-EPR NTS1(B)

Further CW-EPR spectra of NTS1(B) referred to in chapter 4 are presented here.
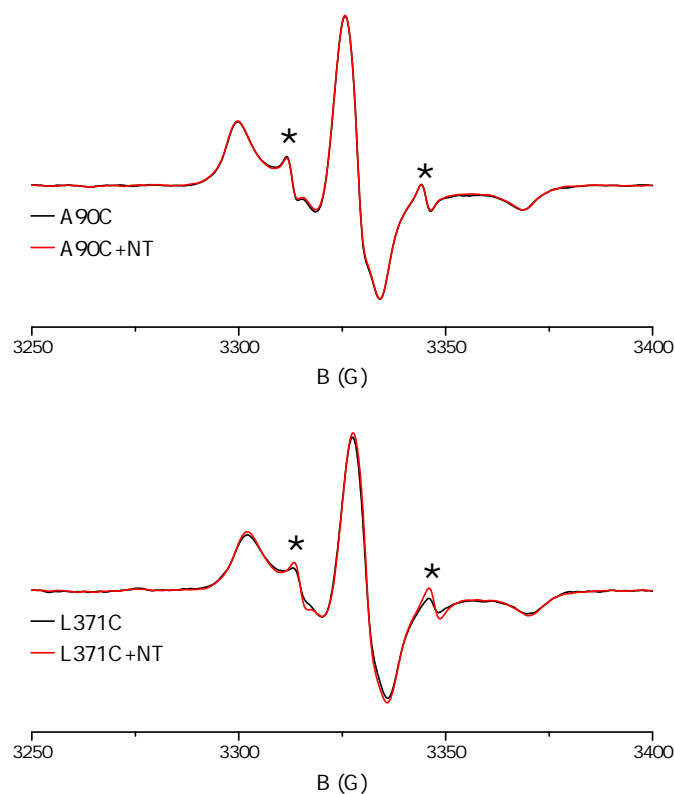
Figure D.1: Spectra of spin-labelled A90C and L371C before subtraction of free spin label component. CW-EPR spectra recorded at 277 K showed evidence of a minor free spin label component (marked with *) for A90C and L371C. The integrated intensity of these components was ~1 and 0.5% of the total intensity, respectively. The component was removed by matching a spectrum of free MTSL selected from a library of MTSL spectra recorded at different glycerol concentrations to the experimental spectrum and subtracting it from the NTS1B spectrum. The resulting spectra are shown in Figure 4.6.
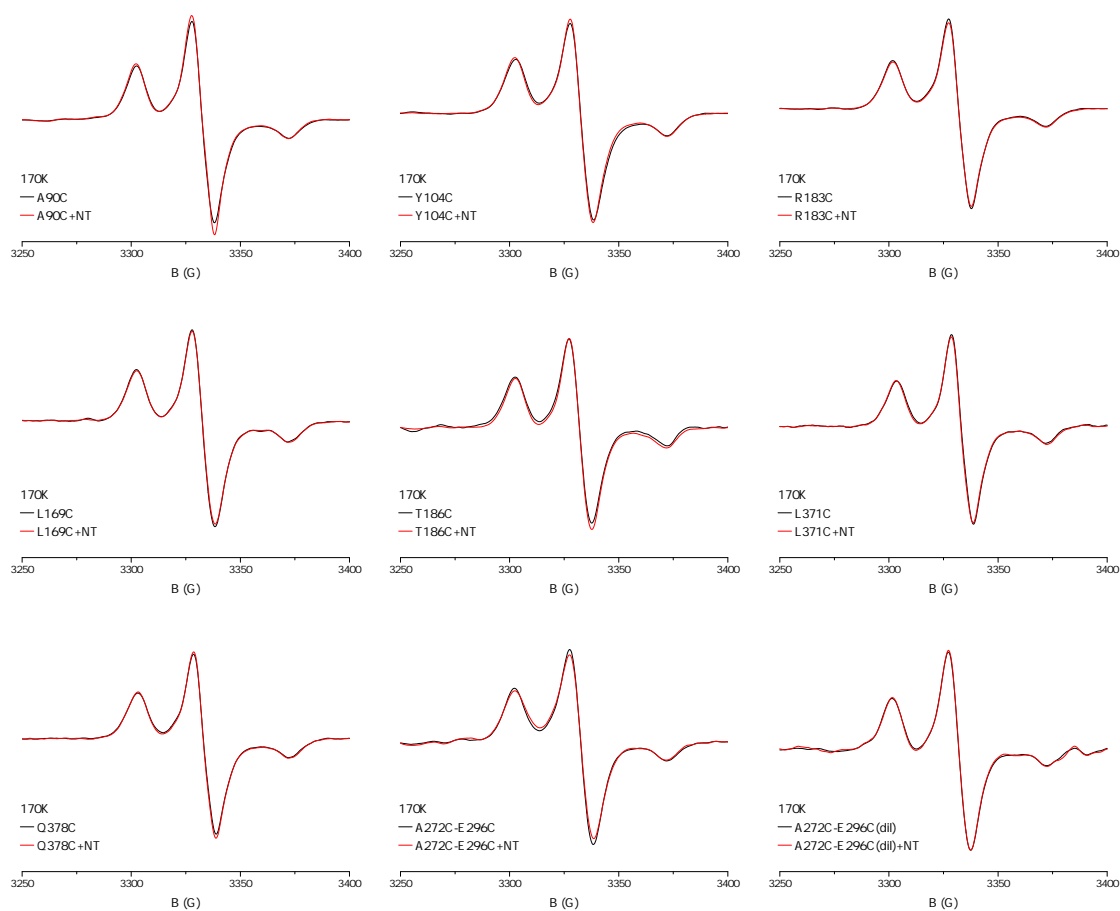
Figure D.2: Rigid-limit CW-EPR spectra of NTS1B cysteine mutants. Spectra were recorded at 170 K in the absence and presence of agonist neurotensin (+NT).
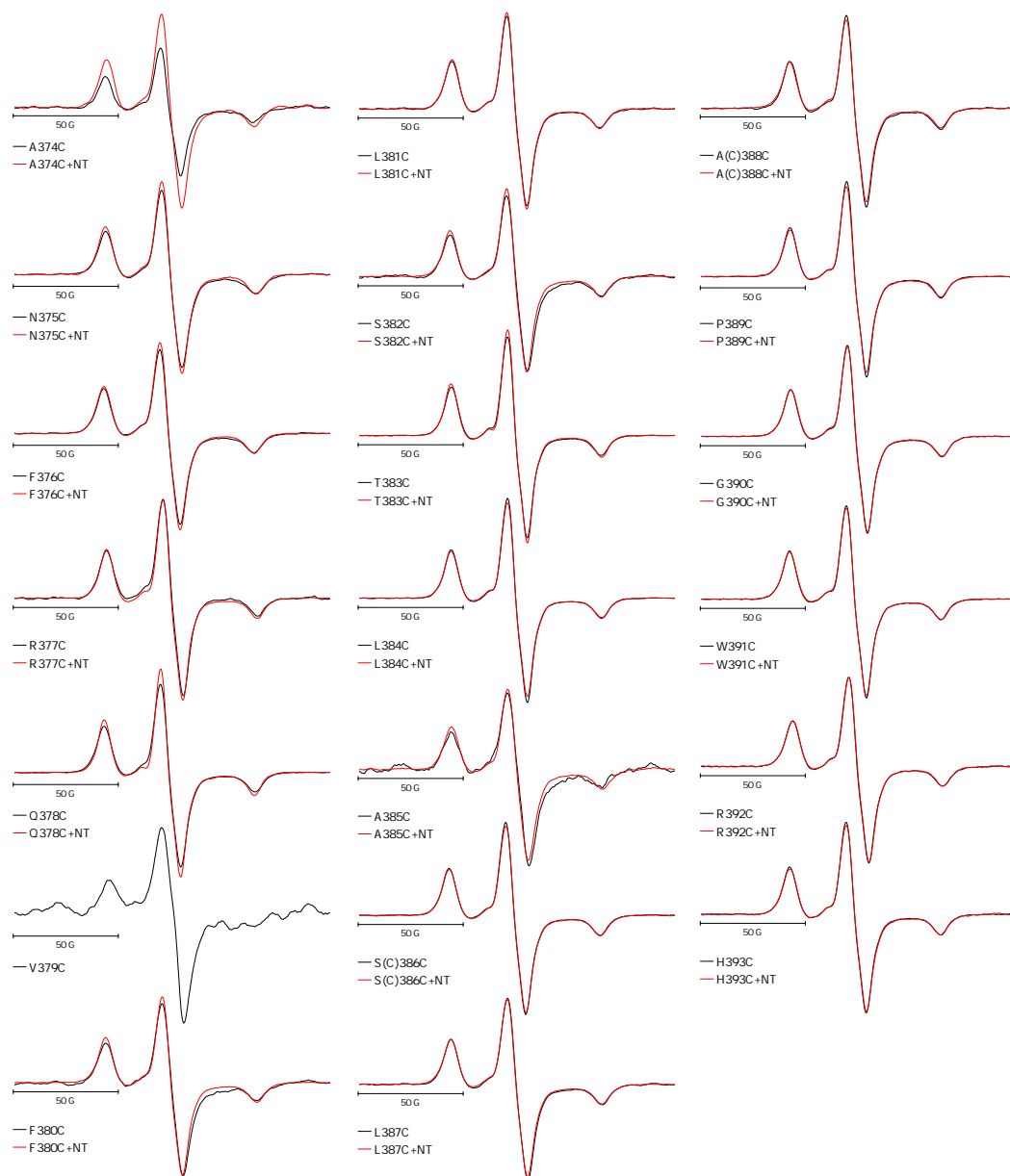
Figure D.3: Rigid-limit CW-EPR spectra H8 and C-terminus. Rigid-limit EPR spectra were recorded at 170 K for residues along the C-terminal stretch after TM7, encompassing the putative H8. Spectra were recorded in the absence and presence of agonist neurotensin (+NT), except for mutant V379C for which only the sample without NT was recorded at 170 K as the S/N ratio for this mutant was poor.

E | Bulk FRET Analysis

E.1 Introduction

Bulk FRET data was analysed using the Bayesian statistical method BEST (Bayesian estimation) as described by Kruschke in [450], which is a Bayesian alternative to the t-test.[1] Instead of assuming the collected data points are a representative sample of a population that is normally distributed with the same mean (μ) and standard deviation (σ) as the measured sample, Bayesian estimation uses the data to infer a population distribution. This is done by a Markov chain Monte Carlo (MCMC) algorithm, which generates large number of population distributions with parameters (μ and σ) that accommodate the observed data (see Figure E.1A); the generated MCMC chain (containing all the fitting distributions) is averaged to give a distribution which credibly accommodates the data. From this averaged MCMC distribution, parameters of interest such as μ and σ can be derived (Figure E.1B); parameter distributions generated for two datasets, can be used to examine the credible difference between parameters of the two datasets (*e.g.* μ_1-μ_2) by computing the difference between the distributions (see Figure E.1C). The method generates a complete distribution of credible values for the group means and their difference, providing more information than the typical t-test.

Thus, to test whether the values found for a parameter (such as the mean, μ) are significantly distinguishable between two data sets, the probability that the difference is non-zero can be gauged by what percentage of the generated population distribution of the difference $\Delta\mu$ falls above the $\Delta\mu$=0 line (probability of a difference greater than zero), and what percentage falls below it (probability of a difference smaller than zero, *i.e.* a negative difference, see Figure E.1C).

The threshold for reasonable distinguishability is chosen judiciously, and often the 68-95-99.7 rule is employed, where results are binned according to whether they fall within one,

---

[1]R script for statistical analysis was set up with help from Stijn van Weezel, Department of Economics, Royal Holloway, University of London.
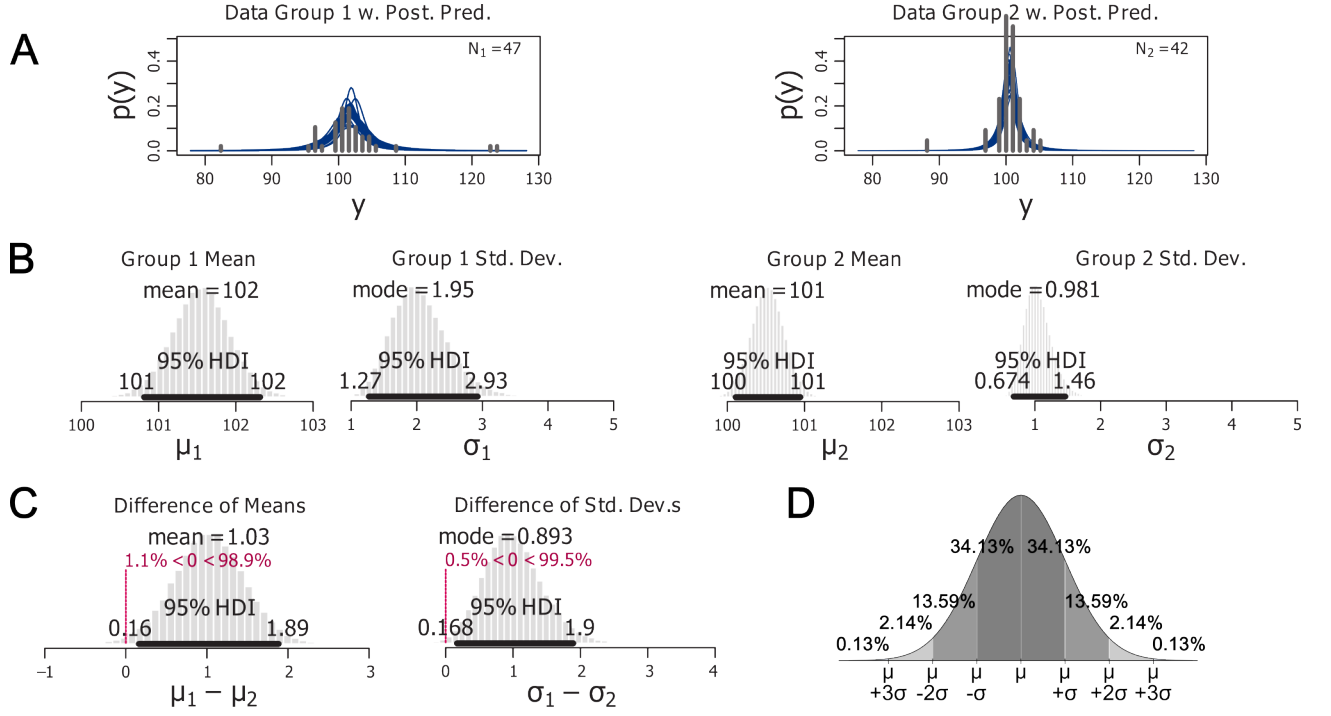
Figure E.1: Example of Bayesian BEST method. Two data sets are compared; **(A)** histograms of the data in the two groups (grey bars) are shown, with representative examples of MCMC generated distributions describing the data (posterior predictive distributions, Post. Pred.) superimposed (blue lines). **(B)** Histograms for the probability of the derived mean (μ) and standard deviation (σ), derived from the averaged MCMC chain are shown for both data sets. **(C)** The probability distributions of the differences between the means of the two data sets ($\mu_1 - \mu_2$) and their standard deviation $\sigma_1 - \sigma_2$) as calculated from the parameter distributions shown in **(B)** are shown here; the probability of a difference below or greater than zero is highlighted (pink dotted line) for each. **(E)** Diagram illustrating the probability distribution of a parameter described by a normal distribution with mean value μ and standard deviation σ; 68.27% of the values lie within one standard deviation of the mean; 95.45% of the values lie within two standard deviations of the mean; and 99.73% of the values lie within three standard deviations of the mean. Figure adapted from [450].

two, or three standard deviations of the mean, *i.e.*

$$Pr(\mu - \sigma \le x \le \mu + \sigma) \approx 0.6827 \tag{E.1a}$$

$$Pr(\mu - 2\sigma \le x \le \mu + 2\sigma) \approx 0.9545 \tag{E.1b}$$

$$Pr(\mu - 3\sigma \le x \le \mu + 3\sigma) \approx 0.9973 \tag{E.1c}$$

where x is a normally distributed variable with mean μ and standard deviation σ (see Figure E.1E).

E.2 Bayesian analysis of bulk FRET data

Firstly, the difference between the mean FRET efficiencies (Δμ) for each mutant compared to the others (TM_i-TM_j) was tested (Table E.1). The probability that the differences between

sites are non-zero ($\Pr(\Delta\mu\neq 0)$) was calculated, and thus whether sites can be reasonably said to have differing FRET efficiencies. The threshold for reasonable distinguishability was set at one standard deviation (0.683), in accordance with the 68-96-99.7 rule, and results were binned according to having probabilities $\Pr(\Delta\mu\neq 0)$ in accordance with values falling within one (at least 0.683), two (at least 0.955), or three (at least 0.997) standard deviations.

The cells in Table E.1 are shaded for visual guidance, with probabilities for a particular mutant (row) to have E_{cor} bigger or smaller than another mutant (column) being shaded red or blue, respectively. Darker shading corresponds to a higher probability (see also table legend).

The analysis confirms that indeed for TM1, 4 and 7 there is a high probability of observing lower E_{cor} compared to TM2, 3, 5, 6 and H8. Among the low E_{cor} sites (TM1, 4, and 7) in the absence of NT, the results can only be distinguished with low probability (one standard deviation), with TM7 giving lowest E_{cor}, followed by TM1, and TM4, respectively. For the group of high E_{cor} sites (TM2, 3, 5, 6 and H8) in the absence of NT, the only likely difference observed is for H8 having lower E_{cor} than TM3, 5 and 6 (at least two σ), with other differences having a low probability of one σ or smaller.

Table E.2 summarizes the Bayesian analysis on the effect of agonist on E_{cor} for each of the TMs, giving the probability for $\Delta\mu$ being larger or smaller than zero. Thus for sites where $\Pr(\Delta\mu< 0)$ and $\Pr(\Delta\mu> 0)$ differ greatly (or, using the same threshold as above, one of them is above 0.68 (one σ) or 0.95 (two σ)) NT can be said to have a reasonably likely effect on E_{cor}, and the sign of $\Delta\mu$ gives the direction of the effect, that is, whether E_{cor} is lower (-) or higher (+) in the absence of NT. The analysis shows that the largest effect of NT is observed in TM6, with a ~99% probability that NT decreases E_{cor}, followed by TM1 and 5, with a small probability of ~73% and ~70%, respectively, that NT decreases E_{cor} (Table E.2). For all other TMs smaller effects and/or effects with lower probabilities (<0.68) were observed. This effect of agonist of course influences the differences between the individual TMs (Table E.1, bottom half), but the overall pattern is largely unchanged, with high probabilities for observing high E_{cor} for TM3 and 5 in particular. The main difference is seen for TM6, with the large decrease in observed mean E_{cor} upon addition of NT, reducing its distinguishability from the "low E_{cor}" samples (TM1, 4 and 7) to only distinguishable with a probability of ~0.7-0.8 (corresponding to one standard deviation). Among the low E_{cor} sites (TM1, 4 and 7) in the presence of NT, the results are now indistinguishable under the chosen threshold.

Table E.1: Bayesian analysis of difference in E_{cor} in NTS1 dimers for samples labelled at different sites. The difference between the mean apparent FRET efficiencies for all possible pairs of mutants in the absence (top) and presence (bottom) of neurotensin agonist is analysed by Bayesian methods to calculate the probability that the differences between sites are non-zero, or in other words that the likelihood of finding the same FRET efficiency for both sites is small, and thus that the sites can be reasonably said to have differing FRET efficiencies. Probabilities for a particular mutant (row) to have E_{cor} bigger (>, red shading) or smaller (<, blue shading) than another mutant (column) are classified as being <0.683 (bellow one standard deviation, σ, light shading), and thus not likely distinguishable, or at least 0.683-0.955 (σ, medium shading), 0.955-0.997 (2σ, dark shading), or >0.997 (3σ, darkest shading), and thus reasonably distinguishable.

TM/H (Residue)	1 (A90C)	2 (Y104C)	3 (S172C)	4 (T186C)	5 (A261C)	6 (V307C)	7 (L371C)	8 (Q378C)
1 (A90C)	-	<0.896	<0.992	<0.770	<0.990	<1	>0.722	<0.999
2 (Y104C)	>0.896	-	<0.735	>0.855	<0.624	<0.681	>0.911	>0.591
3 (S172C)	>0.992	>0.735	-	>0.989	>0.684	>0.659	>0.988	>0.949
4 (T186C)	>0.770	<0.855	>0.989	-	<0.981	<1	>0.830	<0.977
5 (A261C)	>0.990	>0.624	<0.684	>0.981	-	<0.573	>0.979	>0.860
6 (V307C)	>1	>0.681	<0.659	>1	>0.573	-	>0.992	>0.977
7 (L371C)	<0.722	<0.911	<0.988	<0.830	<0.979	<0.992	-	<0.974
8 (Q378C)	>0.999	<0.591	<0.949	<0.977	<0.860	<0.977	>0.974	-
+NT								
1 (A90C)	-	<0.758	<0.998	<0.566	<0.974	<0.774	>0.522	<0.978
2 (Y104C)	>0.758	-	<0.856	>0.738	<0.832	>0.622	>0.703	<0.553
3 (S172C)	>0.998	>0.856	-	>0.998	<0.590	>0.993	>0.923	>0.993
4 (T186C)	>0.566	<0.738	<0.998	-	<0.946	<0.743	>0.563	<0.977
5 (A261C)	>0.974	>0.832	>0.590	>0.946	-	>0.946	>0.909	>0.910
6 (V307C)	>0.774	<0.622	<0.993	>0.743	<0.946	-	>0.669	<0.869
7 (L371C)	<0.522	<0.703	<0.923	<0.563	<0.909	<0.669	-	<0.808
8 (Q378C)	>0.987	>0.553	<0.993	>0.977	<0.910	>0.869	>0.808	-

Table E.2: Bayesian analysis of agonist effect on E_{cor} in NTS1 dimers. The difference between the mean apparent FRET efficiencies (Δμ) for each mutant in the presence and absence of neurotensin agonist is given. Bayesian data analysis methods are used to calculate the probability that this difference is non-zero, and the probability of Δμ being larger or smaller than zero is given.

TM/H (Residue)	Δμ	Pr(Δμ > 0)	Pr(Δμ < 0)
1 (A90C)	-0.038	0.73	0.27
2 (Y104C)	0.054	0.40	0.60
3 (S172C)	0.0056	0.49	0.51
4 (T186C)	-0.010	0.57	0.43
5 (A261C)	-0.073	0.70	0.30
6 (V307C)	0.17	0.99	0.01
7 (L371C)	-0.073	0.67	0.33
8 (Q378C)	0.0047	0.43	0.57

F | Pulsed EPR data NTS1
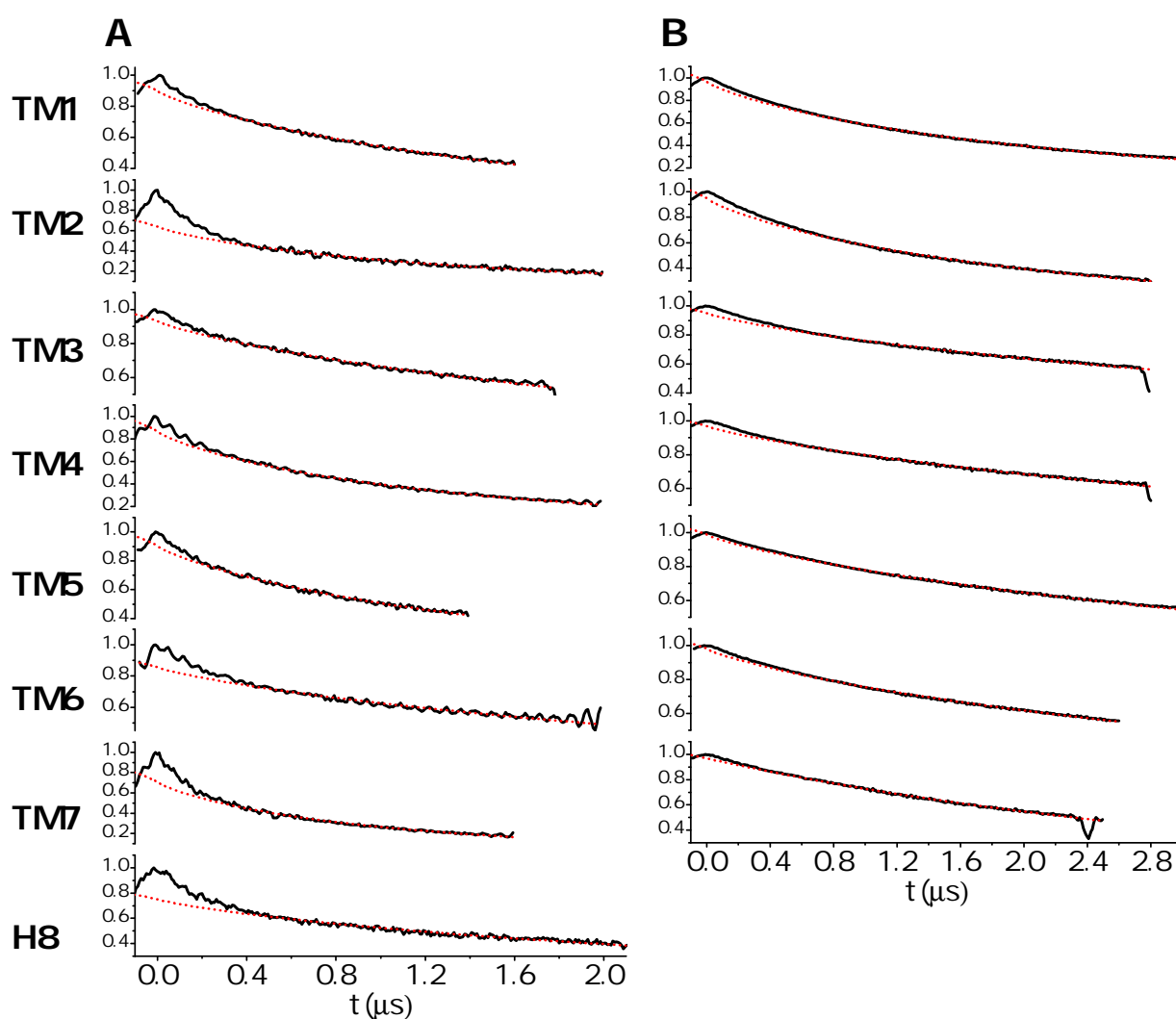
Figure F.1: Dipolar evolution functions before background correction for X- and Q-band DEER on NTS1 dimers. DEER traces were recorded at **(A)** X-band and **(B)** Q-band for NTS1 samples spin-labelled at the intracellular side of TM1-7 and H8. Recorded dipolar evolution functions (black) and fitted stretched exponential backgrounds (d=2.5, red) are shown. Fitted data and derived distance distributions are shown in Figure 5.7.

G | Nanodisc preparation

For the production of BPL nanodiscs, the optimal lipid-to-MSP ratio was determined empirically to be 70:1 (mol:mol), assuming an average molecular weight of 650 g/mol for BPL (Figure G.1).
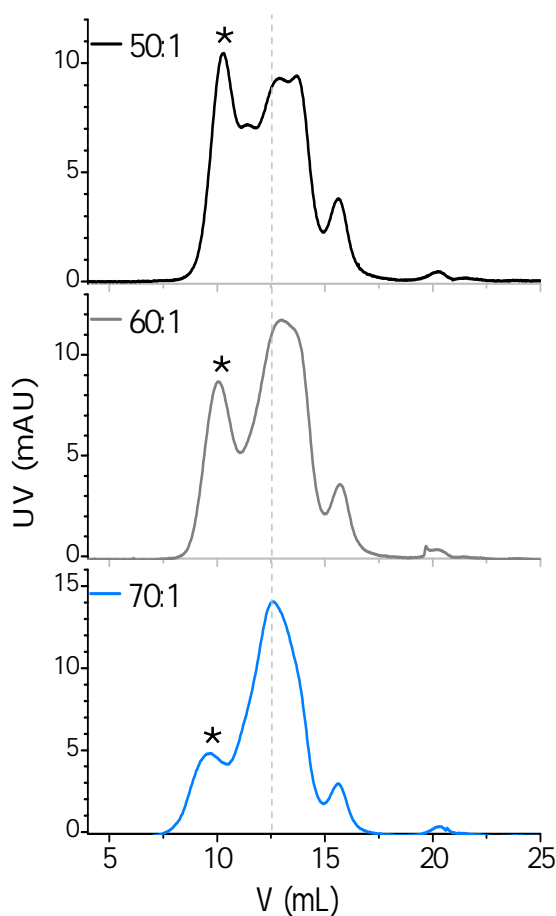
Figure G.1: Optimisation of BPL nanodisc formation. The formation of BPL nanodisc was tested at different lipid-to-MSP ratios, 50:1, 60:1 and 70:1 (mol:mol, assuming an average molecular weight for BPL of 650 g/mol). The void volume peak (indicated by *) was smaller, and a more symmetric peak around 12.5 mL (corresponding to a hydrodynamic radius of ~10 nm, indicated by dashed grey line) at higher lipid-to-MSP ratios.

The hydrodynamic (Stokes) radius (R_{st}) of NTS1 nanodiscs was determined by analytical gel filtration. Standards of known R_{st} (GE Healthcare) were run on the same Superdex 200 10/300 gel filtration column (GE Healthcare) used for nanodisc separation.[1] The partition coefficient K_{av} was determined from the elution volume V_e of the samples by

$$K_{av} = \frac{V_e - V_0}{V_c - V_0} \tag{G.1}$$

where V_0 is the void volume of the column (determined to be 8.03 mL by passing Blue dextran (GE Healthcare) over the column in a separate run, not shown here), and V_c is the geometric column volume of the column (24 mL, as specified by the manufacturer). A calibration curve can be created by plotting of $\sqrt{-\log K_{av}}$ versus R_{st}, and fitting a linear function to the data (Figure G.2). The K_{av} for each of the nanodisc preparations (PCPG, PCPGBPL, and BPL) was then determined from the gel filtration elution volume of the nanodisc peak, and the corresponding stokes radius was calculated from the calibration curve (shown in table in Figure G.2).
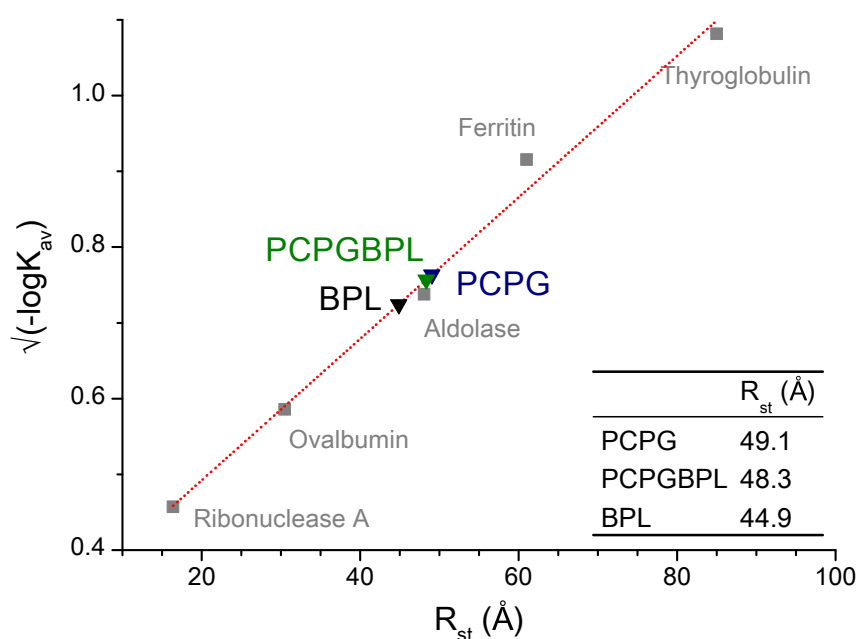
Figure G.2: Hydrodynamic radius of nanodiscs determined by analytical gel filtration. Using a calibration curve of reference samples, the hydrodynamic radii (or Stokes radii, R_{st}) for nanodisc preparations of PCPG, PCPGBPL, and BPL lipid composition were determined from their gel filtration partition coefficients K_{av} calculated from their elution volume, as described in the text.

---

[1] Run of standard samples was performed by Roslin Adamson (Department of Biochemistry, University of Oxford.)

H | CW-EPR: brief experimental background

H.1   CW-EPR experimental set-up

Figure H.1 gives a simplified scheme of a CW-EPR spectrometer [565]. The microwave source (a klystron or a Gunn oscillator) produces the electromagnetic radiation, and an in-line attenuator controls the power that reaches the sample. EPR uses reflection spectrometers:
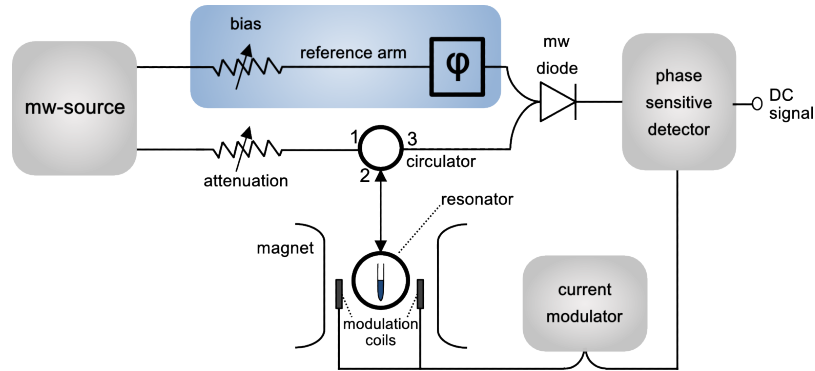
Figure H.1: Schematic of CW-EPR experimental set-up. Based on figure from [565]. A klystron or a Gunn oscillator produces microwaves. Output power is controlled by an attenuator. Microwaves coming in port 1 of the circulator only go to the cavity via port 2 and not directly to the detector via port 3, and reflected microwaves are directed only to the detector and not back to the microwave source. Other parts are discussed in the text.

these measure the changes (due to spectroscopic transitions) in the amount of radiation reflected back from the cavity that holds the sample. The circulator ensures that only reflected microwaves reach the detector. The resonator cavity is a metal box that helps amplify the weak sample signals by resonating with the microwaves. At resonance the cavity stores the microwave energy, and no microwaves are reflected back (Figure H.2). Cavities are characterized by their quality factor (Q),

$$Q_L = \frac{\nu_{mw}L}{R_0 n^2 + r} \tag{H.1}$$

where ν_{mw} gives the microwave frequency, L is the inductivity of the resonator, R_0 the
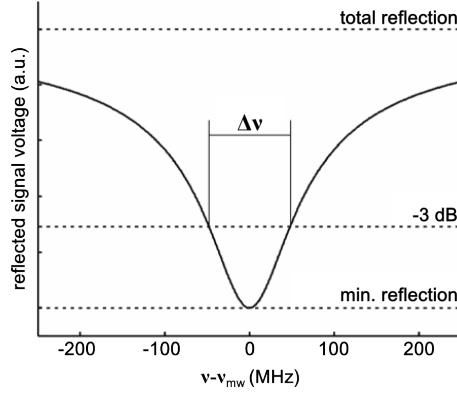
Figure H.2: Reflected microwave power from a resonant cavity. Idealized microwave mode (dip) with $Q_L = 100$ at a frequency of 9.6 GHz. At the 3-dB points, the power that enters the resonator is half as large as that on resonance ($\nu - \nu_{mw} = 0$). The 3-dB resonance bandwidth ($\Delta\nu$) in this example is 96 MHz. Adapted from [565].

impedance of the line that transmits the microwave power from the source to the resonator, n a parameter that characterizes the coupling between the transmission line and the resonator, and r the impedance of the resonator. The impedance of the resonator varies between samples due to dielectric microwave losses in the sample, but it does not include the resonant microwave absorption of electron spin. With the electron spins off-resonance, the reflected power should be zero, which is achieved by critical coupling of the resonator. The coupling is adjusted by the iris (opening between the cavity and the waveguide) so that the condition

$$R_0 n^2 = r \tag{H.2}$$

is fulfilled, and all microwave power that enters the resonator is converted to heat in the impedance r. When during a field sweep the electron spins resonate and the sample absorbs additional microwave power the impedance of the resonator increases due to the additional losses, which means that the cavity is no longer critically coupled (*i.e.* equation H.2 is no longer fulfilled), and microwave power is reflected from the resonator to the detector, resulting in an EPR signal.

The reflected signal is detected by using a barrier diode that converts the microwave power to an electrical current. The reference arm supplies the diode additional microwave power (bias) to ensure that its current is in the linear regime (*i.e.* that its output power is proportional to the input microwave power). The phase shifter in the reference arm ensures that the microwaves coming from this arm are in phase with the reflected signal microwaves when these both reach the diode.

EPR uses phase sensitive detection to enhance sensitivity (see Figure H.3). The derivative of the absorption spectrum is recorded by modulating the magnetic field B_0 sinusoidally at the modulation frequency (typically 100 kHz). For an EPR signal which is approximately
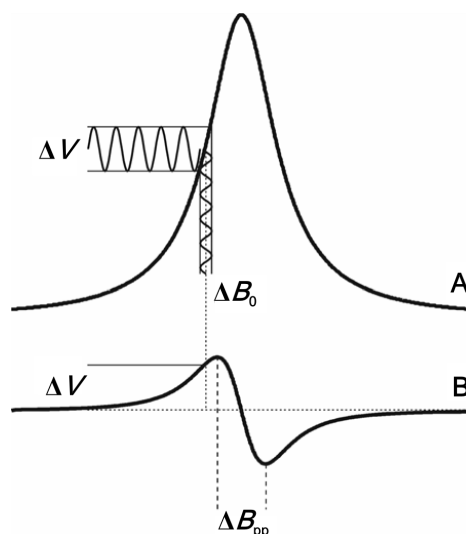
Figure H.3: Frequency modulation in CW-EPR. In EPR the first derivative **(B)** of the absorption spectrum **(A)** is detected by field modulation with amplitude ΔB_0 (modulation coils in H.1). The signal after the microwave diode oscillates with the frequency of the field modulation and with amplitude ΔV. The signal after the phase-sensitive detector is a DC (direct-current) signal with amplitude ΔV. The peak-to-peak linewidth in the derivative spectrum, ΔB_{pp}, corresponds to the field difference between the inflection points of the absorption peak. Adapted from [565].

linear over an interval as wide as the modulation amplitude, the EPR signal is transformed into a sinusoid with an amplitude proportional to the slope of the signal, which is measured with a phase-sensitive detector, giving the derivative spectrum. This results in an increased signal-to-noise ratio, as noise that does not oscillate with the modulation frequency and non-resonant microwave absorption that does not depend on the magnetic field are rejected. In addition to this, the derivative spectrum is better resolved than the absorption spectrum (linewidths can be easily measured, as these are the peak-to-peak distance in the derivative spectrum, see Figure 1.11). A disadvantage is that signals that are much broader than the maximum modulation amplitude can be hard to detect, as field modulation then causes only very small signal oscillations.

References

[1] M. Sud, E. Fahy, D. Cotter, A. Brown, E. a. Dennis, C. K. Glass, A. H. Merrill, R. C. Murphy, C. R. H. Raetz, D. W. Russell, and S. Subramaniam, "LMSD: LIPID MAPS structure database," *Nucleic Acids Res.*, vol. 35, pp. D527–32, Jan. 2007.

[2] G. van Meer, D. R. Voelker, and G. W. Feigenson, "Membrane lipids: where they are and how they behave," *Nat. Rev. Mol. Cell Biol.*, vol. 9, pp. 112–24, Feb. 2008.

[3] A. G. Lee, "Functional properties of biological membranes: a physical-chemical approach," *Prog. Biophys. Mol. Biol.*, vol. 29, no. 1, pp. 3–56, 1976.

[4] A. G. Lee, "How lipids affect the activities of integral membrane proteins," *Biochim. Biophys. Acta*, vol. 1666, pp. 62–87, Nov. 2004.

[5] D. Marsh, "Lateral pressure profile, spontaneous curvature frustration, and the incorporation and conformation of proteins in membranes," *Biophys. J.*, vol. 93, pp. 3884–99, Dec. 2007.

[6] J. M. Boggs, "Intermolecular hydrogen bonding between lipids: influence on organization and function of lipids in membranes," *Can. J. Biochem.*, vol. 58, pp. 755–770, 1980.

[7] B. Ramstedt and J. P. Slotte, "Sphingolipids and the formation of sterol-enriched ordered membrane domains.," *Biochim. Biophys. Acta*, vol. 1758, pp. 1945–56, Dec. 2006.

[8] T. P. McMullen, R. N. Lewis, and R. N. McElhaney, "Cholesterol-phospholipid interactions, the liquid-ordered phase and lipid rafts in model and biological membranes," *Curr. Opin. Colloid & Interface Sci.*, vol. 8, pp. 459–468, Apr. 2004.

[9] D. A. Brown and E. London, "Structure of detergent-resistant membrane domains: does phase separation occur in biological membranes?," *Biochem. Biophys. Res. Commun.*, vol. 240, pp. 1–7, Nov. 1997.

[10] S. Munro, "Lipid rafts: elusive or illusive?," *Cell*, vol. 115, pp. 377–388, 2003.

[11] K. Simons and M. J. Gerl, "Revitalizing membrane rafts: new tools and insights.," *Nat. Rev. Mol. Cell Biol.*, vol. 11, pp. 688–99, Oct. 2010.

[12] A. Kusumi, K. G. N. Suzuki, R. S. Kasai, K. Ritchie, and T. K. Fujiwara, "Hierarchical mesoscale domain organization of the plasma membrane," *Trends Biochem. Sci.*, vol. 36, pp. 604–15, Nov. 2011.

[13] M. L. Kraft, "Plasma membrane organization and function: moving past lipid rafts," *Mol. Biol. Cell*, vol. 24, pp. 2765–8, Sept. 2013.

[14] P. L. Yeagle, "The membranes of cells," 1993.

[15] A. A. Spector and M. A. Yorek, "Membrane lipid composition and cellular function," *J. Lipid Res.*, vol. 26, pp. 1015–1035, Sept. 1985.

[16] M. Opekarová and W. Tanner, "Specific lipid requirements of membrane proteins–a putative bottleneck in heterologous expression," *Biochim. Biophys. Acta - Biomembr.*, vol. 1610, pp. 11–22, Feb. 2003.

[17] J. S. Owen, K. R. Bruckdorfer, R. C. Day, and N. McIntyre, "Decreased erythrocyte membrane fluidity and altered lipid composition in human liver disease," *J. Lipid Res.*, vol. 23, pp. 124–132, Jan. 1982.

[18] G. Nelson, "Lipid composition of erythrocytes in various mammalian species," *Biochim. Biophys. Acta*, vol. 144, pp. 221–232, 1967.

[19] W. Renooij, L. M. Olde, R. F. Zwaal, and L. L. Van Deenen, "Topological asymmetry of phospholipid metabolism in rat erythrocyte membranes," *Eur. J. Biochem.*, vol. 61, pp. 53–58, 1976.

[20] W. Breckenridge, G. Gombos, and I. Morgan, "The lipid composition of adult rat brain synaptosomal plasma membranes," *Biochim. Biophys. Acta*, vol. 266, pp. 695–707, 1972.

[21] K. Marheineke, S. Grünewald, W. Christie, and H. Reiländer, "Lipid composition of Spodoptera frugiperda (Sf9) and Trichoplusia ni (Tn) insect cells used for baculovirus infection.," *FEBS Lett.*, vol. 441, pp. 49–52, Dec. 1998.

[22] B. Hille, "Diversity of phosphoinositide signaling," *Biochem. Suppl. Ser. A Membr. Cell Biol.*, vol. 6, pp. 113–119, June 2012.

[23] T. Balla, M. Wymann, and J. York, eds., *Phosphoinositides II: The Diverse Biological Functions*, vol. 59. Springer, 2012.

[24] A. D. Tepper, P. Ruurs, T. Wiedmer, P. J. Sims, J. Borst, and W. J. van Blitterswijk, "Sphingomyelin hydrolysis to ceramide during the execution phase of apoptosis results from phospholipid scrambling and alters cell-surface morphology," *J. Cell Biol.*, vol. 150, pp. 155–64, July 2000.

[25] M. A. Lemmon, "Membrane recognition by phospholipid-binding domains," *Nat. Rev. Mol. Cell Biol.*, vol. 9, pp. 99–111, Feb. 2008.

[26] F.-X. Contreras, L. Sánchez-Magraner, A. Alonso, and F. M. Goñi, "Transbilayer (flip-flop) lipid motion and lipid scrambling in membranes," *FEBS Lett.*, vol. 584, pp. 1779–86, May 2010.

[27] M. Nakano, M. Fukuda, T. Kudo, N. Matsuzaki, T. Azuma, K. Sekine, H. Endo, and T. Handa, "Flip-flop of phospholipids in vesicles: kinetic analysis with time-resolved small-angle neutron scattering," *J. Phys. Chem. B*, vol. 113, pp. 6745–8, May 2009.

[28] I. López-Montero, N. Rodriguez, S. Cribier, A. Pohl, M. Vélez, and P. F. Devaux, "Rapid transbilayer movement of ceramides in phospholipid vesicles and in human erythrocytes," *J. Biol. Chem.*, vol. 280, pp. 25811–9, July 2005.

[29] J. C. M. Holthuis and T. P. Levine, "Lipid traffic: floppy drives and a superhighway," *Nat. Rev. Mol. Cell Biol.*, vol. 6, pp. 209–20, Mar. 2005.

[30] S. Garg, L. Porcar, A. C. Woodka, P. D. Butler, and U. Perez-Salas, "Noninvasive neutron scattering measurements reveal slower cholesterol transport in model lipid membranes," *Biophys. J.*, vol. 101, pp. 370–7, July 2011.

[31] T. Pomorski and A. K. Menon, "Lipid flippases and their biological functions," *Cell. Mol. Life Sci.*, vol. 63, pp. 2908–21, Dec. 2006.

[32] R. L. Lopez-Marques, L. Theorin, M. G. Palmgren, and T. G. Pomorski, "P4-ATPases: lipid flippases in cell membranes," *Pflugers Arch.*, pp. 1227–1240, Sept. 2013.

[33] D. L. Daleke, "Phospholipid flippases," *J. Biol. Chem.*, vol. 282, pp. 821–5, Jan. 2007.

[34] P. Devaux and R. Morris, "Transmembrane asymmetry and lateral domains in biological membranes," *Traffic*, vol. 5, pp. 241–246, 2004.

[35] J. Silvius, "Role of cholesterol in lipid raft formation: lessons from lipid model systems," *Biochim. Biophys. Acta*, vol. 1610, pp. 174–183, Mar. 2003.

[36] B. C. Lagerholm, G. E. Weinreb, K. Jacobson, and N. L. Thompson, "Detecting microdomains in intact cell membranes," *Annu. Rev. Phys. Chem.*, vol. 56, pp. 309–36, Jan. 2005.

[37] A. Kusumi, C. Nakada, K. Ritchie, K. Murase, K. Suzuki, H. Murakoshi, R. S. Kasai, J. Kondo, and T. Fujiwara, "Paradigm shift of the plasma membrane concept from the two-dimensional continuum fluid to the partitioned fluid: high-speed single-molecule tracking of membrane molecules," *Annu. Rev. Biophys. Biomol. Struct.*, vol. 34, pp. 351–78, Jan. 2005.

[38] G. Conforti, A. Zanetti, I. Pasquali-Ronchetti, D. Quaglino, P. Neyroz, and E. Dejana, "Modulation of vitronectin receptor binding by membrane lipid composition," *J. Biol. Chem.*, vol. 265, no. 7, pp. 4011–4019, 1990.

[39] T. J. Pucadyil and A. Chattopadhyay, "Cholesterol modulates ligand binding and G-protein coupling to serotonin$_{1A}$ receptors from bovine hippocampus," *Biochim. Biophys. Acta*, vol. 1663, pp. 188–200, May 2004.

[40] J. Oates, B. Faust, H. Attrill, P. Harding, M. Orwick, and A. Watts, "The role of cholesterol on the activity and stability of neurotensin receptor 1," *Biochim. Biophys. Acta - Biomembr.*, vol. 1818, pp. 2228–2233, Sept. 2012.

[41] H. Zheng, E. A. Pearsall, D. P. Hurst, Y. Zhang, J. Chu, Y. Zhou, P. H. Reggio, H. H. Loh, and P.-Y. Law, "Palmitoylation and membrane cholesterol stabilize μ-opioid receptor homodimerization and G protein coupling.," *BMC Cell Biol.*, vol. 13, p. 6, Jan. 2012.

[42] S. Inagaki, R. Ghirlando, J. F. White, J. Gvozdenovic-Jeremic, J. K. Northup, and R. Grisshammer, "Modulation of the interaction between neurotensin receptor NTS1 and Gq protein by lipid," *J. Mol. Biol.*, vol. 417, pp. 95–111, Mar. 2012.

[43] R. Mani, S. D. Cady, M. Tang, A. J. Waring, R. I. Lehrer, and M. Hong, "Membrane-dependent oligomeric structure and pore formation of a β-hairpin antimicrobial peptide in lipid bilayers from solid-state NMR," *Proc. Natl. Acad. Sci.*, vol. 103, pp. 16242–16247, Oct. 2006.

[44] S. W. Wong, M.-J. Kwon, A. M. K. Choi, H.-P. Kim, K. Nakahira, and D. H. Hwang, "Fatty acids modulate Toll-like receptor 4 activation through regulation of receptor dimerization and recruitment into lipid rafts in a reactive oxygen species-dependent," *J. Biol. Chem.*, vol. 284, pp. 27384–27392, Oct. 2009.

[45] D. Marsh and L. I. Horváth, "Structure, dynamics and composition of the lipid-protein interface. Perspectives from spin-labelling," *Biochim. Biophys. Acta*, vol. 1376, pp. 267–296, Nov. 1998.

[46] J. A. Killian, "Hydrophobic mismatch between proteins and lipids in membranes," *Biochim. Biophys. Acta*, vol. 1376, pp. 401–15, Nov. 1998.

[47] T. H. Harroun, W. T. Heller, T. M. Weiss, L. Yang, and H. W. Huang, "Experimental evidence for hydrophobic matching and membrane-mediated interactions in lipid bilayers containing gramicidin," *Biophys. J.*, vol. 76, pp. 937–945, Feb. 1999.

[48] S. H. Park and S. J. Opella, "Tilt angle of a trans-membrane helix is determined by hydrophobic mismatch," *J. Mol. Biol.*, vol. 350, pp. 310–318, July 2005.

[49] N. J. Ryba and D. Marsh, "Protein rotational diffusion and lipid/protein interactions in recombinants of bovine rhodopsin with saturated diacylphosphatidylcholines of different chain lengths studied by conventional and saturation-transfer electron spin resonance," *Biochemistry*, vol. 31, pp. 7511–7518, Aug. 1992.

[50] R. J. Webb, J. M. East, R. P. Sharma, and A. G. Lee, "Hydrophobic mismatch and the incorporation of peptides into lipid bilayers: a possible mechanism for retention in the Golgi," *Biochemistry*, vol. 37, pp. 673–679, Jan. 1998.

[51] G. von Heijne, "Membrane-protein topology," *Nat. Rev. Mol. Cell Biol.*, vol. 7, pp. 909–918, Dec. 2006.

[52] M. A. Yildirim, K.-I. Goh, M. E. Cusick, A.-L. Barabási, and M. Vidal, "Drug-target network," *Nat. Biotechnol.*, vol. 25, pp. 1119–1126, Oct. 2007.

[53] M. Rask-Andersen, M. S. Almén, and H. B. Schiöth, "Trends in the exploitation of novel drug targets," *Nat. Rev. Drug Discov.*, vol. 10, pp. 579–590, Aug. 2011.

[54] O. Halskau, A. Muga, and A. Martínez, "Linking new paradigms in protein chemistry to reversible membrane-protein interactions," *Curr. protein & Pept. Sci.*, vol. 10, pp. 339–359, Aug. 2009.

[55] A. L. Lomize, I. D. Pogozheva, M. A. Lomize, and H. I. Mosberg, "The role of hydrophobic interactions in positioning of peripheral proteins in membranes," *BMC Struct. Biol.*, vol. 7, Jan. 2007.

[56] A. Mulgrew-Nesbitt, K. Diraviyam, J. Wang, S. Singh, P. Murray, Z. Li, L. Rogers, N. Mirkovic, and D. Murray, "The role of electrostatics in protein-membrane interactions," *Biochim. Biophys. Acta*, vol. 1761, pp. 812–826, Aug. 2006.

[57] M. A. Lemmon and K. M. Ferguson, "Signal-dependent membrane targeting by pleckstrin homology (PH) domains," *Biochem. J.*, vol. 350, pp. 1–18, Aug. 2000.

[58] W. Cho, "Membrane targeting by C1 and C2 domains," *J. Biol. Chem.*, vol. 276, pp. 32407–32410, Aug. 2001.

[59] W. Cho and R. V. Stahelin, "Membrane-protein interactions in cell signaling and membrane trafficking," *Annu. Rev. Biophys. Biomol. Struct.*, vol. 34, pp. 119–151, Jan. 2005.

[60] M. A. Lemmon, K. M. Ferguson, and C. S. Abrams, "Pleckstrin homology domains and the cytoskeleton," *FEBS Lett.*, vol. 513, pp. 71–76, Feb. 2002.

[61] H. Ikezawa, "Glycosylphosphatidylinositol (GPI)-anchored proteins," *Biol. Pharm. Bull.*, vol. 25, no. 4, pp. 409–417, 2002.

[62] S. Mayor and H. Riezman, "Sorting GPI-anchored proteins," *Nat. Rev. Mol. Cell Biol.*, vol. 5, pp. 110–120, Feb. 2004.

[63] K. Hanada, M. Nishijima, Y. Akamatsu, and R. E. Pagano, "Both sphingolipids and cholesterol participate in the detergent insolubility of alkaline phosphatase, a glycosylphosphatidylinositol-anchored protein, in mammalian membranes," *J. Biol. Chem.*, vol. 270, no. 11, pp. 6254–6260, 1995.

[64] R. Varma and S. Mayor, "GPI-anchored proteins are organized in submicron domains at the cell surface.," *Nature*, vol. 394, pp. 798–7801, Aug. 1998.

[65] A. G. D. Tse, A. N. Barclay, A. Watts, and A. F. Williams, "A glycophospholipid tail at the carboxyl terminus of the Thy-1 glycoprotein of neurons and thymocytes," *Science*, vol. 230, pp. 1003–1008, Nov. 1985.

[66] Y. Maeda and T. Kinoshita, "Structural remodeling, trafficking and functions of glycosylphosphatidylinositol-anchored proteins," *Prog. Lipid Res.*, vol. 50, pp. 411–424, Oct. 2011.

[67] M. Fujita and T. Kinoshita, "GPI-anchor remodeling: potential functions of GPI-anchors in intracellular trafficking and membrane dynamics," *Biochim. Biophys. Acta*, vol. 1821, pp. 1050–1058, Aug. 2012.

[68] G. von Heijne, "Membrane protein assembly: rules of the game," *BioEssays*, vol. 17, no. 1, pp. 25–30, 1995.

[69] M. B. Ulmschneider, M. S. P. Sansom, and A. Di Nola, "Properties of integral membrane protein structures: derivation of an implicit membrane potential," *Proteins*, vol. 59, pp. 252–265, May 2005.

[70] W. M. Yau, W. C. Wimley, K. Gawrisch, and S. H. White, "The preference of tryptophan for membrane interfaces," *Biochemistry*, vol. 37, pp. 14713–14718, Oct. 1998.

[71] M. A. Lemmon and D. M. Engelman, "Helix-helix interactions inside lipid bilayers," *Curr. Opin. Struct. Biol.*, vol. 2, pp. 511–518, 1992.

[72] V. K. Mishra, M. N. Palgunachari, J. P. Segrest, and G. Anantharamaiah, "Interactions of synthetic peptide analogs of the class A amphipathic helix with lipids. Evidence for the snorkel hypothesis," *J. Biol. Chem.*, vol. 269, no. 10, pp. 7185–7191, 1994.

[73] J. A. Killian and G. von Heijne, "How proteins adapt to a membrane-water interface," *Trends Biochem. Sci.*, vol. 25, pp. 429–434, Sept. 2000.

[74] A. K. Chamberlain, Y. Lee, S. Kim, and J. U. Bowie, "Snorkeling preferences foster an amino acid composition bias in transmembrane helices," *J. Mol. Biol.*, vol. 339, pp. 471–479, May 2004.

[75] G. von Heijne, "The distribution of positively charged residues in bacterial inner membrane proteins correlates with the trans-membrane topology," *EMBO J.*, vol. 5, pp. 3021–3027, Nov. 1986.

[76] J. Nilsson, B. Persson, and G. von Heijne, "Comparative analysis of amino acid distributions in integral membrane proteins from 107 genomes," *Proteins*, vol. 60, pp. 606–616, Sept. 2005.

[77] M. Eilers, S. C. Shekar, T. Shieh, S. O. Smith, and P. J. Fleming, "Internal packing of helical membrane proteins," *Proc. Natl. Acad. Sci.*, vol. 97, pp. 5796–5801, May 2000.

[78] R. Aurora and G. D. Rose, "Helix capping," *Protein Sci.*, vol. 7, pp. 21–38, Jan. 1998.

[79] F. X. Zhou, M. J. Cocco, W. P. Russ, A. T. Brunger, and D. M. Engelman, "Interhelical hydrogen bonding drives strong interactions in membrane proteins," *Nat. Struct. Biol.*, vol. 7, pp. 154–160, Feb. 2000.

[80] D. Schneider, "Rendezvous in a membrane: close packing, hydrogen bonding, and the formation of transmembrane helix oligomers," *FEBS Lett.*, vol. 577, pp. 5–8, Nov. 2004.

[81] T. Magee and M. C. Seabra, "Fatty acylation and prenylation of proteins: what's hot in fat," *Curr. Opin. Cell Biol.*, vol. 17, pp. 190–196, Apr. 2005.

[82] P. A. Konstantinopoulos, M. V. Karamouzis, and A. G. Papavassiliou, "Post-translational modifications and regulation of the RAS superfamily of GTPases as anticancer targets," *Nat. Rev. Drug Discov.*, vol. 6, pp. 541–555, July 2007.

[83] C. A. Chen and D. R. Manning, "Regulation of G proteins by covalent modification," *Oncogene*, vol. 20, pp. 1643–1652, 2001.

[84] Q. Al-Awqati, "One hundred years of membrane permeability: does Overton still rule?," *Nat. Cell Biol.*, vol. 1, pp. E201–202, Dec. 1999.

[85] A. Pohorille, K. Schweighofer, and M. Wilson, "The origin and early evolution of membrane channels," *Astrobiology*, vol. 5, no. 1, pp. 1–17, 2005.

[86] I. B. Levitan, "Signaling protein complexes associated with neuronal ion channels," *Nat. Neurosci.*, vol. 9, pp. 305–310, Mar. 2006.

[87] H. C. Lai and L. Y. Jan, "The distribution and targeting of neuronal voltage-gated ion channels," *Nat. Rev. Neurosci.*, vol. 7, pp. 548–562, July 2006.

[88] K. M. Giacomini, S.-M. Huang, D. J. Tweedie, L. Z. Benet, K. L. R. Brouwer, X. Chu, A. Dahlin, R. Evers, V. Fischer, K. M. Hillgren, K. A. Hoffmaster, T. Ishikawa, D. Keppler, R. B. Kim, C. A. Lee, M. Niemi, J. W. Polli, Y. Sugiyama, P. W. Swaan, J. A. Ware, S. H. Wright, S. W. Yee, M. J. Zamek-Gliszczynski, and L. Zhang, "Membrane transporters in drug development," *Nat. Rev. Drug Discov.*, vol. 9, pp. 215–236, Mar. 2010.

[89] M. H. Saier, "A functional-phylogenetic classification system for transmembrane solute transporters," *Microbiol. Mol. Biol. Rev.*, vol. 64, no. 2, pp. 354–411, 2000.

[90] L. R. Forrest, R. Krämer, and C. Ziegler, "The structural basis of secondary active transport mechanisms," *Biochim. Biophys. Acta*, vol. 1807, pp. 167–188, Feb. 2011.

[91] Y. Jiang, A. Lee, J. Chen, M. Cadene, B. T. Chait, and R. MacKinnon, "The open pore conformation of potassium channels," *Nature*, vol. 417, pp. 523–526, May 2002.

[92] J. P. Morth, B. P. Pedersen, M. J. Buch-Pedersen, J. P. Andersen, B. Vilsen, M. G. Palmgren, and P. Nissen, "A structural overview of the plasma membrane Na^+,K^+-ATPase and H^+-ATPase ion pumps," *Nat. Rev. Mol. Cell Biol.*, vol. 12, pp. 60–70, Jan. 2011.

[93] D. C. Gadsby, "Ion channels versus ion pumps: the principal difference, in principle," *Nat. Rev. Mol. Cell Biol.*, vol. 10, pp. 344–352, May 2009.

[94] M. S. Sonders and S. G. Amara, "Channels in transporters," *Curr. Opin. Neurobiol.*, vol. 6, pp. 294–302, June 1996.

[95] V. Vasiliou, K. Vasiliou, and D. Nebert, "Human ATP-binding cassette (ABC) transporter family," *Hum. Genomics*, vol. 3, no. 3, pp. 281–290, 2009.

[96] R. Poole, "Energy coupling for membrane transport," *Annu. Rev. Plant Physiol.*, vol. 29, pp. 437–460, 1978.

[97] R. Fredriksson and H. B. Schiöth, "The repertoire of G-protein-coupled receptors in fully sequenced

genomes," *Mol. Pharmacol.*, vol. 67, no. 5, pp. 1414–1425, 2005.

[98] H. B. Schiöth and R. Fredriksson, "The GRAFS classification system of G-protein coupled receptors in comparative perspective," *Gen. Comp. Endocrinol.*, vol. 142, pp. 94–101, May 2005.

[99] I. S. Moreira, "Structural features of the G-protein/GPCR interactions," *Biochim. Biophys. Acta*, vol. 1840, pp. 16–33, Jan. 2014.

[100] C. Ellis, "The state of GPCR research in 2004," *Nat. Rev. Drug Discov.*, vol. 3, no. 7, pp. 577–626, 2004.

[101] V. Katritch, V. Cherezov, and R. C. Stevens, "Structure-function of the G protein-coupled receptor superfamily," *Annu. Rev. Pharmacol. Toxicol.*, vol. 53, pp. 531–556, Jan. 2013.

[102] R. T. Dorsam and J. S. Gutkind, "G-protein-coupled receptors and cancer," *Nat. Rev. Cancer*, vol. 7, pp. 79–94, Feb. 2007.

[103] M. J. Marinissen and J. S. Gutkind, "G-protein-coupled receptors and signaling networks: emerging paradigms," *Trends Pharmacol. Sci.*, vol. 22, pp. 368–376, July 2001.

[104] S. G. F. Rasmussen, B. T. DeVree, Y. Zou, A. C. Kruse, K. Y. Chung, T. S. Kobilka, F. S. Thian, P. S. Chae, E. Pardon, D. Calinski, J. M. Mathiesen, S. T. A. Shah, J. A. Lyons, M. Caffrey, S. H. Gellman, J. Steyaert, G. Skiniotis, W. I. Weis, R. K. Sunahara, and B. K. Kobilka, "Crystal structure of the β₂ adrenergic receptor-Gs protein complex," *Nature*, vol. 477, pp. 549–555, Sept. 2011.

[105] J. A. Brzostowski and A. R. Kimmel, "Signaling at zero G: G-protein-independent functions for 7-TM receptors," *Trends Biochem. Sci.*, vol. 26, pp. 291–297, May 2001.

[106] S. S. G. Ferguson, "Evolving concepts in G protein-coupled receptor endocytosis: the role in receptor desensitization and signaling," *Pharmacol. Rev.*, vol. 53, pp. 1–24, Mar. 2001.

[107] S. S. G. Ferguson, "Phosphorylation-independent attenuation of GPCR signalling," *Trends Pharmacol. Sci.*, vol. 28, pp. 173–179, Apr. 2007.

[108] K. L. Pierce and R. J. Lefkowitz, "Classical and new roles of β-arrestins in the regulation of G-protein-coupled receptors," *Nat. Rev. Neurosci.*, vol. 2, pp. 727–733, 2001.

[109] K. L. Pierce, L. M. Luttrell, and R. J. Lefkowitz, "New mechanisms in heptahelical receptor signaling to mitogen activated protein kinase cascades," *Oncogene*, vol. 20, pp. 1532–1539, Mar. 2001.

[110] A. C. Hanyaloglu and M. von Zastrow, "Regulation of GPCRs by endocytic membrane trafficking and its potential implications," *Annu. Rev. Pharmacol. Toxicol.*, vol. 48, pp. 537–568, Jan. 2008.

[111] S. L. Garland, "Are GPCRs still a source of new targets?," *J. Biomol. Screen.*, vol. 18, pp. 947–966, Oct. 2013.

[112] B. K. Shoichet and B. K. Kobilka, "Structure-based drug screening for G-protein-coupled receptors," *Trends Pharmacol. Sci.*, vol. 33, pp. 268–272, May 2012.

[113] A. Helenius and K. Simons, "Solubilization of membranes by detergents," *Biochim. Biophys. Acta*, vol. 415, pp. 29–79, 1975.

[114] T. Arnold and D. Linke, "The use of detergents to purify membrane proteins," *Curr. Protoc. Protein Sci.*, vol. 4, pp. 4.8.1–4.8.30, Aug. 2008.

[115] A. M. Seddon, P. Curnow, and P. J. Booth, "Membrane proteins, lipids and detergents: not just a soap opera," *Biochim. Biophys. Acta*, vol. 1666, pp. 105–117, Nov. 2004.

[116] G. G. Privé, "Detergents for the stabilization and crystallization of membrane proteins," *Methods*, vol. 41, pp. 388–397, Apr. 2007.

[117] A. A. Thompson, J. J. Liu, E. Chun, D. Wacker, H. Wu, V. Cherezov, and R. C. Stevens, "GPCR stabilization using the bicelle-like architecture of mixed sterol-detergent micelles," *Methods*, vol. 55, pp. 310–317, Dec. 2011.

[118] M. le Maire, P. Champeil, and J. V. Møller, "Interaction of membrane proteins and lipids with solubilizing detergents," *Biochim. Biophys. Acta*, vol. 1508, pp. 86–111, Nov. 2000.

[119] J.-L. Rigaud, D. Lévy, and D. Levy, "Reconstitution of membrane proteins into liposomes," in *Methods Enzymol.*, vol. 372, ch. 4, pp. 65–86, Elsevier Inc., Jan. 2003.

[120] A. Diller, C. Loudet, F. Aussenac, G. Raffard, S. Fournier, M. Laguerre, A. Grélard, S. J. Opella, F. M. Marassi, and E. J. Dufourc, "Bicelles: A natural 'molecular goniometer' for structural, dynamical and topological studies of molecules in membranes," *Biochimie*, vol. 91, pp. 744–751, June 2009.

[121] U. H. N. Dürr, M. Gildenberg, and A. Ramamoorthy, "The magic of bicelles lights up membrane protein structure," *Chem. Rev.*, vol. 112, pp. 6054–6074, Nov. 2012.

[122] S. H. Park, S. Prytulla, A. A. De Angelis, J. M. Brown, H. Kiefer, and S. J. Opella, "High-resolution NMR spectroscopy of a GPCR in aligned bicelles," *J. Am. Chem. Soc.*, vol. 128, pp. 7402–7403, June 2006.

[123] A. Jesorka and O. Orwar, "Liposomes: technologies and analytical applications," *Annu. Rev. Anal. Chem.*, vol. 1, pp. 801–832, Jan. 2008.

[124] M. Montal and P. Mueller, "Formation of bimolecular membranes from lipid monolayers and a study

of their electrical properties," *Proc. Natl. Acad. Sci.*, vol. 69, pp. 3561–3566, Dec. 1972.

[125] R. P. Richter, R. Bérat, and A. R. Brisson, "Formation of solid-supported lipid bilayers: an integrated view," *Langmuir*, vol. 22, no. 12, pp. 3497–3505, 2006.

[126] M. Winterhalter, "Black lipid membranes," *Curr. Opin. Colloid & Interface Sci.*, vol. 5, pp. 250–255, July 2000.

[127] G. Boheim, "Statistical analysis of alamethicin channels in black lipid membranes," *J. Membr. Biol.*, vol. 19, pp. 277–303, Jan. 1974.

[128] W. Römer and C. Steinem, "Impedance analysis and single-channel recordings on nano-black lipid membranes based on porous alumina," *Biophys. J.*, vol. 86, pp. 955–965, Feb. 2004.

[129] J. Jass, T. Tjärnhage, and G. Puu, "From liposomes to supported, planar bilayer structures on hydrophilic and hydrophobic surfaces: an atomic force microscopy study," *Biophys. J.*, vol. 79, pp. 3153–3163, Dec. 2000.

[130] E. Sackmann and M. Tanaka, "Supported membranes on soft polymer cushions: fabrication, characterization and applications," *Trends Biotechnol.*, vol. 18, pp. 58–64, Feb. 2000.

[131] E. T. Castellana and P. S. Cremer, "Solid supported lipid bilayers: From biophysical studies to sensor design," *Surf. Sci. Rep.*, vol. 61, pp. 429–444, Nov. 2006.

[132] M. C. Woodle and D. Papahadjopoulos, "Liposome preparation and size characterization," in *Methods Enzymol.* (S. Fleischer, B. Fleischer, J. Abelson, and M. Simon, eds.), vol. 171, ch. 5, pp. 193–271, Elsevier B.V., 1989.

[133] D. E. Warschawski, A. A. Arnold, M. Beaugrand, A. Gravel, E. Chartrand, and I. Marcotte, "Choosing membrane mimetics for NMR structural studies of transmembrane proteins," *Biochim. Biophys. Acta*, vol. 1808, pp. 1957–1974, Aug. 2011.

[134] P. Walde, K. Cosentino, H. Engel, and P. Stano, "Giant vesicles: preparations and applications," *ChemBioChem*, vol. 11, pp. 848–865, May 2010.

[135] T. H. Bayburt, J. W. Carlson, and S. G. Sligar, "Reconstitution and imaging of a membrane protein in a nanometer-size phospholipid bilayer," *J. Struct. Biol.*, vol. 123, pp. 37–44, Sept. 1998.

[136] M. Schuler, I. Denisov, and S. Sligar, "Nanodiscs as a new tool to examine lipid-protein interactions," in *Lipid-Protein Interact. Methods Protoc. Methods Mol. Biol.* (J. H. Kleinschmidt, ed.), vol. 974, pp. 415–433, Springer Science and Business Media, New York, 2013.

[137] J. Frauenfeld, J. Gumbart, E. O. Van Der Sluis, S. Funes, M. Gartmann, B. Beatrix, T. Mielke, O. Berninghausen, T. Becker, K. Schulten, and R. Beckmann, "Cryo-EM structure of the ribosome-SecYE complex in the membrane environment," *Nat. Struct. & Mol. Biol.*, vol. 18, pp. 614–621, May 2011.

[138] I. G. Denisov, Y. V. Grinkova, A. A. Lazarides, and S. G. Sligar, "Directed self-assembly of monodisperse phospholipid bilayer nanodiscs with controlled size," *J. Am. Chem. Soc.*, vol. 126, pp. 3477–3487, Mar. 2004.

[139] T. K. Ritchie, Y. V. Grinkova, T. H. Bayburt, I. G. Denisov, J. K. Zolnerciks, W. M. Atkins, and S. G. Sligar, "Reconstitution of membrane proteins in phospholipid bilayer nanodiscs," in *Methods Enzymol.*, vol. 464, pp. 211–231, Elsevier Inc., 1 ed., Jan. 2009.

[140] A. Leitz, T. Bayburt, A. Barnakov, B. Springer, and S. Sligar, "Functional reconstitution of β_2-adrenergic receptors utilizing self-assembling Nanodisc technology," *Biotechniques*, vol. 40, pp. 601–612, May 2006.

[141] D. E. Moustaine, S. Granier, E. Doumazane, P. Scholler, R. Rahmeh, P. Bron, B. Mouillac, J.-L. Banères, P. Rondard, and J.-P. Pin, "Distinct roles of metabotropic glutamate receptor dimerization in agonist activation and G-protein coupling," *Proc. Natl. Acad. Sci.*, vol. 109, no. 40, pp. 16342–16347, 2012.

[142] T. H. Bayburt, A. J. Leitz, G. Xie, D. D. Oprian, and S. G. Sligar, "Transducin activation by nanoscale lipid bilayers containing one and two rhodopsins," *J. Biol. Chem.*, vol. 282, pp. 14875–14881, May 2007.

[143] M. C. Orwick, P. J. Judge, J. Procek, L. Lindholm, A. Graziadei, A. Engel, G. Groebner, and A. Watts, "Detergent-Free Formation and Physicochemical Characterization of Nanosized Lipid-Polymer Complexes: Lipodisq," *Angew. Chemie*, vol. 124, no. 19, pp. 4731–4735, 2012.

[144] M. Orwick-Rydmark, J. E. Lovett, A. Graziadei, L. Lindholm, M. R. Hicks, and A. Watts, "Detergent-free incorporation of a seven-transmembrane receptor protein into nanosized bilayer Lipodisq particles for functional and biophysical studies," *Nano Lett.*, vol. 12, pp. 4687–4692, Sept. 2012.

[145] S. Paulin, M. Jamshad, T. R. Dafforn, J. Garcia-Lara, S. J. Foster, N. F. Galley, D. I. Roper, H. Rosado, and P. W. Taylor, "Surfactant-free purification of membrane protein complexes from bacteria: application to the staphylococcal penicillin-binding protein complex PBP2/PBP2a," *Nanotechnology*, vol. 25, p. 285101, June 2014.

[146] R. Zhang, I. D. Sahu, L. Liu, A. Osatuke, R. G. Comer, C. Dabney-Smith, and G. A. Lorigan,

"Characterizing the structure of lipodisq nanoparticles for membrane protein spectroscopic studies," *Biochim. Biophys. Acta*, pp. 4–8, May 2014.

[147] A. R. Long, C. C. O'Brien, K. Malhotra, C. T. Schwall, A. D. Albert, A. Watts, and N. N. Alder, "A detergent-free strategy for the reconstitution of active enzyme complexes from native biological membranes into nanoscale discs," *BMC Biotechnol.*, vol. 13, Jan. 2013.

[148] I. D. Sahu, R. M. McCarrick, K. R. Troxel, R. Zhang, H. J. Smith, M. M. Dunagan, M. S. Swartz, P. V. Rajan, B. M. Kroncke, C. R. Sanders, and G. A. Lorigan, "DEER EPR measurements for membrane protein structures via bifunctional spin labels and lipodisq nanoparticles," *Biochemistry*, vol. 52, pp. 6627–6632, Sept. 2013.

[149] S. H. White, "Biophysical dissection of membrane proteins," *Nature*, vol. 459, pp. 344–346, May 2009.

[150] R. M. Bill, P. J. F. Henderson, S. Iwata, E. R. S. Kunji, H. Michel, R. Neutze, S. Newstead, B. Poolman, C. G. Tate, and H. Vogel, "Overcoming barriers to membrane protein structure determination," *Nat. Biotechnol.*, vol. 29, pp. 335–340, Apr. 2011.

[151] S. H. White, "The progress of membrane protein structure determination," *Protein Sci.*, vol. 13, pp. 1948–1949, 2004.

[152] V. Cherezov, "Lipidic cubic phase technologies for membrane protein structural studies," *Curr. Opin. Struct. Biol.*, vol. 21, pp. 559–566, Aug. 2011.

[153] R. L. Lieberman, J. A. Culver, K. C. Entzminger, J. C. Pai, and J. A. Maynard, "Crystallization chaperone strategies for membrane proteins," *Methods*, vol. 55, pp. 293–302, Dec. 2011.

[154] J. K. Lee and R. M. Stroud, "Unlocking the eukaryotic membrane protein structural proteome," *Curr. Opin. Struct. Biol.*, vol. 20, pp. 464–470, Aug. 2010.

[155] C. G. Tate and G. F. X. Schertler, "Engineering G protein-coupled receptors to facilitate their structure determination," *Curr. Opin. Struct. Biol.*, vol. 19, no. 4, pp. 386–395, 2009.

[156] H. N. Chapman, P. Fromme, A. Barty, T. A. White, R. A. Kirian, A. Aquila, M. S. Hunter, J. Schulz, D. P. DePonte, U. Weierstall, R. B. Doak, F. R. N. C. Maia, A. V. Martin, I. Schlichting, L. Lomb, N. Coppola, R. L. Shoeman, S. W. Epp, R. Hartmann, D. Rolles, A. Rudenko, L. Foucar, N. Kimmel, G. Weidenspointner, P. Holl, M. Liang, M. Barthelmess, C. Caleman, S. Boutet, M. J. Bogan, J. Krzywinski, C. Bostedt, S. Bajt, L. Gumprecht, B. Rudek, B. Erk, C. Schmidt, A. Hömke, C. Reich, D. Pietschner, L. Strüder, G. Hauser, H. Gorke, J. Ullrich, S. Herrmann, G. Schaller, F. Schopper, H. Soltau, K.-U. Kühnel, M. Messerschmidt, J. D. Bozek, S. P. Hau-Riege, M. Frank, C. Y. Hampton, R. G. Sierra, D. Starodub, G. J. Williams, J. Hajdu, N. Timneanu, M. M. Seibert, J. Andreasson, A. Rocker, O. Jönsson, M. Svenda, S. Stern, K. Nass, R. Andritschke, C.-D. Schröter, F. Krasniqi, M. Bott, K. E. Schmidt, X. Wang, I. Grotjohann, J. M. Holton, T. R. M. Barends, R. Neutze, S. Marchesini, R. Fromme, S. Schorb, D. Rupp, M. Adolph, T. Gorkhover, I. Andersson, H. Hirsemann, G. Potdevin, H. Graafsma, B. Nilsson, and J. C. H. Spence, "Femtosecond X-ray protein nanocrystallography," *Nature*, vol. 470, pp. 73–77, Feb. 2011.

[157] J. L. Smith, R. F. Fischetti, and M. Yamamoto, "Micro-crystallography comes of age," *Curr. Opin. Struct. Biol.*, vol. 22, pp. 602–612, Oct. 2012.

[158] L. C. Johansson, A. B. Wöhri, G. Katona, S. Engström, and R. Neutze, "Membrane protein crystallization from lipidic phases," *Curr. Opin. Struct. Biol.*, vol. 19, pp. 372–378, Aug. 2009.

[159] H.-X. Zhou and T. A. Cross, "Influences of membrane mimetic environments on membrane protein structures," *Annu. Rev. Biophys.*, vol. 42, pp. 361–392, Jan. 2013.

[160] J. Torres, T. J. Stevens, and M. Samsó, "Membrane proteins: the 'Wild West' of structural biology," *Trends Biochem. Sci.*, vol. 28, no. 3, pp. 137–144, 2003.

[161] J. W. Taraska, "Mapping membrane protein structure with fluorescence.," *Curr. Opin. Struct. Biol.*, vol. 22, pp. 507–13, Aug. 2012.

[162] D. T. Murray, N. Das, and T. A. Cross, "Solid state NMR strategy for characterizing native membrane protein structures," *Acc. Chem. Res.*, vol. 46, no. 9, pp. 2172–2181, 2013.

[163] H. S. Mchaourab, P. R. Steed, and K. Kazmier, "Toward the fourth dimension of membrane protein structure: insight into dynamics from spin-labeling EPR spectroscopy," *Structure*, vol. 19, pp. 1549–1561, Nov. 2011.

[164] A. Bartesaghi and S. Subramaniam, "Membrane protein structure determination using cryo-electron tomography and 3D image averaging," *Curr. Opin. Struct. Biol.*, vol. 19, pp. 402–407, Aug. 2009.

[165] A. Engel and H. E. Gaub, "Structure and mechanics of membrane proteins," *Annu. Rev. Biochem.*, vol. 77, pp. 127–148, Jan. 2008.

[166] S. A. I. Seidel, P. M. Dijkman, W. A. Lea, M. Jerabek-Willemsen, A. Lazic, J. S. Joseph, P. Srinivasan, P. Baaske, A. Simeonov, I. Katritch, G. van den Bogaart, F. A. Melo, J. E. Ladbury, G. Schreiber, A. Watts, D. Braun, and S. Duhr, "Microscale thermophoresis quantifies biomolecular interactions under previously challenging conditions," *Methods*, vol. 59, pp. 301–315, Mar. 2013.

[167] A. Schweiger and G. Jeschke, "Principles of pulse electron paramagnetic resonance," *Oxford Univ. Press*, 2001.

[168] W. L. Hubbell and C. Altenbach, "Investigation of structure and dynamics in membrane proteins using site-directed spin labeling," *Curr. Opin. Struct. Biol.*, vol. 4, no. 4, pp. 566–573, 1994.

[169] A. Abragam and M. Pryce, "Theory of the nuclear hyperfine structure of paramagnetic resonance spectra in crystals," *Proc. R. Soc. London. Ser. A. Math. Phys. Sci.*, vol. 205, no. 1080, pp. 135–153, 1951.

[170] B. R. Knauer and J. J. Napier, "The nitrogen hyperfine splitting constant of the nitroxide functional group as a solvent polarity parameter. The relative importance for a solvent polarity parameter of its being a cybotactic probe vs. its being a model process," *J. Am. Chem. Soc.*, vol. 98, no. 15, pp. 4395–4400, 1976.

[171] J. A. Weil and J. R. Bolton, *Electron paramagnetic resonance: elementary theory and practical applications.* Wiley, second ed., 2007.

[172] O. H. Griffith, D. W. Cornell, and H. M. McConnell, "Nitrogen Hyperfine Tensor and g Tensor of Nitroxide Radicals," *J. Chem. Phys.*, vol. 43, no. 8, pp. 2909–2910, 1965.

[173] H. M. McConnell and B. Gaffney McFarland, "Physics and chemistry of spin labels," *Q. Rev. Biophys.*, vol. 3, pp. 91–136, Feb. 1970.

[174] P. P. Borbat, A. J. Costa-Filho, K. A. Earle, J. K. Moscicki, and J. H. Freed, "Electron spin resonance in studies of membranes and proteins," *Science*, vol. 291, pp. 266–269, Jan. 2001.

[175] C. S. Klug and J. B. Feix, "Methods and applications of site-directed spin labeling EPR spectroscopy," *Methods Cell Biol.*, vol. 84, pp. 617–658, 2008.

[176] V. Livshits, B. Dzikovski, and D. Marsh, "Anisotropic motion effects in CW non-linear EPR spectra: relaxation enhancement of lipid spin labels," *J. Magn. Reson.*, vol. 162, pp. 429–442, June 2003.

[177] D. Kurad, G. Jeschke, and D. Marsh, "Lateral ordering of lipid chains in cholesterol-containing membranes: high-field spin-label EPR," *Biophys. J.*, vol. 86, no. 1, pp. 264–271, 2004.

[178] H. S. McHaourab, M. A. Lietzow, K. Hideg, and W. L. Hubbell, "Motion of Spin-Labeled Side Chains in T4 Lysozyme. Correlation with Protein Structure and Dynamics," *Biochemistry*, vol. 35, no. 24, pp. 7692–7704, 1996.

[179] J. M. Isas, R. Langen, H. T. Haigler, and W. L. Hubbell, "Structure and dynamics of a helical hairpin and loop region in annexin 12: a site-directed spin labeling study," *Biochemistry*, vol. 41, pp. 1464–1473, Feb. 2002.

[180] A. Keith, G. Bulfield, and W. Snipes, "Spin-labeled *Neurospora* mitochondria," *Biophys. J.*, vol. 10, pp. 618–629, July 1970.

[181] S. Goldman, G. Bruno, and J. H. Freed, "Estimating slow-motional rotational correlation times for nitroxides by electron spin resonance," *J. Phys. Chem.*, vol. 76, no. 13, pp. 1858–1860, 1972.

[182] R. P. Mason and J. H. Freed, "Estimating microsecond rotational correlation times from lifetime broadening of nitroxide electron spin resonance spectra near the rigid limit," *J. Phys. Chem.*, vol. 78, no. 13, pp. 1321–1323, 1974.

[183] J. H. Freed, "Theory of slow tumbling ESR spectra for nitroxides," in *Spin labeling theory Appl.* (L. J. Berliner, ed.), vol. I, pp. 53–132, Academic Press, 1976.

[184] D. Marsh, "Experimental methods in spin-label spectral analysis," in *Biol. Magn. Reson.* (L. J. Berliner and J. Reuben, eds.), vol. 8: Spin la, pp. 255–303, Springer, 1989.

[185] M. D. Rabenstein and Y.-K. Shin, "Determination of the distance between two spin labels attached to a macromolecule," *Proc. Natl. Acad. Sci.*, vol. 92, no. 18, pp. 8239–8243, 1995.

[186] J. E. Banham, C. M. Baker, S. Ceola, I. J. Day, G. H. Grant, E. J. J. Groenen, C. T. Rodgers, G. Jeschke, and C. R. Timmel, "Distance measurements in the borderline region of applicability of CW EPR and DEER: A model study on a homologous series of spin-labelled peptides," *J. Magn. Reson.*, vol. 191, no. 2, pp. 202–218, 2008.

[187] H.-J. Steinhoff, N. Radzwill, W. Thevis, V. Lenz, D. Brandenburg, A. Antson, G. Dodson, and A. Wollmer, "Determination of interspin distances between spin labels attached to insulin: comparison of electron paramagnetic resonance data with the X-ray structure," *Biophys. J.*, vol. 73, no. 6, pp. 3287–3298, 1997.

[188] E. J. Hustedt, R. A. Stein, L. Sethaphong, S. Brandon, Z. Zhou, and S. C. DeSensi, "Dipolar coupling between nitroxide spin labels: the development and application of a tether-in-a-cone model," *Biophys. J.*, vol. 90, no. 1, pp. 340–356, 2006.

[189] A. Kokorin, "Forty Years of the d_1/d Parameter," in *Nitroxides - Theory, Exp. Appl.* (A. I. Kokorin, ed.), pp. 113–164, InTech, 2012.

[190] G. Jeschke, "Determination of the nanostructure of polymer materials by electron paramagnetic resonance spectroscopy," *Macromol. Rapid Commun.*, vol. 23, no. 4, pp. 227–246, 2002.

[191] A. Gross, L. Columbus, K. Hideg, C. Altenbach, and W. L. Hubbell, "Structure of the KcsA potassium channel from Streptomyces lividans: a site-directed spin labeling study of the second transmembrane segment," *Biochemistry*, vol. 38, pp. 10324–10335, Aug. 1999.

[192] J. Van Vleck, "The dipolar broadening of magnetic resonance lines in crystals," *Phys. Rev.*, vol. 74, no. 9, pp. 1168–1183, 1948.

[193] A. D. Milov, K. M. Salikhov, and M. D. Shchirov, "Application of the double resonance method to electron spin echo in a study of the spatial distribution of paramagnetic centers in solids," *Sov. Physics, Solid State*, vol. 23, pp. 565–569, 1981.

[194] A. D. Milov, A. G. Maryasov, and Y. D. Tsvetkov, "Pulsed electron double resonance (PELDOR) and its applications in free-radicals research," *Appl. Magn. Reson.*, vol. 15, pp. 107–143, Aug. 1998.

[195] M. Pannier, S. Veit, A. Godt, G. Jeschke, and H. W. Spiess, "Dead-time free measurement of dipole-dipole interactions between electron spins," *J. Magn. Reson.*, vol. 142, no. 2, pp. 331–340, 2000.

[196] A. Milov, Y. Grishin, S. Dzuba, and Y. D. Tsvetkov, "Effect of pumping pulse duration on echo signal amplitude in four-pulse PELDOR," *Appl. Magn. Reson.*, vol. 41, pp. 59–67, May 2011.

[197] J. E. Lovett, B. W. Lovett, and J. Harmer, "DEER-Stitch: combining three- and four-pulse DEER measurements for high sensitivity, deadtime free data," *J. Magn. Reson.*, vol. 223, pp. 98–106, Oct. 2012.

[198] G. Jeschke, "Interpretation of dipolar EPR data in terms of protein structure," in *Struct. Inf. from Spin-Labels Intrinsic Paramagn. Centres Biosci.*, vol. Structure, pp. 83–120, Springer, 2011.

[199] G. Jeschke and Y. Polyhach, "Distance measurements on spin-labelled biomacromolecules by pulsed electron paramagnetic resonance," *Phys. Chem. Chem. Phys.*, vol. 9, pp. 1895–1910, Apr. 2007.

[200] Y. Polyhach, E. Bordignon, R. Tschaggelar, S. Gandra, A. Godt, and G. Jeschke, "High sensitivity and versatility of the DEER experiment on nitroxide radical pairs at Q-band frequencies," *Phys. Chem. Chem. Phys.*, vol. 14, pp. 10762–10773, Aug. 2012.

[201] R. Dastvan, B. E. Bode, M. P. R. Karuppiah, A. Marko, S. Lyubenova, H. Schwalbe, and T. F. Prisner, "Optimization of transversal relaxation of nitroxides for pulsed electron-electron double resonance spectroscopy in phospholipid membranes," *J. Phys. Chem. B*, vol. 114, pp. 13507–13516, Oct. 2010.

[202] G. Jeschke, V. Chechik, P. Ionita, A. Godt, H. Zimmermann, J. E. Banham, C. R. Timmel, D. Hilger, and H. Jung, "DeerAnalysis2006 – a comprehensive software package for analyzing pulsed ELDOR data," *Appl. Magn. Reson.*, vol. 30, pp. 473–498, 2006.

[203] F. Ciruela, J.-P. Vilardaga, and V. Fernández-Dueñas, "Lighting up multiprotein complexes: lessons from GPCR oligomerization," *Trends Biotechnol.*, vol. 28, no. 8, pp. 407–415, 2010.

[204] R. S. Kasai and A. Kusumi, "Single-molecule imaging revealed dynamic GPCR dimerization," *Curr. Opin. Cell Biol.*, vol. 27, pp. 78–86, Dec. 2014.

[205] M. C. Overton and K. J. Blumer, "Use of fluorescence resonance energy transfer to analyze oligomerization of G-protein-coupled receptors expressed in yeast," *Methods*, vol. 27, no. 4, pp. 324–332, 2002.

[206] P. J. Harding, H. Attrill, J. Boehringer, S. Ross, G. H. Wadhams, E. Smith, J. P. Armitage, and A. Watts, "Constitutive dimerization of the G-protein coupled receptor, neurotensin receptor 1, reconstituted into phospholipid bilayers," *Biophys. J.*, vol. 96, no. 3, pp. 964–973, 2009.

[207] T. Heyduk, "Measuring protein conformational changes by FRET/LRET," *Curr. Opin. Biotechnol.*, vol. 13, no. 4, pp. 292–296, 2002.

[208] Y. Taniguchi, T. Ikehara, N. Kamo, Y. Watanabe, H. Yamasaki, and Y. Toyoshima, "Application of fluorescence resonance energy transfer (FRET) to investigation of light-induced conformational changes of the phoborhodopsin/transducer complex," *Photochem. Photobiol.*, vol. 83, no. 2, pp. 311–316, 2007.

[209] S. Granier, S. Kim, A. M. Shafer, V. R. P. Ratnala, J. J. Fung, R. N. Zare, and B. Kobilka, "Structure and conformational changes in the C-terminal domain of the β_2-adrenoceptor: insights from fluorescence resonance energy transfer studies," *J. Biol. Chem.*, vol. 282, pp. 13895–13905, May 2007.

[210] R. V. Agafonov, I. V. Negrashov, Y. V. Tkachev, S. E. Blakely, M. A. Titus, D. D. Thomas, and Y. E. Nesmelov, "Structural dynamics of the myosin relay helix by time-resolved EPR and FRET," *Proc. Natl. Acad. Sci.*, vol. 106, pp. 21625–21630, Dec. 2009.

[211] R. M. Clegg, "Fluorescence Resonance Energy transfer and Nucleic Acids," *Methods Enzymol.*, vol. 211, pp. 353–388, 1992.

[212] R. M. Clegg, "Fluorescence resonance energy transfer," *Curr. Opin. Biotechnol.*, vol. 6, pp. 103–110, Feb. 1995.

[213] C. Berney and G. Danuser, "FRET or no FRET: a quantitative comparison," *Biophys. J.*, vol. 84, pp. 3992–4010, June 2003.

[214] E. A. Bykova and J. Zheng, "Spectra FRET: A Fluorescence Resonance Energy Transfer Method in Live Cells," in *Rev. Fluoresc.*, vol. 4 of *Reviews in Fluorescence*, pp. 87–101, New York, NY: Springer

New York, 2009.

[215] J. Wlodarczyk, A. Woehler, F. Kobe, E. Ponimaskin, A. Zeug, and E. Neher, "Analysis of FRET signals in the presence of free donors and acceptors.," *Biophys. J.*, vol. 94, pp. 986–1000, Feb. 2008.

[216] M. A. Rizzo, G. H. Springer, B. Granada, and D. W. Piston, "An improved cyan fluorescent protein variant useful for FRET," *Nat Biotech*, vol. 22, no. 4, pp. 445–449, 2004.

[217] T. Nagai, K. Ibata, E. S. Park, M. Kubota, K. Mikoshiba, and A. Miyawaki, "A variant of yellow fluorescent protein with fast and efficient maturation for cell-biological applications," *Nat Biotech*, vol. 20, pp. 87–90, Jan. 2002.

[218] T. H. Evers, E. M. W. M. van Dongen, A. C. Faesen, E. W. Meijer, and M. Merkx, "Quantitative Understanding of the Energy Transfer between Fluorescent Proteins Connected via Flexible Peptide Linkers," *Biochemistry*, vol. 45, no. 44, pp. 13183–13192, 2006.

[219] C. Hoffmann, G. Gaietta, M. Bünemann, S. R. Adams, S. Oberdorff-Maass, B. Behr, J.-P. Vilardaga, R. Y. Tsien, M. H. Ellisman, and M. J. Lohse, "A FlAsH-based FRET approach to determine G protein-coupled receptor activation in living cells," *Nat. Methods*, vol. 2, no. 3, pp. 171–176, 2005.

[220] A. Keppler, M. Kindermann, S. Gendreizig, H. Pick, H. Vogel, and K. Johnsson, "Labeling of fusion proteins of O^6-alkylguanine-DNA alkyltransferase with small molecules in vivo and in vitro," *Methods*, vol. 32, no. 4, pp. 437–444, 2004.

[221] A. Gautier, A. Juillerat, C. Heinis, I. Reis Corrêa, M. Kindermann, F. Beaufils, and K. Johnsson, "An Engineered Protein Tag for Multiprotein Labeling in Living Cells," *Chem. & Biol.*, vol. 15, pp. 128–136, Feb. 2008.

[222] N. George, H. Pick, H. Vogel, N. Johnsson, and K. Johnsson, "Specific Labeling of Cell Surface Proteins with Chemically Diverse Compounds," *J. Am. Chem. Soc.*, vol. 126, no. 29, pp. 8896–8897, 2004.

[223] J. Yin, P. D. Straight, S. M. McLoughlin, Z. Zhou, A. J. Lin, D. E. Golan, N. L. Kelleher, R. Kolter, and C. T. Walsh, "Genetically encoded short peptide tag for versatile protein labeling by Sfp phosphopantetheinyl transferase," *Proc. Natl. Acad. Sci.*, vol. 102, no. 44, pp. 15815–15820, 2005.

[224] R. A. Scheck and A. Schepartz, "Surveying protein structure and function using bis-arsenical small molecules," *Acc. Chem. Res.*, vol. 44, no. 9, pp. 654–665, 2011.

[225] C. Klammt, D. Schwarz, N. Eifler, A. Engel, J. Piehler, W. Haase, S. Hahn, V. Dötsch, and F. Bernhard, "Cell-free production of G protein-coupled receptors for functional and structural studies," *J. Struct. Biol.*, vol. 158, no. 3, pp. 482–493, 2007.

[226] T. Hohsaka, R. Abe, K. Shiraga, and M. Sisido, "Incorporation of fluorescently labeled nonnatural amino acids into proteins in an E. coli in vitro translation system," in *Nucleic Acids Symp. Ser.*, vol. 3, pp. 271–272, Oxford Univ Press, 2003.

[227] S.-H. Kang, S.-Y. Jun, and D.-M. Kim, "Fluorescent labeling of cell-free synthesized proteins by incorporation of fluorophore-conjugated nonnatural amino acids," *Anal. Biochem.*, vol. 360, no. 1, pp. 1–6, 2007.

[228] Y. Kawahashi, N. Doi, H. Takashima, C. Tsuda, Y. Oishi, R. Oyama, M. Yonezawa, E. Miyamoto-Sato, and H. Yanagawa, "In vitro protein microarrays for detecting protein-protein interactions: Application of a new method for fluorescence labeling of proteins," *Proteomics*, vol. 3, no. 7, pp. 1236–1243, 2003.

[229] N. Panchuk-Voloshina, R. P. Haugland, J. Bishop-Stewart, M. K. Bhalgat, P. J. Millard, F. Mao, W.-Y. Leung, and R. P. Haugland, "Alexa Dyes, a Series of New Fluorescent Dyes that Yield Exceptionally Bright, Photostable Conjugates," *J. Histochem. & Cytochem.*, vol. 47, pp. 1179–1188, Sept. 1999.

[230] R. B. Mujumdar, L. A. Ernst, S. R. Mujumdar, C. J. Lewis, and A. S. Waggoner, "Cyanine dye labeling reagents: Sulfoindocyanine succinimidyl esters," *Bioconjug. Chem.*, vol. 4, no. 2, pp. 105–111, 1993.

[231] D. Klose, J. P. Klare, D. Grohmann, C. W. M. Kay, F. Werner, and H.-J. Steinhoff, "Simulation vs. reality: a comparison of in silico distance predictions with DEER and FRET measurements," *PLoS One*, vol. 7, p. e39492, Jan. 2012.

[232] Y. Polyhach, E. Bordignon, and G. Jeschke, "Rotamer libraries of spin labelled cysteines for protein studies," *Phys. Chem. Chem. Phys.*, vol. 13, pp. 2356–2366, Mar. 2011.

[233] D. Braun and A. Libchaber, "Trapping of DNA by Thermophoretic Depletion and Convection," *Phys. Rev. Lett.*, vol. 89, p. 188103, Oct. 2002.

[234] S. Duhr, S. Arduini, and D. Braun, "Thermophoresis of DNA determined by microfluidic fluorescence," *Eur. Phys. journal. E*, vol. 15, pp. 277–286, Nov. 2004.

[235] C. J. Wienken, P. Baaske, U. Rothbauer, D. Braun, and S. Duhr, "Protein-binding assays in biological liquids using microscale thermophoresis," *Nat. Commun.*, vol. 1, p. 100, Jan. 2010.

[236] P. Baaske, C. J. Wienken, P. Reineck, S. Duhr, and D. Braun, "Optical thermophoresis for quantifying the buffer dependence of aptamer binding," *Angew. Chemie*, vol. 49, pp. 2238–2241, Mar. 2010.

[237] P. Mazur and S. R. de Groot, *Non-Equilibrium Thermodynamics*. North-Holland, 1963.

[238] S. Duhr and D. Braun, "Why molecules move along a temperature gradient," *Proc. Natl. Acad. Sci.*, vol. 103, pp. 19678–19682, Dec. 2006.

[239] S. Duhr and D. Braun, "Thermophoretic Depletion Follows Boltzmann Distribution," *Phys. Rev. Lett.*, vol. 96, p. 168301, Apr. 2006.

[240] W. Dandliker and G. Feigen, "Quantification of the antigen-antibody reaction by the polarization of fluorescence," *Biochem. Biophys. Res. Commun.*, vol. 5, no. 4, pp. 299–304, 1961.

[241] W. A. Lea and A. Simeonov, "Fluorescence polarization assays in small molecule screening," *Expert Opin. Drug Discov.*, vol. 6, pp. 17–32, Jan. 2011.

[242] S. Leavitt and E. Freire, "Direct measurement of protein binding energetics by isothermal titration calorimetry," *Curr. Opin. Struct. Biol.*, vol. 11, no. 5, pp. 560–566, 2001.

[243] S. Fujime and S. Ishiwata, "Dynamic study of F-actin by quasielastic scattering of laser light," *J. Mol. Biol.*, vol. 62, pp. 251–265, Nov. 1971.

[244] A. D. Hanlon, M. I. Larkin, and R. M. Reddick, "Free-solution, label-free protein-protein interactions characterized by dynamic light scattering," *Biophys. J.*, vol. 98, pp. 297–304, Jan. 2010.

[245] B. Nguyen, F. A. Tanious, and W. D. Wilson, "Biosensor-surface plasmon resonance: quantitative analysis of small molecule-nucleic acid interactions," *Methods*, vol. 42, pp. 150–161, June 2007.

[246] P. Schuck, "Use of surface plasmon resonance to probe the equilibrium and dynamic aspects of interactions between biological macromolecules," *Annu. Rev. Biophys. Biomol. Struct.*, vol. 26, pp. 541–566, Jan. 1997.

[247] M. M. Baksh, A. K. Kussrow, M. Mileni, M. G. Finn, and D. J. Bornhop, "Label-free quantification of membrane-ligand interactions using backscattering interferometry," *Nat. Biotechnol.*, vol. 29, pp. 357–360, Apr. 2011.

[248] I. Rasnik, S. A. McKinney, and T. Ha, "Surfaces and orientations: much to FRET about?," *Acc. Chem. Res.*, vol. 38, pp. 542–548, July 2005.

[249] D. S. Talaga, W. L. Lau, H. Roder, J. Tang, Y. Jia, W. F. DeGrado, and R. M. Hochstrasser, "Dynamics and folding of single two-stranded coiled-coil peptides studied by fluorescent energy transfer confocal microscopy," *Proc. Natl. Acad. Sci.*, vol. 97, pp. 13021–13026, Nov. 2000.

[250] S. A. I. Seidel, C. J. Wienken, S. Geissler, M. Jerabek-Willemsen, S. Duhr, A. Reiter, D. Trauner, D. Braun, and P. Baaske, "Label-free microscale thermophoresis discriminates sites and affinity of protein-ligand binding," *Angew. Chemie*, vol. 51, pp. 10656–10659, Oct. 2012.

[251] G. van den Bogaart, K. Meyenberg, U. Diederichsen, and R. Jahn, "Phosphatidylinositol 4,5-bisphosphate increases Ca^{2+} affinity of synaptotagmin-1 by 40-fold," *J. Biol. Chem.*, vol. 287, pp. 16447–16453, May 2012.

[252] J. L. Parker and S. Newstead, "Molecular basis of nitrate uptake by the plant nitrate transporter NRT1.1," *Nature*, vol. 507, pp. 68–72, Mar. 2014.

[253] M. Jerabek-Willemsen, T. André, R. Wanner, H. M. Roth, S. Duhr, P. Baaske, and D. Breitsprecher, "MicroScale Thermophoresis: Interaction analysis and beyond," *J. Mol. Struct.*, Mar. 2014.

[254] S. Newstead, "Towards a structural understanding of drug and peptide transport within the proton-dependent oligopeptide transporter (POT) family," *Biochem. Soc. Trans.*, vol. 39, pp. 1353–1358, Oct. 2011.

[255] H. Daniel, B. Spanier, G. Kottra, and D. Weitz, "From bacteria to man: archaic proton-dependent peptide transporters at work," *Physiology*, vol. 21, pp. 93–102, Apr. 2006.

[256] D. M. Matthews, "Intestinal absorption of peptides," *Physiol. Rev.*, vol. 55, pp. 537–608, Dec. 1975.

[257] H. Daniel and G. Kottra, "The proton oligopeptide cotransporter family SLC15 in physiology and pharmacology," *Pflügers Arch. Eur. J. Physiol.*, vol. 447, pp. 610–618, Feb. 2004.

[258] N. Yan, "Structural advances for the major facilitator superfamily (MFS) transporters," *Trends Biochem. Sci.*, vol. 38, pp. 151–159, Mar. 2013.

[259] M. E. Ganapathy, W. Huang, H. Wang, V. Ganapathy, and F. H. Leibach, "Valacyclovir: a substrate for the intestinal and renal peptide transporters PEPT1 and PEPT2," *Biochem. Biophys. Res. Commun.*, vol. 246, pp. 470–475, May 1998.

[260] H. K. Han and G. L. Amidon, "Targeted prodrug design to optimize drug delivery," *AAPS J.*, vol. 2, p. E6, Jan. 2000.

[261] I. Rubio-Aliaga and H. Daniel, "Mammalian peptide transporters as targets for drug delivery," *Trends Pharmacol. Sci.*, vol. 23, pp. 434–440, Sept. 2002.

[262] M. Brandsch, I. Knütter, and E. Bosse-Doenecke, "Pharmaceutical and pharmacological importance of peptide transporters," *J. Pharm. Pharmacol.*, vol. 60, pp. 543–585, May 2008.

[263] M. Sugawara, W. Huang, Y. J. Fei, F. H. Leibach, V. Ganapathy, and M. E. Ganapathy, "Transport of valganciclovir, a ganciclovir prodrug, via peptide transporters PEPT1 and PEPT2," *J. Pharm. Sci.*, vol. 89, pp. 781–789, June 2000.

[264] A. Ezra, A. Hoffman, E. Breuer, I. S. Alferiev, J. Mönkkönen, N. El Hanany-Rozen, G. Weiss, D. Stepensky, I. Gati, H. Cohen, S. Törmälehto, G. L. Amidon, and G. Golomb, "A peptide prodrug approach for improving bisphosphonate oral absorption," *J. Med. Chem.*, vol. 43, pp. 3641–3652, Oct. 2000.

[265] X. Song, P. L. Lorenzi, C. P. Landowski, B. S. Vig, J. M. Hilfinger, and G. L. Amidon, "Amino acid ester prodrugs of the anticancer agent gemcitabine: synthesis, bioconversion, metabolic bioevasion, and hPEPT1-mediated transport," *Mol. Pharm.*, vol. 2, no. 2, pp. 157–167, 2005.

[266] S. Newstead, D. Drew, A. D. Cameron, V. L. G. Postis, X. Xia, P. W. Fowler, J. C. Ingram, E. P. Carpenter, M. S. P. Sansom, M. J. McPherson, S. A. Baldwin, and S. Iwata, "Crystal structure of a prokaryotic homologue of the mammalian oligopeptide-proton symporters, PepT1 and PepT2," *EMBO J.*, vol. 30, pp. 417–426, Jan. 2011.

[267] N. Solcan, J. Kwok, P. W. Fowler, A. D. Cameron, D. Drew, S. Iwata, and S. Newstead, "Alternating access mechanism in the POT family of oligopeptide transporters," *EMBO J.*, vol. 31, pp. 3411–3421, Aug. 2012.

[268] S. Doki, H. E. Kato, N. Solcan, M. Iwaki, M. Koyama, M. Hattori, N. Iwase, T. Tsukazaki, Y. Sugita, H. Kandori, S. Newstead, R. Ishitani, and O. Nureki, "Structural basis for dynamic mechanism of proton-coupled symport by the peptide transporter POT," *Proc. Natl. Acad. Sci.*, vol. 110, pp. 11343–11348, July 2013.

[269] F. Guettou, E. M. Quistgaard, M. Raba, P. Moberg, C. Löw, and P. Nordlund, "Selectivity mechanism of a bacterial homolog of the human drug-peptide transporters PepT1 and PepT2," *Nat. Struct. & Mol. Biol.*, vol. 21, pp. 728–731, July 2014.

[270] L. R. Forrest, "Structural biology. (Pseudo-)symmetrical transport," *Science*, vol. 339, pp. 399–401, Jan. 2013.

[271] S. Radestock and L. R. Forrest, "The alternating-access mechanism of MFS transporters arises from inverted-topology repeats," *J. Mol. Biol.*, vol. 407, pp. 698–715, Apr. 2011.

[272] M. Schushan, A. Rimon, T. Haliloglu, L. R. Forrest, E. Padan, and N. Ben-Tal, "A model-structure of a periplasm-facing state of the NhaA antiporter suggests the molecular underpinnings of pH-induced conformational changes," *J. Biol. Chem.*, vol. 287, pp. 18249–18261, May 2012.

[273] I. Smirnova, V. Kasho, J.-Y. Choe, C. Altenbach, W. L. Hubbell, and H. R. Kaback, "Sugar binding induces an outward facing conformation of LacY," *Proc. Natl. Acad. Sci.*, vol. 104, pp. 16504–16509, Oct. 2007.

[274] E. R. Georgieva, P. P. Borbat, C. Ginter, J. H. Freed, and O. Boudker, "Conformational ensemble of the sodium-coupled aspartate transporter," *Nat. Struct. & Mol. Biol.*, vol. 20, pp. 215–221, Feb. 2013.

[275] I. Hänelt, D. Wunnicke, E. Bordignon, H.-J. Steinhoff, and D. J. Slotboom, "Conformational heterogeneity of the aspartate transporter GltPh," *Nat. Struct. & Mol. Biol.*, vol. 20, pp. 210–214, Feb. 2013.

[276] D. P. Claxton, M. Quick, L. Shi, F. D. de Carvalho, H. Weinstein, J. A. Javitch, and H. S. McHaourab, "Ion/substrate-dependent conformational dynamics of a bacterial homolog of neurotransmitter:sodium symporters," *Nat. Struct. & Mol. Biol.*, vol. 17, pp. 822–829, July 2010.

[277] P. R. Steed, P. Zou, K. E. Trone, and H. S. Mchaourab, "Structure and pH-induced structural rearrangements of the putative multidrug efflux pump EmrD in liposomes probed by site-directed spin labeling," *Biochemistry*, vol. 52, pp. 7964–7974, Nov. 2013.

[278] M. Masureel, C. Martens, R. A. Stein, S. Mishra, J.-M. Ruysschaert, H. S. Mchaourab, and C. Govaerts, "Protonation drives the conformational switch in the multidrug transporter LmrP," *Nat. Chem. Biol.*, vol. 10, pp. 149–155, Feb. 2014.

[279] S. T. Amadi, H. A. Koteiche, S. Mishra, and H. S. McHaourab, "Structure, dynamics, and substrate-induced conformational changes of the multidrug transporter EmrE in liposomes," *J. Biol. Chem.*, vol. 285, pp. 26710–26718, Aug. 2010.

[280] I. Smirnova, V. Kasho, J. Sugihara, J. L. Vázquez-Ibar, and H. R. Kaback, "Role of protons in sugar binding to LacY," *Proc. Natl. Acad. Sci.*, vol. 109, pp. 16835–16840, Oct. 2012.

[281] S. Wagner, M. L. Bader, D. Drew, and J.-W. de Gier, "Rationalizing membrane protein overexpression," *Trends Biotechnol.*, vol. 24, pp. 364–371, Aug. 2006.

[282] P. J. Loll, "Membrane protein structural biology: the high throughput challenge," *J. Struct. Biol.*, vol. 142, no. 1, pp. 144–153, 2003.

[283] L. Bamber, M. Harding, P. J. G. Butler, and E. R. S. Kunji, "Yeast mitochondrial ADP/ATP carriers are monomeric in detergents," *Proc. Natl. Acad. Sci.*, vol. 103, pp. 16224–16229, Oct. 2006.

[284] V. Cherezov, D. M. Rosenbaum, M. A. Hanson, S. G. F. Rasmussen, F. S. Thian, T. S. Kobilka, H.-J. Choi, P. Kuhn, W. I. Weis, B. K. Kobilka, and R. C. Stevens, "High-resolution crystal structure of an engineered human β_2-adrenergic G protein-coupled receptor," *Science*, vol. 318, pp. 1258–1265, Nov. 2007.

[285] K. Corin, H. Pick, P. Baaske, B. L. Cook, S. Duhr, C. J. Wienken, D. Braun, H. Vogel, and S. Zhang, "Insertion of T4-lysozyme (T4L) can be a useful tool for studying olfactory-related GPCRs.," *Mol. Biosyst.*, vol. 8, pp. 1750–1759, June 2012.

[286] T. Warne, M. J. Serrano-Vega, C. G. Tate, and G. F. X. Schertler, "Development and crystallization of a minimal thermostabilised G protein-coupled receptor," *Protein Expr. Purif.*, vol. 65, pp. 204–213, 2009.

[287] C. A. Sarkar, I. Dodevski, M. Kenig, S. Dudli, A. Mohr, E. Hermans, and A. Plückthun, "Directed evolution of a G protein-coupled receptor for expression, stability, and binding selectivity," *Proc. Natl. Acad. Sci.*, vol. 105, pp. 14808–14813, Sept. 2008.

[288] K. M. Schlinkmann, A. Honegger, E. Türeci, K. E. Robison, D. Lipovšek, and A. Plückthun, "Critical features for biosynthesis, stability, and functionality of a G protein-coupled receptor uncovered by all-versus-all mutations," *Proc. Natl. Acad. Sci.*, vol. 109, pp. 9810–9815, June 2012.

[289] C. G. Tate, "A crystal clear solution for determining G-protein-coupled receptor structures," *Trends Biochem. Sci.*, vol. 37, no. 9, pp. 343–352, 2012.

[290] J. H. Park, P. Scheerer, K. P. Hofmann, H. W. Choe, and O. P. Ernst, "Crystal structure of the ligand-free G-protein-coupled receptor opsin," *Nature*, vol. 454, no. 7201, pp. 183–187, 2008.

[291] V.-P. Jaakola, M. T. Griffith, M. A. Hanson, V. Cherezov, E. Y. T. Chien, J. R. Lane, A. P. IJzerman, and R. C. Stevens, "The 2.6 angstrom crystal structure of a human A_{2A} adenosine receptor bound to an antagonist," *Science*, vol. 322, no. 5905, pp. 1211–1217, 2008.

[292] B. Wu, E. Y. T. Chien, C. D. Mol, G. Fenalti, W. Liu, V. Katritch, R. Abagyan, A. Brooun, P. Wells, F. C. Bi, D. J. Hamel, P. Kuhn, T. M. Handel, V. Cherezov, and R. C. Stevens, "Structures of the CXCR4 chemokine GPCR with small-molecule and cyclic peptide antagonists," *Science*, vol. 330, pp. 1066–1071, Nov. 2010.

[293] Y. Shibata, J. F. White, M. J. Serrano-Vega, F. Magnani, A. L. Aloia, R. Grisshammer, and C. G. Tate, "Thermostabilization of the Neurotensin Receptor NTS1," *J. Mol. Biol.*, vol. 390, no. 2, pp. 262–277, 2009.

[294] J. F. White, N. Noinaj, Y. Shibata, J. Love, B. Kloss, F. Xu, J. Gvozdenovic-Jeremic, P. Shah, J. Shiloach, C. G. Tate, and R. Grisshammer, "Structure of the agonist-bound neurotensin receptor," *Nature*, vol. 490, no. 7421, pp. 508–513, 2012.

[295] P. Egloff, M. Hillenbrand, C. Klenk, A. Batyuk, P. Heine, S. Balada, K. M. Schlinkmann, D. J. Scott, M. Schütz, and A. Plückthun, "Structure of signaling-competent neurotensin receptor 1 obtained by directed evolution in *Escherichia coli*," *Proc. Natl. Acad. Sci.*, vol. 111, pp. E655–662, Feb. 2014.

[296] A. S. Doré, N. Robertson, J. C. Errey, I. Ng, K. Hollenstein, B. Tehan, E. Hurrell, K. Bennett, M. Congreve, F. Magnani, C. G. Tate, M. Weir, and F. H. Marshall, "Structure of the adenosine A_{2A} receptor in complex with ZM241385 and the xanthines XAC and caffeine," *Structure*, vol. 19, pp. 1283–1293, Sept. 2011.

[297] T. H. Kim, K. Y. Chung, A. Manglik, A. L. Hansen, R. O. Dror, T. J. Mildorf, D. E. Shaw, B. K. Kobilka, and R. S. Prosser, "The role of ligands on the equilibria between functional states of a G protein-coupled receptor," *J. Am. Chem. Soc.*, vol. 135, pp. 9465–9474, 2013.

[298] R. Grisshammer, J. F. White, L. B. Trinh, and J. Shiloach, "Large-scale expression and purification of a G-protein-coupled receptor for structure determination – an overview," *J. Struct. Funct. Genomics*, vol. 6, pp. 159–163, Jan. 2005.

[299] K. Tanaka, M. Masu, and S. Nakanishi, "Structure and functional expression of the cloned rat neurotensin receptor," *Neuron*, vol. 4, pp. 847–854, June 1990.

[300] N. Vita, P. Laurent, S. Lefort, P. Chalon, X. Dumont, M. Kaghad, D. Gully, G. Le Fur, P. Ferrara, and D. Caput, "Cloning and expression of a complementary DNA encoding a high affinity human neurotensin receptor," *FEBS Lett.*, vol. 317, no. 1-2, pp. 139–142, 1993.

[301] P. R. Dobner, D. L. Barber, L. Villa-Komaroff, and C. McKiernan, "Cloning and sequence analysis of cDNA for the canine neurotensin/neuromedin N precursor," *Proc. Natl. Acad. Sci.*, vol. 84, pp. 3516–3520, May 1987.

[302] J. Tucker and R. Grisshammer, "Purification of a rat neurotensin receptor expressed in *Escherichia coli*," *Biochem. J.*, vol. 317, no. 3, pp. 891–899, 1996.

[303] P. Kitabgi, R. Carraway, J. Van Rietschoten, C. Granier, J. L. Morgat, A. Menez, S. Leeman, and P. Freychet, "Neurotensin: specific binding to synaptic membranes from rat brain," *Proc. Natl. Acad. Sci. U. S. A.*, vol. 74, pp. 1846–1850, May 1977.

[304] P. Chalon, N. Vita, M. Kaghad, M. Guillemot, J. Bonnin, B. Delpech, G. Le Fur, P. Ferrara, and D. Caput, "Molecular cloning of a levocabastine-sensitive neurotensin binding site," *FEBS Lett.*, vol. 386, pp. 91–94, May 1996.

[305] J. Mazella, N. Zsürger, V. Navarro, J. Chabry, M. Kaghad, D. Caput, P. Ferrara, N. Vita, D. Gully, J.-

P. Maffrand, and J.-P. Vincent, "The 100-kDa neurotensin receptor is gp95/sortilin, a non-G-protein-coupled receptor," *J. Biol. Chem.*, vol. 273, pp. 26273–26276, Oct. 1998.

[306] J.-P. Vincent, J. Mazella, and P. Kitabgi, "Neurotensin and neurotensin receptors," *Trends Pharmacol. Sci.*, vol. 20, no. 7, pp. 302–309, 1999.

[307] J. Mazella and J.-P. Vincent, "Functional roles of the NTS2 and NTS3 receptors," *Peptides*, vol. 27, pp. 2469–2475, Oct. 2006.

[308] P. R. Dobner, "Multitasking with neurotensin in the central nervous system," *Cell. Mol. Life Sci.*, vol. 62, pp. 1946–1963, Sept. 2005.

[309] W. C. Mustain, P. G. Rychahou, and B. M. Evers, "The role of neurotensin in physiologic and pathologic processes," *Curr. Opin. Endocrinol. Diabetes. Obes.*, vol. 18, pp. 75–82, Feb. 2011.

[310] R. Cáceda, B. Kinkead, and C. B. Nemeroff, "Neurotensin: role in psychiatric and neurological diseases," *Peptides*, vol. 27, no. 10, pp. 2385–2404, 2006.

[311] R. M. Myers, J. W. Shearman, M. O. Kitching, A. Ramos-montoya, D. E. Neal, and S. V. Ley, "Cancer, chemistry, and the cell: molecules that interact with the neurotensin receptors," *ACS Chem. Biol.*, vol. 4, no. 7, pp. 503–525, 2009.

[312] J. F. White, L. B. Trinh, J. Shiloach, and R. Grisshammer, "Automated large-scale purification of a G protein-coupled receptor for neurotensin," *FEBS Lett.*, vol. 564, pp. 289–293, Apr. 2004.

[313] H. Attrill, P. J. Harding, E. Smith, S. Ross, and A. Watts, "Improved yield of a ligand-binding GPCR expressed in *E. coli* for structural studies," *Protein Expr. Purif.*, vol. 64, pp. 32–38, Mar. 2009.

[314] C. Altenbach, A. K. Kusnetzow, O. P. Ernst, K. P. Hofmann, and W. L. Hubbell, "High-resolution distance mapping in rhodopsin reveals the pattern of helix movement due to activation," *Proc. Natl. Acad. Sci.*, vol. 105, no. 21, pp. 7439–7444, 2008.

[315] J. A. Ballesteros and H. Weinstein, "Integrated methods for the construction of three-dimensional models and computational probing of structure-function relations in G protein-coupled receptors," *Methods Neurosci.*, vol. 25, pp. 366–428, 1995.

[316] A. Urbani and T. Warne, "A colorimetric determination for glycosidic and bile salt-based detergents: applications in membrane protein research," *Anal. Biochem.*, vol. 336, no. 1, pp. 117–124, 2005.

[317] M. D. Abràmoff, P. J. Magalhães, and S. J. Ram, "Image processing with ImageJ," *Biophotonics Int.*, vol. 11, no. 7, pp. 36–42, 2004.

[318] Y. Fang, Y. Hong, B. Webb, and J. Lahiri, "Applications of Biomembranes in Drug Discovery," *MRS Bull.*, vol. 31, pp. 541–545, Jan. 2006.

[319] P. J. Harding, H. Attrill, S. Ross, J. Koeppe, A. Kapanidis, and A. Watts, "Neurotensin receptor type 1: Escherichia coli expression, purification, characterization and biophysical study," *Biochem. Soc. Trans.*, vol. 35, pp. 760–763, 2007.

[320] D. Pelaprat, "Interactions between neurotensin receptors and G proteins," *Peptides*, vol. 27, pp. 2476–2487, Oct. 2006.

[321] J. F. White, J. Grodnitzky, J. M. Louis, L. B. Trinh, J. Shiloach, J. Gutierrez, J. K. Northup, and R. Grisshammer, "Dimerization of the class A G protein-coupled neurotensin receptor NTS1 alters G protein interaction," *Proc. Natl. Acad. Sci.*, vol. 104, no. 29, pp. 12199–12204, 2007.

[322] R. Grisshammer, "Purification of recombinant G-protein-coupled receptors," in *Methods Enzymol.*, vol. 466, ch. 6, pp. 631–645, San Diego: Elsevier Academic Press Inc, 2009.

[323] J. Lu and C. Deutsch, "Pegylation: A Method for Assessing Topological Accessibilities in Kv1.3," *Biochemistry*, vol. 40, no. 44, pp. 13288–13301, 2001.

[324] E. Burmeister Getz, M. Xiao, T. Chakrabarty, R. Cooke, and P. R. Selvin, "A Comparison between the Sulfhydryl Reductants Tris (2-carboxyethyl) phosphine and Dithiothreitol for Use in Protein Biochemistry," *Anal. Biochem.*, vol. 273, pp. 73–80, Aug. 1999.

[325] Y. Zou, W. I. Weis, and B. K. Kobilka, "N-terminal T4 lysozyme fusion facilitates crystallization of a G protein coupled receptor.," *PLoS One*, vol. 7, p. e46039, Jan. 2012.

[326] P. Scheerer, J. H. Park, P. W. Hildebrand, Y. J. Kim, N. Krausz, H.-W. Choe, K. P. Hofmann, and O. P. Ernst, "Crystal structure of opsin in its G-protein-interacting conformation," *Nature*, vol. 455, no. 7212, pp. 497–502, 2008.

[327] D. L. Farrens, C. Altenbach, K. Yang, W. L. Hubbell, and H. G. Khorana, "Requirement of rigid-body motion of transmembrane helices for light activation of rhodopsin," *Science*, vol. 274, no. 5288, pp. 768–770, 1996.

[328] W. L. Hubbell, C. Altenbach, C. M. Hubbell, and H. G. Khorana, "Rhodopsin structure, dynamics, and activation: a perspective from crystallography, site-directed spin labeling, sulfhydryl reactivity, and disulfide cross-linking," *Adv. Protein Chem.*, vol. 63, pp. 243–290, 2003.

[329] T. Warne, R. Moukhametzianov, J. G. Baker, R. Nehmé, P. C. Edwards, A. G. W. Leslie, G. F. X. Schertler, and C. G. Tate, "The structural basis for agonist and partial agonist action on a β_1-

adrenergic receptor," *Nature*, vol. 469, pp. 241–244, Jan. 2011.

[330] U. Gether, S. Lin, and B. K. Kobilka, "Fluorescent Labeling of Purified Adrenergic Receptor," *J. Biol. Chem.*, vol. 270, no. 47, pp. 28268–28275, 1995.

[331] A. Dam Jensen, F. Guarnieri, G. Rasmussen, F. Asmar, J. A. Ballesteros, and U. Gether, "Agonist-induced conformational changes at the cytoplasmic side of transmembrane segment 6 in the β_2 adrenergic receptor mapped by site-selective fluorescent labeling," *J. Biol. Chem.*, vol. 276, pp. 9279–9290, Mar. 2001.

[332] P. Ghanouni, J. J. Steenhuis, D. L. Farrens, and B. K. Kobilka, "Agonist-induced conformational changes in the G-protein-coupling domain of the β_2 adrenergic receptor," *Proc. Natl. Acad. Sci.*, vol. 98, no. 11, pp. 5997–6002, 2001.

[333] P. Ghanouni, Z. Gryczynski, J. J. Steenhuis, T. W. Lee, D. L. Farrens, J. R. Lakowicz, and B. K. Kobilka, "Functionally different agonists induce distinct conformations in the G protein coupling domain of the β_2 adrenergic receptor," *J. Biol. Chem.*, vol. 276, pp. 24433–24436, July 2001.

[334] S. Vanni, M. Neri, I. Tavernelli, and U. Rothlisberger, "A conserved protonation-induced switch can trigger "ionic-lock" formation in adrenergic receptors," *J. Mol. Biol.*, vol. 397, pp. 1339–1349, Apr. 2010.

[335] S. D. C. Ward, F. F. Hamdan, L. M. Bloodworth, N. A. Siddiqui, J. H. Li, and J. Wess, "Use of an in Situ Disulfide Cross-Linking Strategy To Study the Dynamic Properties of the Cytoplasmic End of Transmembrane Domain VI of the M3 Muscarinic Acetylcholine Receptor," *Biochemistry*, vol. 45, no. 3, pp. 676–685, 2006.

[336] A. C. Kruse, J. Hu, A. C. Pan, D. H. Arlow, D. M. Rosenbaum, E. Rosemond, H. F. Green, T. Liu, P. S. Chae, R. O. Dror, D. E. Shaw, W. I. Weis, J. Wess, and B. K. Kobilka, "Structure and dynamics of the M3 muscarinic acetylcholine receptor," *Nature*, vol. 482, pp. 552–556, Feb. 2012.

[337] S. K. Kim, Z. G. Gao, P. Van Rompaey, A. S. Gross, A. Chen, S. Van Calenbergh, and K. A. Jacobson, "Modeling the adenosine receptors: comparison of the binding domains of A_{2A} agonists and antagonists," *J. Med. Chem*, vol. 46, no. 23, pp. 4847–4859, 2003.

[338] W. I. Weis and B. K. Kobilka, "Structural insights into G-protein-coupled receptor activation," *Curr. Opin. Struct. Biol.*, vol. 18, no. 6, pp. 734–740, 2008.

[339] C. Hoffmann, A. Zürn, M. Bünemann, and M. J. Lohse, "Conformational changes in G-protein-coupled receptors-the quest for functionally selective conformations is open," *Br. J. Pharmacol.*, vol. 153, pp. S358–366, Mar. 2008.

[340] M. Yamada, M. A. Watson, and E. Richelson, "Deletion mutation in the putative third intracellular loop of the rat neurotensin receptor abolishes polyphosphoinositide hydrolysis but not cyclic AMP formation in CHO-K1 cells," *Mol. Pharmacol.*, vol. 46, no. 3, pp. 470–476, 1994.

[341] A. J. Venkatakrishnan, X. Deupi, G. Lebon, C. G. Tate, G. F. Schertler, and M. M. Babu, "Molecular signatures of G-protein-coupled receptors," *Nature*, vol. 494, pp. 185–194, Feb. 2013.

[342] D. Latek, P. Pasznik, T. Carlomagno, and S. Filipek, "Towards improved quality of GPCR models by usage of multiple templates and profile-profile comparison," *PLoS One*, vol. 8, p. e56742, Jan. 2013.

[343] T. D. Romo, A. Grossfield, and M. C. Pitman, "Concerted interconversion between ionic lock substates of the β_2-adrenergic receptor revealed by microsecond timescale molecular dynamics," *Biophys. J.*, vol. 98, pp. 76–84, Jan. 2010.

[344] J. Ballesteros, S. Kitanovic, F. Guarnieri, P. Davies, B. J. Fromme, K. Konvicka, L. Chi, R. P. Millar, J. S. Davidson, H. Weinstein, and S. C. Sealfon, "Functional microdomains in G-protein-coupled receptors the conserved arginine-cage motif in the gonadotropin-releasing hormone receptor," *J. Biol. Chem.*, vol. 273, pp. 10445–10453, Apr. 1998.

[345] M. Audet and M. Bouvier, "Restructuring G-protein- coupled receptor activation," *Cell*, vol. 151, pp. 14–23, Sept. 2012.

[346] L. Shi, G. Liapakis, R. Xu, F. Guarnieri, J. A. Ballesteros, and J. A. Javitch, "β_2-adrenergic receptor activation: modulation of the proline kink in transmembrane 6 by a rotamer toggle switch," *J. Biol. Chem.*, vol. 277, pp. 40989–40996, Oct. 2002.

[347] M. Bouvier, "Unraveling the structural basis of GPCR activation and inactivation," *Nat. Struct. Mol. Biol.*, vol. 20, pp. 539–541, May 2013.

[348] C. Zhang, Y. Srinivasan, D. H. Arlow, J. J. Fung, D. Palmer, Y. Zheng, H. F. Green, A. Pandey, R. O. Dror, D. E. Shaw, W. I. Weis, S. R. Coughlin, and B. K. Kobilka, "High-resolution crystal structure of human protease-activated receptor 1," *Nature*, vol. 492, pp. 387–392, Dec. 2012.

[349] V. Isberg, B. Vroling, R. van der Kant, K. Li, G. Vriend, and D. Gloriam, "GPCRDB: an information system for G protein-coupled receptors," *Nucleic Acids Res.*, vol. 42, pp. D422–425, Jan. 2014.

[350] M. Katragadda, M. W. Maciejewski, and P. L. Yeagle, "Structural studies of the putative helix 8 in the human β_2 adrenergic receptor: an NMR study," *Biochim. Biophys. Acta*, vol. 1663, pp. 74–81,

May 2004.

[351] G. Choi, J. Guo, and A. Makriyannis, "The conformation of the cytoplasmic helix 8 of the CB1 cannabinoid receptor using NMR and circular dichroism," *Biochim. Biophys. Acta*, vol. 1668, pp. 1–9, Feb. 2005.

[352] A. Bruno, G. Costantino, G. de Fabritiis, M. Pastor, and J. Selent, "Membrane-sensitive conformational states of helix 8 in the metabotropic Glu2 receptor, a class C GPCR," *PLoS One*, vol. 7, p. e42023, Jan. 2012.

[353] N. M. Delos Santos, L. A. Gardner, S. W. White, and S. W. Bahouth, "Characterization of the residues in helix 8 of the human β_1-adrenergic receptor that are involved in coupling the receptor to G proteins," *J. Biol. Chem.*, vol. 281, pp. 12896–12907, May 2006.

[354] S. Anavi-Goffer, D. Fleischer, D. P. Hurst, D. L. Lynch, J. Barnett-Norris, S. Shi, D. L. Lewis, S. Mukhopadhyay, A. C. Howlett, P. H. Reggio, and M. E. Abood, "Helix 8 Leu in the CB$_1$ cannabinoid receptor contributes to selective signal transduction mechanisms," *J. Biol. Chem.*, vol. 282, pp. 25100–25113, Aug. 2007.

[355] J. Huynh, W. G. Thomas, M.-I. Aguilar, and L. K. Pattenden, "Role of helix 8 in G protein-coupled receptors based on structure-function studies on the type 1 angiotensin receptor," *Mol. Cell. Endocrinol.*, vol. 302, pp. 118–127, Apr. 2009.

[356] D. Yasuda, T. Okuno, T. Yokomizo, T. Hori, N. Hirota, T. Hashidate, M. Miyano, T. Shimizu, and M. Nakamura, "Helix 8 of leukotriene B$_4$ type-2 receptor is required for the folding to pass the quality control in the endoplasmic reticulum," *FASEB J.*, vol. 23, pp. 1470–1481, May 2009.

[357] K. H. Ahn, A. Nishiyama, D. F. Mierke, and D. A. Kendall, "Hydrophobic residues in helix 8 of cannabinoid receptor 1 are critical for structural and functional properties," *Biochemistry*, vol. 49, pp. 502–511, Jan. 2010.

[358] J. Feierler, M. Wirth, B. Welte, S. Schüssler, M. Jochum, and A. Faussner, "Helix 8 plays a crucial role in bradykinin B$_2$ receptor trafficking and signaling," *J. Biol. Chem.*, vol. 286, pp. 43282–43293, Dec. 2011.

[359] R. G. Kaye, J. W. Saldanha, Z.-L. Lu, and E. C. Hulme, "Helix 8 of the M$_1$ muscarinic acetylcholine receptor: scanning mutagenesis delineates a G protein recognition site," *Mol. Pharmacol.*, vol. 79, no. 4, pp. 701–709, 2011.

[360] F. Xu, H. Wu, V. Katritch, G. W. Han, K. A. Jacobson, Z.-G. G. Gao, V. Cherezov, and R. C. Stevens, "Structure of an agonist-bound human A$_{2A}$ adenosine receptor," *Science*, vol. 322, pp. 322–327, Apr. 2011.

[361] Y. Polyhach, E. Bordignon, and G. Jeschke, "Rotamer libraries of spin labelled cysteines for protein studies," *Phys. Chem. Chem. Phys.*, 2010.

[362] R. Langen, K. J. Oh, D. Cascio, and W. L. Hubbell, "Crystal structures of spin labeled T4 lysozyme mutants: implications for the interpretation of EPR spectra in terms of structure," *Biochemistry*, vol. 39, pp. 8396–8405, July 2000.

[363] A. K. Kusnetzow, C. Altenbach, and W. L. Hubbell, "Conformational states and dynamics of rhodopsin in micelles and bilayers," *Biochemistry*, vol. 45, no. 17, pp. 5538–5550, 2006.

[364] M. Raba, S. Dunkel, D. Hilger, K. Lipiszko, Y. Polyhach, G. Jeschke, S. Bracher, J. P. Klare, M. Quick, H. Jung, and H.-J. Steinhoff, "Extracellular loop 4 of the proline transporter PutP controls the periplasmic entrance to ligand binding sites," *Structure*, vol. 22, pp. 769–780, May 2014.

[365] A. Manglik and B. Kobilka, "The role of protein dynamics in GPCR function: insights from the β$_2$AR and rhodopsin," *Curr. Opin. Cell Biol.*, vol. 27, pp. 136–143, Apr. 2014.

[366] S. M. Khan, W. Bolen, P. A. Hargrave, M. M. Santoro, and J. H. McDowell, "Differential scanning calorimetry of bovine rhodopsin in rod-outer-segment disk membranes," *Eur. J. Biochem.*, vol. 200, pp. 53–59, Aug. 1991.

[367] C. Altenbach, K. Cai, H. G. Khorana, and W. L. Hubbell, "Structural Features and Light-Dependent Changes in the Sequence 306- 322 Extending from Helix VII to the Palmitoylation Sites in Rhodopsin: A Site-Directed Spin-Labeling Study," *Biochemistry*, vol. 38, no. 25, pp. 7931–7937, 1999.

[368] M. Najimi, P. Gailly, J. M. Maloteaux, and E. Hermans, "Distinct regions of C-terminus of the high affinity neurotensin receptor mediate the functional coupling with pertussis toxin sensitive and insensitive G-proteins," *FEBS Lett.*, vol. 512, pp. 329–333, Mar. 2002.

[369] M. Bouvier, "Oligomerization of G-protein-coupled transmitter receptors," *Nat. Rev. Neurosci.*, vol. 2, pp. 274–286, Apr. 2001.

[370] G. Milligan, "The prevalence, maintenance, and relevance of G protein-coupled receptor oligomerization," *Mol. Pharmacol.*, vol. 84, pp. 158–169, July 2013.

[371] S. Ferré, V. Casadó, L. A. Devi, M. Filizola, R. Jockers, M. J. Lohse, G. Milligan, J.-P. Pin, and X. Guitart, "G protein-coupled receptor oligomerization revisited: functional and pharmacological

perspectives," *Pharmacol. Rev.*, vol. 66, pp. 413–434, Apr. 2014.

[372] D. Maurel, L. Comps-Agrar, C. Brock, M.-L. Rives, E. Bourrier, M. A. Ayoub, H. Bazin, N. Tinel, T. Durroux, L. Prézeau, E. Trinquet, and J.-P. Pin, "Cell-surface protein-protein interaction analysis with time-resolved FRET and snap-tag technologies: application to GPCR oligomerization," *Nat. Methods*, vol. 5, pp. 561–5617, June 2008.

[373] M.-L. Rives, C. Vol, Y. Fukazawa, N. Tinel, E. Trinquet, M. A. Ayoub, R. Shigemoto, J.-P. Pin, and L. Prézeau, "Crosstalk between GABA$_B$ and mGlu1a receptors reveals new insight into GPCR signal integration," *EMBO J.*, vol. 28, pp. 2195–2208, Aug. 2009.

[374] J.-P. Pin, L. Comps-Agrar, D. Maurel, C. Monnier, M. L. Rives, E. Trinquet, J. Kniazeff, P. Rondard, and L. Prézeau, "G-protein-coupled receptor oligomers: two or more for what? Lessons from mGlu and GABAB receptors.," *J. Physiol.*, vol. 587, pp. 5337–44, Nov. 2009.

[375] J. Kniazeff, L. Prézeau, P. Rondard, J.-P. Pin, and C. Goudet, "Dimers and beyond: The functional puzzles of class C GPCRs," *Pharmacol. Ther.*, vol. 130, pp. 9–25, Apr. 2011.

[376] K. A. Jones, B. Borowsky, J. A. Tamm, D. A. Craig, M. M. Durkin, M. Dai, W.-j. Yao, M. Johnson, C. Gunwaldsen, L.-y. Huang, C. Tang, Q. Shen, J. A. Salon, K. Morse, T. Laz, K. E. Smith, D. Nagarathnam, S. A. Noble, T. A. Branchek, and C. Gerald, "GABA$_B$ receptors function as a heteromeric assembly of the subunits GABA$_B$R1 and GABA$_B$R2," *Nature*, vol. 396, no. 6712, pp. 674–679, 1998.

[377] G. Milligan and M. Bouvier, "Methods to monitor the quaternary structure of G protein-coupled receptors," *FEBS J.*, vol. 272, pp. 2914–2925, June 2005.

[378] M. Bai, "Dimerization of G-protein-coupled receptors: roles in signal transduction," *Cell. Signal.*, vol. 16, pp. 175–186, Feb. 2004.

[379] S. Terrillon and M. Bouvier, "Roles of G-protein-coupled receptor dimerization.," *EMBO Rep.*, vol. 5, pp. 30–4, Jan. 2004.

[380] M. R. Whorton, M. P. Bokoch, S. r. G. F. Rasmussen, B. Huang, R. N. Zare, B. Kobilka, and R. K. Sunahara, "A monomeric G protein-coupled receptor isolated in a high-density lipoprotein particle efficiently activates its G protein," *Proc. Natl. Acad. Sci.*, vol. 104, pp. 7682–7687, May 2007.

[381] M. R. Whorton, B. Jastrzebska, P. S.-H. Park, D. Fotiadis, A. Engel, K. Palczewski, and R. K. Sunahara, "Efficient coupling of transducin to monomeric rhodopsin in a phospholipid bilayer," *J. Biol. Chem.*, vol. 283, pp. 4387–4394, Feb. 2008.

[382] A. J. Kuszak, S. Pitchiaya, J. P. Anand, H. I. Mosberg, N. G. Walter, and R. K. Sunahara, "Purification and functional reconstitution of monomeric μ-opioid receptors: allosteric modulation of agonist binding by Gi2," *J. Biol. Chem.*, vol. 284, pp. 26732–41, Sept. 2009.

[383] O. P. Ernst, V. Gramse, M. Kolbe, K. P. Hofmann, and M. Heck, "Monomeric G protein-coupled receptor rhodopsin in solution activates its G protein transducin at the diffusion limit.," *Proc. Natl. Acad. Sci.*, vol. 104, pp. 10859–64, June 2007.

[384] F. Concepcion, A. Mendez, and J. Chen, "The carboxyl-terminal domain is essential for rhodopsin transport in rod photoreceptors," *Vision Res.*, vol. 42, pp. 417–426, Feb. 2002.

[385] G. Milligan, "The role of dimerisation in the cellular trafficking of G-protein-coupled receptors.," *Curr. Opin. Pharmacol.*, vol. 10, pp. 23–29, Feb. 2010.

[386] L. T. May, L. J. Bridge, L. A. Stoddart, S. J. Briddon, and S. J. Hill, "Allosteric interactions across native adenosine-A$_3$ receptor homodimers: quantification using single-cell ligand-binding kinetics," *FASEB J.*, vol. 25, pp. 3465–3476, Oct. 2011.

[387] L. Albizu, M. Balestre, C. Breton, J.-P. Pin, M. Manning, B. Mouillac, C. Barberis, and T. Durroux, "Probing the existence of G protein-coupled receptor dimers by positive and negative ligand-dependent cooperative binding," *Mol. Pharmacol.*, vol. 70, no. 5, pp. 1783–1791, 2006.

[388] L. Albizu, M. Cottet, M. Kralikova, S. Stoev, R. Seyer, I. Brabet, T. Roux, H. Bazin, E. Bourrier, L. Lamarque, C. Breton, M.-L. Rives, A. Newman, J. Javitch, E. Trinquet, M. Manning, J.-P. Pin, B. Mouillac, and T. Durroux, "Time-resolved FRET between GPCR ligands reveals oligomers in native tissues.," *Nat. Chem. Biol.*, vol. 6, pp. 587–94, Aug. 2010.

[389] B. Jastrzebska, T. Maeda, L. Zhu, D. Fotiadis, S. Filipek, A. Engel, R. E. Stenkamp, and K. Palczewski, "Functional characterization of rhodopsin monomers and dimers in detergents," *J. Biol. Chem.*, vol. 279, pp. 54663–54675, Dec. 2004.

[390] L. Arcemisbéhère, T. Sen, L. Boudier, M.-N. Balestre, G. Gaibelet, E. Detouillon, H. Orcel, C. Mendre, R. Rahmeh, S. Granier, C. Vivès, F. Fieschi, M. Damian, T. Durroux, J.-L. Banères, and B. Mouillac, "Leukotriene BLT2 receptor monomers activate the G$_{i2}$ GTP-binding protein more efficiently than dimers," *J. Biol. Chem.*, vol. 285, pp. 6337–6347, Feb. 2010.

[391] L. P. Pellissier, G. Barthet, F. Gaven, E. Cassier, E. Trinquet, J.-P. Pin, P. Marin, A. Dumuis, J. Bockaert, J.-L. Banères, and S. Claeysen, "G protein activation by serotonin type 4 receptor dimers: evidence that turning on two protomers is more efficient," *J. Biol. Chem.*, vol. 286, pp. 9985–9997,

Mar. 2011.

[392] K. Herrick-Davis, E. Grinde, T. J. Harrigan, and J. E. Mazurkiewicz, "Inhibition of serotonin 5-hydroxytryptamine2C receptor function through heterodimerization: receptor dimers bind two molecules of ligand and one G-protein," *J. Biol. Chem.*, vol. 280, pp. 40144–40151, Dec. 2005.

[393] W. Guo, L. Shi, M. Filizola, H. Weinstein, and J. A. Javitch, "Crosstalk in G protein-coupled receptors: changes at the transmembrane homodimer interface determine activation," *Proc. Natl. Acad. Sci.*, vol. 102, pp. 17495–17500, Nov. 2005.

[394] N. Sartania, S. Appelbe, J. D. Pediani, and G. Milligan, "Agonist occupancy of a single monomeric element is sufficient to cause internalization of the dimeric β₂-adrenoceptor," *Cell. Signal.*, vol. 19, pp. 1928–1938, Sept. 2007.

[395] N. J. Smith and G. Milligan, "Allostery at G protein-coupled receptor homo-and heteromers: uncharted pharmacological landscapes," *Pharmacol. Rev.*, vol. 62, no. 4, pp. 701–725, 2010.

[396] D. Mesnier and J.-L. Banères, "Cooperative conformational changes in a G-protein-coupled receptor dimer, the leukotriene B₄ receptor BLT1," *J. Biol. Chem.*, vol. 279, pp. 49664–49670, Nov. 2004.

[397] A. Rivero-Müller, Y.-Y. Chou, I. Ji, S. Lajic, A. C. Hanyaloglu, K. Jonas, N. Rahman, T. H. Ji, and I. Huhtaniemi, "Rescue of defective G protein-coupled receptor function in vivo by intermolecular cooperation," *Proc. Natl. Acad. Sci.*, vol. 107, pp. 2319–2324, Feb. 2010.

[398] M. Zhang, R. Guan, and D. L. Segaloff, "Revisiting and questioning functional rescue between dimerized LH receptor mutant," *Mol. Endocrinol.*, vol. 26, pp. 655–668, Apr. 2012.

[399] G. Milligan and N. J. Smith, "Allosteric modulation of heterodimeric G-protein-coupled receptors," *Trends Pharmacol. Sci.*, vol. 28, pp. 615–620, Dec. 2007.

[400] E. Goupil, S. A. Laporte, and T. E. Hébert, "GPCR heterodimers: asymmetries in ligand binding and signalling output offer new targets for drug discovery.," *Br. J. Pharmacol.*, vol. 168, pp. 1101–3, Mar. 2013.

[401] M. Brugarolas, G. Navarro, E. Martínez-Pinilla, E. Angelats, V. Casadó, J. L. Lanciego, and R. Franco, "G-Protein-Coupled Receptor Heteromers as Key Players in the Molecular Architecture of the Central Nervous System.," *CNS Neurosci. Ther.*, pp. 1–7, May 2014.

[402] N. Franco and R. Franco, "Understanding the added value of g-protein-coupled receptor heteromers.," *Scientifica (Cairo).*, vol. 2014, p. 362937, Jan. 2014.

[403] V. Casadó, A. Cortés, J. Mallol, K. Pérez-Capote, S. Ferré, C. Lluis, R. Franco, and E. I. Canela, "GPCR homomers and heteromers: a better choice as targets for drug development than GPCR monomers?," *Pharmacol. Ther.*, vol. 124, pp. 248–57, Nov. 2009.

[404] V. V. Gurevich and E. V. Gurevich, "How and why do GPCRs dimerize?," *Trends Pharmacol. Sci.*, vol. 29, no. 5, pp. 234–240, 2008.

[405] T. Hebert, S. Moffett, and J. Morello, "A peptide derived from a β_2-adrenergic receptor transmembrane domain inhibits both receptor dimerization and activation," *J. Biol. Chem.*, vol. 271, no. 27, pp. 16384–16392, 1996.

[406] J. Huang, S. Chen, J. J. Zhang, and X.-Y. Huang, "Crystal structure of oligomeric β₁-adrenergic G protein-coupled receptors in ligand-free basal state," *Nat. Struct. & Mol. Biol.*, vol. 20, pp. 419–425, Apr. 2013.

[407] H. Wu, D. Wacker, M. Mileni, V. Katritch, G. W. Han, E. Vardy, W. Liu, A. A. Thompson, X.-P. Huang, F. I. Carroll, S. W. Mascarella, R. B. Westkaemper, P. D. Mosier, B. L. Roth, V. Cherezov, and R. C. Stevens, "Structure of the human κ-opioid receptor in complex with JDTic," *Nature*, vol. 485, pp. 327–332, May 2012.

[408] A. Manglik, A. C. Kruse, T. S. Kobilka, F. S. Thian, J. M. Mathiesen, R. K. Sunahara, L. Pardo, W. I. Weis, B. K. Kobilka, and S. Granier, "Crystal structure of the μ-opioid receptor bound to a morphinan antagonist," *Nature*, vol. 485, pp. 321–6, May 2012.

[409] J. J. Fung, X. Deupi, L. Pardo, X. J. Yao, G. A. Velez-Ruiz, B. T. Devree, R. K. Sunahara, and B. K. Kobilka, "Ligand-regulated oligomerization of β₂-adrenoceptors in a model lipid bilayer," *EMBO J.*, vol. 28, pp. 3315–3328, Nov. 2009.

[410] K. Suda, S. Filipek, K. Palczewski, A. Engel, and D. Fotiadis, "The supramolecular structure of the GPCR rhodopsin in solution and native disc membranes," *Mol. Membr. Biol.*, vol. 21, no. 6, pp. 435–446, 2004.

[411] P. Kota, P. J. Reeves, U. L. Rajbhandary, and H. G. Khorana, "Opsin is present as dimers in COS1 cells: identification of amino acids at the dimeric interface," *Proc. Natl. Acad. Sci.*, vol. 103, pp. 3054–9, Feb. 2006.

[412] F.-Y. Zeng and J. Wess, "Identification and Molecular Characterization of m3 Muscarinic Receptor Dimers," *J. Biol. Chem.*, vol. 274, pp. 19487–19497, July 1999.

[413] S. M. McMillin, M. Heusel, T. Liu, S. Costanzi, and J. Wess, "Structural basis of M3 muscarinic

receptor dimer/oligomer formation," *J. Biol. Chem.*, vol. 286, pp. 28584–28598, Aug. 2011.

[414] J. Hu, D. Thor, Y. Zhou, T. Liu, Y. Wang, S. M. McMillin, R. Mistry, R. A. J. Challiss, S. Costanzi, and J. Wess, "Structural aspects of M_3 muscarinic acetylcholine receptor dimer formation and activation," *FASEB J.*, vol. 26, pp. 604–16, Feb. 2012.

[415] G. Y. Ng, B. F. O'Dowd, S. P. Lee, H. T. Chung, M. R. Brann, P. Seeman, and S. R. George, "Dopamine D2 receptor dimers and receptor-blocking peptides," *Biochem. Biophys. Res. Commun.*, vol. 227, pp. 200–204, Oct. 1996.

[416] S. P. Lee, B. F. O'Dowd, R. D. Rajaram, T. Nguyen, and S. R. George, "D2 dopamine receptor homodimerization is mediated by multiple sites of interaction, including an intermolecular interaction involving transmembrane domain 4.," *Biochemistry*, vol. 42, pp. 11023–11031, Sept. 2003.

[417] W. Guo, L. Shi, and J. A. Javitch, "The fourth transmembrane segment forms the interface of the dopamine D2 receptor homodimer," *J. Biol. Chem.*, vol. 278, pp. 4385–4388, Feb. 2003.

[418] W. Guo, E. Urizar, M. Kralikova, J. C. Mobarec, L. Shi, M. Filizola, and J. A. Javitch, "Dopamine D2 receptors form higher order oligomers at physiological expression levels," *EMBO J.*, vol. 27, pp. 2293–2304, Sept. 2008.

[419] M. Benkirane, D.-Y. Jin, R. F. Chun, R. A. Koup, and K.-T. Jeang, "Mechanism of Transdominant Inhibition of CCR5-mediated HIV-1 Infection by ccr5Δ32," *J. Biol. Chem.*, vol. 272, pp. 30603–30606, Dec. 1997.

[420] P. Hernanz-Falcón, J. M. Rodríguez-Frade, A. Serrano, D. Juan, A. del Sol, S. F. Soriano, F. Roncal, L. Gómez, A. Valencia, C. Martínez-A, and M. Mellado, "Identification of amino acid residues crucial for chemokine receptor dimerization.," *Nat. Immunol.*, vol. 5, pp. 216–23, Feb. 2004.

[421] J. Wang, L. He, C. A. Combs, G. Roderiquez, and M. A. Norcross, "Dimerization of CXCR4 in living malignant cells: control of cell migration by a synthetic peptide that reduces homologous CXCR4 interactions.," *Mol. Cancer Ther.*, vol. 5, pp. 2474–2483, Oct. 2006.

[422] S. Michineau, F. Alhenc-Gelas, and R. M. Rajerison, "Human bradykinin B2 receptor sialylation and N-glycosylation participate with disulfide bonding in surface receptor dimerization," *Biochemistry*, vol. 45, pp. 2699–707, Feb. 2006.

[423] S. AbdAlla, E. Zaki, H. Lother, and U. Quitterer, "Involvement of the Amino Terminus of the B_2 Receptor in Agonist-induced Receptor Dimerization," *J. Biol. Chem.*, vol. 274, pp. 26079–26084, Sept. 1999.

[424] M. C. Overton and K. J. Blumer, "The extracellular N-terminal domain and transmembrane domains 1 and 2 mediate oligomerization of a yeast G protein-coupled receptor," *J. Biol. Chem.*, vol. 277, pp. 41463–41472, Nov. 2002.

[425] H. X. Wang and J. B. Konopka, "Identification of amino acids at two dimer interface regions of the α-factor receptor (Ste2)," *Biochemistry*, vol. 48, pp. 7132–7139, Aug. 2009.

[426] M. S. Uddin, H. Kim, A. Deyo, F. Naider, and J. M. Becker, "Identification of residues involved in homodimer formation located within a β-strand region of the N-terminus of a Yeast G protein-coupled receptor.," *J. Recept. Signal Transduct. Res.*, vol. 32, pp. 65–75, Apr. 2012.

[427] S. Cvejic and L. A. Devi, "Dimerization of the Opioid Receptor: imiplication for a role in receptor internalisation," *J. Biol. Chem.*, vol. 272, pp. 26959–26964, Oct. 1997.

[428] D. Casciari, D. Dell'Orco, and F. Fanelli, "Homodimerization of neurotensin 1 receptor involves helices 1, 2, and 4: insights from quaternary structure predictions and dimerization free energy estimations," *J. Chem. Inf. Model.*, vol. 48, no. 8, pp. 1669–1678, 2008.

[429] F. Mancia, Z. Assur, A. G. Herman, R. Siegel, and W. A. Hendrickson, "Ligand sensitivity in dimeric associations of the serotonin 5HT2c receptor," *EMBO Rep.*, vol. 9, pp. 363–369, Apr. 2008.

[430] D. Thévenin, T. Lazarova, M. F. Roberts, and C. R. Robinson, "Oligomerization of the fifth transmembrane domain from the adenosine A_{2A} receptor," *Protein Sci.*, vol. 14, pp. 2177–86, Aug. 2005.

[431] J. F. Lopez-Gimenez, M. Canals, J. D. Pediani, and G. Milligan, "The α_{1b}-adrenoceptor exists as a higher-order oligomer: effective oligomerization is required for receptor maturation, surface delivery, and function," *Mol. Pharmacol.*, vol. 71, pp. 1015–1029, Apr. 2007.

[432] J.-L. Banères and J. Parello, "Structure-based Analysis of GPCR Function: Evidence for a Novel Pentameric Assembly between the Dimeric Leukotriene B_4 Receptor BLT1 and the G-protein," *J. Mol. Biol.*, vol. 329, pp. 815–829, June 2003.

[433] L. F. Pisterzi, D. B. Jansma, J. Georgiou, M. J. Woodside, J. T.-C. Chou, S. Angers, V. Raicu, and J. W. Wells, "Oligomeric size of the M_2 muscarinic receptor in live cells as determined by quantitative fluorescence resonance energy transfer," *J. Biol. Chem.*, vol. 285, pp. 16723–16738, May 2010.

[434] S. Patowary, E. Alvarez-Curto, T.-R. Xu, J. D. Holz, J. A. Oliver, G. Milligan, and V. Raicu, "The muscarinic M3 acetylcholine receptor exists as two differently sized complexes at the plasma membrane.," *Biochem. J.*, vol. 452, pp. 303–312, June 2013.

[435]   M. Bouvier and T. E. Hébert, "CrossTalk proposal: Weighing the evidence for Class A GPCR dimers, the evidence favours dimers," *J. Physiol.*, vol. 592, pp. 2439–41, June 2014.

[436]   S. Dorsch, K.-N. Klotz, S. Engelhardt, M. J. Lohse, and M. Bünemann, "Analysis of receptor oligomerization by FRAP microscopy," *Nat. Methods*, vol. 6, pp. 225–30, Mar. 2009.

[437]   J. Fonseca and N. Lambert, "Instability of a class AG protein-coupled receptor oligomer interface," *Mol. Pharmacol.*, vol. 75, no. 6, pp. 1296–1299, 2009.

[438]   J. A. Hern, A. H. Baig, G. I. Mashanov, B. Birdsall, J. E. T. Corrie, S. Lazareno, J. E. Molloy, and N. J. M. Birdsall, "Formation and dissociation of M1 muscarinic receptor dimers seen by total internal reflection fluorescence imaging of single molecules," *Proc. Natl. Acad. Sci.*, vol. 107, pp. 2693–2698, Feb. 2010.

[439]   R. S. Kasai, K. G. N. Suzuki, E. R. Prossnitz, I. Koyama-Honda, C. Nakada, T. K. Fujiwara, and A. Kusumi, "Full characterization of GPCR monomer-dimer dynamic equilibrium by single molecule imaging," *J. Cell Biol.*, vol. 192, pp. 463–480, Feb. 2011.

[440]   D. Calebiro, F. Rieken, J. Wagner, T. Sungkaworn, U. Zabel, A. Borzi, E. Cocucci, A. Zürn, and M. J. Lohse, "Single-molecule analysis of fluorescently labeled G-protein-coupled receptors reveals complexes with distinct dynamics and organization," *Proc. Natl. Acad. Sci.*, vol. 110, pp. 743–748, Jan. 2013.

[441]   N. A. Lambert, "GPCR dimers fall apart," *Sci. Signal.*, vol. 3, p. pe12, Jan. 2010.

[442]   S. Martin, V. Navarro, J. P. Vincent, and J. Mazella, "Neurotensin receptorâĂŞ1 and âĂŞ3 complex modulates the cellular signaling of neurotensin in the HT29 cell line," *Gastroenterology*, vol. 123, pp. 1135–1143, Oct. 2002.

[443]   A. Perron, N. Sharif, P. Sarret, T. Stroh, and A. Beaudet, "NTS2 modulates the intracellular distribution and trafficking of NTS1 via heterodimerization," *Biochem. Biophys. Res. Commun.*, vol. 353, pp. 582–590, Feb. 2007.

[444]   J. R. Hwang, M. W. Baek, J. Sim, H.-S. Choi, J. M. Han, Y. L. Kim, J.-I. Hwang, H. B. Kwon, N. Beaudet, P. Sarret, and J. Y. Seong, "Intermolecular cross-talk between NTR1 and NTR2 neurotensin receptor promotes intracellular sequestration and functional inhibition of NTR1 receptors," *Biochem. Biophys. Res. Commun.*, vol. 391, pp. 1007–1013, Jan. 2010.

[445]   T. Antonelli, M. C. Tomasini, K. Fuxe, L. F. Agnati, S. Tanganelli, and L. Ferraro, "Receptor-receptor interactions as studied with microdialysis. Focus on NTR/D_2 interactions in the basal ganglia," *J. Neural Transm.*, vol. 114, pp. 105–113, Jan. 2007.

[446]   S. Koschatzky and P. Gmeiner, "Selective agonists for dopamine/neurotensin receptor heterodimers," *ChemMedChem*, vol. 7, pp. 509–514, Mar. 2012.

[447]   D. O. Borroto-Escuela, A. Ravani, A. O. Tarakanov, I. Brito, M. Narvaez, W. Romero-Fernandez, F. Corrales, L. F. Agnati, S. Tanganelli, L. Ferraro, and K. Fuxe, "Dopamine D2 receptor signaling dynamics of dopamine D2-neurotensin 1 receptor heteromers," *Biochem. Biophys. Res. Commun.*, vol. 435, pp. 140–146, May 2013.

[448]   A. D. Goddard, P. M. Dijkman, R. J. Adamson, and A. Watts, "Lipid-Dependent GPCR Dimerization," *Methods Cell Biol.*, vol. 117, pp. 341–357, 2013.

[449]   G. W. Gordon, G. Berry, X. H. Liang, B. Levine, and B. Herman, "Quantitative fluorescence resonance energy transfer measurements using fluorescence microscopy," *Biophys. J.*, vol. 74, pp. 2702–2713, May 1998.

[450]   J. K. Kruschke, "Bayesian estimation supersedes the t test.," *J. Exp. Psychol. Gen.*, vol. 142, pp. 573–603, May 2013.

[451]   S. Leptihn, O. K. Castell, B. Cronin, E.-H. Lee, L. C. M. Gross, D. P. Marshall, J. R. Thompson, M. Holden, and M. I. Wallace, "Constructing droplet interface bilayers from the contact of aqueous droplets in oil," *Nat. Protoc.*, vol. 8, pp. 1048–1057, June 2013.

[452]   E. J. Barber, "Calculation of density and viscosity of sucrose solutions as a function of concentration and temperature," *Natl. Cancer Inst. Monogr.*, vol. 21, p. 219, 1966.

[453]   E. J. Cohn and J. T. Edsall, "Proteins, Amino Acids and Peptides as Ions and Dipolar Ions," *Reinhold, New York*, 1943.

[454]   H. Durchschlag, "Specific volumes of biological macromolecules and some other molecules of biological interest," in *Thermodyn. data Biochem. Biotechnol.*, pp. 45–128, Springer, 1986.

[455]   J.-L. Rigaud, G. Mosser, J.-J. Lacapere, A. Olofsson, D. Levy, and J.-L. Ranck, "Bio-Beads: an efficient strategy for two-dimensional crystallization of membrane proteins," *J. Struct. Biol.*, vol. 118, no. 3, pp. 226–235, 1997.

[456]   D. M. Small, "Phase equilibria and structure of dry and hydrated egg lecithin," *J. Lipid Res.*, vol. 8, no. 6, pp. 551–557, 1967.

[457]   J.-F. Mercier, A. Salahpour, S. Angers, A. Breit, and M. Bouvier, "Quantitative assessment of beta 1- and beta 2-adrenergic receptor homo- and heterodimerization by bioluminescence resonance energy

transfer," *J. Biol. Chem.*, vol. 277, pp. 44925–44931, Nov. 2002.

[458] A. T. McGeoch, M. A. Trakselis, R. A. Laskey, and S. D. Bell, "Organization of the archaeal MCM complex on DNA and implications for the helicase mechanism," *Nat. Struct. Mol. Biol.*, vol. 12, pp. 756–762, Sept. 2005.

[459] M. C. Murphy, I. Rasnik, W. Cheng, T. M. Lohman, and T. Ha, "Probing single-stranded DNA conformational flexibility using fluorescence spectroscopy," *Biophys. J.*, vol. 86, pp. 2530–2537, Apr. 2004.

[460] M. S. Parker, R. Sah, A. Balasubramaniam, E. A. Park, F. R. Sallee, and S. L. Parker, "Dimers of G-protein coupled receptors as versatile storage and response units," *Int. J. Mol. Sci.*, vol. 15, pp. 4856–4877, Jan. 2014.

[461] J. M. Johnston, H. Wang, D. Provasi, and M. Filizola, "Assessing the relative stability of dimer interfaces in g protein-coupled receptors," *PLoS Comput. Biol.*, vol. 8, p. e1002649, Jan. 2012.

[462] S. R. Hubbard and W. T. Miller, "Receptor tyrosine kinases: mechanisms of activation and signaling," *Curr. Opin. Cell Biol.*, vol. 19, pp. 117–123, Apr. 2007.

[463] M. Najimi, F. Souazé, M. Méndez, E. Hermans, T. Berbar, W. Rostène, and P. Forgez, "Activation of Receptor Gene Transcription Is Required to Maintain Cell Sensitization after Agonist Exposure: study on neurotensin receptor," *J. Biol. Chem.*, vol. 273, pp. 21634–21641, Aug. 1998.

[464] S. R. Neves, P. T. Ram, and R. Iyengar, "G protein pathways," *Science*, vol. 296, pp. 1636–1639, May 2002.

[465] G. Milligan and E. Kostenis, "Heterotrimeric G-proteins: a short history," *Br. J. Pharmacol.*, pp. S46–S55, Jan. 2006.

[466] B. R. Conklin, Z. Farfel, K. D. Lustig, D. Julius, and H. R. Bourne, "Substitution of three amino acids switches receptor specificity of $G_q\alpha$ to that of $G_i\alpha$," *Nature*, vol. 363, pp. 274–276, 1993.

[467] T. Namba, Y. Sugimoto, M. Negishi, A. Irie, F. Ushikubi, A. Kazizuka, S. Ito, A. Ichikawa, and S. Narumiya, "Alternative splicing of C-terminal tail of prostaglandin E receptor subtype EP3 determines G-protein specificity," *Nature*, vol. 365, pp. 166–170, 1993.

[468] N. Van Eps, A. M. Preininger, N. Alexander, A. I. Kaya, S. Meier, J. Meiler, H. E. Hamm, and W. L. Hubbell, "Interaction of a G protein with an activated receptor opens the interdomain interface in the alpha subunit," *Proc. Natl. Acad. Sci.*, vol. 108, pp. 9420–9424, June 2011.

[469] M. B. Jones, D. P. Siderovski, and S. B. Hooks, "The $G\beta\gamma$ dimer as a novel source of selectivity in G-protein signaling: GGL-ing at convention," *Mol. Interv.*, vol. 4, no. 4, pp. 200–214, 2004.

[470] J. M. Weiss, P. H. Morgan, M. W. Lutz, and T. P. Kenakin, "The cubic ternary complex receptor-occupancy model I. Model description," *J. Theor. Biol.*, vol. 178, pp. 151–167, 1996.

[471] D. Skrzydelski, A.-M. Lhiaubet, A. Lebeau, P. Forgez, M. Yamada, E. Hermans, W. Rostene, and D. Pelaprat, "Differential involvement of intracellular domains of the rat NTS1 neurotensin receptor in coupling to G proteins: a molecular basis for agonist-directed trafficking of receptor stimulus," *Mol. Pharmacol.*, vol. 64, pp. 421–429, Aug. 2003.

[472] B. M. Tyler-McMahon, M. Boules, and E. Richelson, "Neurotensin: peptide for the next millennium," *Regul. Pept.*, vol. 93, no. 1-3, pp. 125–136, 2000.

[473] B. M. Tyler-McMahon, J. A. Stewart, F. Farinas, D. J. McCormick, and E. Richelson, "Highly potent neurotensin analog that causes hypothermia and antinociception," *Eur. J. Pharmacol.*, vol. 390, pp. 107–111, Feb. 2000.

[474] J. B. Thomas, H. Navarro, K. R. Warner, and B. Gilmour, "The identification of nonpeptide neurotensin receptor partial agonists from the potent antagonist SR48692 using a calcium mobilization assay," *Bioorganic & Med. Chem. Lett.*, vol. 19, pp. 1438–1441, Mar. 2009.

[475] P. M. Hershberger, M. P. Hedrick, S. Peddibhotla, A. Mangravita-Novo, P. Gosalia, Y. Li, W. Gray, M. Vicchiarelli, L. H. Smith, T. D. Y. Chung, J. B. Thomas, M. G. Caron, A. B. Pinkerton, L. S. Barak, and G. P. Roth, "Imidazole-derived agonists for the neurotensin 1 receptor," *Bioorganic & Med. Chem. Lett.*, vol. 24, pp. 262–267, Jan. 2014.

[476] P. Kitabgi, "Functional domains of the subtype 1 neurotensin receptor (NTS1)," *Peptides*, vol. 27, no. 10, pp. 2461–2468, 2006.

[477] D. Gully, M. Canton, R. Boigegrain, F. Jeanjean, J. C. Molimard, M. Poncelet, C. Gueudet, M. Heaulme, R. Leyris, and A. Brouard, "Biochemical and pharmacological profile of a potent and selective nonpeptide antagonist of the neurotensin receptor," *Proc. Natl. Acad. Sci.*, vol. 90, pp. 65–69, Jan. 1993.

[478] D. Gully, B. Labeeuw, R. Boigegrain, F. Oury-Donat, A. Bachy, M. Poncelet, R. Steinberg, M. F. Suaud-Chagny, V. Santucci, N. Vita, F. Pecceu, C. Labbé-Jullié, P. Kitabgi, P. Soubrié, G. Le Fur, and J. P. Maffrand, "Biochemical and pharmacological activities of SR 142948A, a new potent neurotensin receptor antagonist," *J. Pharmacol. Exp. Ther.*, vol. 280, pp. 802–812, Feb. 1997.

[479] C. Labbé-Jullié, J. M. Botto, M. V. Mas, J. Chabry, J. Mazella, J. P. Vincent, D. Gully, J. P. Maffrand, and P. Kitabgi, "[^{3}H]SR 48692, the first nonpeptide neurotensin antagonist radioligand: characterization of binding properties and evidence for distinct agonist and antagonist binding domains on the rat neurotensin receptor," *Mol. Pharmacol.*, vol. 47, pp. 1050–1056, May 1995.

[480] C. Betancur, M. Canton, A. Burgos, B. Labeeuw, D. Gully, W. Rostène, and D. Pélaprat, "Characterization of binding sites of a new neurotensin receptor antagonist, [^{3}H]SR 142948A, in the rat brain," *Eur. J. Pharmacol.*, vol. 343, pp. 67–77, Feb. 1998.

[481] R. Grisshammer and E. Hermans, "Functional coupling with $G\alpha_q$ and $G\alpha_{i1}$ protein subunits promotes high-affinity agonist binding to the neurotensin receptor NTS-1 expressed in *Escherichia coli*," *FEBS Lett.*, vol. 493, pp. 101–105, Mar. 2001.

[482] F. Oury-Donat, O. Thurneyssen, N. Gonalons, P. Forgez, D. Gully, G. Le Fur, and P. Soubrie, "Characterization of the effect of SR48692 on inositol monophosphate, cyclic GMP and cyclic AMP responses linked to neurotensin receptor activation in neuronal and non-neuronal cells," *Br. J. Pharmacol.*, vol. 116, pp. 1899–1905, Sept. 1995.

[483] J.-M. Botto, E. Guillemare, J.-P. Vincent, and J. Mazella, "Effects of SR 48692 on neurotensin-induced calcium-activated chloride currents in the Xenopus oocyte expression system: agonist-like activity on the levocabastine-sensitive neurotensin receptor and absence of antagonist effect on the levocabastine insensi," *Neurosci. Lett.*, vol. 223, pp. 193–196, Feb. 1997.

[484] J. P. Vincent, "Neurotensin receptors: binding properties, transduction pathways, and structure," *Cell. Mol. Neurobiol.*, vol. 15, pp. 501–512, Oct. 1995.

[485] E. B. Binder, B. Kinkead, M. J. Owens, and C. B. Nemeroff, "Neurotensin receptor antagonist SR 142948A alters Fos expression and extrapyramidal side effect profile of typical and atypical antipsychotic drugs," *Neuropsychopharmacology*, vol. 29, pp. 2200–2207, Dec. 2004.

[486] M. Portier, T. Combes, D. Gully, J. P. Maffrand, and P. Casellas, "Neurotensin type 1 receptor-mediated activation of krox24, c-fos and Elk-1: preventing effect of the neurotensin antagonists SR 48692 and SR 142948," *FEBS Lett.*, vol. 432, pp. 88–93, July 1998.

[487] A. Blaukat, A. Barac, M. J. Cross, S. Offermanns, and I. Dikic, "G protein-coupled receptor-mediated mitogen-activated protein kinase activation through cooperation of $G\alpha_q$ and $G\alpha_i$ signals," *Mol. Cell. Biol.*, vol. 20, no. 18, pp. 6837–6848, 2000.

[488] T. Kenakin, "Ligand-selective receptor conformations revisited: the promise and the problem," *Trends Pharmacol. Sci.*, vol. 24, no. 7, pp. 346–354, 2003.

[489] S. Barroso, F. Richard, D. Nicolas-Ethève, P. Kitabgi, and C. Labbé-Jullié, "Constitutive activation of the neurotensin receptor 1 by mutation of Phe(358) in Helix seven," *Br. J. Pharmacol.*, vol. 135, pp. 997–1002, Feb. 2002.

[490] E. C. Hulme and M. A. Trevethick, "Ligand binding assays at equilibrium: validation and interpretation," *Br. J. Pharmacol.*, vol. 161, pp. 1219–1237, Nov. 2010.

[491] D. P. McEwen, K. R. Gee, H. C. Kang, and R. R. Neubig, "Fluorescent BODIPY-GTP analogs: real-time measurement of nucleotide binding to G proteins," *Anal. Biochem.*, vol. 291, pp. 109–117, Apr. 2001.

[492] O. Vögler, J. Casas, D. Capó, T. Nagy, G. Borchert, G. Martorell, and P. V. Escribá, "The $G\beta\gamma$ dimer drives the interaction of heterotrimeric G_i proteins with nonlamellar membrane structures," *J. Biol. Chem.*, vol. 279, pp. 36540–36545, Aug. 2004.

[493] T. L. Jones, W. F. Simonds, J. J. Merendino, M. R. Brann, and A. M. Spiegel, "Myristoylation of an inhibitory GTP-binding protein alpha subunit is essential for its membrane attachment," *Proc. Natl. Acad. Sci.*, vol. 87, pp. 568–572, Jan. 1990.

[494] S. M. Mumby, R. O. Heukeroth, J. I. Gordon, and A. G. Gilman, "G-protein α-subunit expression, myristoylation, and membrane association in COS cells," *Proc. Natl. Acad. Sci.*, vol. 87, pp. 728–732, Jan. 1990.

[495] I. D. Alves, Z. Salamon, E. Varga, H. I. Yamamura, G. Tollin, and V. J. Hruby, "Direct observation of G-protein binding to the human δ-opioid receptor using plasmon-waveguide resonance spectroscopy," *J. Biol. Chem.*, vol. 278, pp. 48890–48897, Dec. 2003.

[496] I. D. Alves, G. F. J. Salgado, Z. Salamon, M. F. Brown, G. Tollin, and V. J. Hruby, "Phosphatidylethanolamine enhances rhodopsin photoactivation and transducin binding in a solid supported lipid bilayer as determined using plasmon-waveguide resonance spectroscopy," *Biophys. J.*, vol. 88, pp. 198–210, Jan. 2005.

[497] B. Jastrzebska, A. Debinski, S. Filipek, and K. Palczewski, "Role of membrane integrity on G protein-coupled receptors: Rhodopsin stability and function," *Prog. Lipid Res.*, vol. 50, pp. 267–277, July 2011.

[498] E. Hessel, M. Heck, P. Müller, A. Herrmann, and K. P. Hofmann, "Signal transduction in the visual

cascade involves specific lipid-protein interactions," *J. Biol. Chem.*, vol. 278, pp. 22853–22860, June 2003.

[499] G. Jeschke, "DEER distance measurements on proteins," *Annu. Rev. Phys. Chem.*, vol. 63, pp. 19.1–19.28, 2012.

[500] E. R. Geertsma, N. A. B. N. Mahmood, G. K. Schuurman-Wolters, and B. Poolman, "Membrane reconstitution of ABC transporters and assays of translocator function," *Nat. Protoc.*, vol. 3, pp. 256–266, Jan. 2008.

[501] L. Niu, J.-M. Kim, and H. G. Khorana, "Structure and function in rhodopsin: asymmetric reconstitution of rhodopsin in liposomes," *Proc. Natl. Acad. Sci.*, vol. 99, pp. 13409–13412, Oct. 2002.

[502] S. L. Ritter and R. A. Hall, "Fine-tuning of GPCR activity by receptor-interacting proteins," *Nat. Rev. Mol. Cell Biol.*, vol. 10, pp. 819–830, Dec. 2009.

[503] P. Viitanen, M. J. Newman, D. L. Foster, T. H. Wilson, and H. R. Kaback, "Purification, reconstitution, and characterization of the lac permease of Escherichia coli," *Methods Enzymol.*, vol. 125, pp. 429–452, 1986.

[504] W. K. Greentree and M. E. Linder, "Purification of recombinant G protein alpha subunits from *Escherichia coli*," *Methods Mol. Biol.*, vol. 237, pp. 3–20, Jan. 2004.

[505] K. Palczewski, T. Kumasaka, T. Hori, C. A. Behnke, H. Motoshima, B. A. Fox, I. L. Trong, D. C. Teller, T. Okada, and R. E. Stenkamp, "Crystal structure of rhodopsin: A G protein-coupled receptor," *Science*, vol. 289, no. 5480, pp. 739–745, 2000.

[506] D. C. Teller, T. Okada, C. A. Behnke, K. Palczewski, and R. E. Stenkamp, "Advances in determination of a high-resolution three-dimensional structure of rhodopsin, a model of G-protein-coupled receptors (GPCRs)," *Biochemistry*, vol. 40, no. 26, pp. 7761–7772, 2001.

[507] T. Okada, Y. Fujiyoshi, M. Silow, J. Navarro, E. M. Landau, and Y. Shichida, "Functional role of internal water molecules in rhodopsin revealed by X-ray crystallography," *Proc. Natl. Acad. Sci.*, vol. 99, no. 9, pp. 5982–5987, 2002.

[508] J. Li, P. C. Edwards, M. Burghammer, C. Villa, and G. F. X. Schertler, "Structure of bovine rhodopsin in a trigonal crystal form," *J. Mol. Biol.*, vol. 343, pp. 1409–1438, Nov. 2004.

[509] T. Okada, M. Sugihara, A.-N. Bondar, M. Elstner, P. Entel, and V. Buss, "The retinal conformation and its environment in rhodopsin in light of a new 2.2 Å crystal structure." *J. Mol. Biol.*, vol. 342, pp. 571–583, Sept. 2004.

[510] D. Salom, D. T. Lodowski, R. E. Stenkamp, I. Le Trong, M. Golczak, B. Jastrzebska, T. Harris, J. A. Ballesteros, and K. Palczewski, "Crystal structure of a photoactivated deprotonated intermediate of rhodopsin," *Proc. Natl. Acad. Sci.*, vol. 103, pp. 16123–16128, Oct. 2006.

[511] J. Standfuss, G. Xie, P. C. Edwards, M. Burghammer, D. D. Oprian, and G. F. X. Schertler, "Crystal structure of a thermally stable rhodopsin mutant," *J. Mol. Biol.*, vol. 372, pp. 1179–1188, Oct. 2007.

[512] R. E. Stenkamp, "Alternative models for two crystal structures of bovine rhodopsin," *Acta Crystallogr. D*, vol. 64, pp. 902–904, Aug. 2008.

[513] C. L. Makino, C. K. Riley, J. Looney, R. K. Crouch, and T. Okada, "Binding of more than one retinoid to visual opsins," *Biophys. J.*, vol. 99, pp. 2366–2373, Oct. 2010.

[514] H. Nakamichi and T. Okada, "X-ray crystallographic analysis of 9-cis-rhodopsin, a model analogue visual pigment," *Photochem. Photobiol.*, vol. 83, no. 2, pp. 232–235, 2007.

[515] A. Singhal, M. K. Ostermaier, S. A. Vishnivetskiy, V. Panneels, K. T. Homan, J. J. G. Tesmer, D. Veprintsev, X. Deupi, V. V. Gurevich, G. F. X. Schertler, and J. Standfuss, "Insights into congenital stationary night blindness based on the structure of G90D rhodopsin," *EMBO Rep.*, vol. 14, pp. 520–526, June 2013.

[516] J. Standfuss, P. C. Edwards, A. D'Antona, M. Fransen, G. Xie, D. D. Oprian, and G. F. X. Schertler, "The structural basis of agonist-induced activation in constitutively active rhodopsin," *Nature*, vol. 471, pp. 656–660, Mar. 2011.

[517] J. H. Park, T. Morizumi, Y. Li, J. E. Hong, E. F. Pai, K. P. Hofmann, H.-W. Choe, and O. P. Ernst, "Opsin, a structural model for olfactory receptors?," *Angew. Chem. Int. Ed. Engl.*, vol. 52, pp. 11021–11024, Oct. 2013.

[518] H. Nakamichi and T. Okada, "Crystallographic analysis of primary visual photochemistry," *Angew. Chemie*, vol. 45, pp. 4270–4273, June 2006.

[519] H. Nakamichi and T. Okada, "Local peptide movement in the photoreaction intermediate of rhodopsin," *Proc. Natl. Acad. Sci.*, vol. 103, pp. 12729–12734, Aug. 2006.

[520] H.-W. Choe, Y. J. Kim, J. H. Park, T. Morizumi, E. F. Pai, N. Krauss, K. P. Hofmann, P. Scheerer, and O. P. Ernst, "Crystal structure of metarhodopsin II," *Nature*, vol. 471, pp. 651–655, Mar. 2011.

[521] X. Deupi, P. Edwards, A. Singhal, B. Nickle, D. Oprian, G. Schertler, and J. Standfuss, "Stabilized G protein binding site in the structure of constitutively active metarhodopsin-II," *Proc. Natl. Acad.*

Sci., vol. 109, pp. 119–124, Jan. 2012.

[522] T. Shimamura, K. Hiraki, N. Takahashi, T. Hori, H. Ago, K. Masuda, K. Takio, M. Ishiguro, and M. Miyano, "Crystal structure of squid rhodopsin with intracellularly extended cytoplasmic region," *J. Biol. Chem.*, vol. 283, pp. 17753–17756, June 2008.

[523] M. Murakami and T. Kouyama, "Crystal structure of squid rhodopsin," *Nature*, vol. 453, no. 7193, pp. 363–367, 2008.

[524] M. Murakami and T. Kouyama, "Crystallographic analysis of the primary photochemical reaction of squid rhodopsin," *J. Mol. Biol.*, vol. 413, pp. 615–627, Oct. 2011.

[525] S. G. F. Rasmussen, H.-J. Choi, D. M. Rosenbaum, T. S. Kobilka, F. S. Thian, P. C. Edwards, M. Burghammer, V. R. P. Ratnala, R. Sanishvili, R. F. Fischetti, G. F. X. Schertler, W. I. Weis, and B. K. Kobilka, "Crystal structure of the human β_2 adrenergic G-protein-coupled receptor," *Nature*, vol. 450, no. 7168, pp. 383–387, 2007.

[526] M. P. Bokoch, Y. Zou, S. G. F. Rasmussen, C. W. Liu, R. Nygaard, D. M. Rosenbaum, J. J. Fung, H.-J. Choi, F. S. Thian, T. S. Kobilka, J. D. Puglisi, W. I. Weis, L. Pardo, R. S. Prosser, L. Mueller, and B. K. Kobilka, "Ligand-specific regulation of the extracellular surface of a G-protein-coupled receptor," *Nature*, vol. 463, no. 7277, pp. 108–112, 2010.

[527] M. A. Hanson, V. Cherezov, M. T. Griffith, C. B. Roth, V.-P. Jaakola, E. Y. T. Chien, J. Velasquez, P. Kuhn, and R. C. Stevens, "A specific cholesterol binding site is established by the 2.8 Å structure of the human β_2-adrenergic receptor," *Structure*, vol. 16, pp. 897–905, June 2008.

[528] D. Wacker, G. Fenalti, M. A. Brown, V. Katritch, R. Abagyan, V. Cherezov, and R. C. Stevens, "Conserved binding mode of human β_2 adrenergic receptor inverse agonists and antagonist revealed by X-ray crystallography," *J. Am. Chem. Soc.*, vol. 132, pp. 11443–11445, 2010.

[529] D. M. Rosenbaum, C. Zhang, J. A. Lyons, R. Holl, D. Aragao, D. H. Arlow, S. G. F. Rasmussen, H.-J. Choi, B. T. Devree, R. K. Sunahara, P. S. Chae, S. H. Gellman, R. O. Dror, D. E. Shaw, W. I. Weis, M. Caffrey, P. Gmeiner, and B. K. Kobilka, "Structure and function of an irreversible agonist-β_2 adrenoceptor complex," *Nature*, vol. 469, pp. 236–240, Jan. 2011.

[530] S. G. F. Rasmussen, H. J. Choi, J. J. Fung, E. Pardon, P. Casarosa, P. S. Chae, B. T. DeVree, D. M. Rosenbaum, F. S. Thian, and T. S. Kobilka, "Structure of a nanobody-stabilized active state of the β_2 adrenoceptor," *Nature*, vol. 469, no. 7329, pp. 175–180, 2011.

[531] A. M. Ring, A. Manglik, A. C. Kruse, M. D. Enos, W. I. Weis, K. C. Garcia, and B. K. Kobilka, "Adrenaline-activated structure of β_2-adrenoceptor stabilized by an engineered nanobody," *Nature*, vol. 502, pp. 575–579, Oct. 2013.

[532] D. Weichert, A. C. Kruse, A. Manglik, C. Hiller, C. Zhang, H. Hübner, B. K. Kobilka, and P. Gmeiner, "Covalent agonists for studying G protein-coupled receptor activation," *Proc. Natl. Acad. Sci.*, vol. 111, July 2014.

[533] T. Warne, M. J. Serrano-Vega, J. G. Baker, R. Moukhametzianov, P. C. Edwards, R. Henderson, A. G. W. Leslie, C. G. Tate, and G. F. X. Schertler, "Structure of a β_1-adrenergic G-protein-coupled receptor," *Nature*, vol. 454, no. 7203, pp. 486–491, 2008.

[534] R. Moukhametzianov, T. Warne, P. C. Edwards, M. J. Serrano-vega, A. G. W. Leslie, C. G. Tate, and G. F. X. Schertler, "Two distinct conformations of helix 6 observed in antagonist-bound structures of a β_1-adrenergic receptor," *Proc. Natl. Acad. Sci.*, vol. 108, no. 20, pp. 8228–8232, 2011.

[535] J. L. Miller-Gallacher, R. Nehmé, T. Warne, P. C. Edwards, G. F. X. Schertler, A. G. W. Leslie, and C. G. Tate, "The 2.1 Å resolution structure of cyanopindolol-bound β_1-adrenoceptor identifies an intramembrane Na$^+$ ion that stabilises the ligand-free receptor," *PLoS One*, vol. 9, p. e92727, Jan. 2014.

[536] T. Warne, P. C. Edwards, A. G. W. Leslie, and C. G. Tate, "Crystal structures of a stabilized β_1-adrenoceptor bound to the biased agonists bucindolol and carvedilol," *Structure*, vol. 20, pp. 841–849, May 2012.

[537] J. Christopher and J. Brown, "Biophysical fragment screening of the β_1-adrenergic receptor: identification of high affinity arylpiperazine leads using structure-based drug design," *J. Med. Chem.*, vol. 56, no. 3, pp. 3446–3455, 2013.

[538] W. Liu, E. Chun, A. A. Thompson, P. Chubukov, F. Xu, V. Katritch, G. W. Han, C. B. Roth, L. H. Heitman, A. P. IJzerman, V. Cherezov, and R. C. Stevens, "Structural basis for allosteric regulation of GPCRs by sodium ions," *Science*, vol. 337, pp. 232–236, July 2012.

[539] G. Lebon, T. Warne, P. C. Edwards, K. Bennett, C. J. Langmead, A. G. W. Leslie, and C. G. Tate, "Agonist-bound adenosine A$_{2A}$ receptor structures reveal common features of GPCR activation," *Nature*, vol. 474, pp. 521–525, June 2011.

[540] M. Congreve, S. P. Andrews, A. S. Doré, K. Hollenstein, E. Hurrell, C. J. Langmead, J. S. Mason, I. W. Ng, B. Tehan, A. Zhukov, M. Weir, and F. H. Marshall, "Discovery of 1,2,4-triazine derivatives as

adenosine A_{2A} antagonists using structure based drug design," *J. Med. Chem.*, vol. 55, pp. 1898–1903, 2012.

[541] T. Hino, T. Arakawa, H. Iwanari, T. Yurugi-Kobayashi, C. Ikeda-Suno, Y. Nakada-Nakura, O. Kusano-Arai, S. Weyand, T. Shimamura, N. Nomura, A. D. Cameron, T. Kobayashi, T. Hamakubo, S. Iwata, and T. Murata, "G-protein-coupled receptor inactivation by an allosteric inverse-agonist antibody," *Nature*, vol. 482, pp. 237–240, Feb. 2012.

[542] S. H. Park, B. B. Das, F. Casagrande, Y. Tian, H. J. Nothnagel, M. Chu, H. Kiefer, K. Maier, A. A. De Angelis, F. M. Marassi, and S. J. Opella, "Structure of the chemokine receptor CXCR1 in phospholipid bilayers," *Nature*, vol. 491, pp. 779–783, Nov. 2012.

[543] Q. Tan, Y. Zhu, J. Li, Z. Chen, G. W. Han, I. Kufareva, T. Li, L. Ma, G. Fenalti, J. Li, W. Zhang, X. Xie, H. Yang, H. Jiang, V. Cherezov, H. Liu, R. C. Stevens, Q. Zhao, and B. Wu, "Structure of the CCR5 Chemokine receptor-HIV entry inhibitor maraviroc complex," *Science*, vol. 341, no. September, pp. 1387–1390, 2013.

[544] K. Haga, A. C. Kruse, H. Asada, T. Yurugi-Kobayashi, M. Shiroishi, C. Zhang, W. I. Weis, T. Okada, B. K. Kobilka, T. Haga, and T. Kobayashi, "Structure of the human M2 muscarinic acetylcholine receptor bound to an antagonist," *Nature*, vol. 482, pp. 547–551, Feb. 2012.

[545] A. C. Kruse, A. M. Ring, A. Manglik, J. Hu, K. Hu, K. Eitel, H. Hübner, E. Pardon, C. Valant, P. M. Sexton, A. Christopoulos, C. C. Felder, P. Gmeiner, J. Steyaert, W. I. Weis, K. C. Garcia, J. Wess, and B. K. Kobilka, "Activation and allosteric modulation of a muscarinic acetylcholine receptor," *Nature*, vol. 504, pp. 101–106, Dec. 2013.

[546] S. Granier, A. Manglik, A. C. Kruse, T. S. Kobilka, F. S. Thian, W. I. Weis, and B. K. Kobilka, "Structure of the δ-opioid receptor bound to naltrindole," *Nature*, vol. 485, pp. 400–404, May 2012.

[547] G. Fenalti, P. M. Giguere, V. Katritch, X.-P. Huang, A. A. Thompson, V. Cherezov, B. L. Roth, and R. C. Stevens, "Molecular control of δ-opioid receptor signalling," *Nature*, vol. 506, pp. 191–196, Feb. 2014.

[548] D. Wacker, C. Wang, V. Katritch, G. W. Han, X.-P. Huang, E. Vardy, J. D. McCorvy, Y. Jiang, M. Chu, F. Y. Siu, W. Liu, H. E. Xu, V. Cherezov, B. L. Roth, and R. C. Stevens, "Structural features for functional selectivity at serotonin receptors," *Science*, vol. 340, pp. 615–619, May 2013.

[549] W. Liu, D. Wacker, C. Gati, G. W. Han, D. James, D. Wang, G. Nelson, U. Weierstall, V. Katritch, A. Barty, N. A. Zatsepin, D. Li, M. Messerschmidt, S. Boutet, G. J. Williams, J. E. Koglin, M. M. Seibert, C. Wang, S. T. A. Shah, S. Basu, R. Fromme, C. Kupitz, K. N. Rendek, I. Grotjohann, P. Fromme, R. A. Kirian, K. R. Beyerlein, T. A. White, H. N. Chapman, M. Caffrey, J. C. H. Spence, R. C. Stevens, and V. Cherezov, "Serial Femtosecond Crystallography of G Protein-Coupled Receptors," *Science*, vol. 342, no. 12, pp. 1521–1524, 2013.

[550] C. Wang, Y. Jiang, J. Ma, H. Wu, D. Wacker, V. Katritch, G. W. Han, W. Liu, X.-P. Huang, E. Vardy, J. D. McCorvy, X. Gao, X. E. Zhou, K. Melcher, C. Zhang, F. Bai, H. Yang, L. Yang, H. Jiang, B. L. Roth, V. Cherezov, R. C. Stevens, and H. E. Xu, "Structural basis for molecular recognition at serotonin receptors," *Science*, vol. 340, pp. 610–614, May 2013.

[551] E. Y. T. Chien, W. Liu, Q. Zhao, V. Katritch, G. W. Han, M. A. Hanson, L. Shi, A. H. Newman, J. A. Javitch, V. Cherezov, R. C. Stevens, and G. Won Han, "Structure of the human dopamine D3 receptor in complex with a D2/D3 selective antagonist," *Science*, vol. 330, pp. 1091–1095, Nov. 2010.

[552] T. Shimamura, M. Shiroishi, S. Weyand, H. Tsujimoto, G. Winter, V. Katritch, R. Abagyan, V. Cherezov, W. Liu, G. W. Han, T. Kobayashi, R. C. Stevens, and S. Iwata, "Structure of the human histamine H_1 receptor complex with doxepin," *Nature*, vol. 475, pp. 65–70, July 2011.

[553] A. A. Thompson, W. Liu, E. Chun, V. Katritch, H. Wu, E. Vardy, X.-P. Huang, C. Trapella, R. Guerrini, G. Calo, B. L. Roth, V. Cherezov, and R. C. Stevens, "Structure of the nociceptin/orphanin FQ receptor in complex with a peptide mimetic," *Nature*, vol. 485, pp. 395–399, May 2012.

[554] M. A. Hanson, C. B. Roth, E. Jo, M. T. Griffith, F. L. Scott, G. Reinhart, H. Desale, B. Clemons, S. M. Cahalan, S. C. Schuerer, M. G. Sanna, G. W. Han, P. Kuhn, H. Rosen, and R. C. Stevens, "Crystal structure of a lipid G protein-coupled receptor," *Science*, vol. 335, pp. 851–855, Feb. 2012.

[555] K. Zhang, J. Zhang, Z.-G. Gao, D. Zhang, L. Zhu, G. W. Han, S. M. Moss, S. Paoletta, E. Kiselev, W. Lu, G. Fenalti, W. Zhang, C. E. Müller, H. Yang, H. Jiang, V. Cherezov, V. Katritch, K. A. Jacobson, R. C. Stevens, B. Wu, and Q. Zhao, "Structure of the human $P2Y_{12}$ receptor in complex with an antithrombotic drug," *Nature*, Mar. 2014.

[556] J. Zhang, K. Zhang, Z.-G. Gao, S. Paoletta, D. Zhang, G. W. Han, T. Li, L. Ma, W. Zhang, C. E. Müller, H. Yang, H. Jiang, V. Cherezov, V. Katritch, K. A. Jacobson, R. C. Stevens, B. Wu, and Q. Zhao, "Agonist-bound structure of the human $P2Y_{12}$ receptor," *Nature*, vol. 509, pp. 119–122, May 2014.

[557] A. Srivastava, J. Yano, Y. Hirozane, G. Kefala, F. Gruswitz, G. Snell, W. Lane, A. Ivetac, K. Aert-

geerts, J. Nguyen, A. Jennings, and K. Okada, "High-resolution structure of the human GPR40 receptor bound to allosteric agonist TAK-875," *Nature*, July 2014.

[558] K. Hollenstein, J. Kean, A. Bortolato, R. K. Y. Cheng, A. S. Doré, A. Jazayeri, R. M. Cooke, M. Weir, and F. H. Marshall, "Structure of class B GPCR corticotropin-releasing factor receptor 1," *Nature*, vol. 499, pp. 438–443, July 2013.

[559] F. Y. Siu, M. He, C. de Graaf, G. W. Han, D. Yang, Z. Zhang, C. Zhou, Q. Xu, D. Wacker, J. S. Joseph, W. Liu, J. Lau, V. Cherezov, V. Katritch, M.-W. Wang, and R. C. Stevens, "Structure of the human glucagon class B G-protein-coupled receptor," *Nature*, vol. 499, pp. 444–449, July 2013.

[560] H. Wu, C. Wang, K. J. Gregory, G. W. Han, H. P. Cho, Y. Xia, C. M. Niswender, V. Katritch, J. Meiler, V. Cherezov, P. J. Conn, and R. C. Stevens, "Structure of a class C GPCR metabotropic glutamate receptor 1 bound to an allosteric modulator," *Science*, vol. 344, pp. 58–64, Apr. 2014.

[561] A. S. Doré, K. Okrasa, J. C. Patel, M. Serrano-Vega, K. Bennett, R. M. Cooke, J. C. Errey, A. Jazayeri, S. Khan, B. Tehan, M. Weir, G. R. Wiggin, and F. H. Marshall, "Structure of class C GPCR metabotropic glutamate receptor 5 transmembrane domain," *Nature*, vol. 511, pp. 557–562, July 2014.

[562] C. Wang, H. Wu, V. Katritch, G. W. Han, X.-P. Huang, W. Liu, F. Y. Siu, B. L. Roth, V. Cherezov, and R. C. Stevens, "Structure of the human smoothened receptor bound to an antitumour agent," *Nature*, vol. 497, pp. 338–343, May 2013.

[563] U. Weierstall, D. James, C. Wang, T. A. White, D. Wang, W. Liu, J. C. H. Spence, R. Bruce Doak, G. Nelson, P. Fromme, R. Fromme, I. Grotjohann, C. Kupitz, N. A. Zatsepin, H. Liu, S. Basu, D. Wacker, G. W. Han, V. Katritch, S. Boutet, M. Messerschmidt, G. J. Williams, J. E. Koglin, M. Marvin Seibert, M. Klinker, C. Gati, R. L. Shoeman, A. Barty, H. N. Chapman, R. A. Kirian, K. R. Beyerlein, R. C. Stevens, D. Li, S. T. A. Shah, N. Howe, M. Caffrey, and V. Cherezov, "Lipidic cubic phase injector facilitates membrane protein serial femtosecond crystallography," *Nat. Commun.*, vol. 5, p. 3309, Jan. 2014.

[564] C. Wang, H. Wu, T. Evron, E. Vardy, G. W. Han, X.-P. Huang, S. J. Hufeisen, T. J. Mangano, D. J. Urban, V. Katritch, V. Cherezov, M. G. Caron, B. L. Roth, and R. C. Stevens, "Structural basis for Smoothened receptor modulation and chemoresistance to anticancer drugs," *Nat. Commun.*, vol. 5, p. 4355, Jan. 2014.

[565] G. Jeschke, "Instrumentation and experimental setup," in *ESR Spectrosc. Membr. Biophys.*, pp. 17–47, Springer, 2007.